

Modelling Microstructure-Property Relationships in Polycrystalline Metals using New Fast Fourier Transform- Based Crystal Plasticity Frameworks

by

Jaspreet Singh Nagra

A thesis
presented to the University of Waterloo
in the fulfillment of the
thesis requirement for the degree of
Doctor of Philosophy
in
Mechanical and Mechatronics Engineering

Waterloo, Ontario, Canada, 2019

© Jaspreet Nagra 2019

Examining Committee Membership

The following served on the Examining Committee for this thesis. The decision of the Examining Committee is by majority vote.

External Examiner	Anthony Rollett, PhD Professor, Materials Science & Engineering, Carnegie Mellon University, Pittsburgh, PA, USA
Supervisor(s)	Kaan Inal, PhD NSERC/General Motors Industrial Research Chair in “Integrated Computational Mechanics for Mass Efficient Automotive Structures”; Associate Professor, Mechanical and Mechatronics Engineering, University of Waterloo, Waterloo, ON, Canada Sanjeev Bedi, PhD, PEng NSERC Chair in “Immersive Design Engineering Activities”; Professor, Mechanical and Mechatronics Engineering, University of Waterloo, Waterloo, ON, Canada
Internal Member	Soo Jeon, PhD, PEng Associate Professor, Mechanical and Mechatronics Engineering, University of Waterloo, Waterloo, ON, Canada
Internal Member	Clifford Butcher, PhD Assistant Professor, Mechanical and Mechatronics Engineering, University of Waterloo, Waterloo, ON, Canada
Internal-external Member	Susan Tighe, PhD, PEng Deputy Provost and Associate Vice-President in “Integrated Planning and Budgeting”; Professor, Civil and Environmental Engineering, University of Waterloo, Waterloo, ON, Canada

Author's Declaration

This thesis consists of material all of which I authored or co-authored: see Statement of Contributions included in the thesis. This is a true copy of the thesis, including any required final revisions, as accepted by my examiners.

I understand that my thesis may be made electronically available to the public.

Statement of Contributions

The following co-authors have contributed to the current work as outlined below:

Professor Kaan Inal and Professor Sanjeev Bedi supervised this PhD thesis.

Dr. Ricardo Lebensohn (Scientist and Team Leader, Los Alamos National Laboratory, NM, USA), provided crystal plasticity-based elasto-viscoplastic fast Fourier transform (EVP-FFT) code. He also assisted the authors with editing parts of the work.

Dr. Raja Mishra (Research & Development Center, General Motors, Warren, MI, USA), provided EBSD measurements of the polycrystalline metals studied and the experimental data for calibrating and validation of the numerical frameworks.

Dr. Abhijit Brahme (Research Associate, University of Waterloo), converted EBSD measurements to the synthetic 3D microstructure for simulations and assisted the authors with editing parts of the work.

Dr. Julie Levesque (Project Manager, Research & Development Center, Québec Metallurgy Centre and Adjunct Professor at University of Waterloo), provided Taylor-type elasto-viscoplastic constitutive model for magnesium alloys.

The balance of this work is my own.

Abstract

The present thesis develops several new full-field, fast Fourier transform (FFT)-based crystal plasticity modelling tools for microstructure engineering. These tools are used to explore elasto-viscoplastic deformation, localized deformation, 3D grain morphology, microstructure evolution, dynamic recrystallization and their effects on formability of polycrystalline metals with particular attention paid to sheet alloys of aluminum and magnesium. The new FFT-based crystal plasticity models developed in this work overcome several inherent problems present in the well-known crystal plasticity finite element method (CP-FEM) and elasto-viscoplastic fast Fourier transform method (EVP-FFT) in solving representative volume element (RVE)-based problems. The new models have demonstrated significant fidelity in simulating various deformation phenomena in polycrystalline metals and prove to be faster and accurate alternatives for obtaining full-field solutions of micromechanical fields in aluminum and magnesium sheet alloys.

In particular to the aluminum alloys, which are currently replacing heavier steel parts in the automotive industry, the sheet aluminum alloys have significantly improved corrosion resistance and strength-to-weight properties in comparison to steel. However, aluminum alloys are still outperformed by steel in terms of formability. To improve the formability of an aluminum sheet, one method is to develop physics-based predictive computational tools, which can accurately and efficiently predict the behavior of aluminum alloys and thus allow designing the microstructure with desired properties.

Accordingly, in first part of this thesis, a novel numerical framework for modelling large deformation in aluminum alloys is developed. The developed framework incorporates the rate-dependent crystal plasticity theory into the fast Fourier transform (FFT)-based formulation, and this is named as rate tangent crystal plasticity-based fast Fourier transform (i.e., RTCP-FFT) framework. This framework is used as a predictive tool for obtaining stress-strain response and texture evolution in new strain-paths with minimal calibration for aluminum alloys. The RTCP-FFT framework is benchmarked against an existing FFT-based model at small strains and finite element-based model at large strains, respectively, for the case of an artificial Face Centered Cubic (FCC) polycrystal. The predictive capability as well as the computational efficiency of the developed framework are then demonstrated for aluminum alloy (AA) 5754.

In the second part of this thesis, the RTCP-FFT framework, developed earlier, is coupled with the Marciniak and Kuczynski (MK) approach to establish a new full-field framework for generating forming limit diagrams (FLDs) of aluminum sheet alloys, e.g., AA3003 and AA5754. The new coupled framework is able to investigate the complex effects of grain morphology, local deformation, local texture and grain interactions on the predictions of forming limit strains. This study reveals that among the various microstructural features, the grain morphology has the strongest effect on the predicted FLDs for aluminum alloys. Furthermore, this study also suggests that the FLD predictions can be significantly improved if the actual grain structure of the material is properly accounted for in the crystal plasticity models.

In addition to aluminum alloys, magnesium alloys are getting significant attention by the automotive industry due to their light weight and high specific strength. However, the automotive industry has not been able to take full advantage of the lightweight characteristic of magnesium alloys because of their poor formability at room temperature. Therefore, to enhance the workability and restore their ductility, the magnesium alloys are formed at elevated temperature. High temperature forming of magnesium alloys is often accompanied by dynamic recrystallization (DRX), which allows the final microstructure, as well as the properties of the material (e.g., initial grain size, initial texture, etc.), to be controlled. Therefore, DRX coupled with a full-field crystal plasticity FLD framework can be used as a tool to design microstructure of a material. Since it would be beneficial to be able to redesign the material properties of magnesium alloys using physics-based computational tools than using physical experiments, this work takes a step ahead towards such an outcome by presenting a new framework that predicts DRX and models its effects on the formability of magnesium alloys.

Accordingly, in the third part of this thesis, a new full-field, efficient and mesh-free numerical framework, to model microstructure evolution, dynamic recrystallization (DRX) and formability in hexagonal closed-packed (HCP) metals such as magnesium alloys at warm temperatures, is developed. This coupled framework combines three new FFT-based approaches, namely: (a) crystal plasticity modelling of HCP alloys, (b) DRX model, and (c) MK model. First, a rate tangent-fast Fourier transform-based elasto-viscoplastic crystal plasticity constitutive model for HCP metals (RTCP-FFT-HCP) is developed. Then, it is coupled with a probabilistic cellular automata (CA) approach to model DRX. Furthermore, this new model is coupled with the

Marciniak-Kuczynski (M-K) approach to model formability of magnesium alloys at elevated temperatures.

The RTCP-FFT-HCP model computes macro stress-strain response, twinning volume fraction, micromechanical fields, texture evolution and local dislocation density. Nucleation of new grains and their subsequent growth is modeled using the cellular automata approach with probabilistic state switching rule. This framework is validated at each level of the coupling for magnesium sheet alloy, AZ31. First, the RTCP-FFT-HCP model is validated by comparing the simulated macro stress-strain responses under uniaxial tension and compression with experimental measurements at room temperature. Furthermore, the texture evolution predicted with the new model is compared with experiments. The predictions show a good agreement with experiments with high degree of accuracy. Next, the forming limit diagrams (FLDs) are simulated at 100 °C, 200 °C and 300 °C, respectively, for AZ31 sheet alloy considering the effects of DRX. The predicted FLDs show very good agreement with the experimental measurements. The study reveals that the DRX strongly affects the deformed grain structure, grain size and texture evolution and also highlights the importance accounting for DRX during FLD simulations at high temperatures.

Acknowledgements

I would like to express my sincere gratitude to my supervisors; Professor Kaan Inal and Professor Sanjeev Bedi, for the years of support, leadership, assistance, and guidance they have provided me. My sincere thanks go to Dr. Abhijit Brahme for his amazing expertise and mentorship for the past years during my PhD.

This work was financially supported by the Natural Sciences and Engineering Research Council of Canada (NSERC) and the General Motors of Canada under NSERC-Industrial Research Chair (NSERC-IRC) grant no. IRCPJ-503185-2016.

Table of Contents

List of Figures.....	xiv
List of Tables	xxii
List of Abbreviations.....	xxiii
Chapter 1. Introduction	1
1.1 Background -----	1
1.2 Motivation-----	2
1.3 Research Scope and Research Problems -----	5
1.4 Research Objectives and Associated Tasks-----	7
1.5 Organization of Thesis -----	9
Chapter 2. Literature Review	11
2.1 Introduction -----	11
2.1.1 Crystal Structures.....	12
2.1.2 Crystallographic Texture.....	13
2.1.3 Microstructure and Representative Volume Element	15
2.1.4 Deformation Mechanisms in FCC metals	17
2.1.5 Deformation Mechanisms in HCP Metals	20
2.1.6 Recrystallization	23
2.1.7 Fourier Transform-based Methods	24
2.1.8 Instability, Localization and Failure in Metals	30
2.2 Development of Advanced Crystal Plasticity Models-----	32
2.2.1 Sach's Model.....	34

2.2.2 The Taylor Crystal Theory	34
2.2.3 Relaxed Constraint Models	35
2.2.4 Grain Interaction Models	36
2.2.5 Self-Consistent Schemes	37
2.2.6 Spectral Crystal Plasticity (SCP)	37
2.2.7 Crystal Plasticity Finite Element Method (CP-FEM)	38
2.2.8 Crystal Plasticity Fast Fourier Transform Method (CP-FFT)	40
2.3 Modelling Dynamic Recrystallization	42
2.3.1 Monte Carlo Models	44
2.3.2 Vertex Models	45
2.3.3 Phase-Field Models	46
2.3.4 Cellular Automata	47
2.4 Modelling Forming Limit Diagrams of Polycrystals	49
2.5 Brief Conclusions of Literature Review	52
Chapter 3. – Part 1: Efficient Fast Fourier Transform-based Numerical Implementation to Simulate Large Strain Behavior of Polycrystalline Materials, Published in International Journal of Plasticity 98 (2017) 65-82	54
3.1 Introduction	55
3.2 Model Formulation	57
3.2.1 Crystal Plasticity Constitutive Model	58
3.2.2 Rate Tangent Modulus Method	61
3.2.3 FFT Model and Implementation of the New Crystal Plasticity Framework	64

3.3 Model Calibration and Validation	68
3.4 Application to Aluminum Alloy (AA) 5754	73
3.4.1 Model Setup.....	73
3.4.2 Boundary Conditions	74
3.4.3 Model Calibration	75
3.4.4 Simulations of Balanced Biaxial Tension and Plane Strain Tension.....	76
3.4.5 Predictions of Texture Evolution.....	77
3.4.6 Computational Efficiency	81
3.5 Summary and Conclusions	83
Chapter 4. – Part 2: An Efficient Full-Field Crystal Plasticity-based M-K Framework to Study the Effect of 3D Microstructural Features on the Formability of Polycrystalline Materials, Published in Modelling and Simulation in Materials Science and Engineering (2018), Volume 26, Number 7	85
4.1 Introduction	86
4.2 Constitutive Framework	90
4.3 Results: Application to Aluminum Alloys.....	95
4.3.1 Predicted FLDs for AA5754	96
4.3.2 Predicted FLDs for AA3003	100
4.4 Discussions.....	104
4.4.1 Effects of Grain Morphology on Localized Deformation.....	105
4.4.2 Effects of Local Grain Neighborhoods and Texture Evolution on FLDs	112
4.5 Summary	113
Chapter 5. – Part 3: A New Micromechanics-Based Full-Field Numerical Framework to Simulate the Effects of Dynamic Recrystallization on the Formability of HCP Metals, submitted to International Journal of Plasticity	115

5.1 Introduction -----	116
5.2 Model Description-----	121
5.2.1 Rate Tangent-Crystal Plasticity Fast Fourier Transform Model for HCP alloys (RTCP-FFT-HCP)	121
5.2.2 Dynamic Recrystallization (DRX) Model.....	132
5.2.3 Marciniak and Kuczyński (M-K) Framework.....	138
5.3 Experimental Data-----	140
5.4 Synthetic 3D Microstructure -----	141
5.5 Results and Discussions -----	142
5.5.1 Calibration of RTCP-FFT-HCP Model.....	142
5.5.2 Validation of RTCP-FFT-HCP Model.....	144
5.5.3 Coupled Model Calibration at Elevated Temperatures.....	147
5.5.4 FLD Predictions with and without DRX at Elevated Temperatures	150
5.5.5 Evolving Microstructure during DRX at 300 °C Inside Band	153
5.5.6 Recrystallization Outside and Inside Band	155
5.5.7 Effects of Initial Imperfection on FLD Predictions without DRX	155
5.6 Conclusions -----	156
Chapter 6. Conclusions and Future Work	158
6.1 Advantages of the Developed Models -----	161
6.2 Limitations of the Developed Models-----	161
6.3 Scope for Future Work-----	162
References.....	163

Appendix - A. Comparison of RTCP-FFT Model with CP-FEM Model	191
---------------------------------------------------------------------------	------------

List of Figures

Figure 2.1: Grains and grain boundaries in a polycrystal. To the right, defect in atomic structure: grain boundaries (orange spheres), to the left, grains (in yellow) and grain boundaries (in black) as seen through an optical microscope (Callister Jr, 2000).	12
Figure 2.2: Unit cells of typical metallic crystal structures showing atomic arrangement for: (a) BCC (Body-centered cubic), (b) FCC (Face-centered cubic) and (c) HCP (Hexagonal closed pack) (Conway and Sloane, 1993).	13
Figure 2.3: Experimentally measured texture of (AA) 5754-O tempered sheet (available in-house).	14
Figure 2.4: EBSD observation areas (Brahme et al., 2006).	16
Figure 2.5: RVEs with different grain morphologies generated using Voronoi tessellation algorithm (M-builder). Only full-field crystal plasticity models (e.g., CP-FFT and CP-FEM) can explicitly account for different grain shapes in 3D microstructure.	17
Figure 2.6: Example showing movement of dislocations similar to that of a caterpillar (Callister Jr, 2000).	18
Figure 2.7: (a) $(1\ 1\ 1) \langle 1\ 1\ 0 \rangle$ slip system in FCC unit cell (b) $(1\ 1\ 1)$ Plane from (a) and three slip directions within the plane (shown by arrows) (Callister Jr, 2000).	19
Figure 2.8: Description of Schmid's law: (a) A resolved shear stress, τ_r , is produced on a slip system. (b) Movement of dislocations on the slip system deforms the material (Callister Jr, 2000).	20
Figure 2.9: Unit cell of HCP metals.	21
Figure 2.10: Slip systems and twinning systems in HCP metals (Partridge, 1967).	21
Figure 2.11: Schematic representation of twinning process (Paufler, 1994).	22

Figure 2.12: Microstructure evolution during annealing of Al-0.1% Mn alloy after 95% cold rolling (Gottstein, 2004).	23
Figure 2.13: Decimation in Time method of FFT (Marks, 2009).....	28
Figure 2.14: (a) FLD defined by Keeler (1961) and Goodwin (1968), (b) Probabilistic FLD of four different grades of O-tempered AA5182.....	31
Figure 2.15: Four common types of crystal plasticity models to estimate polycrystal response (Roters et al., 2012).....	33
Figure 2.16: FFT-based methods for composites and polycrystals.	42
Figure 2.17: Schematic representation of the division of the domain for Monte Carlo method (Hallberg, 2011).....	45
Figure 2.18: Schematic of grain boundary definition in vertex model (Miodownik, 2002).	45
Figure 2.19: Schematic representation of the division of the domain in the phase-field model (Miodownik, 2002).	47
Figure 2.20: Schematic representation of the grain boundaries in cellular automata (Janssens, 2003).....	48
Figure 2.21: Schematic of M-K instability criteria (Mohammadi et al., 2014).....	50
Figure 3.1: The synthesized microstructure of copper polycrystal and for an artificial FCC polycrystal with 16 x 16 x 16 Fourier points in 100 grains showing initial texture distribution. .	68
Figure 3.2: Predicted von Mises equivalent stress–strain curves during uniaxial tension along RD using the EVP-FFT model for cases of the copper polycrystal and an artificial FCC polycrystal.	69
Figure 3.3: Comparisons of the predicted von Mises equivalent stress–strain curves during uniaxial tension along RD between the RTCP-FFT and EVP-FFT models for; (a) copper polycrystal, and (b) an artificial polycrystal.	70

Figure 3.4: Comparison of the simulated micromechanical fields for the copper polycrystal ($A = 2.2$) at 5% equivalent strain during uniaxial tension along RD; (a-b) – distribution of the von Mises equivalent stress (MPa), (c-d) – distribution of equivalent strain.....	71
Figure 3.5: Comparison of variations in the local fields for each voxel between the RTCP-FFT and the EVP-FFT models in copper polycrystal ($A = 2.2$) at 5% equivalent strain during uniaxial tension along RD: (a) mismatch in the local equivalent strain, (b) mismatch in the local equivalent stress.	72
Figure 3.6: Comparison of initial texture: (a) pole figure representations of the as-received experimental texture and (b) fitted texture; Comparison of contours of experimental ODFs (c) and fitted ODFs (d) at 0, 45, and 60 degrees of ϕ 2 sections. (e) The generated microstructure with 128 x 128 x 128 points in 8837 equiaxed grains, the colors represent different grains.	74
Figure 3.7: (a) Comparison of macroscopic stress strain curves of measured data (Hu et al., 2011) and simulated response by calibrated-RTCP-FFT model for RD-uniaxial tension. (b) Simulated texture in form of pole figure for RD-uniaxial tension after 15% true strain. (c) and (d) Comparison of ODF sections of measured and simulated texture for RD-uniaxial tension at 5%, 10% and 15% true strain.	75
Figure 3.8: Comparison of predicted and measured (Hu et al., 2011) stress-strain curves for four different strain paths after 15% true strain; (a) equibiaxial tension (σ_{11}, e_{11}), (b) plane-strain tension in RD (σ_{11}, e_{11}), (c) Uniaxial tension in TD (σ_{22}, e_{22}) and (d) plane strain tension in TD (σ_{22}, e_{22}).....	76
Figure 3.9: Comparison of predicted texture in form of pole figures for four different strain paths; (a) equibiaxial tension, (b) plane strain tension along RD, (c) uniaxial tension along TD and (d) plane strain tension along TD.	77
Figure 3.10: Comparison of measured (Hu et al., 2011) and predicted ODF sections at strain levels of 5, 10, and 15% for equibiaxial tension.....	79
Figure 3.11: Comparison of measured (Hu et al., 2011) and predicted ODF sections at strain levels of 5, 10, and 15% for plane strain tension in RD.....	79

Figure 3.12: Comparison of measured (Hu et al., 2011) and predicted ODF sections at strain levels of 5, 10, and 15% for plane strain tension in TD.	80
Figure 3.13: Comparison of measured (Hu et al., 2011) and predicted ODF sections at strain levels of 5, 10, and 15% for uniaxial tension in TD.	80
Figure 3.14: The synthesized microstructure of AA5754 consisting of one Fourier point per grain with 16 Fourier points in each of x, y and z-axis representing 4096 Cube grains, the colors represent different grains. (b) Computational cost comparison of proposed model (RTCP-FFT) and EVP-FFT model for three different strain paths up to 20% true strain.	81
Figure 3.15: A comparison of CPU time required by proposed model (RTCP-FFT) and EVP-FFT model respectively to complete RD uniaxial tension simulation up to 20% true strain versus total number of Fourier points in each of six different RVEs used; (a) Bar chart representation (b) log plot showing proportional limit.	82
Figure 4.1: Graphical abstract of Chapter 4.	86
Figure 4.2: Initial configuration of M-K criteria used for FLD analysis; a) 3D representation of sheet metal, RVEs, boundary conditions and imperfection band, b) Schematic of top surface of sheet showing band direction vectors and initial band angle.	94
Figure 4.3: 2D Electron backscatter diffraction (EBSD) map used to generate synthetic microstructure for AA5754.	95
Figure 4.4: Comparison of initial texture of AA5754-O: pole figure representations of the experimental texture (a) and fitted texture (b); Comparison of contours of experimental ODFs (c) and fitted ODFs (d) at 0, 45, and 60 degrees of ϕ 2 sections. (e) The generated microstructure with 64 x 64 x 64 Fourier points in 278 grains, the colors represent different grains.	97
Figure 4.5: Comparison of overall stress-strain curves of measured data and simulated response by calibrated-RTCP-FFT and Taylor models respectively for RD uniaxial tension at 25 °C.....	98
Figure 4.6: Comparison of FLD predictions of AA5754-O at 25 °C using MK-RTCP-FFT and MK-Taylor models with experiment data (Cyr et al., 2017).	99

Figure 4.7: Evolution of critical imperfection band angle with strain path of AA5754-O predicted using MK-RTCP-FFT and MK-Taylor models.	100
Figure 4.8: 2D Electron backscatter diffraction (EBSD) map used to generate synthetic microstructure for AA3003.	101
Figure 4.9: Comparison of initial texture of AA3003-O: pole figure representations of the experimental texture (a) and fitted texture (b); Comparison of contours of experimental ODFs (c) and fitted ODFs (d) at 0, 45, and 60 degrees of ϕ 2 sections. (e) The generated microstructure with 64 x 64 x 64 Fourier points in 916 grains, the colors represent different grains.	102
Figure 4.10: Comparison of overall stress-strain curves of measured data (Bagheriasl et al., 2011) and simulated response by calibrated-RTCP-FFT and Taylor models for AA3003-O under uniaxial tension along RD at 25 °C.	103
Figure 4.11: (a) Comparison of predicted FLDs for AA3003-O using MK-RTCP-FFT model and MK-Taylor model with experimental observations at 25 °C. (b) Comparison of evolution of imperfection band angle with strain ratio predicted using MK-RTCP-FFT model and MK-Taylor model.	104
Figure 4.12: RVEs for model A, inverse pole figure maps showing initial texture distribution and grain morphology.	105
Figure 4.13: Comparison of overall stress-strain response of the RVEs for model A with columnar, equiaxed and elongated grain structure respectively under uniaxial tension along RD.	106
Figure 4.14: Comparison of predicted FLDs for using different grain morphologies (model A) with experimental observations.	107
Figure 4.15: Results of in-plane plane strain tension: Distribution of equivalent strain on surface of RVEs inside and outside the imperfection band (columns) with different grain morphologies (rows).	108

Figure 4.16: Inverse pole figures (IPFs) of selected 7 grains in (a) Columnar grains, (b) Equiaxed grains, (c) Elongated grains. Blue dot - initial texture, orange dot - deformed texture of grain in IPF after in-plane plane strain tension up to 14.1% true strain.	110
Figure 4.17: Comparison of predicted average and maximum misorientations for columnar grains, equiaxed grains, and Elongated grains after in-plane plane strain tension up to 14.1% true strain.	111
Figure 4.18: RVEs for model B, inverse pole figure maps showing initial texture distribution and grain morphology.	112
Figure 4.19: Comparison of predicted FLDs for models A, B and C; (a) columnar grains, (b) equiaxed grains, (c) elongated grains.	113
Figure 5.1: Modified Moore neighborhood is used in the present work; defining a material point and its neighbors in 3D space using a spherical boundary with 26-point scheme. A material point interacts with all other material points that lie at distance less than the radius of the sphere.	136
Figure 5.2: Flowchart for the proposed numerical framework.	138
Figure 5.3: Schematic of M-K framework: initial configuration of an orthotropic sheet showing imperfection band direction vectors (n and t), band angle, initial thicknesses and boundary conditions.	140
Figure 5.4: Experimentally measured microstructure; (a) EBSD scan, (b) 0001 polefigure, and (c) 10-10 polefigure.	141
Figure 5.5: Regenerated synthetic microstructure with 276 grains, shown in (a), (b) and (c) show 0001 and 10-10 polefigures.	142
Figure 5.6: Comparison of the simulated flow curves (Red) and experimentally measured responses (Blue triangles) for uniaxial; (a) tension, and (b) compression.	143
Figure 5.7: Predicted texture after 8% uniaxial compression, shown in (a) and compared to that reported by Khan et al. (2011) shown in (b).	144

Figure 5.8: Slip and twin system activity during uniaxial compression along RD till 20% uniaxial compression.	145
Figure 5.9: (a) Distribution of volume fraction of twins and (b) stress distribution in the microstructure at 8% uniaxial compression along RD (X).	146
Figure 5.10: Experimental trues stress-strain curves for AZ31 sheet alloy at 100 °C, 200 °C, and 300 °C, respectively, reproduced from Chen et al. (2003).	148
Figure 5.11: Trues stress-strain for AZ31 alloy at (a) 100 °C, (b) 200 °C, and (c) 300 °C. Black dashed line shows experimental data (Chen et al., 2003), the model prediction with and without DRX are shown with red and blue lines, respectively.	149
Figure 5.12: Comparison of predicted FLD (with and without DRX) with experimental FLD of AZ31 sheet alloy strain at (a) 100 °C, (b) 200 °C, and (c) 300 °C.	150
Figure 5.13: Evolution of recrystallized volume fraction (percentage) during deformation for uniaxial tension ($\rho = -0.5$) at 300 °C. The microstructure showing location of the recrystallized grain structure is overlaid on top.	151
Figure 5.14: Showing evolution of (i) recrystallized grains, (ii) grain boundary migration, (iii) DRX wave-front and (iv) the equivalent stress distribution in the microstructure for uniaxial tension ($\rho = -0.5$) at 300 °C.	152
Figure 5.15: Showing at the top the initial RVE, which is identical both inside and outside the band. The resultant microstructure at failure strains outside and inside the band for biaxial tension ($\rho = 0.2$) at 300 °C are shown below. Both these show different evolution with regards to amount of DRX.	153
Figure 5.16: DRX volume fraction (percentage) inside and outside band with minor strain at failure strains at 100, 200 and 300°C.	154
Figure 5.17: Comparison of predicted FLDs without DRX model (re-calibrated plane strain limit strain) with reduced imperfection (i.e., higher imperfection factor, f^{imp} in Equation (5.52)) with	

DRX model as well as with the experimental FLD of AZ31 sheet alloy strain at (a) 100 °C, (b) 200 °C, and (c) 300 °C.	156
Figure 6.1: Summary of the developed models in present thesis.	160
Figure AA - 1: Comparison of local distribution of equivalent stress at 9% true strain in uniaxial tension, results show that the developed model (RTCP-FFT) is in good agreement with CP-FEM model.....	191

List of Tables

Table 2.1: Euler angles (in degrees) for the common texture components in FCC metals (Kocks et al., 2005). -----	15
Table 3.1: Adopted elastic constants for copper polycrystal (Simmons and Wang, 1971) and for an artificial polycrystal (Lebensohn et al., 2012). -----	73
Table 3.2: Constitutive parameters used to calibrate RTCP-FFT model for uniaxial tension along RD. -----	74
Table 4.1: Constitutive parameters used to calibrate models for RD uniaxial tension. -----	98
Table 4.2: Constitutive parameters used to calibrate RTCP-FFT and Taylor models for RD uniaxial tension. -----	101
Table 4.3: Volume fraction of different texture components (within 15° from the exact component location); initial and after in-plane plane strain tension up to 14.1% true strain. -----	111
Table 5.1: Slip and twinning systems used in proposed framework. -----	122
Table 5.2: Constitutive parameters used to calibrate proposed model for RD uniaxial tension and compression at room temperature. -----	144
Table 5.3: Constitutive parameters used to calibrate coupled MK-CA-RTCPFFT-HCP model for RD uniaxial tension at 100 °C, 200 °C and 300 °C, respectively. -----	147

List of Abbreviations

BCC	body centered cubic	IPF	inverse pole figure
CA	cellular automata	LAGB	low angle grain boundary
CP	crystal plasticity	MK	Marciniak and Kuczynski
CP-FE	crystal plasticity-finite element	ND	normal direction
CP-FFT	crystal plasticity-fast Fourier transform	ODF	orientation distribution function
CRSS	critical resolved shear stress	PF	pole figure
DFT	discrete Fourier transform	RC	relaxed constraint
DRX	dynamic recrystallization	RD	rolling direction
EBSD	electron back-scattering diffraction	RGC	relaxed grain cluster
FC	full-constraint	RTCP-FFT	rate tangent crystal plasticity fast Fourier transform
FCC	face centered cubic	RVE	representative volume element
FFT	fast Fourier transform	SC	self-consistent
FLD	forming limit diagram	SCP	spectral crystal plasticity
GIA	grain interactions model	SRX	static recrystallization
HAGB	high angle grain boundary	TD	transverse direction
HCP	hexagonal closed pack	VPSC	viscoplastic self-consistent

Chapter 1. Introduction

1.1 Background

Almost every aspect of present-day life involves materials and benefits from the advances in materials research. Laptops, mobile phones, automobiles, aircrafts, power stations, fuels, medications, and much else that we now take for granted, all rely on materials. In addition, numerous processes in the world, ranging from the growth of ice in the upper atmosphere, all the way down to diseases caused by protein mis-folding, also involve the properties of materials. Moreover, many of today's challenges, such as climate change, energy production and healthcare demand robust methods for probing the properties of a vast range of materials. Thus, materials modelling can drive progress, saving time, effort and resources and can be used to solve real-world problems. Modelling means simplification of reality that is intended to promote understanding of a real-world phenomenon.

Describing a physical phenomenon using numerical models have been used for a long time. Around 430 years ago, Galileo Galilei proposed that it is important to depict the outcomes scientifically once a specific number of trials has been performed. If one succeeds in illustrating the physical phenomenon using the mathematical equations, at that point, the response of the system of interest can be anticipated for an expansive scope of conditions, including the ones for which leading the trials are extremely troublesome, too exorbitant, or impractical by any stretch of the imagination. Although, mathematical equations allow one to understand the physical phenomena, yet it is typically considered as an analytical modelling that can take care of simple problems only. Complex phenomena could not be modeled using the analytics until the advent of computers in 19th century that broke the computing barrier and made numerical modelling of physical mechanisms possible for complex parts in an efficient manner with good precision.

The advancements in numerical modelling led to development of several new material modelling techniques, the most popular one among those was finite element method (FEM). Due to its robustness and general applicability, FEM was pleasantly adopted by the academia and the industries all over the world to test large spectrum of problems and thus the applications of

numerical modelling mushroomed drastically over the past few decades. As the usage increased, the roadblocks in numerical modelling also increased, which challenged the assumptions made during the initial development of numerical methods as the technology was hitting its limits. For example, it is easy to predict linear behavior in a homogeneous material using FEM but when it comes to model fracture, the conventional FEM fails. These kinds of problems shifted the focus of researchers to improve the numerical models. In addition, harnessing the increased computational ability of computers, going beyond the macro scale, and analyzing behavior of crystals, atoms, molecules etc. that further led to generation of various material models.

Nowadays, the leading engineering companies, for example, General Electric (GE), General Motors (GM), Ford, Airbus and Boeing use computer simulations to demonstrate, test mechanical and aerodynamic attributes of their products, for example, cars, jet engines and aircrafts, before assembling them or even before testing a prototype model in a wind tunnel or crashing them into a wall. Among the various advantages of the modelling materials, one is that if any issues found in the design amid modelling, it can be fixed before sending the technical illustrations to the assembling unit of the company and thus the expensive economical misfortunes can be avoided.

1.2 Motivation

When consumers think of buying a new vehicle, they expect it to be safe, affordable and fuel-efficient. They envisage faster, stronger and lighter cars. However, people are seldom aware of the race of automotive materials to meet automakers' demands to deliver the definitive lightweight technologies. Consumer preferences have constrained the downsizing options available to automakers. In addition, the safety and performance benchmarks (e.g., The Corporate Average Fuel Economy (CAFE) standards) limit their ability to further reduce the weight of a vehicle with the conventional materials. Every potential vehicle light weighting aspect is under investigation. The main method that automakers use to reduce weight and boost vehicle fuel economy is the material substitution. Thus, replacing heavier iron and steel with light weight advanced composites, plastics, aluminum alloys, magnesium alloys and advanced high-strength steel.

High strength-to-weight ratio, good formability, good corrosion resistance and recycling potential have made aluminum alloys the ideal candidate for the replacement of heavier materials in the

automotive industry. Most aluminum is used for car parts, e.g., cylinder heads, radiators, cars body and wheel rims. However, it was found that magnesium alloys have several advantages over aluminum alloys due to its light weight and physical properties in terms of manufacturability. Because of the increasing need for alternative materials, interest in magnesium alloys has been revived and magnesium alloys have become more common. They are present in automotive components, e.g., steering wheels, steering column parts, instrument panels, seats, gearboxes, and air intake systems. Even though aluminum alloys are still widely used today, the market for magnesium alloys is predicted to develop and their applications will rapidly increase in the near future due to their superior physical and mechanical properties.

Particular to aluminum applications in automotive and aerospace, advances in aluminum engineering over the past few decades have led to the invention of a wide number of alloys for various applications. Typically, these alloys are labeled as (AA) xxxx where AA represents “aluminum alloy” followed by a 4-digit number corresponding to the major alloying element and alloying content. For example, (AA) 5754 is a common aluminum alloy that is used as sheets in door/roof panels of cars and (AA) 3003 is widely used in aircraft structures, especially in wing and fuselage structures that are usually under extreme amount of tension.

The use of magnesium, copper and zinc as alloying elements change the properties of aluminum in such a way that they can be hardened as well as softened by the use of heat. The different heat treatment results in different temper designations and are indicated by a letter number combination following the 4-digit alloy number. The most common temper designations are T3 and T6. The T3 represents solution heat-treated and cold-worked by the flattening process. T6 is also solution heat-treated but artificially aged.

Even though the sheet aluminum alloys have significantly improved corrosion resistance and strength-to-weight properties, yet it is still outperformed by steel in terms of formability. This is a significant drawback as vehicle designs are becoming more intricate and demands for enhanced mechanical properties such as formability are increasing nowadays. Thus, several methods have been provided by the researchers to improve the formability of an aluminum sheet. Controlling the alloying content and alloying elements can improve the materials ductility, but at the cost of some desired properties such as strength.

The material microstructure can also be controlled; however, this requires complex material processing and is difficult to control experimentally. However, the mechanical properties of aluminum components can be tailored by using numerical tools so that lightweight designs can be achieved (Hausöl et al., 2010; Merklein et al., 2012). Thus, the most effective method is to develop physics-based predictive computational tools that can accurately and efficiently predict the behavior of aluminum alloys.

In addition to aluminum alloys, magnesium, being the lightest of the structural metals, is also garnering significant interest from the automotive industry. While boasting of highest strength-to-weight ratio among all the structural metals, magnesium is also 36% lighter than aluminum, and 76% lighter than iron. Thus, magnesium and its alloys could be used to replace aluminum in vehicles that further reduce the weight and improves fuel efficiency.

At present, the amount of magnesium used in cars ranges between 14 and 26 kg saving about 20% of weight over aluminum. However, mainly the cast magnesium alloys are used as replacements. The reason for the limited use of magnesium alloys in vehicles is because of their poor formability at room temperature caused by the low symmetry of the crystal structure and high anisotropy.

There are several solutions to this problem; one of them is to use rare earth elements in the alloys and the other method is to control the microstructure (i.e., initial grain size and initial texture strength). The latter can be attained by processing magnesium alloys at high temperature, which is inevitably accompanied by the dynamic recrystallization (DRX) that changes the size and shape (i.e., morphology) of the grains as well as the texture. The DRX takes place during hot working of metallic alloys and it leads to material softening and improved ductility. Moreover, the DRX can be used as a tool to control the initial texture and grain size of metals, both of which play a significant role in the formability of the HCP metals.

The process of dynamic recrystallization (DRX) is a complex phenomenon that occurs because of migration of the high angle grain boundaries driven by the stored energy associated with dislocations. At elevated temperatures, DRX plays an important role in the texture evolution. However, using the experimental methods to find the optimal microstructural parameters required to achieve certain characteristics for the magnesium alloys (e.g., initial grain size, initial texture strength) are extremely difficult, time-consuming and expensive.

Therefore, the development of an advanced numerical model, which is able to predict and investigate the effects of various DRX parameters on the texture formation, 3D microstructure evolution and formability in the magnesium alloys, is needed.

1.3 Research Scope and Research Problems

Virtual fabrication is a key ingredient for increasing the competitiveness of the industry, by reducing the time from concept to market and by increasing quality and reliability of the final product. Pushing more and more tasks from the usual design/test/redesign cycles to the computer-based testing of a virtual prototype dramatically reduces the research and development phase. Nowadays, in automotive and aerospace industries, an important part of the virtual factory relies on the numerical simulation of aluminum and magnesium parts by crystal plasticity models.

Better understanding of microstructure evolution of aluminum and magnesium alloys can significantly improve the accuracy of predictions using crystal plasticity theory. To achieve this, the crystal plasticity model must capture, if not all, but some of the important microstructural features such as texture, grain morphology, grain interactions and recrystallization mechanisms.

Although, such crystal plasticity models, e.g., crystal plasticity Finite element method (CP-FEM) and elasto-viscoplastic fast Fourier transform (EVP-FFT) already exist that can capture microstructure evolution explicitly and can predict material's behavior, which is in good agreement with experiments. However, the massive amount of computational cost incurred by these models, hinders their use to replace expensive experiments for testing of aluminum and magnesium parts. Furthermore, the mesh related problems and the degeneration of the finite elements at excessive localized strains are some of its main limitations that render use of CP-FEM impractical for formability analyses. Consequently, the industry prefers using meshless crystal plasticity models that are extremely efficient but are less accurate as they are based on oversimplification schemes of polycrystal behavior such as Taylor-type models (explained in section 2.2.2).

Therefore, a crystal plasticity-based full-field and meshless numerical framework, which can model excessive localization problem and gives similar or better results than CP-FEM with smaller computational cost, is need. The present thesis is a contribution in this direction.

Assessing the current state-of-the-art crystal plasticity models available in literature, in case of aluminum alloys, for example, the existing crystal plasticity-based formability modelling tools does indeed give insightful guidelines with respect to optimized microstructure (Yoshida et al., 2007; Yoshida, 2014). Even though this makes crystal plasticity an appealing approach to predict formability, often no clear improvement in the accuracy of the predictions of forming limit diagrams (FLDs) is obtained from the crystal plasticity models with respect to newly developed phenomenological material modelling approaches (Chiba et al., 2013).

Accordingly, there is a need to improve the existing crystal plasticity models for formability analysis in two major areas: a) computational speed, b) accuracy. Signorelli et al. (2009) suggest that advanced crystal plasticity models, which incorporate grain interactions and non-equiaxed grain morphology, can improve accuracy of FLD predictions compared to a more basic Taylor crystal plasticity model, in which, the local deformation inside each crystal is unaffected by its environment in the microstructure.

To the best knowledge of the author, there is no crystal plasticity framework available in literature that can model the effects of 3D grain morphology on the FLD using a full-field crystal plasticity model that accounts for the 3D spatial distribution of texture to obtain an accurate micromechanical and effective response for aluminum alloys. The present thesis attempts to address this concern.

In case of magnesium alloys, along with crystallographic slip, twinning, initial texture and texture evolution, the dynamic recrystallization (DRX) during magnesium processing at elevated temperatures also play important roles on formability of magnesium alloys (Lévesque et al., 2010, 2016; Samuha et al., 2018). Enhancements in experimental and numerical techniques have increased the understanding of DRX phenomenon in recent years. However, modelling of DRX phenomenon is still a challenging problem. There are several works in literature to model dynamic recrystallization in magnesium and its alloys. These approaches can be classified mainly into Monte-Carlo (MC), Cellular Automata (CA) and Phase Field (PF) methods. Monte-Carlo-based models simulate the microstructure evolution during DRX and can produce many features of the

DRX process (Rollett et al., 1992; Peczak, 1995). However, these models were unable to describe grain growth kinetics because of the lack of physical length and time scale. The PF method is computationally expensive model with focus on a continuous description of grain boundary.

The CA method is able to capture the local effects and is computationally efficient (Hallberg, 2011). However, the CA methods alone lack the ability to predict microstructure evolution during deformation. Therefore, coupling the CA approach with crystal plasticity-based finite element model (CP-FEM) has been shown to be an effective tool for modelling recrystallization (Raabe, 2002; Seyed Salehi and Serajzadeh, 2012; Popova et al., 2015; Madej et al., 2016). However, due to the inherent problems of CP-FEM as discussed earlier, the coupled CA-CP-FEM models cannot be used for simultaneously modelling formability of the magnesium alloys. Therefore, a meshless and efficient full-field model is required that enables synchronous modelling of DRX along with FLD analysis for magnesium alloys.

While the crystal plasticity-based modelling techniques discussed above are able model to various deformation phenomena in magnesium alloys, however, to-date, there is no single framework available in literature that can model effects of dynamic recrystallization (DRX) on formability of magnesium alloys at elevated temperatures. The difficulty lies in proper modelling procedure of DRX phenomenon and the computational cost to generate forming limit strains for 3D microstructure. The present thesis an endeavor to address this concern as well.

1.4 Research Objectives and Associated Tasks

This thesis contributes several new crystal plasticity modelling tools that represent the current state-of-the-art in modelling material behavior in both aluminum and magnesium alloys at room temperature as well as at elevated temperatures. Accordingly, the objectives of this thesis, each of which correspond to a new contribution to the scientific community as a published/submitted journal article, are as follows:

Objective 1:

To develop a novel, fast Fourier transform (FFT)-based numerical framework for modelling deformation in **aluminum alloys** incorporating the rate-dependent crystal plasticity theory with a

semi-explicit forward gradient time-integration scheme. The main goal is to achieve significant gains in terms of computational efficiency of several orders over the existing CP-FEM model while obtaining an accurate full-field response of the 3D microstructure. The novelty of this framework is its extremely small computational cost while accurately predicting both micro and macro stress-strain responses as well as the texture evolution for different strain paths with minimal calibration.

Objective 2:

To develop a novel full-field numerical framework for modelling localized deformation in aluminum alloys that can account for the full richness of the 3D microstructure (texture, grain morphologies, grain interactions, etc.) and their effects on the forming limit diagrams (FLDs) of aluminum alloys at room temperature. The novelty of this framework is its capability to explicitly account for the effects of different 3D grain morphologies on the formability and consequently, the framework is expected to give better predictions of FLDs compared to the existing simplified and efficient crystal plasticity models (i.e., Taylor-type model) with similar computational cost.

Objective 3:

To extend the frameworks developed for aluminum alloys as mentioned above to **magnesium alloys** with an additional essential capability of synchronously modelling dynamic recrystallization (DRX). The goal is to develop a novel full-field numerical framework for modelling complex deformation mechanisms along with formability of magnesium alloys at room temperature and at elevated temperatures. This framework accounts for complex deformation mechanisms such as slip, twinning, slip inside the twinned regions and the DRX while also accounting for the full richness of the 3D microstructure (i.e., texture, grain morphologies, grain interactions, etc.). The novelty of this framework is its ability to synchronously model the effects of DRX on the microstructure evolution, localization and formability which ultimately lead to accurate predictions of FLDs of magnesium alloys at elevated temperatures.

In the studies conducted in this thesis, for each objective mentioned above, first the theory and mathematical frameworks are established, then the in-house codes are developed and validated.

1.5 Organization of Thesis

This thesis consists of six chapters. The first chapter presents the introduction and also describes the motivation, scope and objectives of the different research works conducted in this thesis.

Chapter two presents a comprehensive literature review of the general background knowledge of crystal structures, dislocation theory, slip deformation, deformation twinning, dynamic recrystallization, Fourier transforms and modelling localized deformation in aluminum and magnesium alloys. Chapter two also presents a literature review of available crystal plasticity models and their applications, numerical modelling of forming limit diagrams and the dynamic recrystallization.

Chapters three through five are published and submitted research works. These chapters illustrate the studies that have been conducted in this thesis. In each of these chapters, first the abstract is presented, which is followed by the introduction, model description, results, discussions and finally, the conclusions or summary.

Chapter three - Part 1: A novel numerical framework for modelling deformation in aluminum alloys is developed in this chapter. The developed model is benchmarked against an existing FFT-based model for the case of a Face Centered Cubic (FCC) polycrystal. Finally, the predictive capability as well as the computational efficiency of the developed model are demonstrated, where predictions obtained using the proposed model are compared to the experiments for the aluminum alloy (AA) 5754 and this is followed by the conclusions of the developed framework.

Chapter four - Part 2: The model developed in Part 1 is further coupled with Marciniak-Kuzynski framework to predict forming limit diagrams (FLDs) and investigate the complex effects of grain morphology, local deformation, local texture and grain interactions on the predictions of forming limit strains of different aluminum sheets.

Chapter five - Part 3: A new coupled probabilistic cellular automata-full-field crystal plasticity-fast Fourier transform based framework to model effects of dynamic recrystallization on formability of hcp metals is developed in this chapter. First the model is validated and then the FLDs are obtained at 100 °C, 200 °C and 300 °C, respectively, considering the effects of DRX.

The predicted FLDs are then compared with those obtained by turning off DRX in the code and the corresponding experimental observations. The results are then discussed, and the conclusions are presented.

Finally, Chapter six summarizes this thesis with conclusions of the contributions of the developed computational tools for microstructure engineering and presents some opportunities for future work.

Chapter 2. Literature Review

2.1 Introduction

Numerical models serve as powerful, economical and efficient tools since they can dramatically improve strategies for part optimization and can reduce time-to-market by enabling ‘virtual laboratory’ of manufacturing processes. Mainly there are two types of numerical constitutive models available to simulate the deformation behavior of magnesium alloys, i.e., phenomenological and microstructural.

Several phenomenological constitutive laws have been developed recently to study large deformation behavior of aluminum and magnesium alloys (Takuda et al., 2000; Barlat et al., 2003; Yoshida et al., 2007; Chiba et al., 2013; Ghaffari Tari et al., 2014; Muhammad et al., 2015). However, these models do not account for physical deformation mechanisms happening inside the material at different temperatures.

Therefore, in order to accurately model the deformation behavior, the relationship between microstructure and properties of the polycrystalline metals needs to be investigated. Hence, crystal plasticity-based microstructural models are needed that account for temperature dependent material properties, physical deformation mechanisms, gradual evolution of microstructure and texture.

“**Crystal plasticity**” provides a theory that links the constitutive response of a polycrystal with different crystal structures to the key features of its microstructure. The elastic-plastic deformation of a polycrystal depends on the direction of loading, i.e., crystals are mechanically anisotropic. In crystal plasticity-based models, the plastic anisotropy (i.e., unequal amount of plastic deformation in different directions) is analyzed using the crystallographic slip activity in each crystal. The main application of the crystal plasticity-based constitutive equations is to model the rotations of individual grains (a grain is a group of crystals with same orientation) in a polycrystal, and hence to predict the evolution of preferred orientations (i.e., texture) and to account for the effects of texture on the development of anisotropy in a polycrystalline solid.

2.1.1 Crystal Structures

The beautiful hexagonal patterns of snowflakes, the plane faces and hard faceted shapes of minerals and the bright cleavage fracture surfaces of brittle iron have long been recognized as external evidence of an internal order-evidence, that is, of the patterns or arrangements of the underlying building blocks, i.e., **crystal structures**. A graphical representation of crystals, grains and grain boundaries in a polycrystalline material is shown in Figure 2.1.

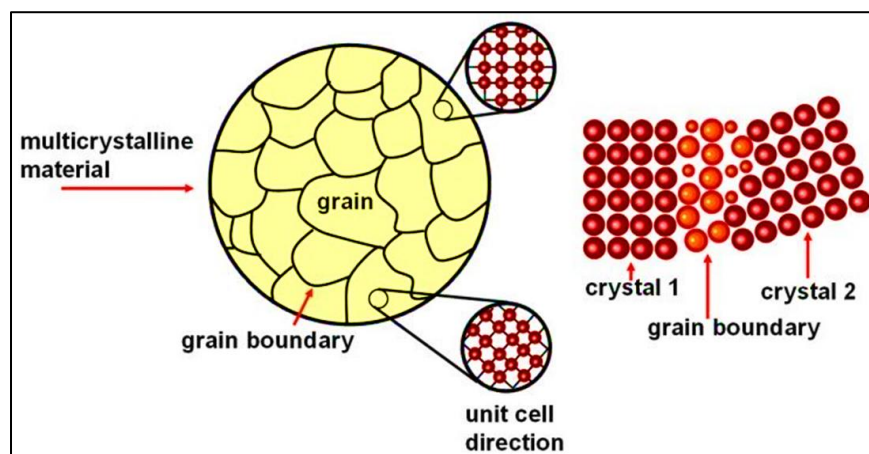


Figure 2.1: Grains and grain boundaries in a polycrystal. To the right, defect in atomic structure: grain boundaries (orange spheres), to the left, grains (in yellow) and grain boundaries (in black) as seen through an optical microscope (Callister Jr, 2000).

Almost all metals are crystalline solids and consist of atoms arranged in different patterns and these patterns are repeated in all directions. This spatial atomic arrangement can be described using a unit cell as shown in Figure 2.2. By repeating these unit cells in all dimensions, a structure of the grain is obtained. Among several types of crystal unit cells, the body-centered cubic (BCC), the face-centered cubic (FCC), and the hexagonal close-packed (HCP) are the typical metallic unit cells shown in Figure 2.2.

Some of the metals that has FCC crystal unit cells are aluminum, gamma iron, copper, brass, nickel etc. Beta iron, potassium and molybdenum have BCC while magnesium, titanium and zirconium have HCP unit cells.

2.1.2 Crystallographic Texture

"**Texture**" in the context of materials science means, "preferred crystallographic orientation". Textures are developed at all stages of any forming process and affect the mechanical, thermal and electrical properties of a material. It has been shown in numerous researches that prediction of the texture developments is important in forming operations since the formability of metals depend highly on their textures. Almost all naturally occurring or artificial materials show preferred crystallographic orientations or textures that means that the crystal axes are not randomly (or, more correctly, uniformly) distributed. The distribution of these orientations within a polycrystalline metal is an important material property that governs the anisotropy of the material.

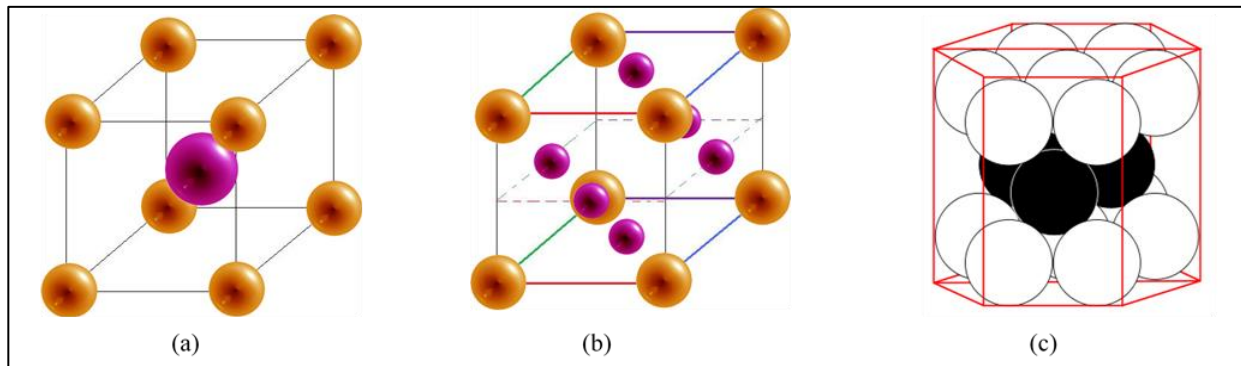


Figure 2.2: Unit cells of typical metallic crystal structures showing atomic arrangement for: (a) BCC (Body-centered cubic), (b) FCC (Face-centered cubic) and (c) HCP (Hexagonal closed pack) (Conway and Sloane, 1993).

Commonly, three independent parameters are used to identify the orientation of a single crystal with respect to a fixed reference frame of sample. These three parameters are known as Euler angles ($\varphi_1, \Phi, \varphi_2$) (Bunge and Esling 1984), which describe rotations from the sample frame coordinate axis to the crystal coordinate axis. Using the Euler angles, there are various ways to represent texture in materials such as pole figure (PF), inverse pole figure (IPF), orientation distribution function (ODF) and 3X3 orthogonal rotation matrices (Kocks et al., 2000). Some of these methods are summarized in the following. A pole figure is simply a stereographic projection of orientations of crystals with its axes defined by an external frame of reference with particular $h k l$ poles plotted onto it from all of the crystallites in the polycrystal (the intersection of the normal line and the sphere is the pole and $h k l$ are the Miller indices). Typically, the external frame is defined by the normal direction, the rolling direction, and the transverse direction in a sheet (ND,

RD and TD respectively). Pole figures do not give information about the orientation of a particular crystal relative to another crystal.

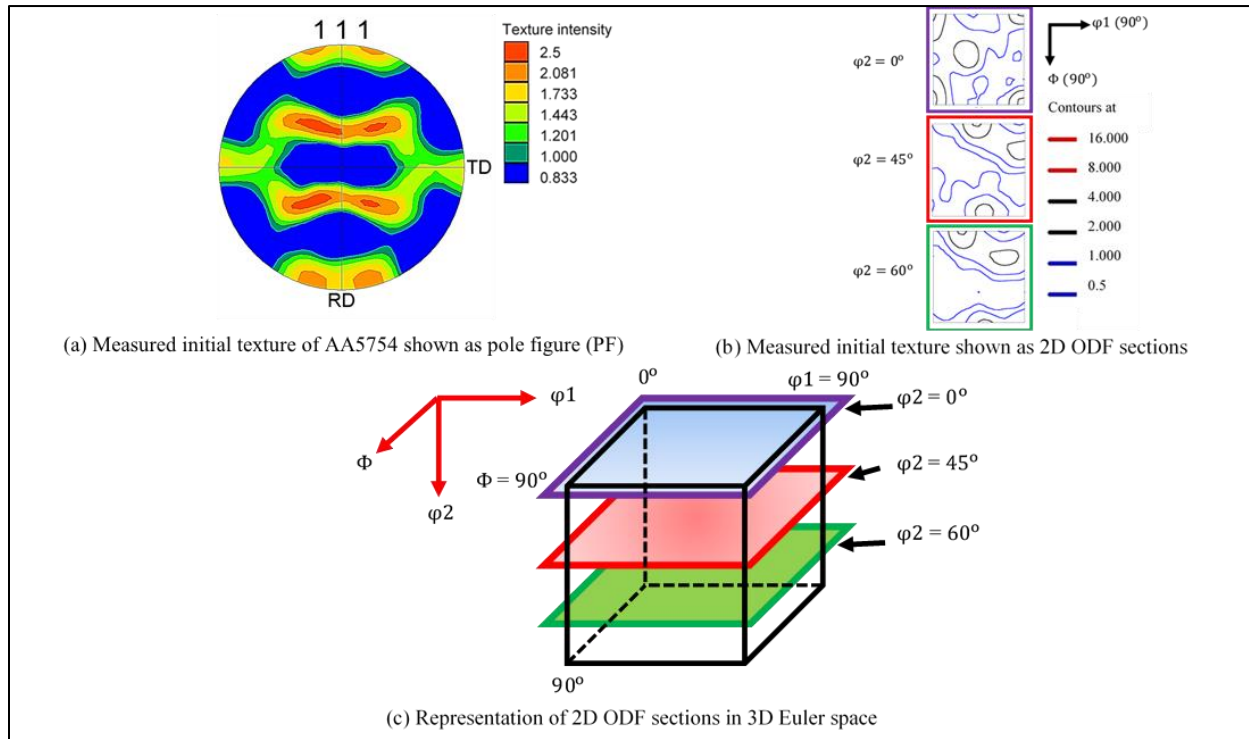


Figure 2.3: Experimentally measured texture of (AA) 5754-O tempered sheet (available in-house).

More information can be gathered from orientations distribution function (ODF) sections (Figure 2.3b). An orientation of a crystal can be completely described by a point in a cube with axes of Euler angles (ϕ_1, Φ, ϕ_2) (Bunge and Esling 1984) as illustrated in Figure 2.3(c). This cube is referred to as Euler space and is often shown as a series of 2D cross-sections (by fixing one angle and varying the other two), which is called as an ODF. Figure 2.3 shows typical texture for an FCC metal in form of pole figure (Figure 2.3a) and in form of ODF (Figure 2.3b) respectively. Furthermore, the texture of a material can be broken down into some frequently occurring preferred crystallographic orientations known as texture components. Some of the common texture components in cold rolled FCC metals are summarized in Table 2.1. Copper, Brass, and S orientations form most of the rolled texture with some small amounts of others present.

2.1.3 Microstructure and Representative Volume Element

“**Microstructure**” is the structure of a metal, comprising of crystal structure, grain orientations, crystal defects and microchemistry, revealed by an optical or electron microscope. The microstructure is a statistical descriptor of the geometrical arrangement of grains and crystal imperfections. It makes sense to define volume averaged properties, which are then independent of the size and position of the volume element considered, provided it is sufficiently large. A volume element that contains all the necessary information for the statistical description of a given microstructure is called a “**Representative Volume Element**” (RVE).

Table 2.1: Euler angles (in degrees) for the common texture components in FCC metals (Kocks et al., 2005).

Component	Euler angles ($\varphi_1, \Phi, \varphi_2$)
Cube	(0, 0, 0)
Copper	(0, 35, 45)
S	(64.93, 74.50, 33.69)
Goss	(0, 45, 0)
Brass	(35, 45, 0)

Using crystal plasticity-based models, material is simulated as a representative volume element (RVE) that assumes repetitive symmetry in the actual material texture. Compared to macro-scale simulations, the accuracy of a crystal plasticity simulation depends on the quality of microstructural information used in the model and on the crystal plasticity-based formulation used to model it. Microstructural information includes both the orientation as well as the position of a crystal in an RVE. Microstructure data characterization for materials is done using the standard grain orientation technique known as EBSD (Electron Backscatter Diffraction). Using EBSD, only a 2D map of the grains on a single plane can be obtained at a time. This 2D map is a list of pixels containing information about x, y coordinates, from a reference point, and the orientation of crystal at each point.

The 3D microstructure of the material is serially sectioned, polished and scanned repeatedly to get multiple 2D surfaces to create a reasonable estimate of the real microstructure. Figure 2.4 shows

the observation planes in a polycrystal sample, grains are assigned colors based on the crystallographic orientations.

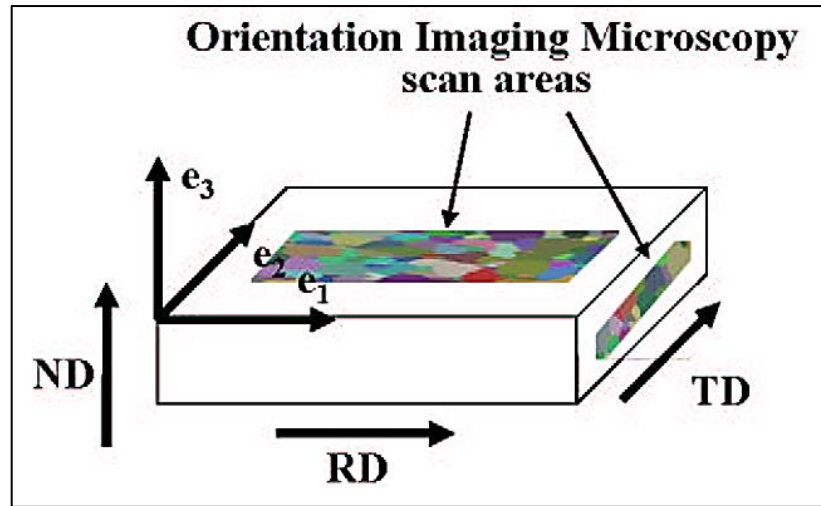


Figure 2.4: EBSD observation areas (Brahme et al., 2006).

Several numerical techniques are available in literature that can be used to develop 3D microstructures without the use of serial sectioning to avoid high equipment costs, alignment of scans and time-consuming material removal. In present work, M-Builder (Brahme et al., 2006) is used to generate the statistically equivalent microstructures. M-Builder takes in two orthogonal 2D scans of the material and analyze them to identify grain size, aspect ratio, orientation distribution, misorientation distribution and grain size.

A volume of space in the material is filled with ellipsoids of different sizes (around the average grain size) with measured material aspect ratios. Points are then randomly introduced and Voronoi tessellation is performed to make non-interference, volume-filled structure. All the created Voronoi cells that reside within the same ellipsoid are merged to make a single grain. Grain orientations are then assigned based on the orientation and misorientation distribution in the real material. An iterative approach is used to compare and reduce the discrepancies between the experimental and calculated orientation space, misorientation distribution and average grain size. In polycrystals, an individual crystal of an irregular shape is determined by the nucleation and growth conditions during manufacturing process that may further lead to grain shape with certain aspect ratios, i.e., columnar, equiaxed and elongated shaped grains can develop in a microstructure. Equiaxed shaped grains are usually observed in O-tempered aluminum sheet alloy (Iadicola et al.,

2008). During severe plastic deformation, e.g., in rolling these grains can become elongated as illustrated by Verlinden (2009). Using M-builder, microstructures with different grain shapes can be created as shown in Figure 2.5. Moreover, different type of grain shapes may lead to different material properties. Depending on the application, one type of grain is preferred, e.g., equiaxed grains in car engines and columnar grains in turbine blades as reported by Reinhart et al. (2005) and Kuangfei et al. (2010).

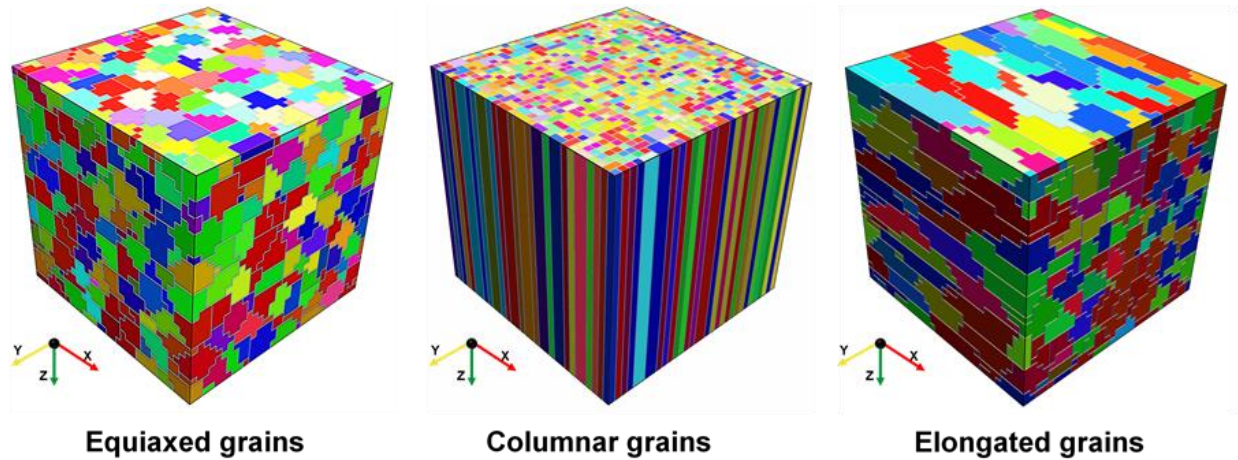


Figure 2.5: RVEs with different grain morphologies generated using Voronoi tessellation algorithm (M-builder). Only full-field crystal plasticity models (e.g., CP-FFT and CP-FEM) can explicitly account for different grain shapes in 3D microstructure.

2.1.4 Deformation Mechanisms in FCC metals

The real crystals may contain different types of imperfections in their lattice (i.e., a lattice is an idealized structure of crystals where each lattice point represent an identical group of atoms). These lattice imperfections could be as a point, line, interfacial, atomic vibrations and bulk defects. The most important line imperfection is known as dislocation. Dislocation may be defined as the shearing of rows of atoms in a crystal propagating throughout the crystal as the stress or temperature changes. The movement of dislocations accommodates the plastic deformation and are described as the areas where atoms are out of place in the crystal lattice.

2.1.4.1 Crystallographic Slip

Dislocation movement is similar to the way a caterpillar moves as shown in Figure 2.6. The caterpillar hump is representative of the extra half-plane of atoms that move along a preferred plane also known as slip plane (the closest packed plane) as shown in Figure 2.7(a) and along a preferred direction (Figure 2.7b) known as slip direction. This movement of the atoms is known as **crystallographic slip**. The combination of crystallographic slip and its direction is called a slip system. The crystallographic slip is anisotropic due to different number of slip systems in each type of crystal structure, i.e., in FCC, BCC, HCP etc.

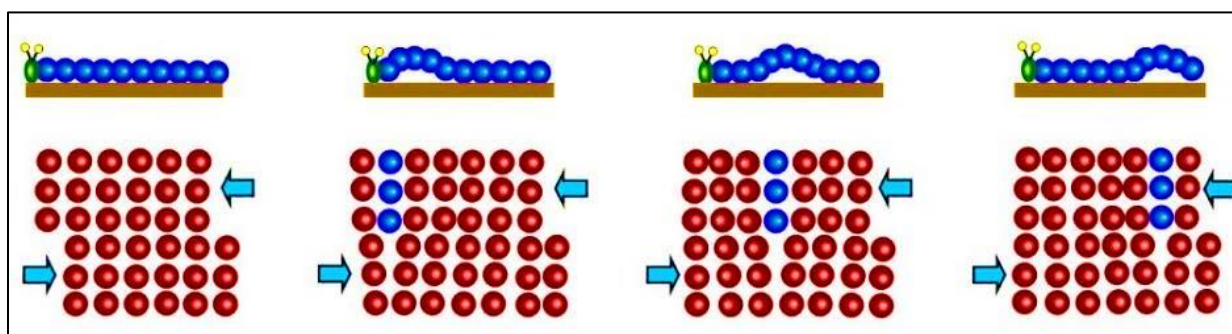


Figure 2.6: Example showing movement of dislocations similar to that of a caterpillar (Callister Jr, 2000).

The main physical mechanism of plastic deformation at ambient temperature is the flow of dislocations along crystal slip systems. Dislocation motion results in no net compression or expansion of the crystal lattice, therefore plastic deformation is volume preserving. The lattice is undistorted when the dislocation has passed through. A very important side effect of crystallographic slip is crystal lattice rotation, which happens due to the finite deformation nature of massive dislocation flow. Due to the finite deformation nature of slip on the slip system, an out of balance moment is generated. To re-establish equilibrium, the lattice, must rotate. This generates bending stresses because of the gripping constraints applied by the surroundings. Generalizing this, one can say that lattice rotation is geometrical in nature and also that rotation does not have to be uniform throughout a crystal; it can be constrained in certain locations, which can result in the generation of stresses in the crystals. A British mineralogist, William Hallowes Miller introduced a notation system in crystallography for planes in crystal (Bravais) lattices (Miller et al., 1839). A family of lattice planes is determined by three integers h , k , and l , the Miller indices

and are written as $(h\ k\ l)$ to represent a plane. For crystal directions, the corresponding notations are $[h\ k\ l]$, with square instead of round brackets, denotes a direction; and similarly, the notation $\langle h\ k\ l \rangle$ denotes the set of all directions that are equivalent to $[h\ k\ l]$ by symmetry.

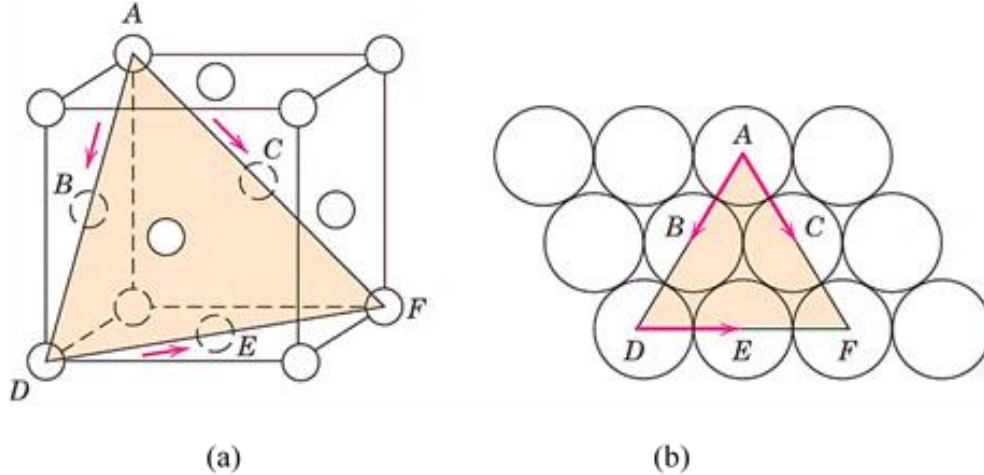


Figure 2.7: (a) $(1\ 1\ 1)\ \langle 1\ 1\ 0 \rangle$ slip system in FCC unit cell (b) $(1\ 1\ 1)$ Plane from (a) and three slip directions within the plane (shown by arrows) (Callister Jr, 2000).

Figure 2.7(a) shows an FCC unit cell with $(1\ 1\ 1)$ slip plane and $\langle 1\ 1\ 0 \rangle$ directions (Figure 2.7b) which means that slip occurs along the $\langle 1\ 1\ 0 \rangle$ directions within the $(1\ 1\ 1)$ slip plane. The number of independent slip systems represents the different combinations where slip can occur. For FCC, there are four unique $(1\ 1\ 1)$ planes and three $\langle 1\ 1\ 0 \rangle$ directions per plane resulting in 12 unique slip systems. At high temperatures, FCC metals can have several plastic deformation mechanisms namely; slip, twinning and grain boundary sliding. However, slip is the most dominant mechanism of plastic deformation at room temperature. In aluminum, the dominant deformation mechanism that operates is slip, which is simpler to model as compared to the other deformation mechanisms.

Schmid's law describes the slip plane and the slip direction of a stressed material, which can resolve the most amount of shear stress. The Schmid's law can be explained using an example of cylinder (Figure 2.8) loaded along its axis by applying a tensile force, F . Assuming the cross-sectional area to be A , the tensile stress developed parallel to the applied force is $\sigma = F/A$. This force has a component in the slip direction $F\cos(\lambda)$ (λ being the angle between the F and the slip direction). This force component acts over the slip surface with an area $A/\cos(\psi)$, where angle ϕ

is the rotation from F to the slip plane normal. The resolved shear stress on a given slip plane and given slip direction can be represented as

$$\tau = \sigma \cos(\lambda) \cos(\psi) \quad (2.1)$$

Throughout this research work, τ is used to represent the shear stress resolved on to a slip system in this way. The translation, $\cos(\lambda) \times \cos(\phi)$, from σ to τ is known as the Schmid factor. Furthermore, if a critical force (F_c) is required to initiate slip, the corresponding shear stress is denoted τ_c or critical resolved shear stress (CRSS). Schmid's Law states that a single crystal yields or deforms plastically, when the resolved shear stress (τ) reaches the critical resolved shear stress (τ_c).

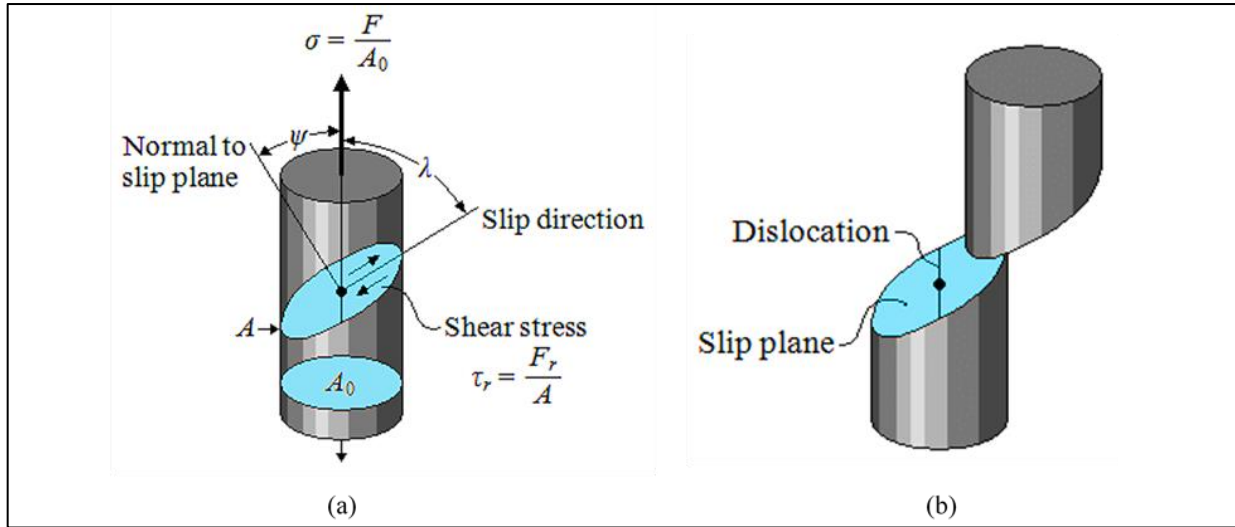


Figure 2.8: Description of Schmid's law: (a) A resolved shear stress, τ_r , is produced on a slip system. (b) Movement of dislocations on the slip system deforms the material (Callister Jr, 2000).

2.1.5 Deformation Mechanisms in HCP Metals

Magnesium with hexagonal closed packed (HCP) structure is the eighth most abundant element in the earth's crust and the third most plentiful element dissolved in the seawater. The orientations in an HCP structure are represented by the four axes $\{a_1, a_2, a_3, c\}$ in the Miller-Bravais coordinate system as shown in Figure 2.9. The c axis is orthogonal to the rest of three axes. The angle between each pair of the axes, i.e., between a_1 and a_2 , a_1 and a_3 , a_2 and a_3 , respectively, is 120° . The ratio

of lengths of axes, e.g., c/a in pure magnesium is 1.624 which is close to the ratio in an ideal HCP structure ($c/a=1.633$) (Partridge, 1967). In present work, these axes are transformed to the orthonormal Miller coordinate system from Miller-Bravais coordinate system for computational convenience using the well-known procedure, which can be found in literature, see, e.g., Niewczas (2010).

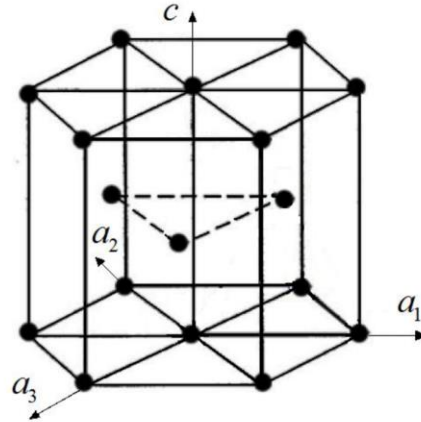


Figure 2.9: Unit cell of HCP metals.

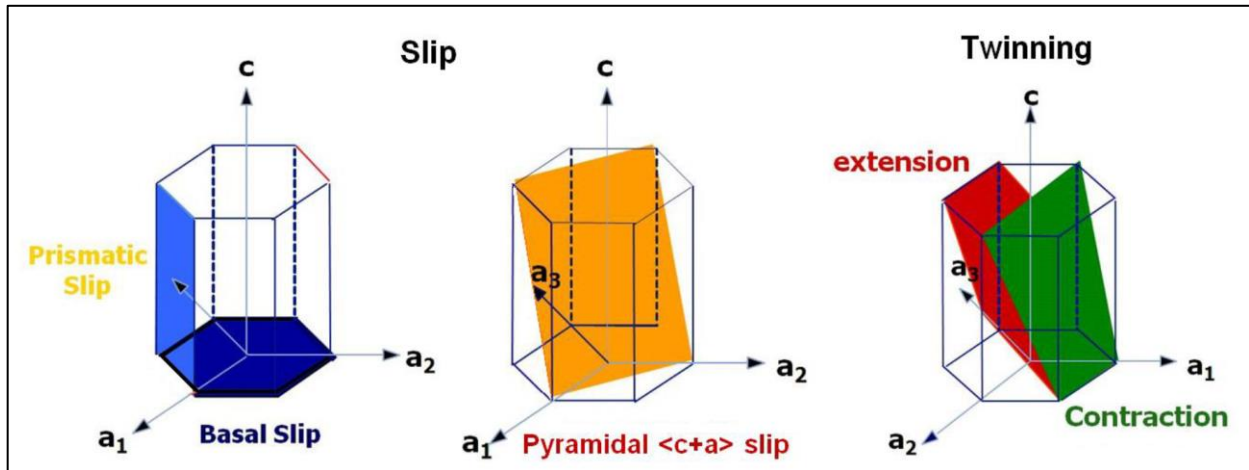


Figure 2.10: Slip systems and twinning systems in HCP metals (Partridge, 1967).

2.1.5.1 Crystallographic Slip

Slip is the major deformation mechanism in magnesium and its alloys. Unlike FCC crystal structure, the HCP crystal structure has more complex deformation systems. There are total 24 deformation systems, out of which, 18 are the primary slip systems and the remaining 6 are

twinning systems. Figure 2.10 shows the primary slip planes in the HCP crystal structure. In magnesium alloys, the basal slip system has the lowest CRSS value, while pyramidal ($c + a$) slip system has the highest CRSS at room temperature. Thus, most of the plastic deformation is accommodated by the basal slip system at room temperature.

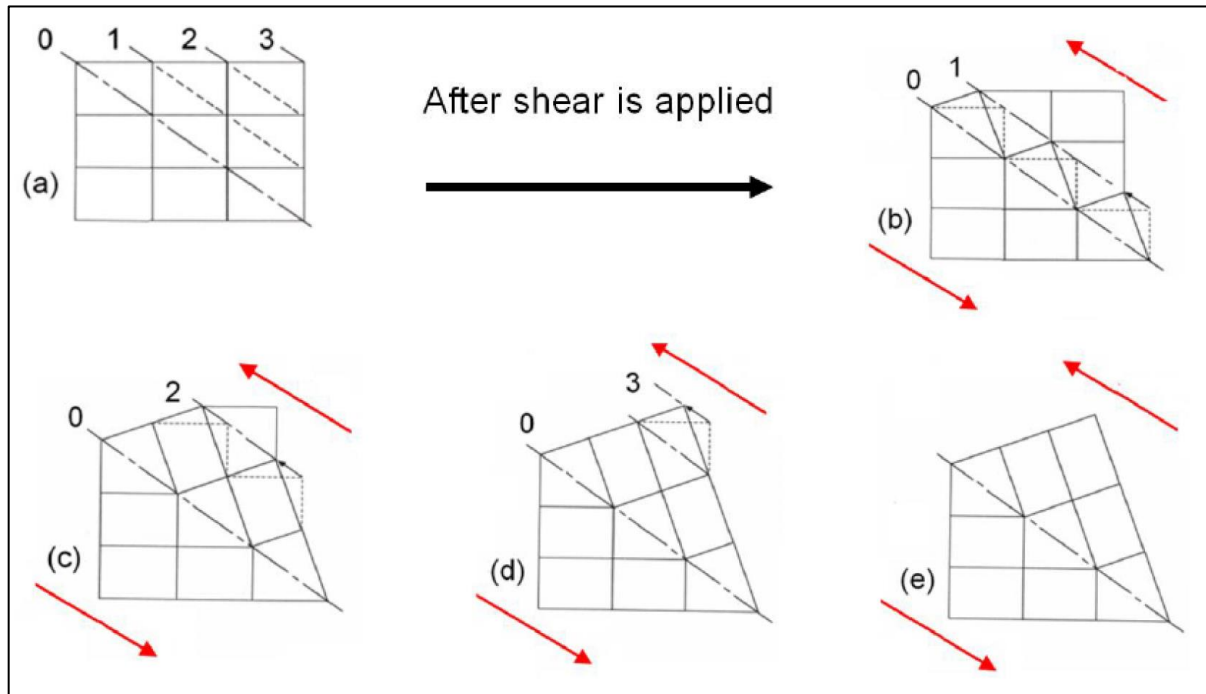


Figure 2.11: Schematic representation of twinning process (Paufler, 1994).

Based on the Von Mises criterion, activity of five independent plastic deformation mechanisms were required to accommodate an arbitrary plastic deformation in a given material. Basal, prismatic, and pyramidal (a) slip systems provide four independent plastic deformation mechanisms. Pyramidal ($c + a$) slip system, which can be the fifth independent plastic deformation mechanism, is difficult to activate at room temperature, since it has a high CRSS. At room temperature, deformation twinning has a lower CRSS than the pyramidal ($c + a$) slip system, and it can provide the fifth independent plastic deformation mechanism to satisfy the Von Mises criterion. At elevated temperature, the CRSS of pyramidal ($c + a$) slip and other non-basal slip systems decreases, and they can provide the fifth independent plastic deformation mechanism.

2.1.5.2 Deformation Twinning

Twinning is a complex deformation mechanism. Twinning occurs when the lattice undergoes an abrupt rotation relative to specific planes. The newly formed orientation is a mirrored orientation of the initial matrix grain. The schematic representation of twinning is given in the Figure (2.11). In HCP metals, twins can be divided into two different types: extension and contraction twins. The extension twin occurs, when the c-axis is under tensile loading, rotating the lattice by 86.6° , while contraction twin occurs when c-axis is under compression and the rotation angle is 56.6° . The main difference of twinning from slip is the magnitude of rotation. Slip causes a slight rotation to the crystal lattice, while the rotation due to twinning is much larger. Another difference is that the shear displacement due to twinning is one directional, i.e., shear in one direction is not the same as in its opposite direction while slip can occur on the specific plane in both directions.

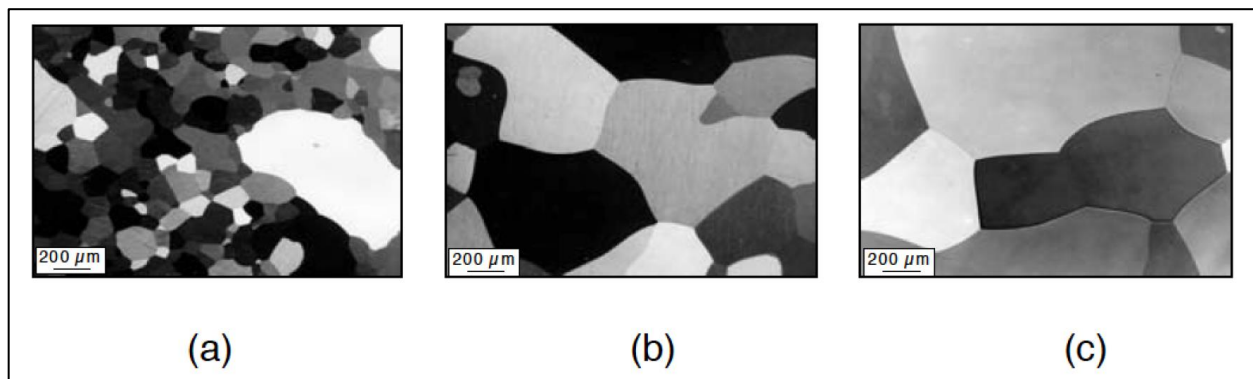


Figure 2.12: Microstructure evolution during annealing of Al-0.1% Mn alloy after 95% cold rolling (Gottstein, 2004).

2.1.6 Recrystallization

Recrystallization is a collective term to describe the change in orientations of grains by grain boundary motion. It proceeds via formation and migration of high-angle grain boundaries driven by the stored energy associated with dislocations. After plastic deformation, the stored energy renders a driving force for further deformation or the recovery process. Static recrystallization (SRX) happens during annealing treatment of the material, while dynamic recrystallization (DRX) occurs during plastic deformation at elevated temperatures. In Figure 2.12, a few steps of

recrystallization process are shown. As it can be seen from the final microstructure, a few grains have grown consuming the other small grains. In the literature, dynamic recrystallization mechanisms are divided into three main types, discontinuous DRX states for nucleation and growth of high-angle boundaries; continuous DRX states for a recovery process of low-angle boundary movement consuming dislocations and forming high-angle boundaries and twinning DRX. It is known that DRX and SRX take place by the grain growth phenomenon. Normal grain growth is a process when all grains grow roughly at the same rate of boundary migration resulting with almost the same size. Abnormal grain growth is the growth of a few orientations (nuclei) at the expense of other grains.

2.1.7 Fourier Transform-based Methods

For the derivation of the elasto-viscoplastic crystal plasticity fast-Fourier transform formulation developed in this thesis in the chapters five, six and seven, the basic mathematical background of the Green's function method and the Fourier transforms are presented in this section.

2.1.7.1 Green's Function Method (Hantson and Jaeger, 2006)

In the present work, Green's function is used to solve the equation of stress equilibrium for the prediction of microstructure-property relations in FCC and HCP polycrystalline aggregates. A general derivation of Green's function is given in the following section. In a 3D space resolved grid of Fourier points in the RVE, to define the displacement $u(x)$ of a Fourier point x , a Green's function $G(x, x')$ gives solution of the equation of form

$$L(x)G(x, x') = \delta(x - x') \quad (2.2)$$

where δ is the unit impulse function (Dirac delta), x' is the new position of Fourier point x and $L(x)$ a linear differential operator.

Green's function method can be used to solve any heterogenous linear differential equations of form

$$L(x)u(x) = f(x) \quad (2.3)$$

A convolution operator $G(x - x')$ can be used for $G(x, x')$ for a translation invariant operator $L(x)$ that has constant coefficients with respect to x . Multiplying Equation (2.2) with $f(x')$ and integrating over x' results in

$$\int L(x)G(x - x')f(x')dx' = \int \delta(x - x')f(x')dx' \quad (2.4)$$

By virtue of the properties of the Dirac delta function, the right-hand side of above equation equals $f(x)$. Thus, inserting above expression into Equation (2.3) results in

$$L(x)u(x) = \int L(x)G(x - x')f(x')dx' \quad (2.5)$$

and, since $L(x)$ does not depend on x' and acts on both sides, Equation (2.5) is rewritten as

$$u(x) = \int G(x - x')f(x')dx' \quad (2.6)$$

In this thesis, the Equation (2.6) is solved by finding $G(x - x')$ using fast Fourier transform and carrying out the integration as simple product in the Fourier space. The Fourier transform and ways to compute the Green's function are presented next.

2.1.7.2 Fourier Transform (Marks, 2009)

The forward Fourier transform (\mathcal{F}) is a mathematical operation that transforms a time dependent continuous integrable function of space, $f(x)$, from cartesian coordinate system to a function of frequency in Fourier space, i.e. it is denoted by adding a circumflex $\hat{f}(\xi)$. The Fourier transform is a useful tool in solving in linear differential equations and is widely used in image and digital

signal processing. Several common conventions for defining the Fourier transform of an integrable function are available. In present work, we will use the following definition

$$\mathcal{F}(f(x)) = \hat{f}(\xi) = \int_{-\infty}^{\infty} f(x) e^{-2\pi i x \xi} dx \quad \forall \xi \in \mathcal{R} \quad (2.7)$$

Negative sign is used in this convention because at frequency, $\xi=0$, the function $f(x)e^{-2\pi i x \xi} dx$ represents only amplitude of $\hat{f}(\xi)$.

Under suitable conditions, the inverse Fourier transform is performed via an equation as follows

$$f(x) = \int_{-\infty}^{\infty} \hat{f}(\xi) e^{2\pi i x \xi} d\xi \quad \forall x \in \mathcal{R} \quad (2.8)$$

In the Fourier space, the advantage of the Fourier transform is the simple way of differentiating and integrating, i.e., the derivative is simply the original function multiplied by $2\pi i \xi$ as follows

$$\mathcal{F}\left(\frac{d}{dx}f(x)\right) = (2\pi i \xi) \cdot \hat{f}(\xi) \quad (2.9)$$

2.1.7.3 Discrete Fourier Transform (Marks, 2009; Rao et al., 2010)

The discrete Fourier transform (DFT) can be used as an approximation of the continuous Fourier transform if the data is properly discretized. The DFT is applicable only if the discrete data represents a single period in an infinitely extended periodic function. Furthermore, each discrete data represents one wavenumber, where the total number of waves is equal to the number of input data sets. For the DFT to be applicable on the input data, the space has to be discretized into a regular grid of Fourier points and the periodic boundary conditions must be set.

For one-dimensional problem, the DFT is defined for a sequence x_n , where n counts the discrete values of the variable x .

Accordingly, the DFT of a function $f(x_n)$, with N complex numbers, where $n = 0, 1, 2, \dots, N - 1$, is the transformed sequence, $\hat{f}(\xi_j)$, with $j = 0, 1, 2, \dots, N - 1$ of N wavenumbers ξ_0, \dots, ξ_{N-1} defined as follows

$$\hat{f}(\xi) = \sum_{n=0}^{N-1} f(x_n) \cdot e^{-i\frac{2\pi}{N}jn}, \quad j = 0, 1, 2, \dots, N - 1 \quad (2.10)$$

The wavenumbers are selected with Δ being the sampling interval such that

$$\xi = \frac{j}{\Delta N}, j = -\frac{N}{2}, \dots, 0, \dots, \frac{N}{2} \quad (2.11)$$

Note that, ξ in above equation is defined for $N + 1$ wavenumbers. As the extremum values at $-\frac{N}{2}$ and $\frac{N}{2}$, respectively, give the same result, it does not clash with the definition given in Equation (2.9). The inverse DFT is given by

$$f(x_n) = \frac{1}{N} \sum_{j=0}^{N-1} \hat{f}(\xi) \cdot e^{-i\frac{2\pi}{N}jn}, \quad n = 0, 1, 2, \dots, N - 1 \quad (2.12)$$

Equation (2.12) computes the values at each discrete Fourier point that results from the operations conducted in Fourier space. For an input of pure real data, i.e., $\Im m(f(x))=0$, the transformed data $\hat{f}(\xi)$ in wavenumber domain is the conjugate complex of $\hat{f}(-\xi)$: $\hat{f}(\xi) = \Re e \left(\hat{f}(-\xi) \right) - \Im m \left(\hat{f}(-\xi) \right)$. The transformed data is anti-symmetric in the imaginary domain and symmetric with respect to the origin in the real domain. Thus, only the half of the outputs have to be computed using a DFT algorithm for this case. The other half of the outputs can be directly obtained from the transformed data of the first half. In the same way, for the inverse transform for a data set with $\hat{f}(\xi)$: $\hat{f}(-\xi) = \Re e \left(\hat{f}(-\xi) \right) - \Im m \left(\hat{f}(-\xi) \right)$ only half of it is needed to transform to a set of real data.

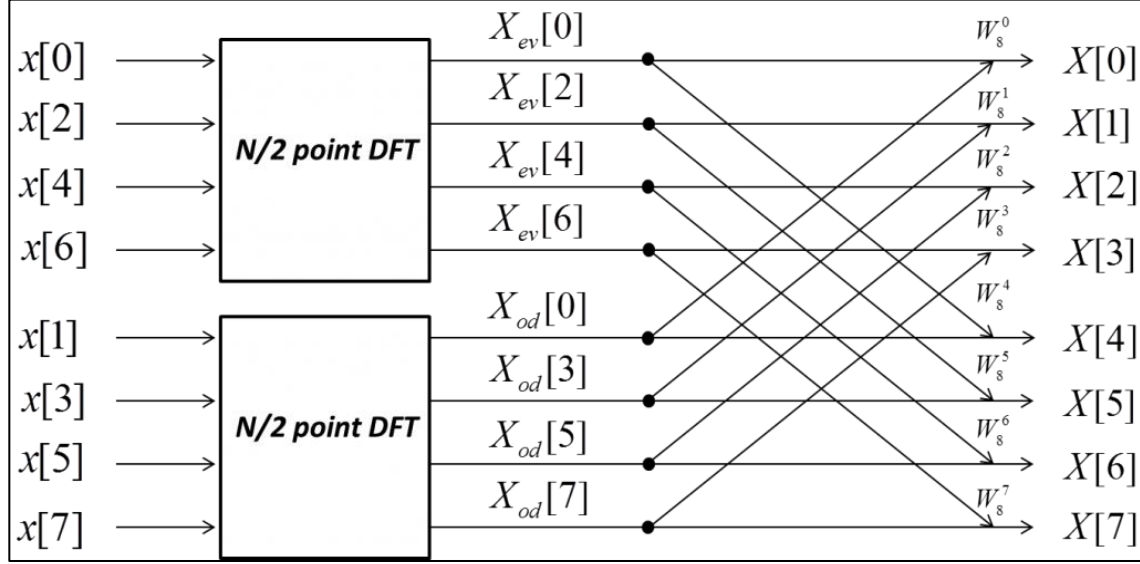


Figure 2.13: Decimation in Time method of FFT (Marks, 2009).

For a three-dimensional function depending on vector x with discrete values $n_x = 0, 1, 2, \dots, N_x - 1$; $n_y = 0, 1, 2, \dots, N_y - 1$; $n_z = 0, 1, 2, \dots, N_z - 1$ for the components x, y, z , respectively. The forward DFT, is a discrete function depending on $\xi = (\xi_1; \xi_2; \xi_3)$ and $j_1 = 0, 1, 2, \dots, N_x - 1$; $j_2 = 0, 1, 2, \dots, N_y - 1$; $j_3 = 0, 1, 2, \dots, N_z - 1$, is given by

$$\hat{f}(\xi) = \sum_{n_x=0}^{N_x-1} \sum_{n_y=0}^{N_y-1} \sum_{n_z=0}^{N_z-1} f(x) \cdot e^{-i2\pi\left(\frac{n_x j_1}{N_x} + \frac{n_y j_2}{N_y} + \frac{n_z j_3}{N_z}\right)} \quad (2.13)$$

Accordingly, the inverse of the three-dimensional DFT is given by

$$f(x) = \frac{1}{N_x \times N_y \times N_z} \sum_{j_1=0}^{N_x-1} \sum_{j_2=0}^{N_y-1} \sum_{j_3=0}^{N_z-1} \hat{f}(\xi) \cdot e^{-i2\pi\left(\frac{n_x j_1}{N_x} + \frac{n_y j_2}{N_y} + \frac{n_z j_3}{N_z}\right)} \quad (2.14)$$

2.1.7.4 Fast Fourier Transform: An Efficient Class of Algorithms (Rao et al., 2010)

The computation of the DFT as introduced in Equations (2.13) and (2.14) require $\mathcal{O}(N^2)$ operations. The computation time increases quadratically with the number of Fourier points under consideration. The fast-growing computation cost makes the direct DFT unattractive for its application on large number of data sets. Thus, another method known as the fast Fourier transform (FFT) is preferred. FFT a group of algorithms that calculate the DFT in only $\mathcal{O}(N \log N)$ operations. The block diagram below illustrates how an N point DFT can be split into two $N/2$ -point DFTs to handle the even and odd values of a length 8 sequence. This method saves computation time and so the process would necessarily be continued. Therefore, each $N/2$ -point DFT can be divided into two $N/4$ -point DFTs and so on (Figure 2.13).

The most common type of FFT-algorithms is the Cooley-Tukey algorithm. The algorithm first divides the DFT of a sequence $x(n)$ into two parts, the odd elements, and the even:

$$X(j) = \sum_{n=0}^{\frac{N}{2}-1} x(2n) \cdot e^{-i\frac{2\pi}{N}j(2n)} + \sum_{n=0}^{\frac{N}{2}-1} x(2n+1) \cdot e^{-i\frac{2\pi}{N}j(2n+1)} \quad (2.15)$$

A common multiplier of $e^{-i\frac{2\pi}{N}j}$ is then factored out of the second term

$$X(j) = \sum_{n=0}^{\frac{N}{2}-1} x(2n) \cdot e^{-i\frac{2\pi}{N/2}j(2n)} + e^{-i\frac{2\pi}{N}j} \sum_{n=0}^{\frac{N}{2}-1} x(2n+1) \cdot e^{-i\frac{2\pi}{N/2}j(2n)} \quad (2.16)$$

Therefore, the two expressions above are now in the form of two $N/2$ -point DFTs and can be written explicitly as a sum of even and odd terms

$$X(j) = X_{ev}(n) + e^{-i\frac{2\pi}{N}j} X_{odd}(n) \quad (2.17)$$

The index j must extend to $N-1$, and using the periodic property of the even and odd DFTs it can be seen that

$$X_{ev}(j) = X_{ev}(j + N/2) \quad (2.18)$$

$$X_{odd}(j) = X_{odd}(j + N/2)$$

The FFT also exploits the periodic nature of $e^{-i\frac{2\pi}{N}j(2n)}$ term:

$$e^{-i\frac{2\pi}{N}(j+N/2)} = e^{-i\frac{2\pi}{N}j} \cdot e^{-j\pi} = e^{-i\frac{2\pi}{N}j} \quad (2.19)$$

This allows the number of calculations involving FFT term to be cut in half and for $0 \leq k \leq N/2$
The FFT is

$$\begin{aligned} X(j) &= X_{ev}(j) + e^{-i\frac{2\pi}{N}j} X_{odd}(j) \\ X(j + N/2) &= X_{ev}(j) - e^{-i\frac{2\pi}{N}j} X_{odd}(j) \end{aligned} \quad (2.20)$$

“**Cooley-Tukey**” algorithm is a Divide et impera method, that means it will divide the whole transformation into smaller parts that are simpler (and faster) to compute. It is based on the idea of breaking down the DFT with $N = N_1 \times N_2$ points into several DFTs of N_1 and N_2 . The most efficient and common implementation is dividing N repeatedly by 2, resulting in $N_1 = N_2 = N/2$. Therefore, it has the requirement that the total number of input data of Fourier points has to be a power of two. It is known as the “radix-2” variant of the algorithm. Divisions based on prime numbers are also possible but are computationally less efficient.

2.1.8 Instability, Localization and Failure in Metals

The ‘**formability**’ or ‘**forming limit**’ is determined by the onset of localized necking. The forming limit diagram (FLD) gives an indication whether the material can sustain certain values of strains without failing. During the sheet metal operations, the tearing of a polycrystalline sheet metal is the most common mode of failure, resulting from an uneven or exorbitant amount of plastic deformation forming a localized neck and therefore limiting the formability of the polycrystalline sheet metal.

During the forming of sheet metal into a more complex shape, a number of plastic instabilities may occur subsequently. A ‘plastic instability’ occurs when the zone of plastic deformation is suddenly confined to a smaller zone. The first plastic instability that usually occurs in forming processes is

the onset of diffuse necking, in which plastic deformation is confined to a smaller zone, but with typical dimensions that are still in the order of magnitude of the actual part's dimensions. As often observed in uniaxial tensile tests of sheet metal, diffuse necking is followed by localized necking. While the size of a diffuse neck is of the order of magnitude of the sample width, the width of the localized neck is only of the order of the sheet thickness. After the onset of localized necking, strain is concentrated within the neck while the surrounding material returns to the elastic state. Consequently, the thickness within the neck drops drastically compared to the elastic surrounding. Localized necking is therefore also known as thinning instability. Moreover, the macroscopic shear localization (over multiple grains) can also occur within the developed neck. It is observed that shear localization initiates at the free surface within the neck, and multiple shear bands can be found within a single localized neck that can eventually lead to fracture.

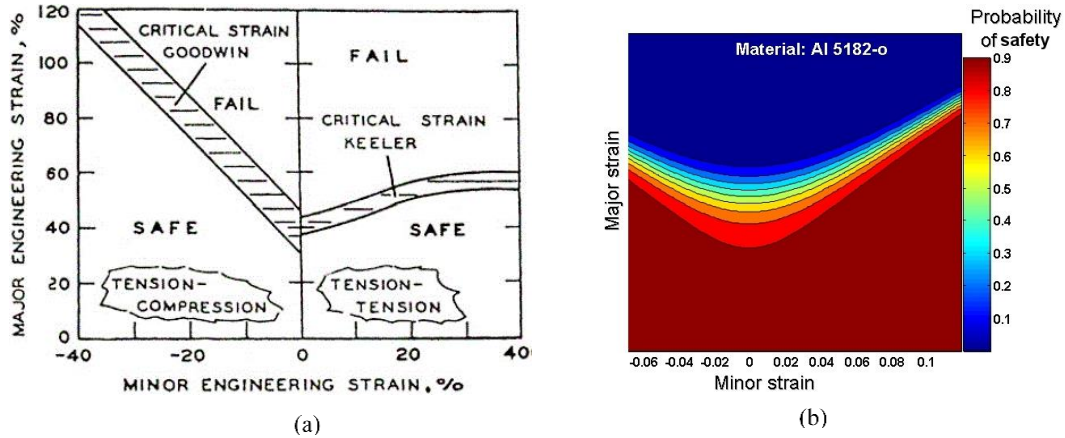


Figure 2.14: (a) FLD defined by Keeler (1961) and Goodwin (1968), (b) Probabilistic FLD of four different grades of O-tempered AA5182.

In the sheet-metal forming industry, it is of high importance that the failure of metal sheets due to localized necking must be analyzed. The concept of forming limit curve (FLC) also known as the forming limit diagram (FLD) was introduced by Keeler (1961) and Goodwin (1968) that provide an approximation of how close the material is to neck. FLDs have been extensively used thereafter to quantify the formability of a sheet metal. To generate an FLD, the strain in the loading direction (major strain) is plotted with strain along width of the sample (minor strain) at the onset of necking for different strain paths as shown in Figure 2.14(a). Figure 2.14(b) shows a probabilistic map of safety for four different grades of aluminum alloy sheet.

To obtain the FLD experimentally, the surface of the blank of a sheet metal is printed using a regular grid and is then subjected to stretching using a hemispherical punch, the regular grid deforms and the principal strains (major strain and minor strain) at localization are calculated using a high-resolution digital image correlation (DIC) technique. The FLD represents, in one graph, all combinations of critical-limit surface strains corresponding to failure. Within the FLD, a line called the forming-limit curve (FLC) marks the onset of local necking and divides strain space into safe and failure zones. The objective of sheet-metal process design is to ensure that strains in the sheet do not approach this limit curve. Though the concept of the FLD is simple, a material's ability to deform plastically depends on a large number of coupled effects, making its experimental determination non-trivial and a very time-consuming procedure. As a result, considerable effort has recently been made to develop theoretical predictive models, based on the theory of crystal plasticity and different instability criteria.

2.2 Development of Advanced Crystal Plasticity Models

Polycrystalline materials are ubiquitous in industrial and technological applications due to their inexpensiveness and ease of manufacturing. The response of an aggregate of crystallites of varying size and orientation subjected to plastic deformation is governed by the spatial distribution and dynamics of crystalline defects. The development of advanced characterization tools has enabled very detailed characterization of polycrystalline materials. For example, Scanning Electron Microscope (SEM) and Transmission Electron Microscope (TEM) (Lee and Lam, 1996; Nieh et al., 1998; Salem et al., 2003; Armstrong and Walley, 2008; Karel et al., 2016; Wickramarachchi et al., 2016) are used for surface analysis of the material's microstructure. Synchrotron-based X-Ray Diffraction (XRD) and Focus-Ion-Beam (FIB) combined with Electron Back-Scattering Diffraction (EBSD) are used to measure the chemical composition and crystal structure (Ohashi et al., 2009; Gardner et al., 2010; Jeong et al., 2015; Abdolvand et al., 2015; Erinosho et al., 2016).

These advanced experimental techniques bestow highly sophisticated microstructure information and generate large amounts of data creating a difficult task for computational techniques to interpret and harness relevant information. In order to establish the relationship between microstructure and macroscopic properties of polycrystalline materials undergoing plastic

deformation, an accurate prediction of the micromechanical behavior based on directional material properties along with gradual development of substructure of the constituent grains is required. Therefore, efficient crystal plasticity-based computational schemes are needed to investigate the microstructure-property relations.

A polycrystal deformation model should be able to describe some phenomena, which cannot be illustrated by phenomenological theories (e.g., continuum mechanics-based models), such as crystallographic slip, textures, grain morphology etc. Usually, such model can be obtained from single crystal deformation models, but the concern is how to build the relationships between microstructural mechanisms of deformation operating on level of single crystal and overall response of a polycrystal. In the early models of crystal plasticity, some assumptions were made about the distribution of stresses and strains in the polycrystal to relate the behavior of a polycrystal to its constituent single crystals. In these crystal plasticity models, the behavior of polycrystal is obtained using some appropriate averaging technique for the response of its constituent single crystals.

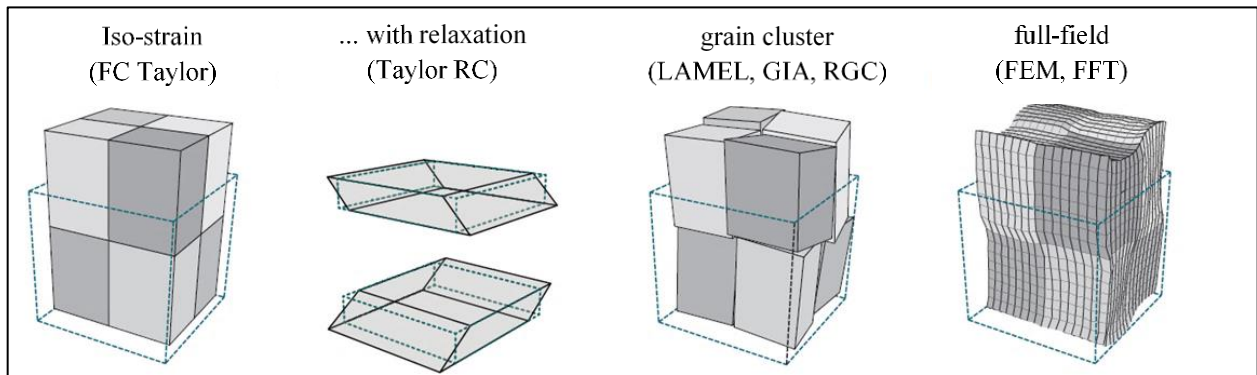


Figure 2.15: Four common types of crystal plasticity models to estimate polycrystal response (Roters et al., 2012).

During the 19th century, several such models have been proposed that have provided much useful understanding about the development of preferred crystallographic orientations (texture) and strain hardening behavior in the polycrystal. These models are based on the concept of plastic deformation due to crystallographic slip. Other deformation mechanisms, such as grain boundary sliding and diffusion, are not covered in this review. Figure 2.15 illustrates four commonly used homogenization schemes, namely the iso-strain or full constraints Taylor scheme, Taylor-based schemes allowing for relaxation (e.g., cluster models; LAMEL, GIA or RGC), and full-field

estimation by FEM or spectral methods using an FFT. These schemes are explained in detail in following sections.

2.2.1 Sach's Model

Sachs (1928) model, one of the earliest epitomes of polycrystal models, assumes that each crystal is subjected to the same stress state. In this “iso-stress” model, the grains are treated as if they were an array of single crystals that can deform independently of each other. For a better understanding of this model, let us apply the Schmid's law to each of the crystals. It can be found, on increasing stress level gradually, that at first there would be no plastic deformation anywhere, until a critical level of stress is reached after which the plastic deformation would start in the grain/grains with the most favorable lattice orientation. Since all the grains are assumed to be experiencing the same state of stress in this model, the plastic deformation that results from it can vary from one grain to another, thus the compatibility conditions in the aggregate are violated. As a result, continuity of strain across a grain boundary is violated. Moreover, in this model, strain and orientation changes are deduced from the stress in the same way as in the case of a free single crystal submitted to a known stress. In general, this theory was not found to be very successful in predicting deformation textures. Nowadays, the iso-stress assumption is acknowledged as an oversimplification, so this model is hardly used anymore.

2.2.2 The Taylor Crystal Theory

In order to overcome the disapproval to Sach's model, Taylor proposed an alternative model. There are two important aspects in the original Taylor theory: (a) a criterion for selecting the active slip systems in a deformed single crystal (Schmid's Law), and (b) the assumptions for linking the deformation behavior between the constituent grains, and the polycrystalline aggregate. The basic idea underlying the Taylor model rests on experimental observations. By examining a micrograph of the cross section of a drawn wire, Taylor observed that all the grains were elongated in the direction of extension, and contracted in the two perpendicular directions. He concluded that the strain field throughout the polycrystal is homogeneous, implying that each grain deforms exactly in the same way as the polycrystal. This assumption has served as a tool for linking the deformation behavior among all constituent grains, and between individual grains and polycrystals. It is now

known that it is not exactly true, but the assumption has the advantage of assuring continuity of the strain rate across the grain boundaries so that no voids are created.

With the Taylor assumption, the stress state is not continuous, but varies abruptly from grain to grain, depending on different grain orientations. In the classical Taylor-type models, out of 12, at least five independent slip systems have to be activated to guarantee deformation compatibility of the whole specimen for FCC polycrystal. Since the number of strain conditions (the “number of constraints”) is as large as five, such models are referred to as “full constraint” (FC) models. Summarizing, two main points that emerge from the Taylor theory regarding the relation between the deformations of single crystals and that of polycrystals:

1. The deformation in each crystal is the same as the macroscopic deformation; the shapes of the constituent crystals do not enter in the idealization; and
2. The macroscopic stress of a polycrystal is the average of the stresses of all constituent single crystals.

An in-house Taylor model-based code will be used in this research for comparison of predictions of forming limit strains with the proposed model in this work (see, e.g., Chapter 4).

2.2.3 Relaxed Constraint Models

It is well recognized that the Taylor-type models overestimate both texture and the stresses in a polycrystal. To answer these limitations, several improvements have been proposed, one of which is the Relaxed Constraint Taylor model (Houtte, 1982; Raphanel and Houtte, 1985). The idea here is to assume that when grains re-orient and take on much distorted shapes, characterized by large aspect ratios of the principal lengths, it is possible to partially relax the strict compatibility requirements imposed in the Taylor model. Non-uniform deformations are envisaged to occur at the grain boundaries that accommodate the incompatibilities implied by the non-imposed strain components. When applied to certain deformation states such as axisymmetric tension and compression they argue that the dimensionality of the problem is reduced so that less than five independent slip systems are needed. The authors (Houtte, 1982; Raphanel and Houtte, 1985) have used the methodology of relaxed constraints to analyze deformation textures in FCC polycrystals following several strain histories such as axisymmetric tension and compression, along with large

simple shear. Since the imposed strain increments differ from those that would be imposed in a full constraint (Taylor) model, the slip modes and lattice rotations predicted by the two approaches are different.

2.2.4 Grain Interaction Models

The relaxations are the integral part of so-called ‘grain interaction models’ (also known as ‘cluster’ models), which include advanced homogenization schemes. The homogenization is done on a small cluster of grains instead of single crystals as compared to the schemes explained in previous section. In these models, the average plastic velocity gradient of the cluster is assumed equal to the macroscopic velocity gradient. Therefore, these ‘cluster’ models introduce interactions between crystals in the polycrystal. One of these cluster models, “the Advanced LAMEL” (ALAMEL) model was proposed by Van Houtte et al. (2005) as a generalization of the LAMEL Houtte et al. (1999) and Liu et al. (2002) . The ALAMEL model analyze interactions in different clusters containing two grains each, separated by an interface of grain boundary. The grain boundary is usually arbitrarily oriented according to a certain distribution function.

In the ALAMEL model, according to admissible relaxation modes, the local strains of crystals deviate from the macroscopic strain, and the extent of the relaxation is obtained by minimizing the collective plastic work inside the grain cluster. Recently, Arul Kumar et al. (2011), Mahesh (2010) proposed several improvements to the original ALAMEL model. Delannay et al. (2009, 2002) and Houtte et al. (2002) proposed another multisite approach which extends the ALAMEL and assumes that each grain interacts exclusively with one or several of the immediate surrounding grains, furthermore, adding elastic part to the governing equations. Another Grain Interaction (GIA) model, which also use the concept of grain clusters, was proposed by Crumbach et al. (2002) and was further developed by Engler et al. (2005). This GIA model considers short-range interactions between first-order neighbor grains in a group of grains consisting of eight hexahedral grains. Recently, the formulation of GIA was further developed by Eisenlohr et al. (2009), Tjahjanto et al. (2015) and they proposed the Relaxed Grain Cluster (RGC) model. Tjahjanto et al. (2015) extended to this model for modelling multi-phase materials.

2.2.5 Self-Consistent Schemes

Another type of homogenization model is the self-consistent scheme initially developed by Lebensohn and Tomé (1993), Molinari et al. (1997, 1987) which was inspired by Eshelby (1957)'s analytical solution of elasticity problem for an ellipsoidal inclusion embedded in an effective medium and was then extended to viscoplastic regime by Lebensohn et al. (2007) known as Visco-Plastic Self-Consistent model (VPSC). In the VPSC, all the grains in the RVE are considered as an effective medium, which is assumed to be homogeneous. Each crystal is treated as ellipsoidal inclusions that can deform plastically and is constrained by the effective medium; therefore, the short-range interactions are neglected. However, the model accounts for long-range interactions the in the polycrystalline, using the interactions of all the crystals with the effective medium in an average sense. In addition, the VPSC model enforces both strain compatibility and stress equilibrium between grains and their surroundings, as opposed to the Taylor-type models that assume homogeneous strain in the RVE. Based on the original SC method, Molinari et al. (1987) and Tóth et al. (1996) were able to predict the texture evolution for FCC and BCC polycrystals during rolling and torsion, respectively.

Later on, Lebensohn and Tomé (1993) predicted texture evolution during rolling and axisymmetric deformation and determined the plastic anisotropy of a rolled zirconium alloy sheet. Choi et al. (2000) also used the SC method to investigate the effects of crystallographic and morphological texture on the macroscopic anisotropic properties (R-value and normalized yield stress) for AA5019 sheets in H48 and O temper conditions using the full-constraint Taylor and a visco-plastic self-consistent polycrystal model. They have presented results in which spherical and ellipsoidal grain shapes were analyzed. For cubic metals, such as FCC polycrystals, textures predicted by the SC models are rather similar to those obtained with the FC and RC models.

2.2.6 Spectral Crystal Plasticity (SCP)

The Spectral crystal plasticity (SCP) can be seen as a special case of database-type coupling. Whereas it also relies on sampling responses of a crystal plasticity framework, the way in which the results are stored and queried greatly differentiates the SCP from the approach presented in the previous section. The database techniques store the homogenized responses of the RVE, while the

SCP stores the intermediate results of a Taylor-type model. Observe that if a Taylor-type model is used, each crystal is treated separately, and any per-grain solution of the crystal plasticity model depends solely on the orientation of the crystal and the strain rate imposed on it. The solution may include stress, lattice spin, shearing rates, Taylor factor etc. It is then possible to first evaluate a Taylor-type model for a large number of orientations, strain rates, and subsequently store the results in an easily retrievable manner. As long as no other factors are considered, such as hardening of slip systems or grain interactions, these calculations can be done once and for all.

To achieve this, Fourier (spectral) representation of orientation distribution function (Bunge and Esling 1984) can be conveniently used for storing the results of a Taylor-type model, see, e.g., Kalidindi and Duvvuru (2005) and Kalidindi et al. (2006). The one-time, but time-consuming task is to find coefficients in Fourier series of the spectral representation for the functions that represent the per-grain solutions of the Taylor-type CP model. These solutions must be computed for each crystal orientation in Euler space subjected to all possible strain rates. This way, a database of spectral coefficients is generated. The advantage of the approach is that the result of the CP model can be later retrieved just by querying the database without doing any actual CP calculations. The computational advantage of the SCP comes with certain drawbacks, though. Independent sampling of individual grains is implicitly required; thus, the accuracy of the SCP is bound by the limitations of the Taylor assumptions. It is now well known that Taylor-type models do not offer best texture and anisotropy prediction. Furthermore, the SCP approach is hardly capable of going beyond quite simple Taylor-type models. For instance, adding internal variable hardening models would render the SCP impractical, since constructing the database of spectral coefficients would require exploring a high dimensional space.

2.2.7 Crystal Plasticity Finite Element Method (CP-FEM)

Early approaches to describe plastic anisotropy with simple boundary conditions such as Sachs (1928) and Taylor (1938) formulations were developed by simplifying assumptions of strain or stress homogeneity. They were not designed to consider explicitly the mechanical interactions among crystals in a polycrystal or for responding to complex internal and external loading boundary conditions. To overcome these issues, variational methods in the form of finite-element approximations have gained tremendous momentum in the field of plasticity. These crystal

plasticity finite-element (CP-FEM) models are based on the variational solution of equilibrium between forces and compatibility of displacements using a weak form of the principle of virtual work within a finite-volume element. The FE model is built using the discretization of the specimen into these elements. The CP-FE method employs the extensive knowledge gained from experimental and theoretical studies on single crystal deformation and dislocation dynamics (Curtin and Miller, 2003; Arsenlis et al., 2004; Vitek et al., 2004) to inform the further development of continuum field theories (Zienkiewicz et al., 1977).

The constitutive framework offered through variational crystal plasticity formulations provides a desirable tool for developing comprehensive theories of plasticity that apply the current knowledge of the physics of deformation processes to continuum mechanics computational tools with the goal of developing advanced and physically-based engineering design methods (Roters et al., 2010). The success of CPFE methods can also be attributed to the ability to include various constitutive formulations for plastic flow and hardening at an elementary slip system level. The constitutive flow rules that have been suggested over the past few decades are developed from empirical viscoplastic formulations (Asaro and Rice, 1977; Rice, 1971) to physics-based models (Arsenlis et al., 2004; Arsenlis and Parks, 2002, 1999; Evers et al., 2002; Raabe and Roters, 2004). It should be reiterated at this point that the FEM itself is not the actual model but the variational solver for the applied constitutive equations that maps the material anisotropy of elastic-plastic shear associated with various lattice defects (specifically dislocations in aluminum).

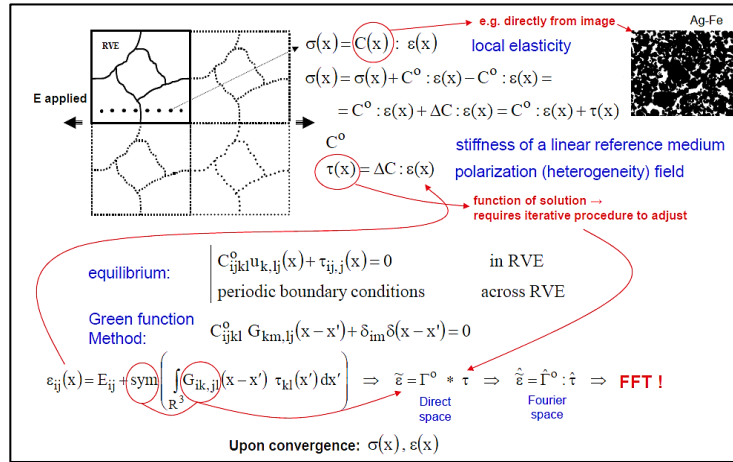
The first introduction of this method by Peirce et al. (1982) has matured into a wide collection of constitutive and numerical formulations to be applied to a very wide variety of crystal-mechanical problems. A large body of work exists on incorporating crystal plasticity frameworks as constitutive relation in the Finite Element method. An excellent review of these attempts has been published by Roters et al. (2010) that contains a comprehensive overview of the constitutive laws, kinematics, homogenization and multiscale methods in the CP-FEM modelling. Constitutive models extending the works of Asaro and Needleman (1984), Asaro and Rice (1977), Peirce et al. (1983), Peirce et al. (1982) are very commonly used and include visco-plastic, elasto-viscoplastic and elastic-plastic constitutive behavior. Plastic deformation of the material and evolution of texture results from activation of deformation mechanisms, such as slip and twinning.

In “CP-FEM”, the FE mesh represents an aggregate of grains, each having a specific set of attributes, such as shape, orientation, phase, etc. The method offers several advantages over statistical approaches. Most remarkably: If several finite elements constitute a grain, the gradients of stress and strain inside individual crystal can be considered. This holds even if low order elements (e.g., linear) are used to discretize the domain. Gradients of other fields inside the grains can be captured as well. For instance, crystal orientation gradient may be accounted for, which is crucial in modelling intra-granular localization processes. Complicated geometry of individual crystals can be explicitly dealt with in the model. Since the grains are spatially bound by each other, explicit grain boundaries are introduced in the model. This also allows to take into consideration grain boundary properties. The CP-FEM models are formulated as either rate-dependent or rate-insensitive with respect to the material response. The hardening at the level of crystallographic slip and twinning is considered as well. A power law is often chosen to relate the applied resolved shear stress on the slip or twinning system to the shear rate in the slip or twinning direction. Large inelastic deformation can be reached in CP-FEM. However, we have to keep in mind that accuracy of the FEM may be undermined if large distortions of elements are experienced. This issue can be addressed by advanced mesh refinement methods, see, e.g., Resk et al. (2009) and Quey et al. (2011).

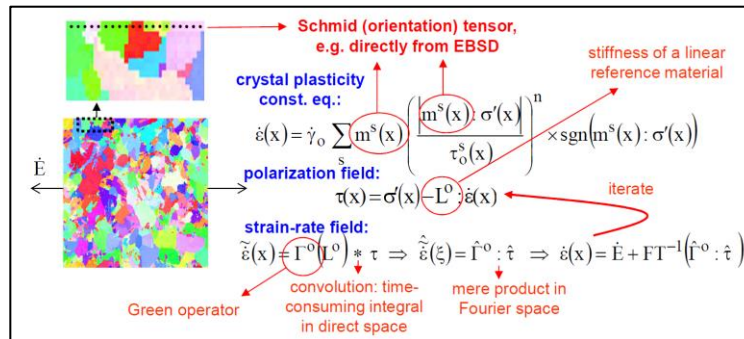
2.2.8 Crystal Plasticity Fast Fourier Transform Method (CP-FFT)

The “**FFT-based Crystal Plasticity**” methods are based on the fact that the local mechanical response of a heterogeneous medium can be calculated as a convolution integral between Green function associated with appropriate fields of a linear reference homogeneous medium and the actual heterogeneity field. This approach is suitable for finding the solution of a unit cell problem with periodic boundary conditions. If a periodic medium is considered, one can use the Fourier transform to reduce convolution integrals in real space to simple products in Fourier space. Thus, the fast Fourier transform algorithm can be utilized to transform the heterogeneity field into Fourier space. Afterwards, the mechanical fields can be calculated by applying the transformation back to real space. The FFT solvers can only make use of uniform grid, which might be too coarse to properly approximate stress and strain fields near grain boundaries.

An efficient alternative to CP-FEM, is given by the FFT-based method. Recently, considerable attention has been attracted by the crystal plasticity fast Fourier transform (CP-FFT) methods (Lebensohn, 2001; Lebensohn et al., 2004; Prakash and Lebensohn, 2009; Liu et al., 2010; Eisenlohr et al., 2013; Shanthraj et al., 2015), which promise substantial improvement over the CP-FEM in terms of calculation time, while keeping high spatial resolution in order to capture the details of complex microstructures. This formulation, originally developed by Moulinec and Suquet (1994), (1998) to compute the macro and micro response of composites, consists in solving Lippmann-Schwinger equation by an iterative method that involves the use of the Green's operator associated to a linear reference medium. Since then, several authors have proposed modifications or improvements of the original Moulinec-Suquet ("basic scheme") (Eyre and Milton, 1999; Brisard and Dormieux, 2010; Zeman et al., 2010; Zeman and Marek, 2014).



a) Original FFT scheme for modeling elastic behavior of heterogeneous composites (Moulinec and Suquet 1994, 1998)



b) FFT-based approach adapted by Lebensohn (2001) for polycrystals from original technique proposed by Moulinec and Suquet (1994), (1998)

Figure 2.16: FFT-based methods for composites and polycrystals.

Specifically, Zeman et al. (2010) proposed accelerated algorithms to overcome the low convergence rate of the basic scheme for materials with high mechanical contrast but only small computational gains were achieved. This scheme has been successful in achieving acceleration on the convergence rate proportional to the square root of the mechanical contrast; however, the scheme fails to converge for infinite contrast. The basic scheme has been further developed for polycrystalline material deforming in elastic regime (Brenner et al., 2009), rigid-viscoplastic regime (Lebensohn, 2001; Lebensohn et al., 2008), elasto-viscoplastic regime (Lebensohn et al., 2012) for infinitesimal strains, recently extended to finite strains (Eisenlohr et al., 2013; Geus et al., 2016; Kabel et al., 2016).

As opposed to the CP-FEM, the CP-FFT method is meshless, so it uses voxels to discretize domain. As shown in Figure 2.16, the CP-FFT-based formulation consists in finding a strain-rate field, associated with a kinematically admissible velocity field that minimizes the average of local work-rate, under the compatibility and equilibrium constraints (Lebensohn, 2001). To keep the grid regular, simplifications to the kinematic equations have to be made, see, e.g., Prakash and Lebensohn (2009) and Liu et al. (2010). Moreover, the fundamental requirement of periodic boundary conditions renders the CP-FFT somewhat less flexible than the CP-FEM.

2.3 Modelling Dynamic Recrystallization

Hot working of magnesium alloys is inevitably accompanied by dynamic recrystallization (DRX). Experimental measurements of DRX are difficult, too expensive and time consuming to provide a processing window for each alloy. Thus, being able to predict material behavior and modelling microstructure evolution would provide an opportunity to control different material properties (Hallberg, 2011). For example, improving the understanding of kinetics of grain boundary movement as well as controlling texture evolution and grain size during the plastic deformation are some of key advantages of accurate modelling of DRX (Rollett, 1997). Nevertheless, the modelling of DRX still remains a difficult and challenging problem. As the power of computational resources have increased in last few years, several computationally intensive,

physics-based tools are now available for modelling DRX phenomenon, e.g., atomistic simulations, molecular dynamics, and crystal plasticity models.

Initial attempts to model DRX were taken in 1930s, when the the so-called JMAK theory (i.e., an analytical model) was developed by Avrami (1939) and Shiryayev (1992). In this model, the volume fraction of DRX, f , is represented in terms of the nucleation rate k and time t as

$$f = 1 - \exp(-kt^n) \quad (2.21)$$

where n is the Avrami exponent. This expression describes the evolution of the volume fraction of recrystallized grains and it is used by researchers for model verification. Sandström (1977) developed a theoretical model for subgrain growth during annealing. The authors modeled subgrain growth by defining a criteria for grain boundary migration. They applied this model to two-phase alloys and pure metals. In later years, Furu et al. (1995) proposed an another subgrain growth model for severely deformed aluminum alloy. Taking into account the dynamic recovery as well as grain size, Sandström and Lagneborg (1975) developed a model that predicts stress-strain curve during DRX. However, with the increase in power of computational resources, several new numerical models have been developed to simulate the process of recrystallization. As expected, each of these models has its own weaknesses and strengths. Accordingly, the most common models can be divided into the following categories:

- Monte Carlo models
- Vertex models
- Phase-field models
- Cellular Automata

The literature on each of these models is briefly discussed below.

2.3.1 Monte Carlo Models

The Monte Carlo models with probabilistic methods are used in the Potts model, which is a modified Ising model, for modelling recrystallization. Modelling recrystallization and grain growth using the Monte Carlo methods, extensive studies were performed by Srolovitz et al. (1988), Anderson et al. (1989) and Rai et al. (2007).

In the Monte Carlo models, the domain of interest is divided into lattice sites by using a discretized grid of points. Each grain is assigned a site index s_i and the state variables. Accordingly, the switching parameter ω_{switch} that defines a new nucleus depends on the change in internal energy ΔE as

$$\omega_{switch}(\Delta E) = \frac{1}{2} \omega_0 \left[1 - \tanh\left(\frac{\Delta E}{2kT}\right) \right] \quad (2.22)$$

where ω_0 is the grain boundary mobility between the current s_i and neighbouring s_j sites, T is the temperature and k is the Boltzmann constant. According to the Monte Carlo method, the switch is accepted if the generated random number $\xi \leq \omega_{switch}(\Delta E)$. Then the orientation of site s_i is swapped with the orientation of the neighbouring site s_j . The schematic representation of the Monte Carlo model is given in the Figure 2.17, where the bold lines represent the grain boundaries.

a deterministic grain boundary (Piekoř et al., 2008) compared to the Monte Carlo models, where the curvature of the grain boundary cannot be well described. In the vertex method, the vertices are located at triple junctions (2D) of the grain boundary and are assumed to be in equilibrium. Line segments connecting these vertices define the grain boundary. The grain boundary velocity v is described as a function of grain boundary mobility μ and the grain boundary energy γ as follows

$$v = \gamma(\theta, T) \cdot \mu(\theta, T)k \quad (2.23)$$

where T is the simulation temperature, θ is the misorientation between two grains and k is the grain boundary curvature. As shown in Figure 2.18, depending on the translation rules, the triple junctions are moved to the directions perpendicular to the plane. The triple junction angles ϕ_i of the nodes can be defined in terms of the grain boundary energies γ_i as follows

$$\frac{\gamma_1}{\sin\phi_1} = \frac{\gamma_2}{\sin\phi_2} = \frac{\gamma_3}{\sin\phi_3} \quad (2.24)$$

Further details of the kinematics formulation of the vertex models can be found in Nakashima et al. (1989).

2.3.3 Phase-Field Models

Unlike in Monte Carlo models, where the boundary is not identified explicitly, in the phase-field models, the grain boundary is explicitly defined as a separate phase (Figure 2.19). In the phase-field model, the volume fraction of k phase is represented by phase-field parameter, n_k . In this model, n_k represents a grain in the polycrystalline aggregate with N number of grains. In that case, n_k is equal to 1 in the k^{th} grain, and equal to 0 in the other grains.

Since the phase-field method is based on the energy minimization that depends the phase-field variables and their gradients, the method is computationally very expensive. Consequently, the model is not commonly used and is usually limited to 2D applications.

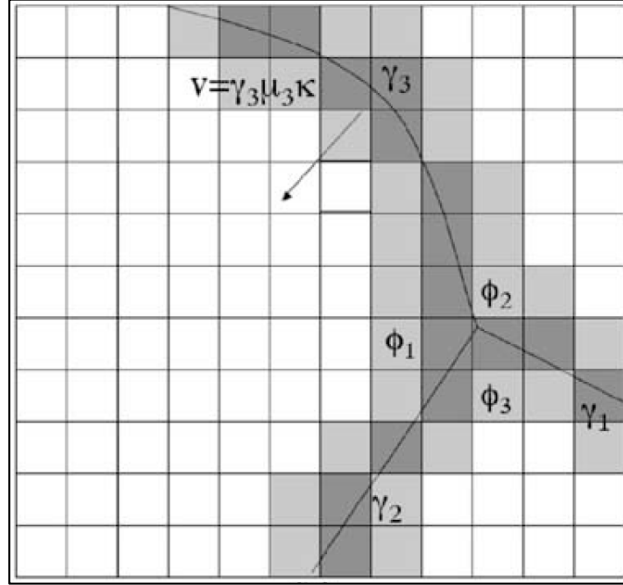


Figure 2.19: Schematic representation of the division of the domain in the phase-field model (Miodownik, 2002).

In Takaki et al. (2009), a multi-phase-field model for dynamic recrystallization (MPF-DRX) was developed. In this model, the deformation of the grain is taken into account by resizing the grid. Their simulation results of the single grain growth were in good agreement with theory. Tikare et al. (1998) presented a comparison study of phase-field modelling with Monte Carlo model for a grain growth problem. Both models gave very similar results. Further details of the phase-field modelling studies can also be found in Tikare et al. (1998), Gurtin and Lusk (1999), Lusk (1999) and Muramatsu et al. (2010).

2.3.4 Cellular Automata

von Neumann introduced the cellular automata (CA) for a Turing machine (Schwartz et al., 1967). In later years, it was adopted for modelling recrystallization problems (Raabe, 2002). For the recrystallization problems, the CA method is based on the discretization of physical space, time and the orientation space. The domain of interest is divided into discrete cells that represent grains and each cell has its own state variables that define its current status. Commonly, the dislocation density and the crystal orientation are used as state variables in the CA-based recrystallization problems. The CA can be defined on the discretized 2D or 3D lattice cells considering the first,

second, and third order neighbors for the calculation of the local driving forces in a representative volume element (RVE) of the microstructure.

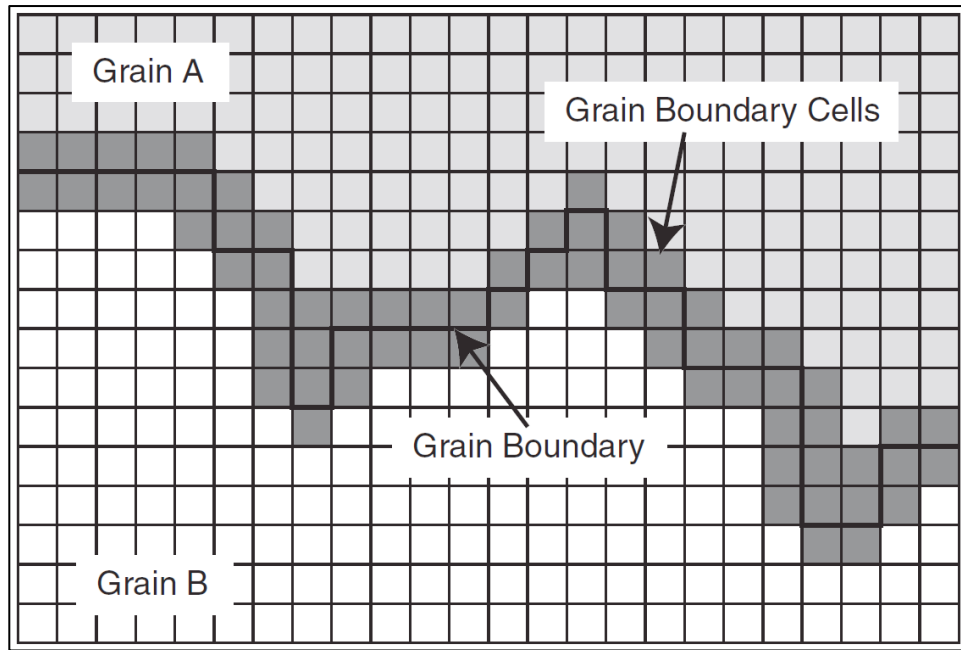


Figure 2.20: Schematic representation of the grain boundaries in cellular automata (Janssens, 2003).

For CA method, an illustration of the grain boundary determination is presented in Figure 2.20. In this model, the current state of each cell depends on the state of the neighbouring cells. In recrystallization problems, a cell would be recrystallized in the current time step only if any neighbouring cells were recrystallized in the time steps before (Janssens, 2003). Once the recrystallization update of the grains is done, the state variables of the entire aggregate of grains is also updated simultaneously.

The so-called the probabilistic CA first computes the switching probability of each cell and then makes the switching based on a probabilistic step (Raabe, 2002) while the deterministic CA switches the state of a cell due to recrystallization by the neighbor cells depending on the rate equation. Due to ease of implementation and low computational cost, the CA is defined as a general algorithm with a possibility to use a wide range of state variables and transition rules. Therefore, it is very useful candidate for modelling recrystallization problems. Similar to other recrystallization models discussed above, one of the major complications with the CA models is the association of the simulation time with real time,. Nonetheless, the CA model has been

successfully used in the recrystallization problems (Goetz and Seetharaman, 1998; Janssens, 2003, 2010; Seyed Salehi and Serajzadeh, 2012; Popova et al., 2015, 2016; Li et al., 2016; Madej et al., 2016).

2.4 Modelling Forming Limit Diagrams of Polycrystals

The concept of a forming limit diagram (FLD), first introduced by (Keeler and Backofen, 1964) from his investigation of plastic instability and fracture in sheets stretched over steel punches, has proved to be extremely useful for representing conditions for the onset of sheet necking. It is now a standard tool for characterizing materials in terms of their drawability. Early calculations of forming limit diagrams were based on Hill's criterion (Hill, 1952) for localized necking along a direction of zero-extension. In Hill's bifurcation analysis for rate-insensitive materials, J2 flow theory (The von Mises theory is often called "J2 plasticity" because it is usually described in terms of the so-called second invariant of the stress and is based on macroscopic material behavior only) was employed together with a power-law stress-strain relationship and smooth yield surface. Hill's predictions only gave the critical strains between the uniaxial tension and plane strain states on the FLD. When the sheet is under biaxial stretching. Hill's direction of zero-extension does not exist.

As an alternative plane stress analysis, Marciniak and Kuczyński developed the most influential plastic instability criteria for analyzing unstable deformation in sheet metals also known as the M-K analysis (Marciniak and Kuczyński, 1967) as shown in Figure 2.21. Marciniak and Kuczyński postulated that a sheet metal contains different types of intrinsic imperfections. For example, uneven thickness of the sheet, surface defects, voids and inclusions are some of the inhomogeneities that can develop during the manufacturing process of the sheet metal. These imperfections further evolve during the forming process which become the sites of the localized plastic flow.

In the M-K analysis (Marciniak and Kuczyński, 1967), plastic instability was considered to originate in the imperfection groove with a thickness lesser than the thickness of the surrounding material, subsequently leading to localized necking and failure of the sheet metal. For the first time, Azrin and Backofen (1970) realized the Marciniak and Kuczyński's postulate experimentally by studying the effects of an imperfection patch in a sheet metal on forming limit diagrams.

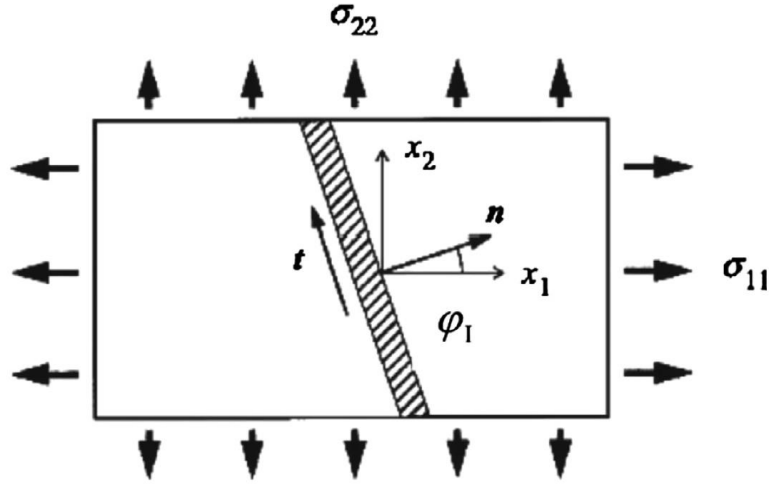


Figure 2.21: Schematic of M-K instability criteria (Mohammadi et al., 2014).

Originally developed as a means of describing localized necking in biaxial stretching for which the minor strain > 0 , the M-K analysis was later extended to the negative minor strain region (Stören and Rice, 1975; Hutchinson and Neale, 1978a). Furthermore, in Hutchinson and Neale's work (Hutchinson and Neale, 1978b), the M-K model, which is based on the flow theory of plasticity framework and quadratic plastic potentials, was also refined by incorporating the J2 deformation theory of plasticity. Another extension, namely the inclusion of strain-rate effects in studies of sheet metal formability, was initially initiated by (Marciniak et al., 1973; Hutchinson and Neale, 1978a; Needleman and Tvergaard, 1984) carried out similar analyses for rate-sensitive materials. In these simulations, the effects of various constitutive features on localized sheet necking were explored.

It is well known that the localization of plastic flow is strongly influenced by deformation-induced textures and anisotropy (Asaro and Needleman, 1985). In turn, this localization then affects, to some degree, the texture development in polycrystals. Considering these factors, polycrystal deformation models can be expected to be very effective for simulating plastic instability processes. A polycrystal model should provide an improved understanding of the relation of localization to the microstructure of the material, and thus be more successful in predicting strain localization phenomena than phenomenological models. Based on the simple M-K-type model, Asaro and Needleman (1985) presented analyses of localized necking in thin sheets subjected to

balanced biaxial stretching with their polycrystal model. Their work enabled, for the first time the study of the effects of texture and path-dependent strain hardening on sheet necking.

Zhou and Neale (1995) have directly applied a rate-sensitive crystal plasticity model in conjunction with the M-K approach to predict FLDs for annealed FCC sheet metals. Their analyses considered the initial texture and its evolution. However, elasticity was neglected and the imperfection groove was restricted to be normal to the major principal stretch direction. Wu et al. (1996) used the Asaro and Needleman (1985) polycrystal plasticity model to calculate the FLDs for FCC polycrystals. They have discussed in detail the effects of initial imperfection intensity and orientation, initial distribution of grain orientations, crystal elasticity, strain rate sensitivity, single slip hardening, and latent hardening on the predicted FLDs.

It is known that the initiation of a neck leads to localized deformation, with further stretching, either strain localizes progressively in this neck or necking triggers the formation of shear bands. In the mathematical description, the formation of localized shear bands in solids is quite similar to localized necking in sheets. However, shear bands represent a material instability, and they do not depend on constraints along the boundary of the solid. Such material instabilities are of significance as a precursor to fracture, and have been observed in a wide variety of materials. The basic phenomenon of shear localization can be studied using a relatively simple approach similar to the above-mentioned M-K analysis where localized shearing is assumed to occur in a thin slice of material, while the strain fields outside this band are assumed to remain uniform throughout the deformation history.

Peirce et al. (1982) presented finite element calculations for non-uniform deformation modes in ductile single crystals based on a rate-independent constitutive model for crystallographic slip. Their analysis, however, highlighted inherent limitations of the rate independent idealization of crystalline slip. These limitations were so severe that an analysis of large strain plastic flow was precluded for a full range of material properties, in particular for materials having high strain hardening. As a result, Peirce et al. (1983) adopted the rate-dependent constitutive theory for crystalline slip, and were able to simulate large strain tension tests of single crystals. Their results provided a general understanding of the roles of rate sensitivity and lattice kinematics in the development of localized modes of deformation. Wu et al. (2004) and Yoshida et al. (2007) showed

that the typical recrystallization texture component (cube texture) improves the right side of the FLD (biaxial formability) while the rolling texture components (Copper, Brass, Goss and S textures) show a decline in the biaxial formability (Yoshida et al., 2007).

Inal et al. (2005) used a rate-sensitive polycrystal plasticity model with the full constraint Taylor type homogenization scheme (FC-Taylor) and suggested that the effect of texture evolution during deformation on formability of body-centered cubic (BCC) polycrystal is much less (higher forming limit curve) as compared to the FCC polycrystals (lower forming-limit curve). Inal et al. (2005) also reported that the number of slip systems strongly affects the occurrence of localized necking in a polycrystalline material, which agrees with what Barlat (1987) demonstrated. The above-mentioned studies show that initial texture of the sheet metal not only affects the slip activity on different slip systems but also play an important role in strain localization that causes failure of the sheet metal.

Serenelli et al. (2011) and Signorelli and Bertinetti (2009, 2012) claimed that FLDs predicted using VPSC-MK models are able to achieve better agreement with the measured FLDs as compared to the MK-Taylor models. However, the MK-VPSC models are computationally very expensive as compared to the MK-Taylor models (Schwindt et al., 2015; Jeong et al., 2016) and thus limiting the application of VPSC to problems with small computational domains. Wang et al. (2011) used both Taylor and VPSC models coupled with the M-K approach to assess the formability of Mg sheet alloy (with HCP crystal structure) and suggested that the texture evolution highly affects the formability for uniaxial and biaxial deformations showing a low forming limit curve, while it has little effect on the formability for plane strain deformation.

2.5 Brief Conclusions of Literature Review

To obtain the failure strains, the M-K approach employs two representative volume elements. To generate the complete forming limit diagram (FLD) using the M-K approach, failure strains are obtained at 16 different strain paths, i.e., imposed strain ratio is changed from -0.5 (i.e., uniaxial tension) to 1.0 (i.e., balanced biaxial tension) with an increment of 0.1. In addition, for each strain path, the initial imperfection band angle is swept from 0° to 90° in in-plane with an increment of 5° and the lowest value of failure strain is selected. Therefore, a total of 288 different simulations

are required to obtain the complete FLD. Thus, to model the DRX and obtain FLDs simultaneously for 3D microstructure of HCP metals, using a full-field crystal plasticity model, large amount of computations is required. Besides, modelling a complex material such as an HCP metal that has eighteen slip systems and six twinning systems is computationally more expensive than modelling similar phenomena in a relatively simple material such as aluminum alloy that has only twelve slip systems. Therefore, a highly efficient full-field crystal plasticity model is required. Thus, efficient FFT-based crystal plasticity model seems to be good candidate for formability analyses. Furthermore, since a simulated area in the cellular automat (CA) is discretized using cells, a grid of Fourier points can be directly coupled to model a real microstructure. If the time-scaling is calibrated correctly, the Fourier points can represent cells. This is one of the main advantages of coupling FFT-based crystal plasticity model and CA.

Chapter 3. – Part 1: Efficient Fast Fourier Transform-based Numerical Implementation to Simulate Large Strain Behavior of Polycrystalline Materials, Published in International Journal of Plasticity 98 (2017) 65-82

Jaspreet S. Nagra¹, Abhijit Brahme¹, Ricardo A. Lebensohn², Kaan Inal¹

¹University of Waterloo, 200 University Ave. West, Waterloo, ON N2L 3G1, Canada

²Los Alamos National Laboratory, MS G755, Los Alamos, NM 87845, USA

Abstract

In this chapter, a new full-field numerical framework is proposed to model large strain phenomena in polycrystals. The proposed framework is based on the elasto-viscoplastic (EVP) fast Fourier transform (FFT) formulation presented by Lebensohn et al. (2012) and the rate dependent crystal plasticity framework developed by Asaro and Needleman (1985). In this implementation, the full-field solutions of micromechanical fields are computed on a regular, voxelized representative volume element (RVE) in which either a single or multiple grid point represent a single grain. The Asaro and Needleman (1985) formulation coupled with a semi-explicit, forward gradient time-integration scheme (Peirce et al., 1983) is used to compute local stresses and the FFT-based method is used to find local strain fluctuations at each grid point. The proposed model is calibrated using experimental uniaxial tensile test results of aluminum alloy (AA) 5754 sheet and then used to predict texture evolution and stress-strain response for balanced biaxial tension and plane-strain tension along rolling (RD) and transverse (TD) directions. The predicted stress-strain and texture results show a good agreement with experimental measurements. The CPU time required by the proposed model is compared with the original EVP-FFT model for two separate cases and the proposed model showed significant improvement in computation time (approximately 100 times faster).

Keywords: Crystal plasticity, Fast Fourier Transforms, Tangent Method, Computational efficiency, Texture, Aluminum alloys, Variable loading path

3.1 Introduction

The response of an aggregate of crystallites of varying size and orientation subjected to plastic deformation is governed by the spatial distribution and dynamics of crystalline defects. The development of advanced characterization tools has enabled very detailed characterization of polycrystalline materials. For example, Scanning Electron Microscopy (SEM) and Transmission Electron Microscopy (TEM) (Lee and Lam, 1996; Nieh et al., 1998; Salem et al., 2003; Armstrong and Walley, 2008; Karel et al., 2016; Wickramarachchi et al., 2016) are used for surface analysis of the material's microstructure. Synchrotron-based X-Ray Diffraction (XRD) and Focus-Ion-Beam (FIB) combined with Electron Back-Scattering Diffraction (EBSD) are used to measure the chemical composition and crystal structure (Ohashi et al., 2009; Gardner et al., 2010; Abdolvand et al., 2015; Jeong et al., 2015; Erinosho et al., 2016). These advanced experimental techniques bestow highly sophisticated microstructure information and generate large amounts of data creating a difficult task for computational techniques to interpret and harness relevant information. In order to establish the relationship between microstructure and properties of polycrystalline materials undergoing plastic deformation, an accurate prediction of the micromechanical behavior based on directional material properties and gradual development of substructure of the constituent grains is required. Therefore, efficient computational schemes are needed to investigate the microstructure-property relations. In this section, we review crystal plasticity formulations that are extensively used to deal with this challenge.

Among the several crystal plasticity formulations available, the Sachs model (Sachs, 1928) and the Taylor model (Taylor, 1938) are the earliest epitomes of the so-called mean-field polycrystal models. According to the Taylor model, every crystal is assumed to have the same strain throughout the material, thus the macro strain of the material is simply equal to the local crystal strain. However, while this approach retains the inter-granular compatibility by definition, it leads to violation of inter-granular stress equilibrium. On the contrary, the Sachs model assumes that every crystal experiences the same stress throughout and the local stress is equal to the macro stress. This preserves inter-granular stress equilibrium but it violates inter-granular compatibility. A more realistic approach known as the self-consistent (SC) model, originally proposed by Molinari et al. (1987) for modelling viscoplastic (VP) behavior in polycrystals, accounts for the

average interactions of the constituent grains of a polycrystal and has been extensively used to predict texture evolution of polycrystals. This approach was further developed by Lebensohn and Tomé (1993) and Lebensohn et al. (2007). The Viscoplastic Self Consistent (VPSC) model consists in treating each constituent crystal is treated as an Eshelby heterogeneity embedded in a Homogeneous Equivalent Medium (HEM) and has been extensively used for polycrystal modelling accounting for texture-induced plastic anisotropy.

Beyond the formulations discussed above, which rely on mean-field approximations to obtain the plastic response of polycrystalline materials undergoing plastic deformation, full-field approaches are also available, which can predict the actual micromechanical stress and strain fields as well as the effective response of polycrystals with a specific microstructure. Full-field approaches, namely crystal plasticity Finite element method (CP-FEM) and crystal plasticity fast Fourier transform (CP-FFT)-based method, provide richer micromechanical information with direct input from an image of microstructure obtained by EBSD (e.g., Kalidindi et al., 1992, Spowart et al., 2003; Brahme et al., 2006). Although CP-FEM is a very powerful tool, the size and resolution of the polycrystal that can be treated with this approach are limited, mainly due the large number of degrees of freedom required by CP-FEM computations.

An efficient alternative to CP-FEM is given by the CP-FFT. The FFT-based formulation was originally developed by Moulinec and Suquet (1994, 1998) to compute the macro and micro response of composites, that consists of solving the Lippmann-Schwinger equation (Lippmann and Schwinger, 1950) by an iterative method that involves the use of the Green's operator associated to a linear reference medium. The CP-FFT-based schemes have been developed for polycrystalline materials deforming in elastic regime (Brenner et al., 2009), rigid-viscoplastic regime (Lebensohn, 2001; Lebensohn et al., 2008), and elasto-viscoplastic regime (Lebensohn et al., 2012, Grennerat et al., 2012) for infinitesimal strains. Furthermore, the CP-FFT-based methods have been recently extended to finite strains (Eisenlohr et al., 2013; Geus et al., 2016; Kabel et al., 2016).

An explicit or an implicit time-integration scheme can be used to update the rate-dependent constitutive behavior simulated in CP-FEM and FFT-based models. In the various FFT-based techniques available, e.g., Lebensohn et al. (2011), Lebensohn et al. (2012), a modified Newton-Raphson method and augmented Lagrangians procedure based on an implicit integration procedure

to iteratively adjust a compatible strain-rate field (or strain field) related to an equilibrated stress has been used. In these FFT-based techniques, the value of temporal step is taken very small. This approach requires relatively longer computational times to reach large deformations. On the other hand, the crystal plasticity models that use semi-explicit time integration schemes are generally more efficient, since larger time steps can be employed in the analysis (e.g., Rashid and Nemat, 1992; Rossiter et al., 2010).

Various researches have shown that CP-FFT methods are more efficient than CP-FEM (e.g., Liu et al., 2010; Prakash and Lebensohn, 2009) in obtaining the response of a polycrystalline material. However, the computationally expensive iterative character of Newton-Raphson type solver and augmented Lagrangians procedure used in most of these FFT-based methods renders them unsuitable for their use in applications that involve larger computational domains deforming under complex strain paths in which large strains are reached (i.e. predictions of forming limit strains). These simulations require highly efficient models to obtain material response expeditiously in order to achieve reasonable computing times. In this chapter, a new numerical framework that incorporates the rate-dependent crystal plasticity theory (Asaro and Needleman, 1985) with a semi-explicit forward gradient time-integration scheme (Peirce et al., 1983) into the FFT-based formulation (Lebensohn et al., 2012) is presented. The new model achieves significant gains in terms of computational efficiency over the existing EVP-FFT method (at least 100 times faster).

The plan of this chapter is as follows: In Section 3.2, the details of the proposed model are presented. In Section 3.3, the proposed model is benchmarked for the case of a Face Centered Cubic (FCC) polycrystal. Finally, the predictive capability as well as the computational efficiency of the proposed model is demonstrated, where predictions obtained using the proposed model are compared to experiments for the aluminum alloy (AA) 5754 in Section 3.4.

3.2 Model Formulation

The proposed model obtains the solutions for a heterogeneous volume element chosen to be statistically representative of the whole microstructure. Periodic boundary conditions are enforced across the RVE. For every discrete material point, the numerical analysis employs the tangent method with a semi-explicit integration scheme to find the equilibrated stress and compatible

strains through the constitutive relations in a single equilibrium iteration. For completeness, first the rate dependent polycrystal formulation (Asaro and Needleman, 1985) is reviewed, followed by the rate tangent method and the new numerical framework.

3.2.1 Crystal Plasticity Constitutive Model

According to rate dependent polycrystal formulation presented by Asaro and Needleman (1985), for single-phase FCC polycrystals, two distinct physical deformation mechanisms result in total deformation of single crystal. Primarily, the dislocation slip on active slip systems is considered to be the only mechanism responsible for plastic deformation in a single crystal, the elastic distortion and rigid body rotations of crystal lattice with embedded material construct the secondary mode of deformation. Hence, the total deformation gradient can be decomposed into product of plastic deformation gradient embodying dislocation slip and elastic deformation containing lattice distortion as proposed by Lee (1969).

Accordingly, the total deformation gradient \mathbf{F} is written as following

$$\mathbf{F} = \mathbf{F}^* \mathbf{F}^P \quad (3.1)$$

where, \mathbf{F} is the deformation gradient that satisfies compatibility within each grain and between grains and \mathbf{F}^P consists of dislocation slip that occurs as plastic shear on twelve slip systems having $\{1\ 1\ 1\}$ slip planes with normal vector $\mathbf{m}_{(\alpha)}$ and $\langle 1\ 1\ 0 \rangle$ slip directions with slip vectors $\mathbf{s}_{(\alpha)}$ with $1 \leq \alpha \leq 12$ in an FCC crystal. Note that, the brackets for the subscripts α indicate that the quantity is computed over the total number of slip systems. \mathbf{F}^* embodies elastic deformation and rigid body rotations of crystal lattice. In the un-deformed state, the lattice vectors $\mathbf{m}_{(\alpha)}$, $\mathbf{s}_{(\alpha)}$, are orthonormal and in the deformed state they rotate and stretch as

$$\mathbf{m}_{(\alpha)}^* = \mathbf{m}_{(\alpha)} \mathbf{F}^{*-1}, \quad \mathbf{s}_{(\alpha)}^* = \mathbf{F}^* \mathbf{s}_{(\alpha)} \quad (3.2)$$

The velocity gradient is written as sum of its elastic and plastic parts as

$$\mathbf{L} = \mathbf{L}^* + \mathbf{L}^P = \dot{\mathbf{F}}\mathbf{F}^{-1} \quad (3.3)$$

where

$$\mathbf{L}^* = \dot{\mathbf{F}}^*\mathbf{F}^{*-1}, \quad \mathbf{L}^P = \mathbf{F}^*(\dot{\mathbf{F}}^P\mathbf{F}^{P-1})\mathbf{F}^{*-1} \quad (3.4)$$

Taking the symmetric and antisymmetric parts of the above relations lead to; (i) the elastic strain rate \mathbf{D}^* (ii) the plastic strain rate \mathbf{D}^P , (iii) the so-called plastic spin \mathbf{W}^P , and (iv) the spin \mathbf{W}^* associated with the rigid lattice rotation. Accordingly, the total strain rate and spin tensors can be written as,

$$\mathbf{D} = \mathbf{D}^* + \mathbf{D}^P \quad (3.5)$$

$$\mathbf{\Omega} = \mathbf{\Omega}^* + \mathbf{\Omega}^P \quad (3.6)$$

By introducing the following symmetric $\mathbf{P}_{(\alpha)}$ and skew symmetric $\mathbf{W}_{(\alpha)}$ second order tensors for each slip system α ,

$$\mathbf{P}_{(\alpha)} = \frac{1}{2}[\mathbf{s}_{(\alpha)}^* \otimes \mathbf{m}_{(\alpha)}^* + \mathbf{m}_{(\alpha)}^* \otimes \mathbf{s}_{(\alpha)}^*] \quad (3.7)$$

$$\mathbf{W}_{(\alpha)} = \frac{1}{2}[\mathbf{s}_{(\alpha)}^* \otimes \mathbf{m}_{(\alpha)}^* - \mathbf{m}_{(\alpha)}^* \otimes \mathbf{s}_{(\alpha)}^*] \quad (3.8)$$

the plastic strain rate \mathbf{D}^P and plastic spin $\mathbf{\Omega}^P$ for the crystal can be written as

$$\mathbf{D}^P = \sum_{\alpha} \mathbf{P}_{(\alpha)} \dot{\gamma}_{(\alpha)}, \quad \mathbf{\Omega}^P = \sum_{\alpha} \mathbf{W}_{(\alpha)} \dot{\gamma}_{(\alpha)} \quad (3.9)$$

where $\dot{\gamma}_{(\alpha)}$ is the shear rate on each slip system α . The constitutive equation for a crystal is specified by the Jaumann rate of the Kirchoff stress, $\boldsymbol{\tau}$, as

$$\overset{\nabla}{\boldsymbol{\tau}} = \boldsymbol{\mathcal{L}} : \mathbf{D} - \sum_{\alpha} \mathbf{R}_{(\alpha)} \dot{\gamma}_{(\alpha)} \quad (3.10)$$

where, $\boldsymbol{\mathcal{L}}$ is the fourth order tensor of elastic moduli based on the anisotropic elastic constants of the FCC crystals which exhibits the appropriate cubic symmetry and, $\mathbf{R}_{(\alpha)}$ is the second-order tensor given as

$$\mathbf{R}_{(\alpha)} = \boldsymbol{\mathcal{L}} : \mathbf{P}_{(\alpha)} + \mathbf{W}_{(\alpha)} \boldsymbol{\tau} - \boldsymbol{\tau} \mathbf{W}_{(\alpha)} \quad (3.11)$$

In order to complete the constitutive description, the shear rate on each slip system needs to be defined. The shear rate $\dot{\gamma}_{(\alpha)}$ on each slip system α is governed by a power-law expression, so that

$$\dot{\gamma}_{(\alpha)} = \dot{\gamma}_0 \operatorname{sgn} \tau_{(\alpha)} \left| \frac{\tau_{(\alpha)}}{g_{(\alpha)}} \right|^{1/m} \quad (3.12)$$

where $\tau_{(\alpha)}$ is the resolved shear stress, $g_{(\alpha)}$ is the hardness, of slip system α , $\dot{\gamma}_0$ is the reference shear rate (same for each slip system) and m is the index of strain rate sensitivity. The hardened state of each slip system α is characterized by $g_{(\alpha)}$. The hardening rate, $\dot{g}_{(\alpha)}$, for multiple slip is defined by hardening law as following

$$\dot{g}_{(\alpha)} = \sum_{\beta} \mathbf{h}_{\alpha\beta} |\dot{\gamma}_{\beta}| \quad (3.13)$$

where, $\mathbf{h}_{(\alpha\beta)}$ is the hardening moduli and $\dot{\gamma}_{(\beta)}$ is the single slip shear stress rate on slip system β . The hardening moduli used here is the one that has been used previously by Peirce et al. (1983) and Asaro and Needleman (1984),

$$\mathbf{h}_{(\alpha\beta)} = \mathbf{q}_{(\alpha\beta)} h_{(\beta)} \text{ (no sum on } \beta) \quad (3.14)$$

where $q_{\alpha\beta}$ matrix describes the latent hardening of the crystallite and h_β is the single slip hardening. Following (Asaro and Needleman, 1985), it is considered that g_α depends on the accumulated sum, γ_a , of the slips, where

$$\gamma_{(a)} = \int_0^t \sum_{\alpha} |\dot{\gamma}_{(\alpha)}| dt \quad (3.15)$$

The model presented by Chang and Asaro (1981) is employed to calculate the single slip hardening. Accordingly,

$$h_{(\beta)} = h_s + (h_0 - h_s) \text{sech}^2 \left\{ \left(\frac{h_0 - h_s}{\tau_s - \tau_0} \right) \gamma_{(a)} \right\} \quad (3.16)$$

where τ_0 is the critical resolved shear stress, τ_s is the value of saturated shear stress, h_s is the asymptotic hardening rate of slip systems and h_0 is the hardening constant.

3.2.2 Rate Tangent Modulus Method

The new numerical framework developed in this research employs the semi-explicit rate tangent modulus method developed by Peirce et al. (1983). According to this method, the increment in slip on each slip system α at time t is given by

$$\Delta \gamma_{(\alpha)} = \gamma_{(\alpha)}^{t+\Delta t} - \gamma_{(\alpha)}^t \quad (3.17)$$

Within the time increment Δt , a linear interpolation of slip increment is employed to give

$$\Delta \gamma_{(\alpha)} = [(1 - \theta) \dot{\gamma}_{(\alpha)}^t + \theta \dot{\gamma}_{(\alpha)}^{t+\Delta t}] \Delta t \quad (3.18)$$

where θ is an interpolation parameter ranging between 0 and 1. $\theta = 0$ corresponds to Euler time stepping scheme ($\theta = 0.5$ is used in the current formulation). The last term in above equation can be approximated by using Taylor series expansion as

$$\dot{\gamma}_{(\alpha)}^{t+\Delta t} \cong \dot{\gamma}_{(\alpha)}^t + \left. \frac{\partial \dot{\gamma}_{(\alpha)}}{\partial \tau_{(\alpha)}} \right|_t \Delta \tau_{(\alpha)} + \left. \frac{\partial \dot{\gamma}_{(\alpha)}}{\partial \mathbf{g}_{(\alpha)}} \right|_t \Delta \mathbf{g}_{(\alpha)} \quad (3.19)$$

Equation (3.19) can be further simplified as (Peirce et al., 1983);

$$\sum_{\beta} \mathbf{N}_{(\alpha\beta)} \Delta \gamma_{(\beta)} = \left(\dot{\gamma}_{(\alpha)}^t + \mathbf{Q}_{(\alpha)} : \mathbf{D} \right) \Delta t \quad (3.20)$$

where $\dot{\gamma}_{(\alpha)}^t$ can be calculated by Equation (3.12) and \mathbf{Q}_{α} is given as

$$\mathbf{Q}_{(\alpha)} = \left(\frac{\theta \Delta t \dot{\gamma}_{(\alpha)}^t}{m \tau_{(\alpha)}} \right) \mathbf{R}_{(\alpha)} \quad (3.21)$$

and

$$\mathbf{N}_{(\alpha\beta)} = \boldsymbol{\delta}_{(\alpha\beta)} + \left(\frac{\theta \Delta t \dot{\gamma}_{(\alpha)}^t}{m} \right) \times \left[\frac{\mathbf{R}_{(\alpha)} : \mathbf{P}_{(\beta)}}{\tau_{(\alpha)}} + \text{sgn}(\tau_{(\beta)}) \frac{\mathbf{h}_{(\alpha\beta)}}{\mathbf{g}_{(\alpha)}} \right] \quad (3.22)$$

Denoting the inverse of $\mathbf{N}_{(\alpha\beta)}$ by $\mathbf{M}_{(\alpha\beta)}$ and then inverting Equation (3.22) leads to a simpler form

$$\Delta \gamma_{(\alpha)} = \left[\dot{\mathbf{f}}_{(\alpha)} + \mathbf{x}_{(\alpha)} : \mathbf{D} \right] \Delta t \quad (3.23)$$

where

$$\dot{\mathbf{f}}_{(\alpha)} = \sum_{\beta} \mathbf{M}_{(\alpha\beta)} \dot{\gamma}_{(\alpha)}^t \text{ and } \boldsymbol{\chi}_{(\alpha)} = \sum_{\beta} \mathbf{M}_{(\alpha\beta)} \mathbf{Q}_{(\alpha)} \quad (3.24)$$

The Equation (3.23) allows Equation (3.10) to be written as

$$\overset{\nabla}{\boldsymbol{\tau}} = \mathcal{C} : \mathbf{D} - \sum_{\alpha} \mathbf{R}_{(\alpha)} \dot{\mathbf{f}}_{(\alpha)} \quad (3.25)$$

where \mathcal{C} is the elasto-viscoplastic moduli given as

$$\mathcal{C} = \mathcal{L} - \sum_{\alpha} \mathbf{R}_{(\alpha)} \boldsymbol{\chi}_{(\alpha)} \quad (3.26)$$

Note that, for $\theta = 0$ the Equation (3.25) reduces to Equation (3.10). Now, expressing constitutive Equation (3.25) in form of Jaumann rate $\overset{\nabla}{\boldsymbol{\sigma}}$ of Cauchy stress $\boldsymbol{\sigma}$

$$\overset{\nabla}{\boldsymbol{\sigma}} = \mathcal{C} : \mathbf{D} - \dot{\boldsymbol{\sigma}}^0 - \boldsymbol{\sigma} \operatorname{tr} \mathbf{D} \quad (3.27)$$

Since, $\sigma = \det \mathbf{F}^{-1} \tau$, the viscoplastic stress-rate is given by

$$\dot{\boldsymbol{\sigma}}^0 = \sum_{\alpha} \mathbf{R}_{(\alpha)} \dot{\gamma}_{(\alpha)} \quad (3.28)$$

Now, updating the Cauchy stress tensor for next time step as following

$$\boldsymbol{\sigma}^{t+\Delta t} = \boldsymbol{\sigma}^t + \dot{\boldsymbol{\sigma}}^0 \Delta t \quad (3.29)$$

The sections above describe the general (Asaro and Needleman, 1985) framework that has been used in various homogenization as well as in full-field schemes (Inal, 2002; Inal et al., 2010; Brahme et al., 2011; Izadbakhsh et al., 2011; Inal and Mishra, 2012; Cyr et al., 2015; Muhammad et al., 2015; Pinna et al., 2015). This formulation, coupled with a rate tangent semi-explicit integration scheme is implemented into an FFT-based model as described next.

3.2.3 FFT Model and Implementation of the New Crystal Plasticity Framework

To predict the evolution of micromechanical fields and intragranular texture during deformation, the space resolved configuration of the regular Fourier grid points and the grain interactions must be considered in the whole RVE. In proposed numerical approach, each Fourier grid point represents a voxel inside a grain. The Fourier grid $\{x_d\}$ is defined as

$$\{x_d\} = \left\{ \left((I_1 - 1) \frac{\ell_1}{N_1}, (I_2 - 1) \frac{\ell_2}{N_2}, (I_3 - 1) \frac{\ell_3}{N_3} \right); I_k = 1, \dots, N_k, k = 1, 3 \right\} \quad (3.30)$$

where ℓ_k is the length of the grid and N_k is the number of Fourier points in each direction k . Note that, from this point onward, index notation will be employed in the formulations. In order to account for the interaction of each grid point with all the other points in the RVE, the following problem for heterogeneous RVE needs to be solved at each grid point written as following:

$$\begin{cases} \sigma_{ij}(x) = \mathcal{L}_{ijkl}(x) \varepsilon_{kl}(x), & \forall x \in \{x_d\} \\ \sigma_{ij,j}(x) = 0 \\ \text{Periodic boundary conditions across RVE} \end{cases} \quad (3.31)$$

where $\varepsilon_{kl}(x)$ and $\sigma_{ij}(x)$ are the local strain and local stress fields and $\mathcal{L}_{ijkl}(x)$ is the local elastic stiffness. The total local strain is given by

$$\varepsilon_{ij}(x) = \tilde{\varepsilon}_{ij}(x) + E_{ij} \quad (3.32)$$

where $\tilde{\varepsilon}_{ij}(x)$ is the strain fluctuation in the crystal due to heterogeneity and E_{ij} is the strain imposed on the RVE. The local strain fluctuation can be found using Green function method if local stress polarization field is known. Finding local stress polarization involves \mathcal{L}^0 , an average elastic moduli of a linear reference medium. Here, linear medium refers to medium that is not yet loaded or is in the un-deformed state.

Accordingly, the stress tensor can be written as;

$$\sigma_{ij}(x) = \sigma_{ij}(x) + \mathcal{L}_{ijkl}^0 \varepsilon_{kl}(x) - \mathcal{L}_{ijkl}^0 \varepsilon_{kl}(x) \quad (3.33)$$

or,

$$\sigma_{ij}(x) = \mathcal{L}_{ijkl}^0 \varepsilon_{kl}(x) + \tilde{\sigma}_{ij}(x) \quad (3.34)$$

where, $\tilde{\sigma}_{ij}(x)$ is the stress polarization and is given by:

$$\tilde{\sigma}_{ij}(x) = \sigma_{ij}(x) - \mathcal{L}_{ijkl}^0 \varepsilon_{kl}(x) \quad (3.35)$$

The strain tensor ε_{kl} is related to displacement gradient $u_{k,l}(x)$ as

$$\varepsilon_{kl} = \left(u_{k,l}(x) + u_{k,l}(x) \right) / 2 \quad (3.36)$$

Thus, the local problem for heterogeneous RVE becomes:

$$\begin{cases} \sigma_{ij}(\mathbf{x}) = \mathcal{L}_{ijkl}^0 \varepsilon_{kl}(\mathbf{x}) + \tilde{\sigma}_{ij}(\mathbf{x}), & \forall \mathbf{x} \in \{\chi_d\} \\ \sigma_{ij,j}(\mathbf{x}) = 0 \\ \text{Periodic boundary conditions across RVE} \end{cases} \quad (3.37)$$

To satisfy equilibrium locally, the divergence of local Cauchy stress tensor must be equal to zero, i.e.,

$$\mathcal{L}_{ijkl}^0 \varepsilon_{kl,j}(\mathbf{x}) + \tilde{\sigma}_{ij}(\mathbf{x}) = 0 \quad (3.38)$$

The Green's function method is used to solve the equilibrium Equation (3.38) for an applied strain ε_{ij} that requires the solution of following problem (Lebensohn et al., 2012):

$$\mathcal{L}_{ijkl}^0 G_{km,lj}(\mathbf{x} - \mathbf{x}') + \delta_{im} \delta(\mathbf{x} - \mathbf{x}') = 0 \quad (3.39)$$

where $G_{km,lj}(\mathbf{x} - \mathbf{x}')$ is the Green's function associated with the displacement field. Accordingly, the local strain fluctuations can be expressed as convolutions in the real space so that

$$\tilde{\varepsilon}_{kl}(\mathbf{x}) = \int_{\mathbb{R}^3} G_{ki,jl}(\mathbf{x} - \mathbf{x}') \tilde{\sigma}_{ij}(\mathbf{x}') d\mathbf{x}' \quad (3.40)$$

Since a convolution integral in real space can be expressed as a product in the Fourier space for a regular Fourier grid, Equation (3.40) is solved in the Fourier space that renders the FFT-based implementations computationally efficient for computing the local response. Using the convolution theorem, the local strain fluctuations in Fourier space are given by

$$\hat{\tilde{\varepsilon}}_{kl}(\xi) = \hat{\Gamma}_{ijkl}^0(\xi) \hat{\tilde{\sigma}}_{kl}(\xi) \quad (3.41)$$

where “ $\widehat{\cdot}$ ” indicates Fourier transform, and ξ is the frequency point in the Fourier space. Furthermore, the Green operator in Fourier space $\widehat{\Gamma}_{ijkl}^0$, which is a function of the stiffness tensor of the reference medium and the frequency, is given by

$$\widehat{\Gamma}_{ijkl}^0(\xi) = -\xi_j \xi_l \widehat{G}_{ik}(\xi), \quad \widehat{G}_{ik}(\xi) = [\mathcal{L}_{ijkl}^0 \xi_l \xi_j]^{-1} \quad (3.42)$$

Accordingly, the local strain fluctuations in real space can be obtained by taking the inverse Fourier transform of Equation (3.41) such as

$$\tilde{\varepsilon}_{kl}(\mathbf{x}) = \text{fft}^{-1}(\text{sym}(\widehat{\Gamma}_{ijkl}^0(\xi)) \widehat{\sigma}_{kl}(\xi))$$

As a part of augmented Lagrangians iterative procedure, (Michel et al., 2001) proposed an alternative method in which the Fourier transform of local stress tensor is computed instead of local perturbation field. This approach is employed in the single iteration procedure presented in this chapter. Accordingly, the total local strain is given by

$$\varepsilon_{ij}(\mathbf{x}) = \text{fft}^{-1}(\text{sym}(\widehat{\Gamma}_{ijkl}^0(\xi)) \widehat{\sigma}_{kl}(\xi)) + E_{ij} \quad (3.43)$$

In the new numerical framework, to calculate the local stress at each material point, the rate tangent method is used to update the rate form of the constitutive equation in a single iteration for equilibrium, (i.e., Equation (3.25)). At first time step, with an imposed macro strain E_{ij} , the algorithm can be initialized with zero strain fluctuation, $\tilde{\varepsilon}_{ij}(\mathbf{x}) = 0$ and $\sigma_{ij}^t(\mathbf{x}) = \mathcal{C}_{ijkl}^t(\mathbf{x}) D_{kl}^t(\mathbf{x})$. For next temporal increment, the algorithm computes the:

1. Current guess of local Cauchy stress $\sigma_{ij}^{t+\Delta t}(\mathbf{x})$ using rate tangent scheme,
2. Fourier transform of current guess of Cauchy stress, $\widehat{\sigma}_{ij}^{t+\Delta t}(\xi) = \text{fft}(\sigma_{ij}^{t+\Delta t}(\mathbf{x}))$,
3. Green operator ($\widehat{\Gamma}_{ijkl}^0(\xi)$) as a function of reference medium stiffness (\mathcal{L}_{ijkl}^0) for each frequency (ξ) as given by Equation (3.41),

4. Local strain fluctuation, $\tilde{\epsilon}_{ij}^{t+\Delta t}(\mathbf{x}) = \text{fft}^{-1}(\text{sym}(\hat{\Gamma}_{ijkl}^0(\xi)) \hat{\sigma}_{kl}(\xi))$,
5. Total local strain as, given by Equation (3.43),
6. Updates of the current local strain rate tensor $D_{ij}^{t+\Delta t}(\mathbf{x})$ and the current Cauchy stress tensor $\sigma_{ij}^{t+\Delta t}(\mathbf{x})$ using rate tangent scheme,
7. The algorithm then repeats steps 1-6 for the next temporal increments.

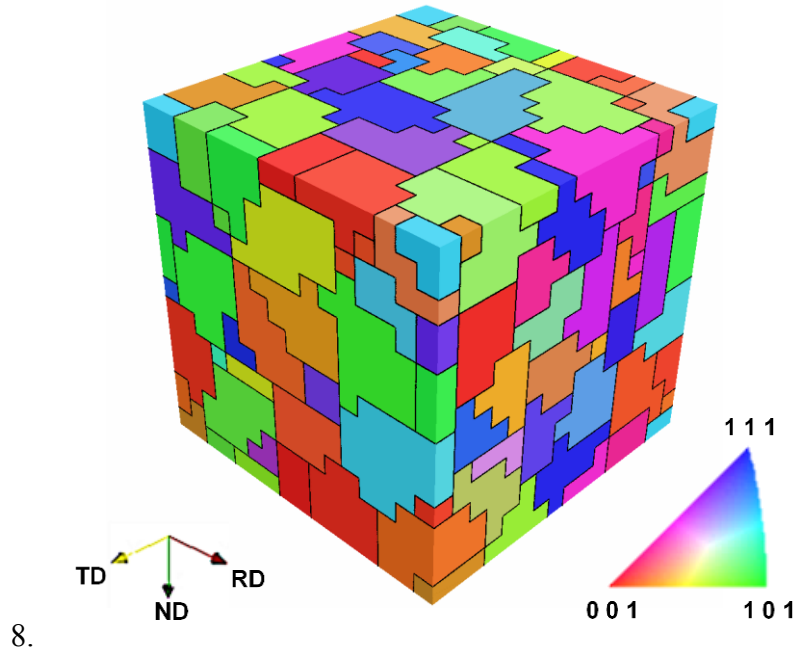


Figure 3.1: The synthesized microstructure of copper polycrystal and for an artificial FCC polycrystal with $16 \times 16 \times 16$ Fourier points in 100 grains showing initial texture distribution.

3.3 Model Calibration and Validation

In this section, the proposed numerical model is validated by comparing the predictions from the new model with the predictions obtained from the well-established elasto-viscoplastic fast Fourier transform (EVP-FFT) model (Lebensohn et al., 2012). The numerical analyses are carried out for a copper polycrystal and an artificial random FCC polycrystal with anisotropic constants, $A=2.2$ and $A=0.5$ respectively ($A = (2 \times C_{44}) / (C_{11}-C_{12})$). The corresponding elastic constants employed in these analyses are presented in Table 3.1. For both cases, the same representative volume

element (RVE) is used where 100 grains with randomly assigned copper orientations are employed in a regular grid of $16 \times 16 \times 16$ Fourier points (to discretize the RVE, Figure 3.1).

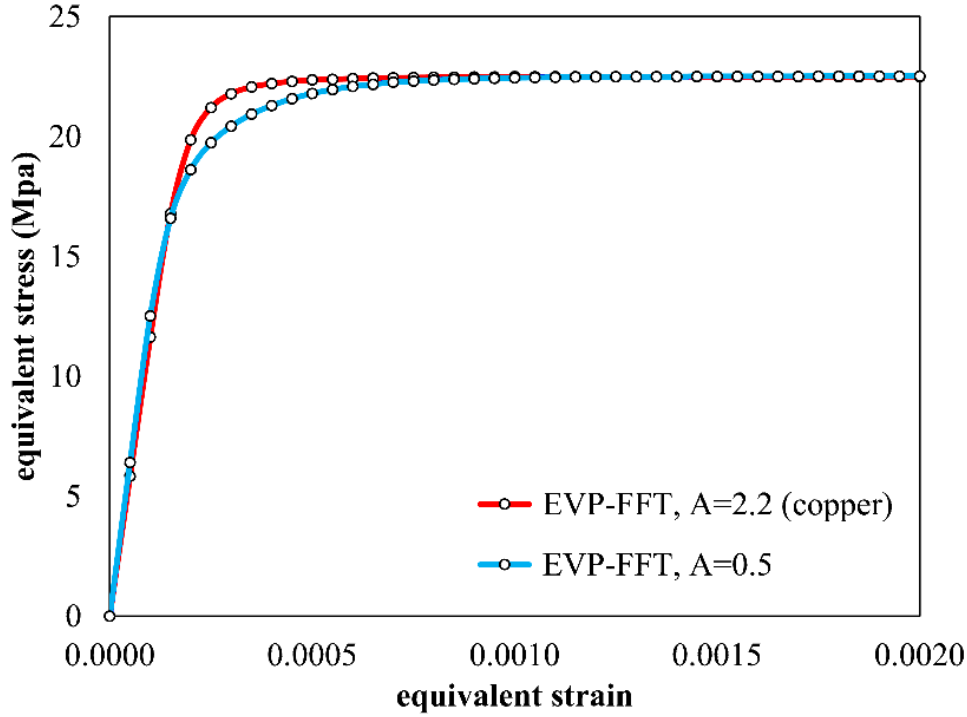
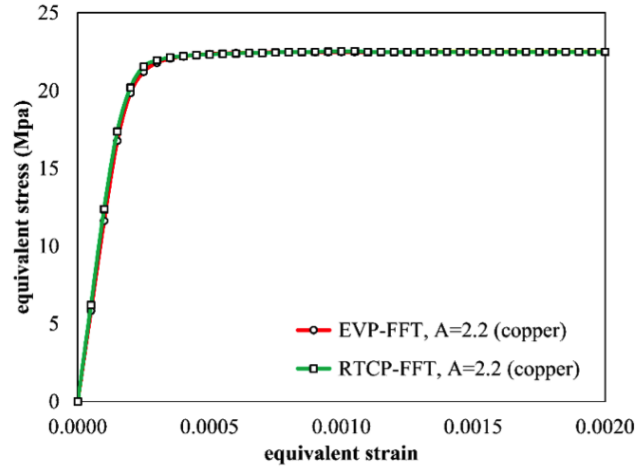


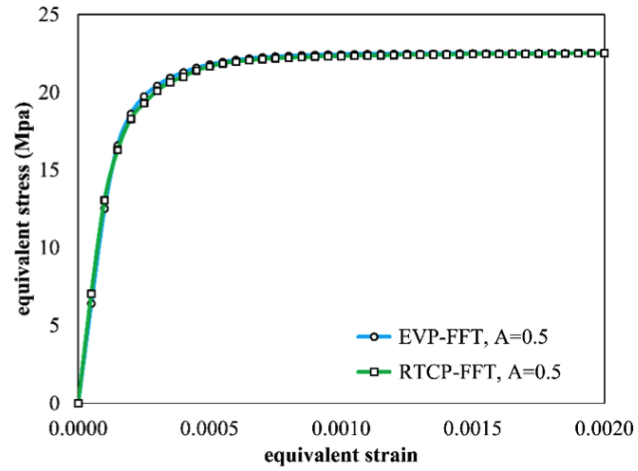
Figure 3.2: Predicted von Mises equivalent stress–strain curves during uniaxial tension along RD using the EVP-FFT model for cases of the copper polycrystal and an artificial FCC polycrystal.

It should be mentioned that the same material parameters and boundary conditions are used for both models during each set of simulations. The polycrystals deform plastically by slip on twelve slip systems for a critical resolved shear stress (CRSS), τ_0 , of 10 MPa (no strain-hardening is assumed) and the strain rate sensitivity index, m , is set to 0.1. The simulations are carried out up to a strain of 0.2% with an applied strain rate of 10^{-4} s^{-1} along the rolling direction (RD). Note that, from now on, the new model will be referred to as RTCP-FFT model.

Figure 3.2 shows the equivalent stress–strain curves predicted by the EVP-FFT model, while Figure 3.3 (a-b) present comparisons between the predictions obtained from the EVP-FFT and the RTCP-FFT models. Note that, for these simulations, the main interest is the elasto-viscoplastic transition zone, which varies with anisotropic constants. For both the analyses (for a copper polycrystal and the artificial FCC polycrystal) the simulations with the RTCP-FFT model are in excellent agreement with the predictions obtained from the EVP-FFT.



(a)



(b)

Figure 3.3: Comparisons of the predicted von Mises equivalent stress–strain curves during uniaxial tension along RD between the RTCP-FFT and EVP-FFT models for; (a) copper polycrystal, and (b) an artificial polycrystal.

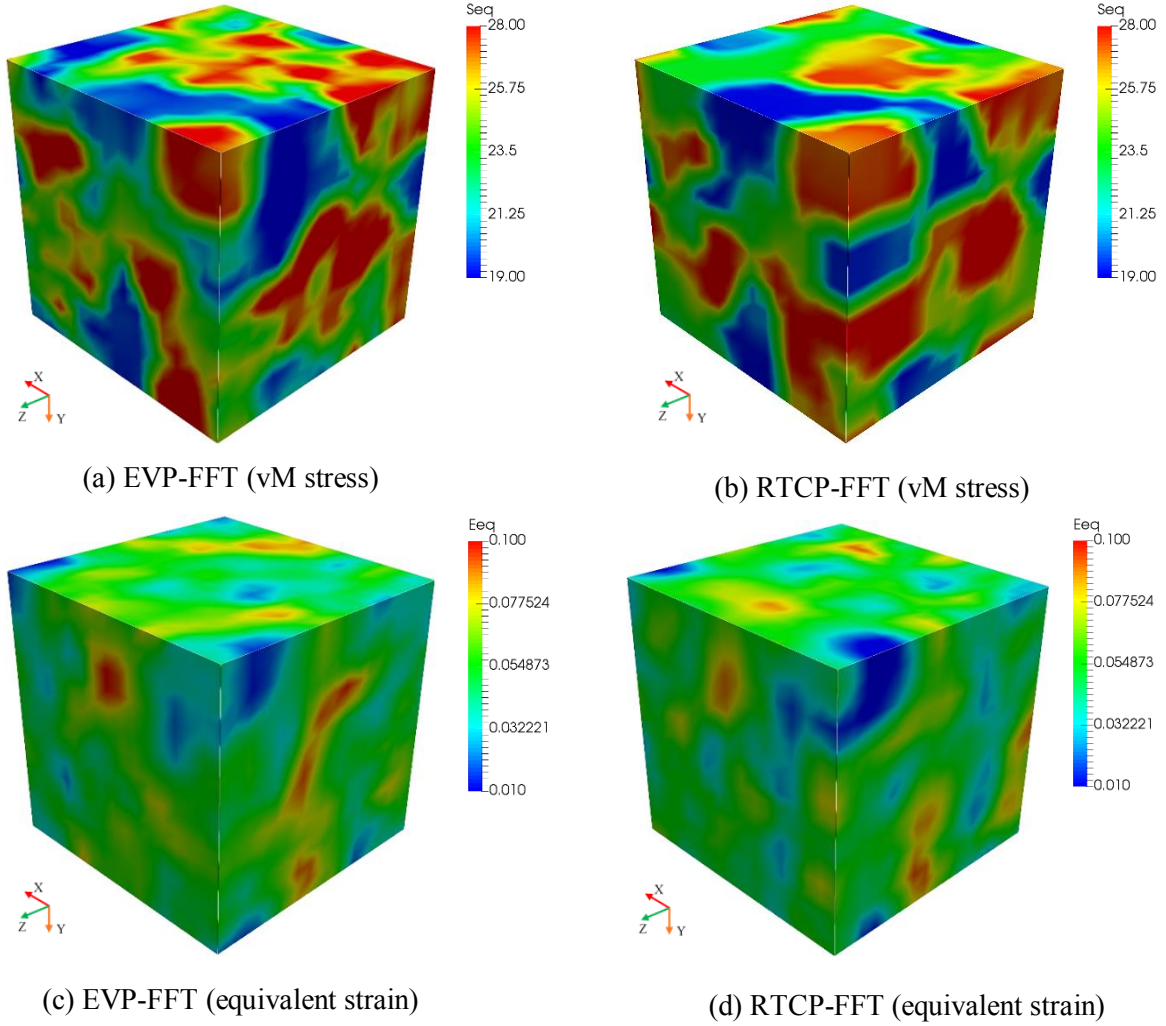


Figure 3.4: Comparison of the simulated micromechanical fields for the copper polycrystal ($A = 2.2$) at 5% equivalent strain during uniaxial tension along RD; (a-b) – distribution of the von Mises equivalent stress (MPa), (c-d) – distribution of equivalent strain.

Next, for the case of the copper polycrystal, the predicted local micromechanical fields obtained with both models obtained at an equivalent strain of 5% are compared (Figure 3.4a-d). A qualitative comparison of the results shows that the proposed model reproduces similar micromechanical fields as compared to the original EVP-FFT model (Figure 3.4); the locations of deviations from uniform stress and strain fields predicted by the RTCP-FFT model, in general, are also in reasonable agreement with those predicted by the original EVP-FFT model. However, some variations are observed between the computed local strains at some locations. These variations are mainly due to the different numerical integration schemes employed in the models. Furthermore, to quantify the variations, the mismatch in terms of both the local equivalent strains and the local

equivalent stresses, normalized by the sum of local equivalent fields, i.e. strains or stresses on all the voxels, are presented in the Figure 3.5.

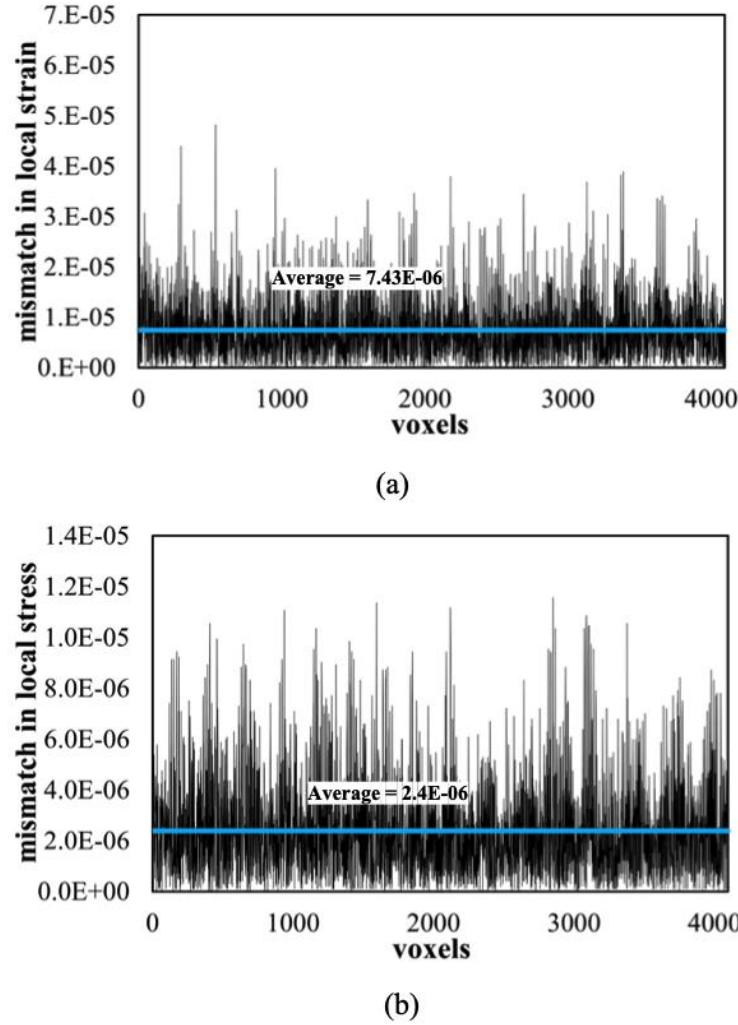


Figure 3.5: Comparison of variations in the local fields for each voxel between the RTCP-FFT and the EVP-FFT models in copper polycrystal ($A = 2.2$) at 5% equivalent strain during uniaxial tension along RD: (a) mismatch in the local equivalent strain, (b) mismatch in the local equivalent stress.

The normalized difference is calculated per voxel as

$$\text{Mismatch in local fields at voxel } i = \frac{2 * |\text{Field}_i^{\text{EVP-FFT}} - \text{Field}_i^{\text{RTCP-FFT}}|}{\sum_{i=1}^N \text{Field}_i^{\text{EVP-FFT}} + \sum_{i=1}^N \text{Field}_i^{\text{RTCP-FFT}}}$$

where N is the total number of voxels. It should be mentioned that even though the local fields calculated by the RTCP-FFT model can be different from those computed by the EVP-FFT model, these differences have a very little impact, if any, on the macroscopic behavior (Figure 3.3a).

Table 3.1: Adopted elastic constants for copper polycrystal (Simmons and Wang, 1971) and for an artificial polycrystal (Lebensohn et al., 2012).

Elastic constants	C_{11}	C_{12}	C_{14}
Copper polycrystal	170.2 GPa	114.9 GPa	61.0 GPa
Artificial polycrystal	233.6 GPa	88.2 GPa	33.8 GPa

3.4 Application to Aluminum Alloy (AA) 5754

In this section, the predictive capability of the new model is demonstrated by comparing predictions from the new model with experiments for the commercial aluminum alloy (AA) 5754. It is important to mention that the proposed model is only calibrated for uniaxial tension along RD, then the same parameters are employed for the predicting the macroscopic stress-strain responses and the texture evolution for various other strain paths. For each case, the predictions obtained with RTCP-FFT model are compared with the measured data presented in Hu et al. (2012).

3.4.1 Model Setup

In this analysis, a representative volume element (RVE) with $128 \times 128 \times 128$ points that represent 8837 equiaxed grains is used to model AA5754 (Figure 3.6e). The pole figures and orientation distribution functions (ODF) of the initial texture of as received O-temper AA5754 are presented in Figure 3.6 (a-d). The synthetic microstructure in the RVE with equiaxed grains is built using a microstructure building software as proposed by (Brahme et al., 2006). In this approach, an optimization technique is used to minimize the error, in both orientation distribution function (ODF) and misorientation distribution function (MDF), between measured and assigned orientations.

Table 3.2: Constitutive parameters used to calibrate RTCP-FFT model for uniaxial tension along RD.

h_0/τ_0	τ_s/τ_0	τ_0	h_s/τ_0	m	q
10.0	2.24	25.5	1.9	0.02	1.0

3.4.2 Boundary Conditions

Simulations of uniaxial tension, balanced biaxial tension and plane strain tension are performed in this section. Uniaxial tension is simulated by applying a velocity gradient in RD (X) and TD (Y) directions respectively while the remaining components of the velocity gradient are kept unconstrained. Equibiaxial tension is simulated by applying a velocity gradient in both RD-TD (X-Y) directions while keeping ND (Z) direction unconstrained. Similarly, plane strain tension is simulated by applying a velocity gradient in the RD (X) and TD (Y) directions respectively while constraining the ND (Z) direction.

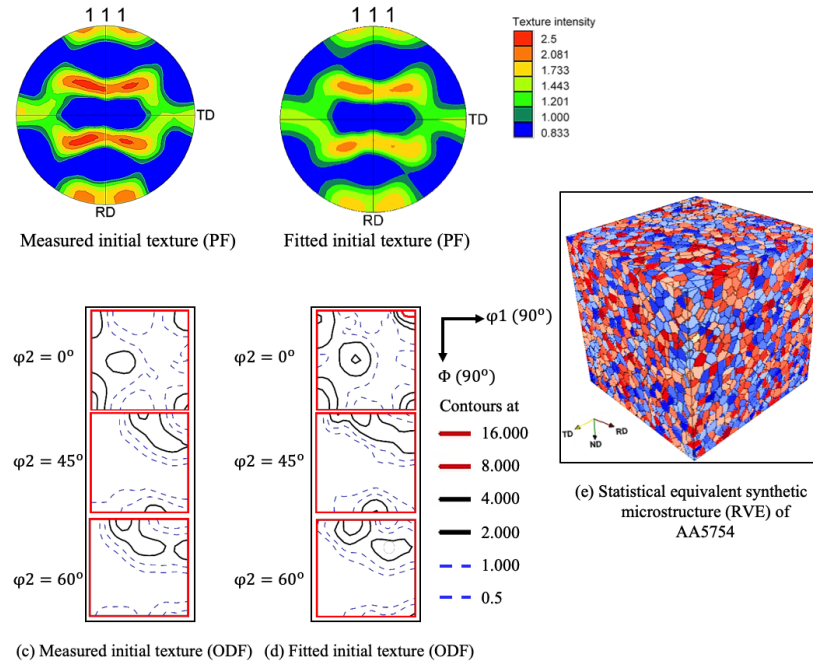


Figure 3.6: Comparison of initial texture: (a) pole figure representations of the as-received experimental texture and (b) fitted texture; Comparison of contours of experimental ODFs (c) and fitted ODFs (d) at 0, 45, and 60 degrees of ϕ_2 sections. (e) The generated microstructure with 128 x 128 x 128 points in 8837 equiaxed grains, the colors represent different grains.

3.4.3 Model Calibration

An initial curve fitting of the macroscopic stress-strain response of the polycrystalline is performed for uniaxial tensile test to calibrate the RTCP-FFT model (Figure 3.7a), and the material parameters employed in the model are presented in Table 3.2. Note that, the same set of material parameters (as presented in Table 3.2) are employed in all of the simulations presented in section 3.4.

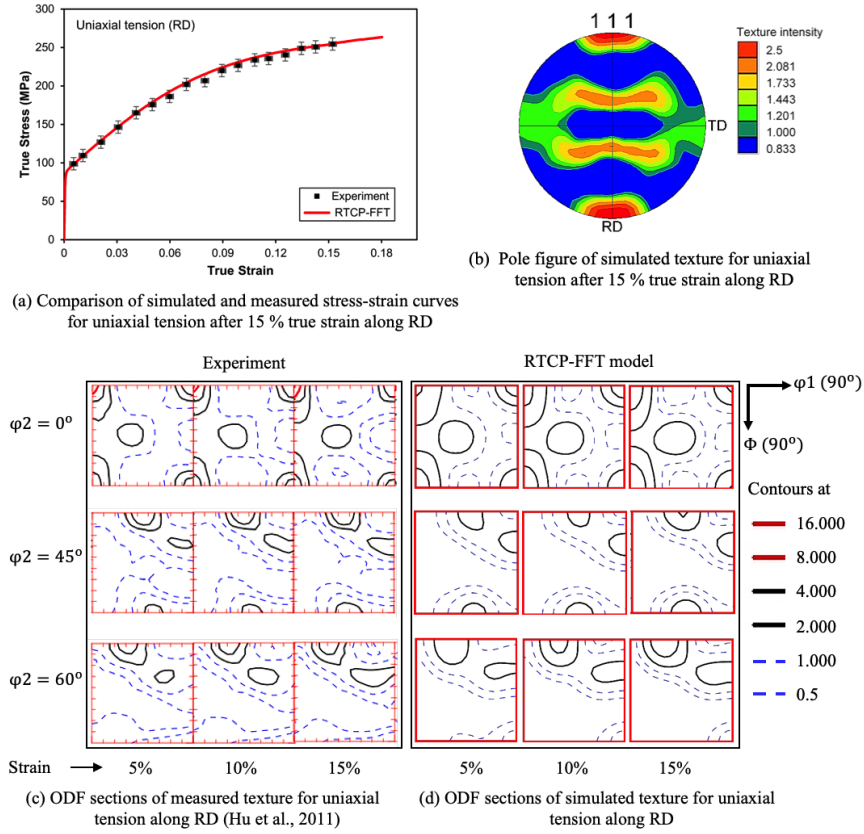


Figure 3.7: (a) Comparison of macroscopic stress strain curves of measured data (Hu et al., 2011) and simulated response by calibrated-RTCP-FFT model for RD-uniaxial tension. (b) Simulated texture in form of pole figure for RD-uniaxial tension after 15% true strain. (c) and (d) Comparison of ODF sections of measured and simulated texture for RD-uniaxial tension at 5%, 10% and 15% true strain.

The predicted texture evolution for 15% strain during uniaxial tension along RD is presented in Figure 3.7b, while Figure 3.7 (c-d), present a comparison of ODF sections of measured and predicted evolved texture at different levels of true strain. Results show that the RTCP-FFT model can accurately capture the major trends of texture evolution. Both the experimentally measured

and the predicted texture (evolved) show an increase in the intensity of Copper and S (typical rolling textures) as the deformation proceeds from 5% to 15% uniaxial tension.

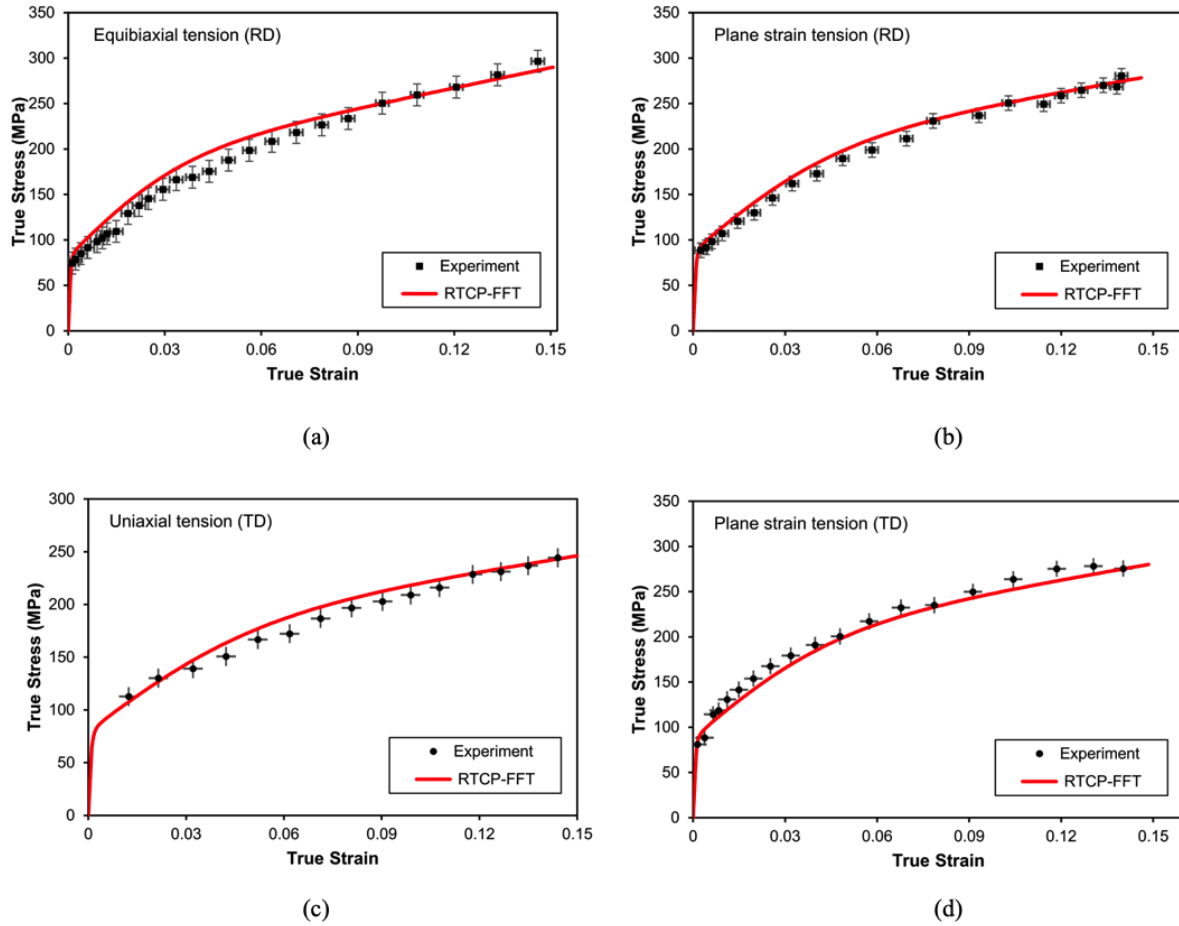


Figure 3.8: Comparison of predicted and measured (Hu et al., 2011) stress-strain curves for four different strain paths after 15% true strain; (a) equibiaxial tension (σ_{11} , e_{11}), (b) plane-strain tension in RD (σ_{11} , e_{11}), (c) Uniaxial tension in TD (σ_{22} , e_{22}) and (d) plane strain tension in TD (σ_{22} , e_{22}).

3.4.4 Simulations of Balanced Biaxial Tension and Plane Strain Tension

In this section, the RTCP-FFT model is employed to simulate the stress-strain response of AA5754 during; balanced biaxial tension, plane strain tension along RD, uniaxial tension and plane strain tension along TD. The predictions are compared with those determined experimentally. The

numerical analyses show that the RTCP-FFT model can accurately predict the macroscopic stress-strain response of AA5754 for the above-mentioned strain paths (Figure 3.8a-d).

Recently, Hu et al. (2012), presented a similar study for AA5754 where they used a Taylor assumption-based model, VPSC model and VP-FFT model. While their predictions were also in good agreement with experiments, it should be mentioned that they employed a single set of hardening parameters that was obtained by simultaneously curve fitting the simulations to all the different experimental strain paths (uniaxial tension, balanced biaxial tension, plane strain tension).

Contrary to their approach, all the predictions presented in this section employ the same set of parameters (Table 3.2) obtained from a single curve fit for uniaxial tension. Thus, the RTCP-FFT model can accurately predict the macroscopic stress-strain response for various strain paths with a single set of parameters that are directly obtained from an experimental uniaxial stress-strain curve.

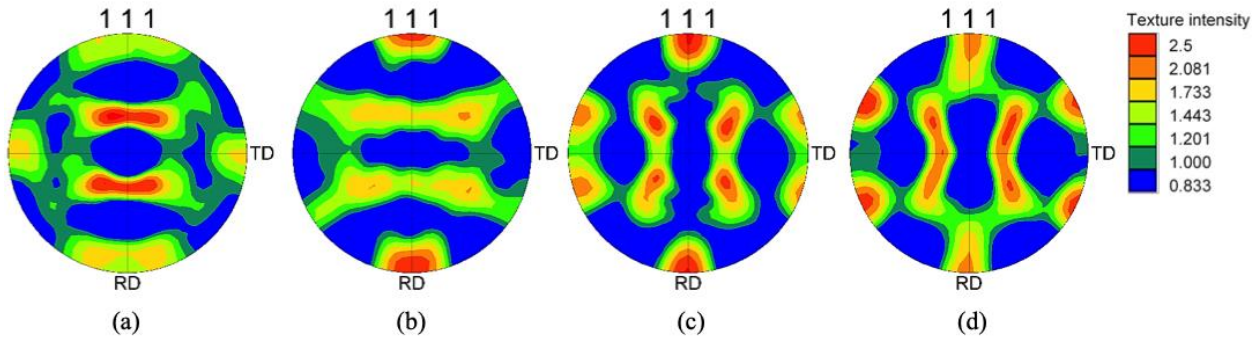


Figure 3.9: Comparison of predicted texture in form of pole figures for four different strain paths; (a) equibiaxial tension, (b) plane strain tension along RD, (c) uniaxial tension along TD and (d) plane strain tension along TD.

3.4.5 Predictions of Texture Evolution

The RTCP-FFT model is also employed to predict texture evolution (Figure 3.9). The initial texture (Figure 3.6b) contains higher amounts of Brass, Cube and S compared to Copper and Goss texture components. In the predicted texture after 15% true strain, an increase in Brass is observed in balanced biaxial tension and uniaxial tension along TD with a decrease in the intensities of cube and S. On the other hand, Copper component is strengthened after 15% strain in cases of plane

strain tension along RD and TD. Overall, a smaller change is observed in intensities of texture components from their initial values in uniaxial tension and plane strain tension cases.

Next, an analysis of texture evolution is presented using ODF sections. The predicted texture evolutions are compared with experimental measurements (Hu et al., 2011) at 5%, 10% and 15% true strain. Figs. 3.10-3.13 show the progress of ODF with strain during balanced biaxial tension, plane strain tension along RD and TD respectively as well as in uniaxial tension along TD. Simulations show that, as the deformation progresses, the grains favor the formation of Brass and Cube orientations during uniaxial tension along TD, the grains tend to form the Brass in case of plane strain tension along TD and the β -fiber rolling texture is further strengthened in plane strain tensions along RD. In case of balanced biaxial tension, a stronger growth of Brass and Copper components are observed. Overall, the RTCP-FFT model successfully predicts the general trends observed in the measured ODF sections for the different strain paths considered in this study.

It should be mentioned that, Hu et al. (2012) presented results where the well-known crystal plasticity models such as VPSC and Taylor-type approximations tend to over predict the texture evolution for AA5754 due lack of proper treatment of grain to grain interaction and strain partitioning.

On the other hand, the results in this research indicate that the RTCP-FFT model can accurately capture the trends of texture evolution due to consideration of the actual interaction of grains and allowing voxels in a grain to deform independently. This leads to an increase in distribution of orientations inside a grain, thus the substantial changes in texture are hindered, which lead to a more realistic texture evolution.

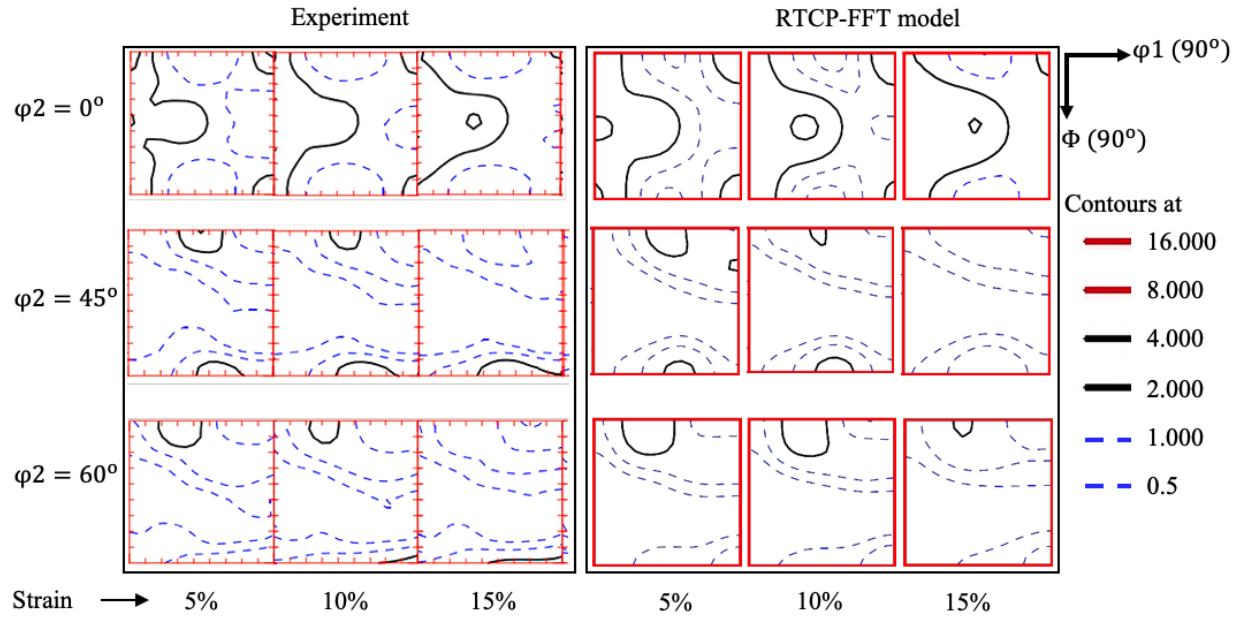


Figure 3.10: Comparison of measured (Hu et al., 2011) and predicted ODF sections at strain levels of 5, 10, and 15% for equibiaxial tension.

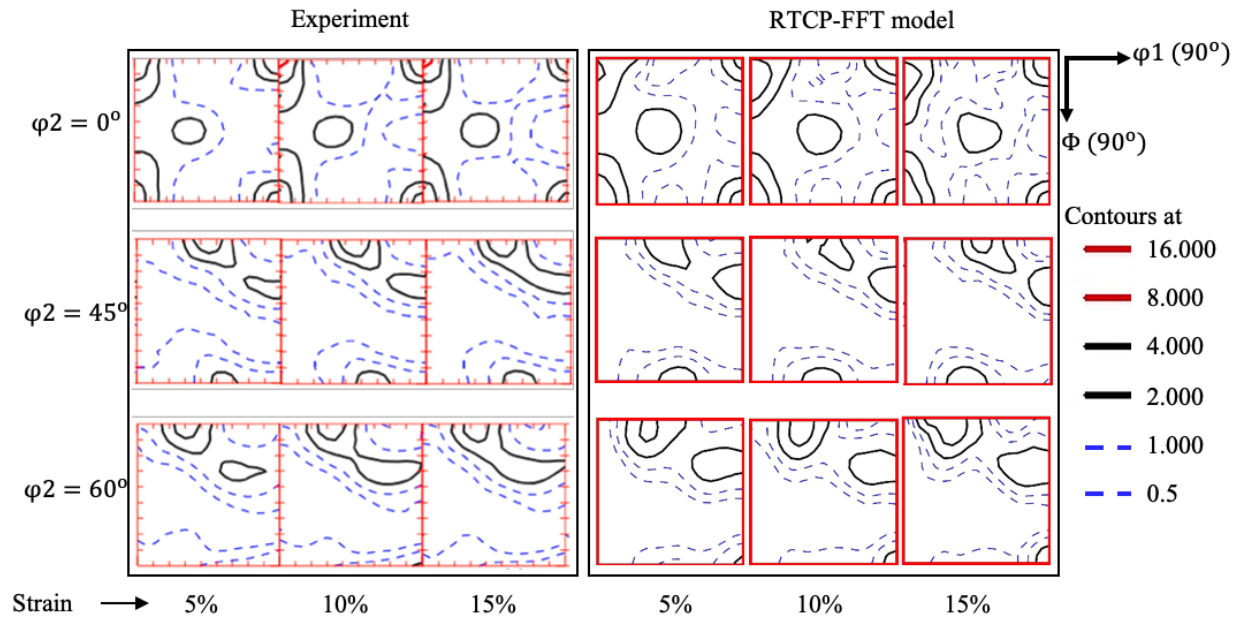


Figure 3.11: Comparison of measured (Hu et al., 2011) and predicted ODF sections at strain levels of 5, 10, and 15% for plane strain tension in RD.

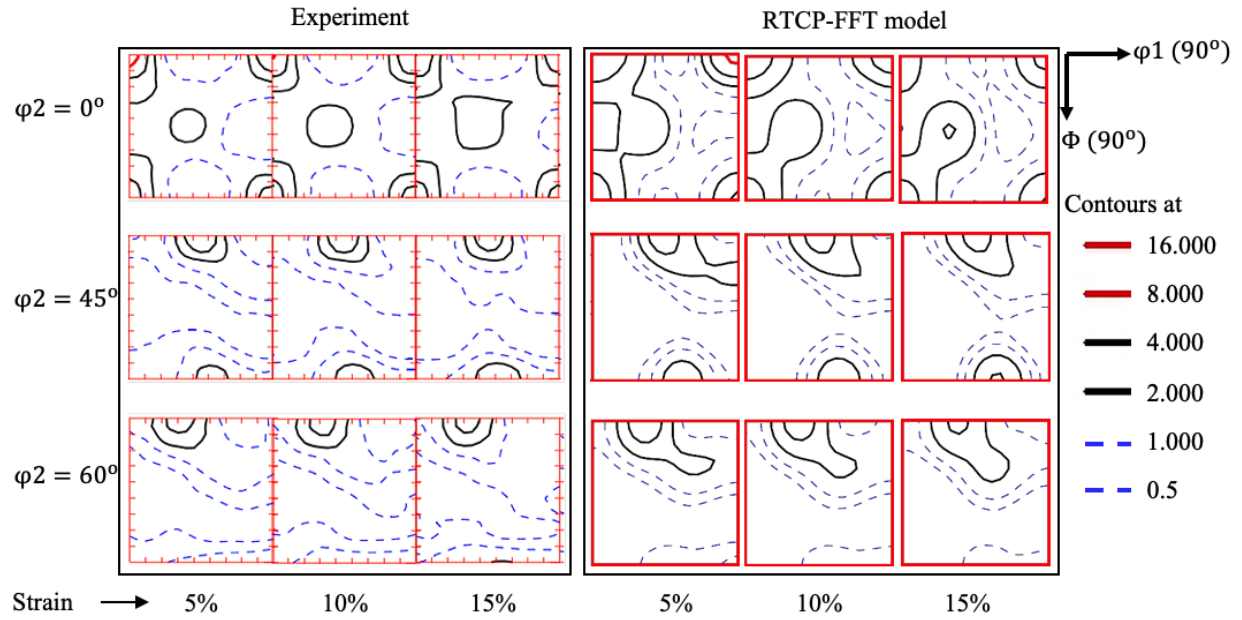


Figure 3.12: Comparison of measured (Hu et al., 2011) and predicted ODF sections at strain levels of 5, 10, and 15% for plane strain tension in TD.

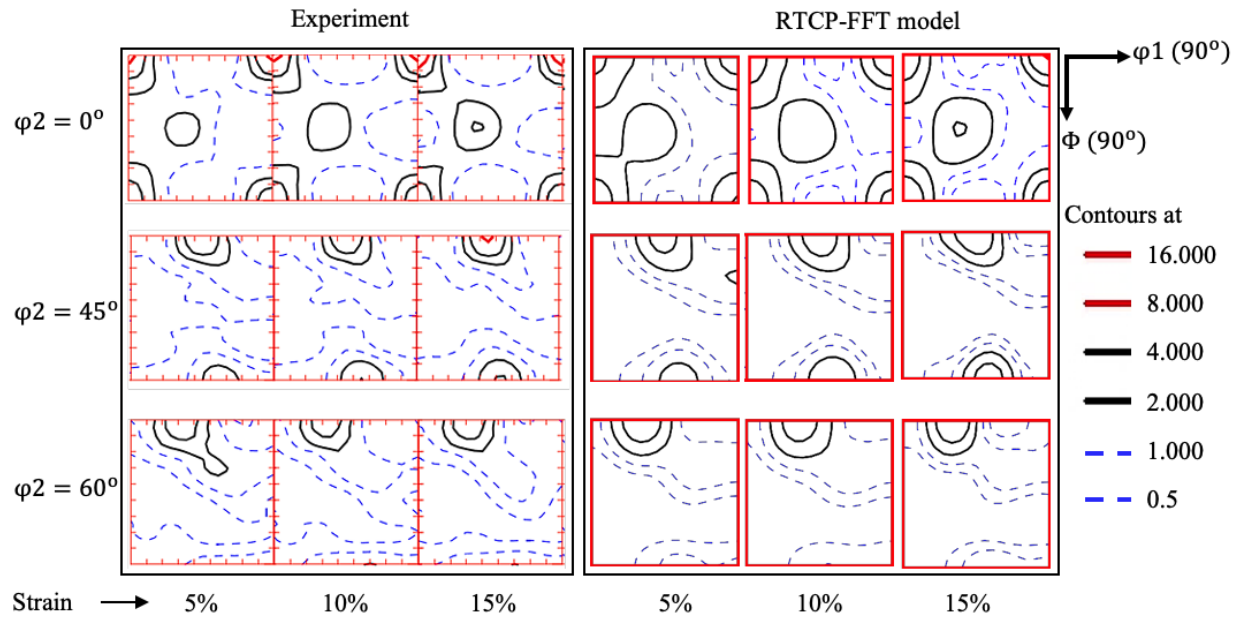


Figure 3.13: Comparison of measured (Hu et al., 2011) and predicted ODF sections at strain levels of 5, 10, and 15% for uniaxial tension in TD.

3.4.6 Computational Efficiency

Previous researches have demonstrated that the augmented Lagrangians scheme-based FFT models are several orders more efficient than FEM-based model in computing polycrystalline response under similar loading conditions (Liu et al., 2010; Prakash and Lebensohn, 2009). In present work, the EVP-FFT model is significantly modified to exploit its use in potential applications based on single-phase polycrystal modelling by further accelerating the FFT scheme using a semi-explicit rate tangent modulus method. In this section, a comparison of computational efficiency, in terms of CPU time, between the proposed RTCP-FFT model and the EVP-FFT model is presented using two different cases up to 20% true strain with a strain rate of 10^{-4} s^{-1} . The simulations were performed on a single processor of Intel(R) Xeon(R) CPU E5-2680 @ 2.70GHz at the University of Waterloo supercomputing centre without using any parallelization schemes.

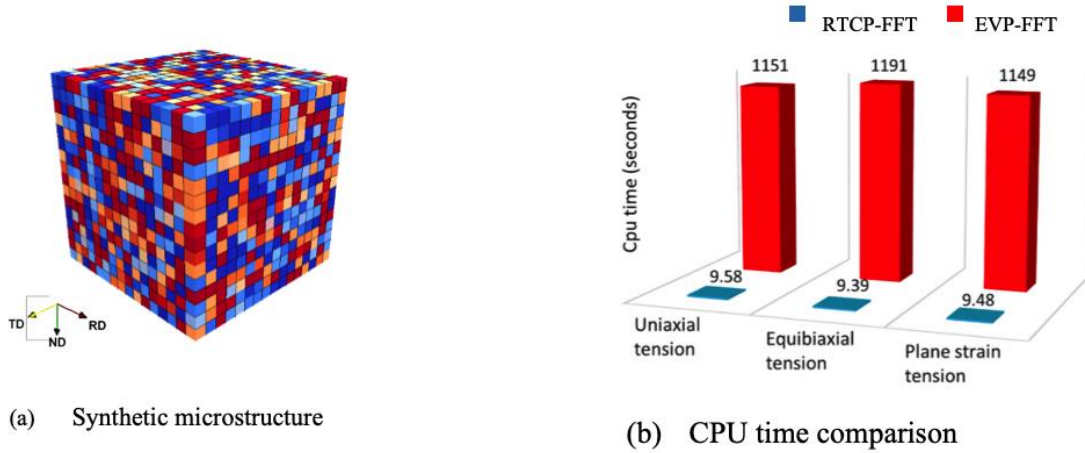


Figure 3.14: The synthesized microstructure of AA5754 consisting of one Fourier point per grain with 16 Fourier points in each of x, y and z-axis representing 4096 Cube grains, the colors represent different grains. (b) Computational cost comparison of proposed model (RTCP-FFT) and EVP-FFT model for three different strain paths up to 20% true strain.

In first case, for AA5754, the effect of different strain paths on CPU time is studied using a $16 \times 16 \times 16$ regular grid of Fourier points in an RVE with 4096 Cube grains (Figure 3.14a) corresponding to a single Fourier point per grain to minimize the number of calculations required for single temporal increment. Both RTCP-FFT and EVP-FFT models were first calibrated with uniaxial tension stress-strain curve along RD and then simulations were performed for plane strain tension along RD and balanced biaxial tension.

The computation times for the RTCP-FFT and the EVP-FFT simulations for three different strain paths up to 20% true strain are summarized in Figure 3.14b. The EVP-FFT model required an average CPU time of 19.39 minutes to simulate the material response for the three strain paths, while the RTCP-FFT model required an average CPU time of only 9.48 seconds. Thus, for the average CPU times, the RTCP-FFT model is 122.7 times faster than the EVP-FFT model. To further investigate the computational costs of the RTCP-FFT and the EVP-FFT models, the simulations of uniaxial tension with no strain hardening are also performed. The analysis shows that the RTCP-FFT model is 83 times faster than the EVP-FFT model when no strain hardening is considered.

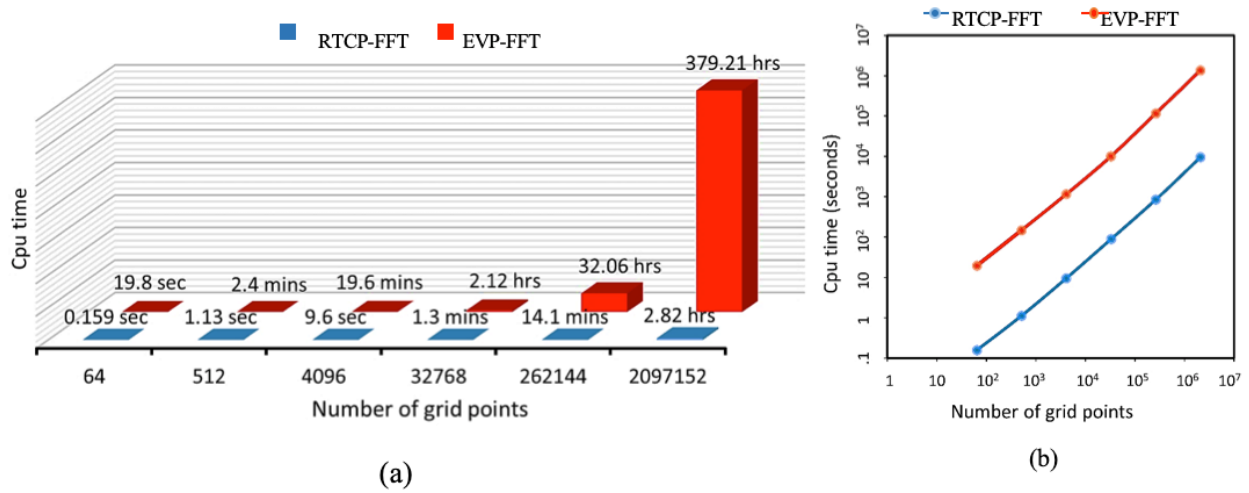


Figure 3.15: A comparison of CPU time required by proposed model (RTCP-FFT) and EVP-FFT model respectively to complete RD uniaxial tension simulation up to 20% true strain versus total number of Fourier points in each of six different RVEs used; (a) Bar chart representation (b) log plot showing proportional limit.

In the second case, the effect of increasing the number of Fourier points per grain on the total CPU time is analyzed. For this case, six different RVEs are used; each consisting of 64 grains with 4 grains in X, Y and Z directions. The orientations of these grains are sampled from the AA5754 texture. Each RVE is then discretized using a regular Fourier grid of; a) $4 \times 4 \times 4 = 64$ points, b) $8 \times 8 \times 8 = 512$ points, c) $16 \times 16 \times 16 = 4096$ points, d) $32 \times 32 \times 32 = 32768$ points, e) $64 \times 64 \times 64 = 262144$, and f) $128 \times 128 \times 128 = 2097152$ points, respectively. Note that, the above-mentioned discretization results in an increase in the number of Fourier points in each grain, with $1 \times 1 \times 1 = 1$, $2 \times 2 \times 2 = 8$, $4 \times 4 \times 4 = 64$, $8 \times 8 \times 8 = 512$, $16 \times 16 \times 16 = 4096$, $32 \times 32 \times 32 =$

32768 Fourier points per grain in RVEs described in a-e respectively. The RVEs are then subjected to uniaxial tension along RD (up to 20% true strain) with both models.

A comparison between the CPU times required by the two models to compute the response of six different RVEs with an applied strain rate of 10^{-4} s^{-1} is presented in Figure 3.15a. For each case, the RTCP-FFT model is, at an average, 110 times faster than EVP-FFT. Note that the computation times of the simulations performed by both RTCP-FFT and EVP-FFT models scale proportionally with the number of Fourier points (Figure 3.15b). This is a direct indication of the efficiency of both the models as both of the models employ an optimum matrix-inversion algorithm in the solver. The CPU times of the RTCP-FFT simulations are much quicker and fall about two orders of magnitude below that of the corresponding CPU times of the EVP-FFT simulations.

3.5 Summary and Conclusions

A new, computationally efficient full-field numerical framework (RTCP-FFT) for single-phase polycrystalline solids is developed by coupling a tangent modulus method-based crystal plasticity formulation with the fast Fourier transform (FFT) method to simulate large strain phenomena. The RTCP-FFT model is able to compute 3-D space-resolved local and overall micromechanical fields with high intragranular resolution using the direct input from images of microstructures of a polycrystalline material with extremely small computational cost.

The proposed numerical framework is verified by using simulations of the elastic-viscoplastic transitions of two polycrystals with the EVP-FFT model as a reference. As the first application with the RTCP-FFT model, for AA5754, the simulated stress-strain curves and texture evolution during five different strain paths are compared to experiments for model validation. Predictions with the RTCP-FFT model showed excellent agreement with experiments.

Simulations showed that the RTCP-FFT model is significantly faster than the EVP-FFT model in terms of CPU time; an acceleration of about two orders of magnitude is achieved over the augmented Lagrangians procedure-based FFT methods. The solutions produced by the RTCP-FFT model can be slightly different locally (per material point) from those produced by the EVP-FFT

model, however, these local variations (due to the difference in the integration algorithms) have with very little/no effect on macroscopic response.

Finally, the computational efficiency of the proposed numerical model makes it an excellent candidate to study the formability of polycrystalline metals since it can account for the richness of three-dimensional microstructures. Research with the proposed model to study the effect of various microstructural features (e.g., 3D grain morphologies) on the forming limit strains is presented in Chapter 4.

Chapter 4. – Part 2: An Efficient Full-Field Crystal Plasticity-based M-K Framework to Study the Effect of 3D Microstructural Features on the Formability of Polycrystalline Materials, Published in Modelling and Simulation in Materials Science and Engineering (2018), Volume 26, Number 7

Jaspreet S. Nagra¹, Abhijit Brahme¹, Raja Mishra², Ricardo A. Lebensohn³, Kaan Inal¹

¹ University of Waterloo, 200 University Ave. West, Waterloo, ON N2L 3G1, Canada

²General Motors Research and Development Center, 30500, Warren, MI 48090, USA

³Los Alamos National Laboratory, MS G755, Los Alamos, NM 87845, USA

Abstract

In this chapter, the new rate tangent-fast Fourier transform-based elasto-viscoplastic crystal plasticity constitutive framework (RTCP-FFT) developed by Nagra et al. (2017) is implemented in the so-called Marciniak-Kuczynski (M-K) (Marciniak and Kuczyński, 1967) framework to predict the forming limit diagrams (FLDs) of FCC polycrystals. The RTCP-FFT approach that accounts for 3D grain morphologies and grain interactions is used to compute the FLDs for aluminum alloys. The model employs two statistically representative volume elements (RVEs) with identical initial microstructure; one inside the imperfection band region (required for M-K analysis) and other outside the imperfection band region of the sheet metal. The proposed RTCP-FFT-based M-K model is a full-field, mesh-free and an efficient crystal plasticity formulation that enables a comprehensive investigation of the effects of 3D microstructural features on the FLDs with extremely small computational times. The new model is validated by comparing the predicted FLDs for AA5754 and AA3003 aluminum alloys with experimental measurements. Furthermore, the predicted FLDs are compared with the well-known Taylor type homogenization scheme-based M-K model (MK-Taylor) predictions. Furthermore, the effects of different grain shapes as well as

local grain interactions on the FLD predictions are studied. The study reveals that among the various microstructural features, the grain morphology has the strongest effect on the predicted FLDs and the FLD predictions can significantly be improved if the actual grain structure of the material is properly accounted for in the numerical models.

Keywords: Crystal plasticity, RTCP-FFT, Forming limit diagram, 3D microstructure, Grain morphology, M-K model

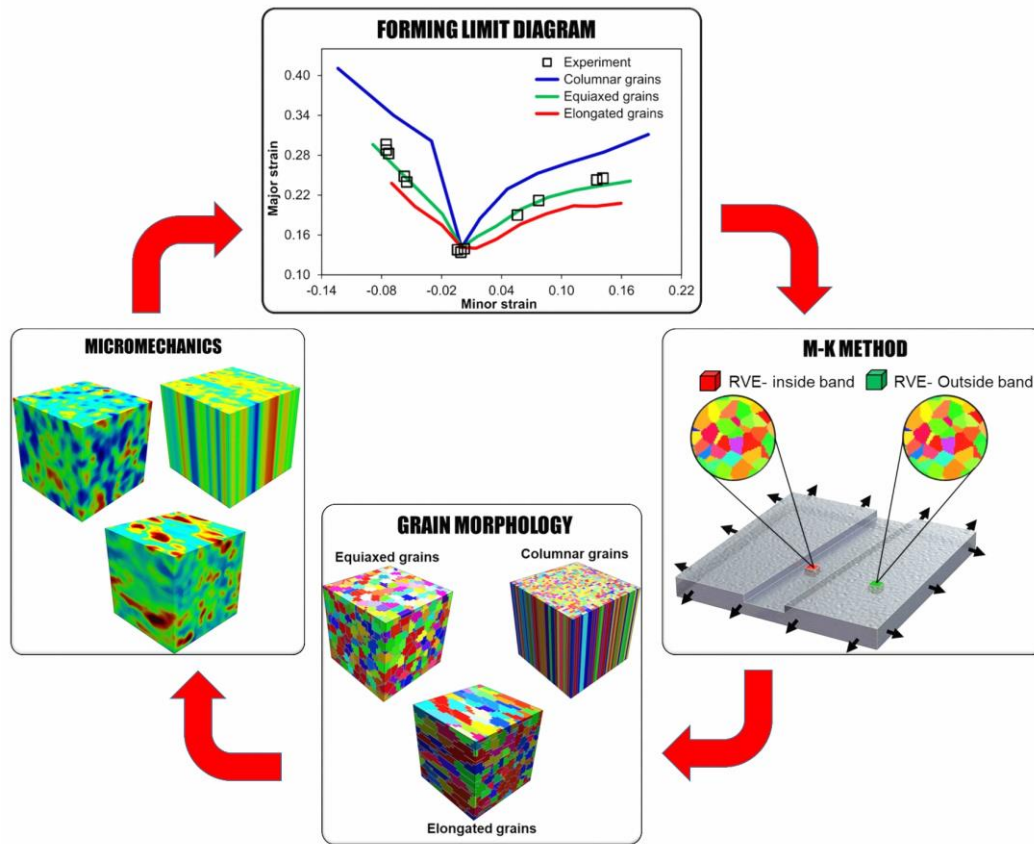


Figure 4.1: Graphical abstract of Chapter 4.

4.1 Introduction

The concept of forming limit curve (FLC) also known as the forming limit diagram (FLD), first introduced by Keeler in 1961, provides an approximation of how close the material is to neck. The FLDs have been extensively used thereafter to quantify the formability of a sheet metal. The response of a sheet metal subjected to plastic deformation is governed by the material's

microstructure (i.e., texture, morphology). However, it is very difficult and time consuming to study the effects of microstructure on the forming experimentally. Hence, theoretical methods are introduced to the analyses and a significant amount of research has been done to characterize the formability of a sheet metal using various computational models. In the available theoretical methods for obtaining the FLD of a sheet metal, the response of a material deforming plastically is obtained either using the phenomenological plasticity models (Takuda et al., 2000; Barlat et al., 2003; Yoshida et al., 2007; Chiba et al., 2013) or using meso-scale crystal plasticity (CP) as material model (Hutchinson and Neale, 1978a, 1978b, Wu et al., 1997, 2004; Inal et al., 2002; Inal et al., 2002; Inal et al., 2005, 2010; Delannay et al., 2009; Signorelli and Bertinetti, 2009; Signorelli et al., 2012; Mohammadi et al., 2014; Lévesque et al., 2016; Cyr et al., 2017) and a separate plastic instability criteria (e.g., Marciniak and Kuczyński (M-K) analysis) is employed to obtain failure strains. It is widely recognized that the deformation-induced texture and anisotropy strongly affects the localization of plastic flow (Barlat, 1987; Zhou and Neale, 1995; Tóth et al., 1996; Wu et al., 1997; Boudeau et al., 1998; Boudeau and Gelin, 2000; Tang and Tai, 2000). Since, the phenomenological plasticity models do not account for texture evolution during deformation of a polycrystalline sheet metal, the crystal plasticity (CP)-based models are usually preferred for more realistic predictions of the FLD.

Marciniak and Kuczyński developed the well-known plastic instability criteria for analyzing unstable deformation in sheet metals also known as the M-K analysis (Marciniak and Kuczyński, 1967). Initial investigations of the plastic instability analysis with crystal plasticity as the material model were based on Taylor-Bishop-Hill yield surfaces and these works provided predictions that were in good agreement with corresponding experimental results (Bassani et al., 1979; Barlat, 1989). Coupling a rate sensitive crystal plasticity model with the M-K analysis, Zhou and Neale (1995) computed the FLDs for a thin, face-centered cubic (FCC) sheet metal, where the initial texture and deformation induced texture evolution were considered in the model. In the later years, Wu et al. (1997) computed the FLDs for FCC polycrystals by employing the Asaro-Needleman crystal plasticity framework in which the imperfection groove was considered to be rotating with respect to the major biaxial stretch direction in the plane of the sheet metal. The effects of various parameters in the numerical model such as the material strain-rate sensitivity, single slip hardening, initial imperfection factor, texture, etc. on the predicted FLDs were investigated in detail by Wu

et al. (1997). Inal et al. (2005) used a rate-sensitive polycrystal plasticity model with the full constraint Taylor type homogenization scheme (FC-Taylor) and suggested that the effect of texture evolution during deformation on formability of body-centered cubic (BCC) polycrystal is much less (higher forming limit curve) as compared to the FCC polycrystals (lower forming-limit curve). Inal et al. (2005) also reported that the number of slip systems strongly affects the occurrence of localized necking in a polycrystalline material.

The studies mentioned above have significantly improved our understanding of FLD modelling, but they could not provide any information about the effects of grain morphologies and local strain partitioning on the FLD predictions since they were based on the Taylor-type homogenization scheme. It is well-known that the Taylor-type homogenization scheme cannot account for grain to grain interactions or grain morphology since each grain is assumed to have the same value of macroscopic strain while the stresses are computed as function of grain orientation. Molinari et al. (1987) proposed a more realistic approach that accounts for the interactions of the constituent grains (on an average sense) of a polycrystal for modelling its viscoplastic (VP) behavior. This approach has been further developed by Lebensohn and Tomé (1993) and Lebensohn et al. (2007) and is also known as viscoplastic self-consistent formulation (VPSC). The Viscoplastic Self Consistent (VPSC) model considers each constituent crystal as an Eshelby heterogeneity embedded in a Homogeneous Equivalent Medium (HEM) and has been extensively used for polycrystal modelling accounting for texture-induced plastic anisotropy (Lebensohn et al., 2007; Signorelli et al., 2009; Signorelli and Bertinetti, 2012; Huang et al., 2010; Jeong et al., 2015; Schwindt et al., 2015). In recent studies, Serenelli et al. (2011); and Signorelli and Bertinetti, (2009, 2012) showed that FLDs predicted using coupled models of VPSC and M-K method (MK-VPSC) are able to provide better agreement with the measured FLDs as compared to the Taylor-based MK models. However, the MK-VPSC models are computationally very expensive as compared to the Taylor-based MK models (Schwindt et al., 2015; Jeong et al., 2016). The formulations discussed above rely on mean-field approximations to obtain the plastic response of polycrystalline materials undergoing plastic deformation. Apart from these models, full-field approaches are also available, that can predict the actual micromechanical stress and strain fields as well as the effective response of polycrystals with a specific microstructure. Full-field approaches, namely crystal plasticity-Finite element (CP-FE) (Bronkhorst et al., 1992; Lee et al.,

2010; Zeng et al., 2014; Alharbi and Kalidindi, 2015; Popova et al., 2015; Zhang et al., 2015; Li et al., 2016; Ardeljan et al., 2017; Pouriaeyali and Xu, 2017; Grilli et al., 2018) and crystal plasticity-fast Fourier transform (CP-FFT)-based methods (Lebensohn, 2001; Prakash and Lebensohn, 2009; Liu et al., 2010; Lebensohn et al., 2011; Lebensohn et al., 2012; Eisenlohr et al., 2013; Nagra et al., 2017), provide richer micromechanical information with direct input from an image of microstructure obtained by EBSD. To the best knowledge of the authors there is no systematic work presenting the effect 3D grain morphology on the FLD using a full-field model that accounts for the 3D spatial distribution of texture to obtain an accurate micromechanical and effective response. Advanced and efficient full-field CP models, that can model 3D microstructures and consider the actual grain morphology, grain to grain interactions and sub-grain texture evolution, can improve the accuracy of FLD predictions as compared to; a) the full constraint-Taylor models (homogenous deformation is assumed throughout the material) and b) VPSC models (Yamanaka, 2016).

In the present work, a new and efficient, full-field numerical framework that can account for the full richness of the 3D microstructure (texture, grain morphologies, grain interactions, etc.) is combined with the well-known M-K plastic instability criteria and the effects of various 3D microstructural features on the formability of aluminum alloys are presented. Accordingly, the rate tangent-based crystal plasticity-fast Fourier transform model (RTCP-FFT) (Nagra et al. 2017) is coupled with the M-K framework (Inal et al., 2005, 2010; Mohammadi et al., 2014; Lévesque et al., 2016; Cyr et al., 2017). The RTCP-FFT model accounts for the 3D microstructure, grain interactions, intragranular texture evolution, and grain morphology while providing full-field solutions to micromechanical fields within reasonable computational times. The RTCP-FFT model gives comparable results to the established full-field models, e.g., CPFE and EVPFFT approaches, with a considerable computation time saving, by a factor ~ 150 and ~ 100 respectively (Nagra et al. 2017). In addition, since the proposed methodology is able to capture the vital 3D microstructural features; the predicted forming limit strain are in excellent agreement with the experiments with significant improvement in FLD predictions compared to the MK-Taylor model. The plan of this chapter is as follows: In section 4.2, the details of the RTCP-FFT model and the M-K method are presented. In section 4.3, the FLD predictions for AA5754 and AA3003 at room temperature are presented using the proposed methodology and are compared with those obtained from MK-Taylor

model as well as with the corresponding measured FLDs. In section 4.4, the effects of microstructural features on FLD predictions for AA3003 polycrystal are discussed and this is followed by section 4.5, where the conclusions of this research are summarized.

4.2 Constitutive Framework

In this numerical framework, the RTCP-FFT model is employed. The RTCP-FFT model is the hybrid combination of the rate-dependent crystal plasticity formulation (Asaro and Needleman, 1985) and the modified FFT algorithm developed from elasto-viscoplastic FFT (EVP-FFT) model (Lebensohn et al. 2012), to compute the full-field solutions of micromechanical fields in a statistically equivalent representative volume element (RVE). The RTCP-FFT model is approximately 100 times faster than the EVP-FFT model and its details of can be found in Nagra et al. (2017). For completeness, a brief summary of the RTCP-FFT model is presented in the following. According to the rate dependent crystal plasticity framework, the total deformation of a single crystal is the result of two distinct physical phenomena:

- a) Plastic deformation due to the movement of dislocations that cause crystallographic slip.
- b) The elastic distortion and rigid body rotations of crystal lattice within embedded material.

For a single crystal, the elastic constitutive equation to update the Jaumann rate $\overset{\nabla}{\boldsymbol{\sigma}}$ of Cauchy stress $\boldsymbol{\sigma}$ can be written as:

$$\overset{\nabla}{\boldsymbol{\sigma}} = \boldsymbol{\mathcal{C}} : \mathbf{D} - \dot{\boldsymbol{\sigma}} - \boldsymbol{\sigma} \text{tr} \mathbf{D} \quad (4.1)$$

In Equation (4.1), \mathbf{D} is the total strain rate tensor, $\dot{\boldsymbol{\sigma}}$ is the viscoplastic stress-rate, $\boldsymbol{\mathcal{C}}$ is the elasto-viscoplastic moduli which is determined using rate tangent method, details of which can be found in Peirce et al. (1983), Rashid and Nemat-Nasser (1992), Nagra et al. (2017). The viscoplastic stress-rate $\dot{\boldsymbol{\sigma}}$ is computed based on the slip rates on each slip system. The shear rate $\dot{\gamma}_{(\alpha)}$ on each slip system α is governed by a power-law expression, so that

$$\dot{\gamma}_{(\alpha)} = \dot{\gamma}_0 \operatorname{sgn} \tau_{(\alpha)} \left| \frac{\tau_{(\alpha)}}{g_{(\alpha)}} \right|^{1/m} \quad (4.2)$$

where $\tau_{(\alpha)}$ is the resolved shear stress, $\dot{\gamma}_0$ is the reference shear rate (same for each slip system) and m is the index of strain rate sensitivity. The hardened state of each slip system α is characterized by $g_{(\alpha)}$. Following Asaro and Needleman (1985), it is considered that g_{α} depends on the accumulated sum, γ_a , of the slips, where

$$\gamma_{(a)} = \int_0^t \sum_{\alpha} |\dot{\gamma}_{(\alpha)}| dt \quad (4.3)$$

In present work, the model originally proposed by Chang and Asaro (1981) is employed. Accordingly, the hardening rate $\dot{g}_{(\alpha)}$ for multiple slip is defined by hardening law as following

$$\dot{g}_{(\alpha)} = \sum_{\beta} \mathbf{h}_{\alpha\beta} |\dot{\gamma}_{\beta}| \quad (4.4)$$

In Equation (4.4), $\mathbf{h}_{(\alpha\beta)}$ is the hardening moduli and $\dot{\gamma}_{(\beta)}$ is the single slip shear stress rate on slip system β . The hardening moduli used here is the one that has been used previously by Peirce et al. (1983) and Asaro and Needleman (1984),

$$\mathbf{h}_{(\alpha\beta)} = \mathbf{q}_{(\alpha\beta)} h_{(\beta)} \text{ (no sum on } \beta) \quad (4.5)$$

where $\mathbf{q}_{\alpha\beta}$ matrix describes the latent hardening of the crystallite and h_{β} is the single slip hardening. The model presented by Chang and Asaro (1981) is employed to calculate the single slip hardening. Accordingly,

$$h_{(\beta)} = h_s + (h_0 - h_s) \text{sech}^2 \left\{ \left(\frac{h_0 - h_s}{\tau_s - \tau_0} \right) \gamma_{(a)} \right\} \quad (4.6)$$

where τ_0 is the critical resolved shear stress, τ_s is the value of saturated shear stress, h_s is the asymptotic hardening rate of slip systems and h_0 is the hardening constant. To compute the micromechanical fields and intragranular texture evolution during the deformation, the space resolved configuration of the grains and their interactions must be considered in the whole RVE. In present work, the FFT-based algorithm is employed to calculate the fluctuations in local strain components and thus, the total strain in one direction can be written as following:

$$\varepsilon_{ij}(\mathbf{x}) = \tilde{\varepsilon}_{ij}(\mathbf{x}) + E_{ij} \quad (4.7)$$

where $\tilde{\varepsilon}_{ij}(\mathbf{x})$ is the strain fluctuation in the crystal due to heterogeneity and E_{ij} is the average strain imposed on the RVE. The FFT technique requires a regular 3D grid $\{\mathbf{x}_d\}$ of Fourier points with length L_k and N_k be the number of Fourier points in each x_k direction, is discretized as following:

$$\{\mathbf{x}_k\} = \left\{ \left((i_1 - 1) \frac{L_1}{N_1}, (i_2 - 1) \frac{L_2}{N_2}, (i_3 - 1) \frac{L_3}{N_3} \right); i_k = 1, \dots, N_k, k = 1, 3 \right\} \quad (4.8)$$

In Equation (4.7), each Fourier point represents a single crystal in the RVE which is modeled as an FCC crystal with 12 distinct slip systems. To compute the full-field solutions of micromechanical fields for a heterogeneous representative volume element (RVE), the local problem is needed to be solved at each grid point written as following:

$$\begin{cases} \sigma_{ij}(\mathbf{x}) = \mathcal{L}_{ijkl}(\mathbf{x}) \varepsilon_{kl}(\mathbf{x}), & \forall \mathbf{x} \in \{\mathbf{x}_d\} \\ \sigma_{ij,j}(\mathbf{x}) = 0 \\ \text{Periodic boundary conditions across RVE} \end{cases} \quad (4.9)$$

where $\varepsilon_{kl}(\mathbf{x})$ and $\sigma_{ij}(\mathbf{x})$ are the local strain and local stress fields and $\mathcal{L}_{ijkl}(\mathbf{x})$ is the local elastic stiffness. After solving the above local problem (Nagra et al., 2017), the total local strain is given by:

$$\varepsilon_{ij}(\mathbf{x}) = \text{fft}^{-1}(\text{sym}(\hat{\Gamma}_{ijkl}^0(\xi)) \hat{\sigma}_{kl}(\xi)) + E_{ij} \quad (4.10)$$

where, “ $\hat{\cdot}$ ” indicates quantities in Fourier space, fft^{-1} indicates inverse Fourier transform into real space, ξ is the frequency point in Fourier space, $\hat{\Gamma}_{ijkl}^0$ is the Green operator in Fourier space, and $\hat{\sigma}_{kl}$ is the forward Fourier transform of the current local stress tensor. Due to the heterogeneity of the material, the set of convected Fourier points no longer forms a regular grid as the deformation progresses. However, a regular Fourier grid is needed in order to compute the strain fluctuation (Eq. 4.10) using convolution theorem. Therefore, in the present work, the following scheme is adopted for updating coordinates of the Fourier points, neglecting contribution from strain fluctuations, so that the Fourier grid remains regular with deformation (Lebensohn et al., 2008)

$$\mathbf{x}_k^{t+1} = \mathbf{x}_k^t + \mathbf{D}\mathbf{x}_k^t \times \Delta t \quad (4.11)$$

After each time step increment, the distances between adjacent Fourier points change, but the Fourier grid remains regular, thus determining an “average stretching” of the grains in the RVE. Using the RTCP-FFT model as outlined above, the full field solutions of micromechanical fields are computed for a polycrystal RVE subjected to periodic boundary conditions. For modelling formability, the RTCP-FFT model is incorporated into the M-K framework (Inal et al., 2005, 2010; Mohammadi et al., 2014; Lévesque et al., 2016; Cyr et al., 2017). Accordingly, the sheet metal is assumed to contain a geometrical imperfection, such as a narrow band or groove across the sheet’s width, which is slightly thinner than the rest of the sheet and this is defined as the imperfection factor (f) given by:

$$f = \frac{h^b(0)}{h(0)} \quad (4.12)$$

where, $h^b(0)$ is the initial thickness of band region and $h(0)$ is the initial thickness of the region outside band.

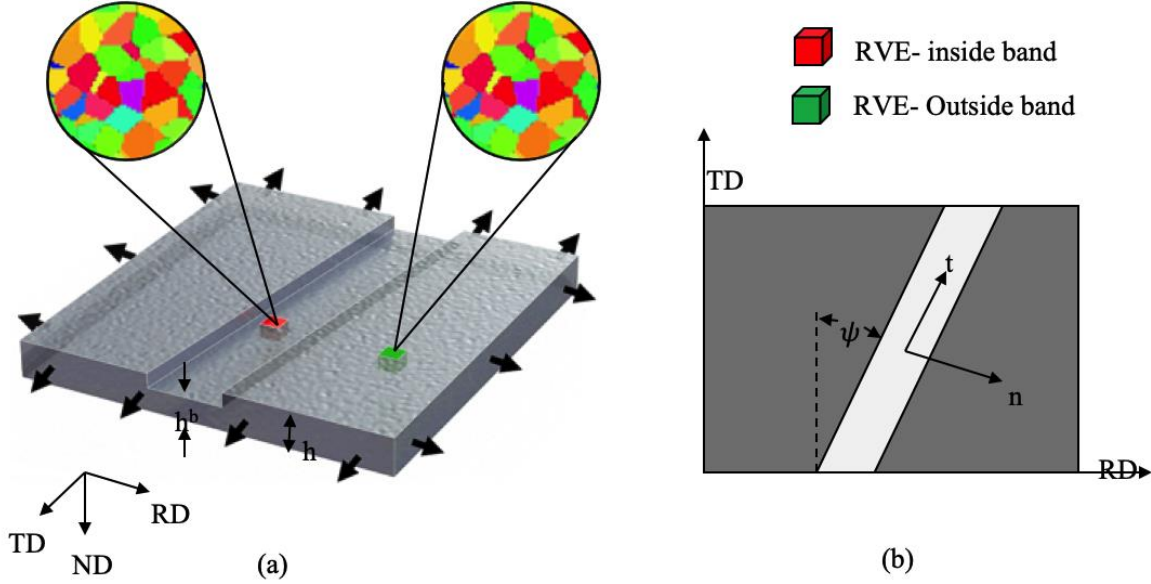


Figure 4.2: Initial configuration of M-K criteria used for FLD analysis; a) 3D representation of sheet metal, RVEs, boundary conditions and imperfection band, b) Schematic of top surface of sheet showing band direction vectors and initial band angle.

To model the effect of this imperfection on sheet formability, two RVEs with identical initial texture and grain morphology, one outside the imperfection band (safe region) and other in the imperfection band (unsafe zone), are employed. Compatibility and equilibrium are satisfied across the band interface assuming with the assumption of plane stress conditions (Figure 4.2). The failure of the sheet is due to the rapid thinning of the sheet in normal direction (ND), when the sheet is subjected to proportional boundary conditions along orthotropic symmetry directions, i.e., in rolling direction (RD) and transverse direction (TD) respectively. In this work, the RVE in the safe region (i.e., outside the imperfection band) is subjected to the proportional loading (Eq. 4.13) and the strain rates in the imperfection band are computed through compatibility and equilibrium equations so that:

$$\begin{cases} \rho = \frac{D_{22}}{D_{11}}, -0.5 \leq \rho \leq 1.0 \\ W_{ij} = 0 \\ D_{ij} = 0 \forall i \neq j \end{cases} \quad (4.13)$$

where, W_{ij} is the spin rate, ρ is the applied strain ratio, D_{11} and D_{22} are principal strain rates. The third principal component of strain-rate tensor (D_{33}) that describes the rate of thinning is found using the plane stress condition imposed in the formulation.

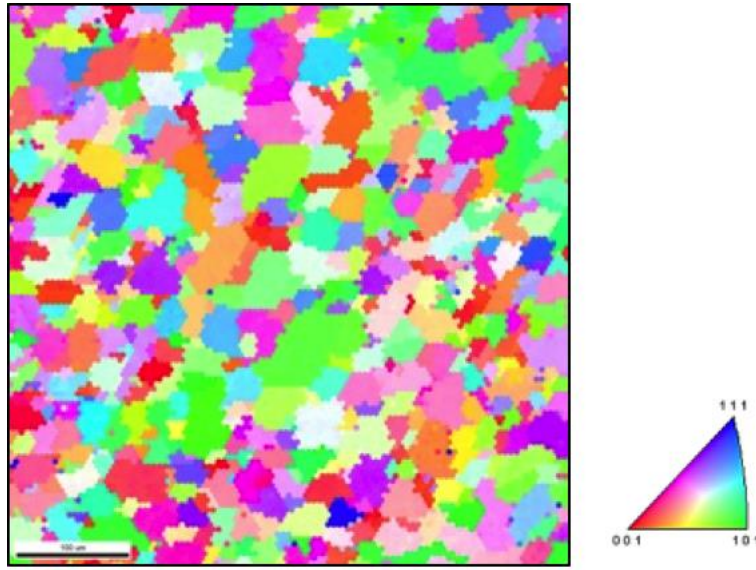


Figure 4.3: 2D Electron backscatter diffraction (EBSD) map used to generate synthetic microstructure for AA5754.

4.3 Results: Application to Aluminum Alloys

The objective of this work is not only to validate the M-K criteria-based RTCP-FFT model (MK-RTCP-FFT) but to also assess the effects of various 3D microstructural features such as neighborhood, grain morphology and texture on the FLDs. These analyses are performed by considering two different materials; two commercial aluminum alloys, AA3003 and AA5754 are employed in this study. Using MK-RTCP-FFT model, the formability of AA 5754 and 3003 sheets are assessed at 25 °C and is compared with predictions of MK criteria-based Taylor type model (MK-Taylor) as well as with experimental observations taken from literature. Since the MK-

RTCP-FFT model accounts for the actual grain morphology and grain interactions, significant differences between the predicted FLDs are observed when compared to MK-Taylor model. These microstructural features are further investigated for AA3003 using three different RVEs with equiaxed grains, columnar grains and elongated (pancake shape) grains, respectively. In all the simulations that are reported in this chapter, the typical values of material parameters for an aluminum alloy are considered; the slip rate sensitivity, m , is taken as 0.01 and the reference plastic shearing rate ($\dot{\gamma}_0$) is assumed to be 0.001 s^{-1} , while the anisotropic crystal elastic constants are taken to be $C_{11} = 206 \text{ GPa}$, $C_{12} = \text{GPa}$, and $C_{44} = 54 \text{ GPa}$ (Cyr et al., 2017).

4.3.1 Predicted FLDs for AA5754

In this section, the formability of an O-temper aluminum alloy (AA) 5754 sheet is studied using both the MK-Taylor and MK-RTCP-FFT models. The AA5754 is commonly used in interior sheet components and flooring in automotive bodies and thus, accurate simulations of forming processes are required to design and fabricate AA5754 sheet components efficiently.

4.3.1.1 Model Setup

The equiaxed grain structure resembles the grain shapes as perceived experimentally in an O-tempered material (Iadicola et al., 2008) and the 2D electron backscatter diffraction (EBSD) map for AA5754 is presented in Figure 4.3. From this EBSD map, Euler angle triplets are extracted and assigned to voxels in each grain. The synthetic microstructure in the RVE is built using microstructure builder as proposed by Brahme et al. (2006), using an optimization technique to minimize the error, in both orientation distribution function (ODF) and misorientation distribution function (MDF), between the measured and assigned orientations. An RVE of AA5754 with $64 \times 64 \times 64$ Fourier points and 278 equiaxed grains, is employed in this study (Figure 4.4). It should be mentioned that, for consistency, the number of Fourier points are kept same in each RVE used throughout this chapter.

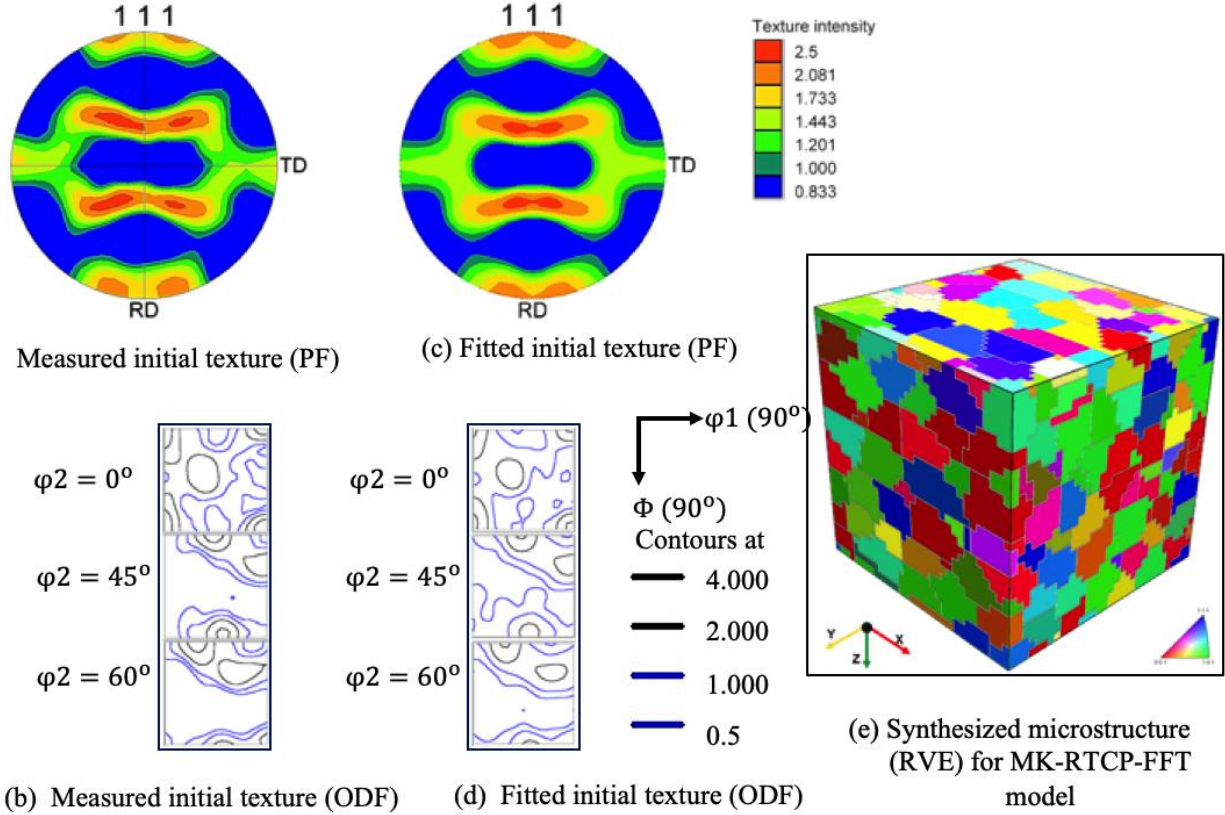


Figure 4.4: Comparison of initial texture of AA5754-O: pole figure representations of the experimental texture (a) and fitted texture (b); Comparison of contours of experimental ODFs (c) and fitted ODFs (d) at 0, 45, and 60 degrees of ϕ_2 sections. (e) The generated microstructure with 64 x 64 x 64 Fourier points in 278 grains, the colors represent different grains.

Figure 4.4(a) and Figure 4.4(b) show the pole figure and orientations distribution function (ODF) of the initial texture of as received O-tempered AA5754. Figure 4.4(c) and Figure 4.4(d) show the pole figure and ODF sections of the initial texture of an equivalent synthesized microstructure generated from the experimental data. A good agreement between the experimental and fitted initial textures can be observed.

4.3.1.2 Model Calibration

The material parameters used in the simulations are obtained by curve fitting simulated uniaxial stress-strain curve to the experimental uniaxial tensile curve (Iadicola et al., 2008). The error bars represent experimental uncertainties as reported in Iadicola et al. (2008) (Figure 4.5). The strain hardening parameters employed for AA5754 are shown in Table 4.1.

Table 4.1: Constitutive parameters used to calibrate models for RD uniaxial tension.

Model	h_0/τ_0	τ_s/τ_0	τ_0	h_s/τ_0	m	q
Taylor	12.5	3.30	23.8	0.28	0.01	1.0
RTCP-FFT	10.0	3.33	23.8	.001	0.01	1.0

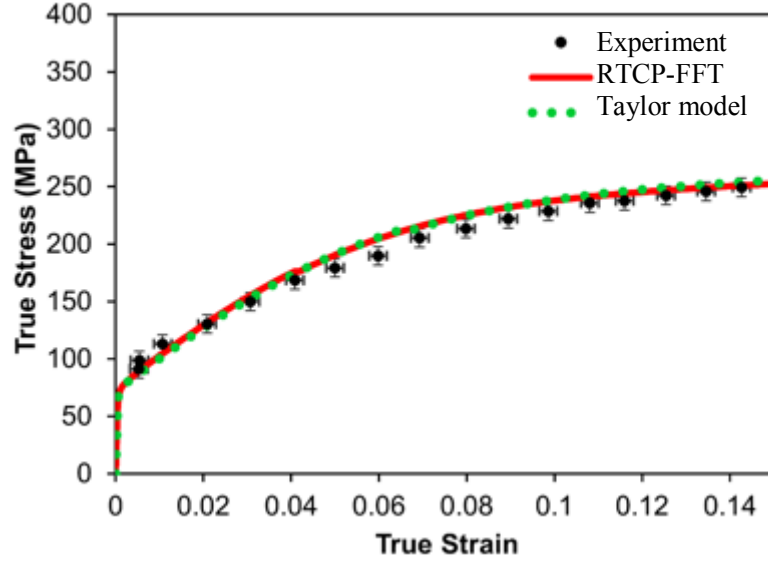


Figure 4.5: Comparison of overall stress-strain curves of measured data and simulated response by calibrated-RTCP-FFT and Taylor models respectively for RD uniaxial tension at 25 °C.

4.3.1.3 FLD Results and Discussion

The predicted FLDs for a direct cast AA5754-O with MK-RTCP-FFT and MK-Taylor models as well as the experimental FLD are presented in Figure 4.6. The imperfection parameter, f , employed with the MK-RTCP-FFT and MK-Taylor model is 0.9945 and 0.9934 respectively. For both models, the imperfection parameter is obtained by matching the limit strain associated with the in-plane plane strain tension case ($\rho = 0.0$) to the corresponding value of the experimental limit strains. Note that, due to a wide spread of limit strains near $\rho = 0.0$, the fitting strain value is chosen relatively arbitrary. In this case, the value of fitted major strain is 14.4% for both MK-RTCP-FFT and MK-Taylor models. On the left-hand side of FLD ($-0.5 \leq \rho \leq 0.0$), the predicted limit strains by both models decrease as strain path changes from uniaxial tension ($\rho = -0.5$) up to

in-plane plane strain tension ($\rho = 0.0$) and are in good agreement with experimental values of forming limit strains.

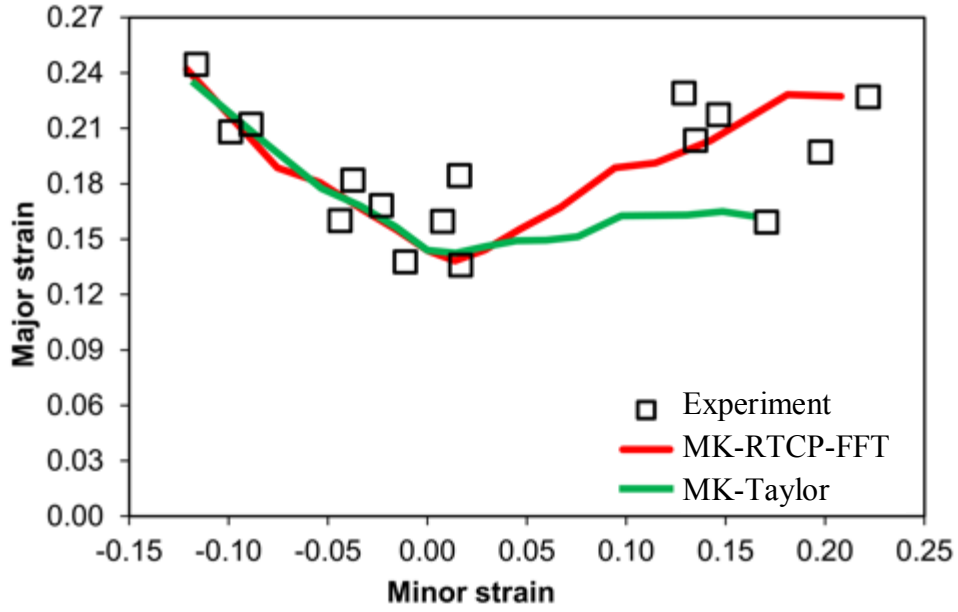


Figure 4.6: Comparison of FLD predictions of AA5754-O at 25 °C using MK-RTCP-FFT and MK-Taylor models with experiment data (Cyr et al., 2017).

On the biaxial side of FLD ($0.0 \leq \rho \leq 1.0$), initially the limiting strains predicted by both models increase but after $\rho = 0.5$, the MK-Taylor model predicts a sudden decrease in limit strains. This sudden dip has also been reported in several other analyses based on the MK-Taylor model (Mohammadi et al., 2014; Lévesque et al., 2016; Cyr et al., 2017). However, the MK-RTCP-FFT model predicts limit strains that are in excellent agreement with the measured FLDs up to equibiaxial tension. It is clear from the results that the microstructural features strongly affect the predicted forming limit strains and a significant improvement, compared to the MK-Taylor model, is achieved by the proposed MK-RTCP-FFT model. It should be noted that the orientation of the imperfection band is also an important factor affecting the limit strains. In Figure 4.7, the band orientations that produce the lowest limit strains are plotted versus the strain ratio. Results show that both models follow similar overall trends. The MK-RTCP-FFT model predicts a lower imperfection band orientation than the MK-Taylor model throughout the biaxial stretching region except at equibiaxial condition where the band is perpendicular to RD.

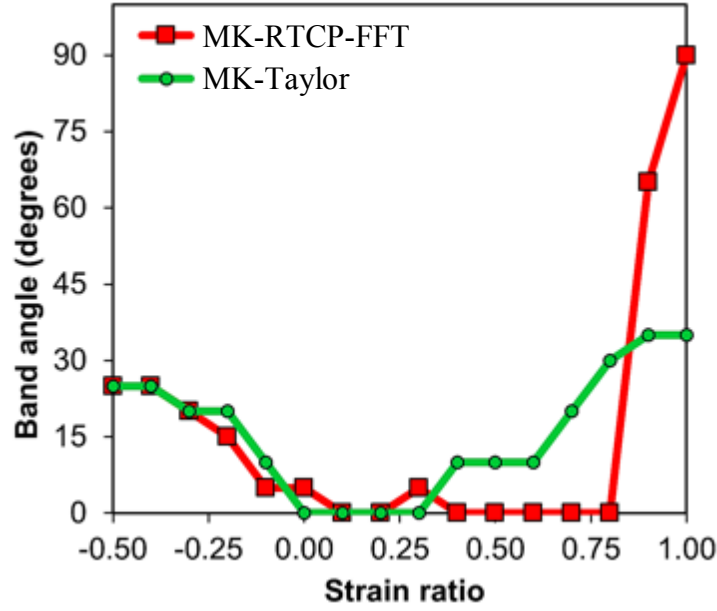


Figure 4.7: Evolution of critical imperfection band angle with strain path of AA5754-O predicted using MK-RTCP-FFT and MK-Taylor models.

4.3.2 Predicted FLDs for AA3003

In this section, the formability of an O-temper AA3003 sheet is studied using both the MK-Taylor and MK-RTCP-FFT models.

4.3.2.1 Model Setup

For AA3003-O sheet alloy, an RVE with $64 \times 64 \times 64$ Fourier points and 916 equiaxed grains, is employed in the simulations. The same methodology as explained in section 4.3.1.1, is used to generate the RVE for AA3003. The 2D EBSD map of the AA3003 from which the 3D microstructure is reconstructed is presented in Figure 4.8. The pole figure and orientations distribution function (ODF) of the initial texture of as received AA3003-O are presented in Figure 4.9(a) and Figure 4.9(b), while Figure 4.9(c) and Figure 4.9(d) show the pole figures and ODFs of the initial texture of the synthesized 3D microstructure (Figure 4.9e).

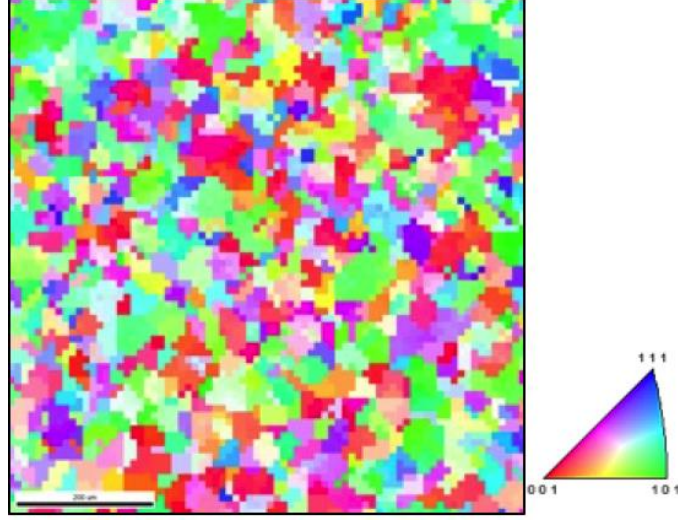


Figure 4.8: 2D Electron backscatter diffraction (EBSD) map used to generate synthetic microstructure for AA3003.

4.3.2.2 Model Calibration

The material parameters (Table 4.2) used in the simulations are obtained by curve fitting simulated uniaxial stress-strain curve to the experimental uniaxial tensile curve (Bagheriasl et al., 2011) as shown in Figure 4.10 using MK-RTCP-FFT and MK-Taylor models respectively.

Table 4.2: Constitutive parameters used to calibrate RTCP-FFT and Taylor models for RD uniaxial tension.

Model	h_0/τ_0	τ_s/τ_0	τ_0	h_s/τ_0	m	q
Taylor	11.9	2.30	20.78	0.66	0.01	1.0
RTCP-FFT	11.9	2.27	21.0	0.6	0.01	1.0

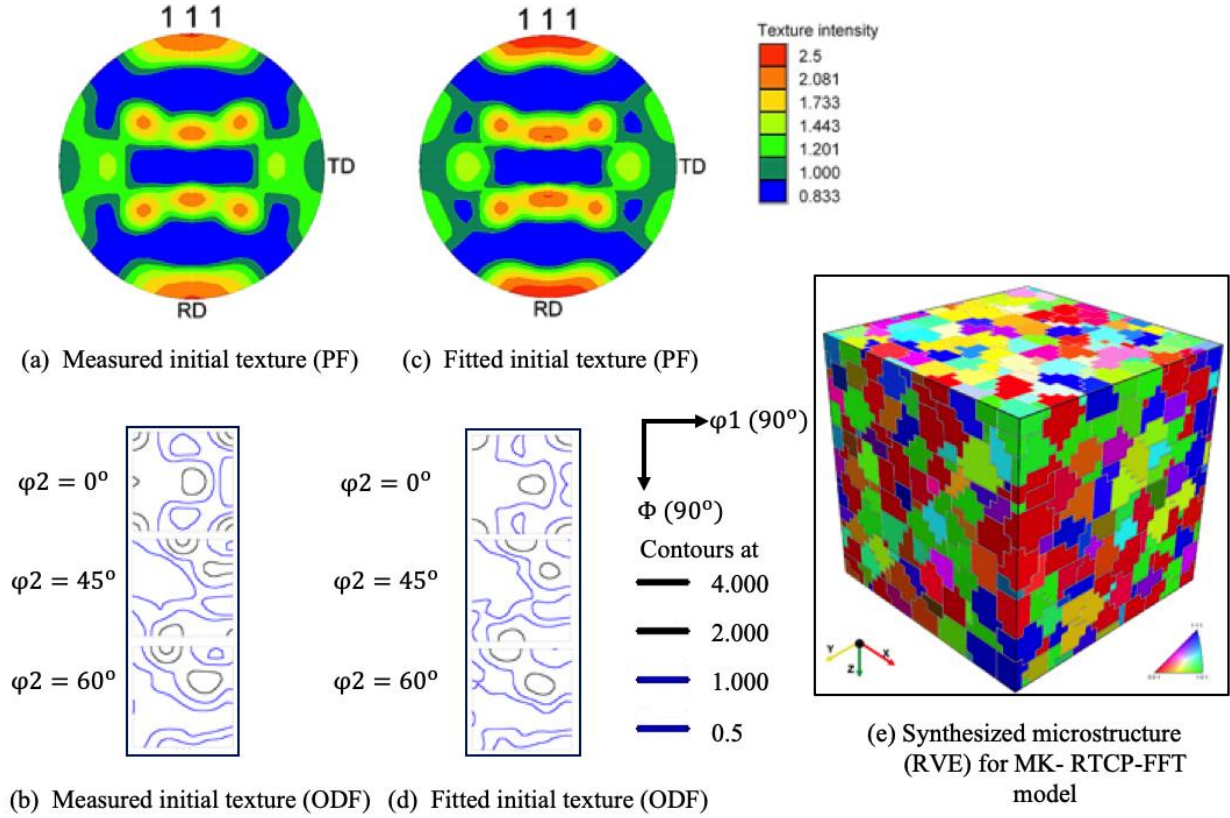


Figure 4.9: Comparison of initial texture of AA3003-O: pole figure representations of the experimental texture (a) and fitted texture (b); Comparison of contours of experimental ODFs (c) and fitted ODFs (d) at 0, 45, and 60 degrees of ϕ_2 sections. (e) The generated microstructure with 64 x 64 x 64 Fourier points in 916 grains, the colors represent different grains.

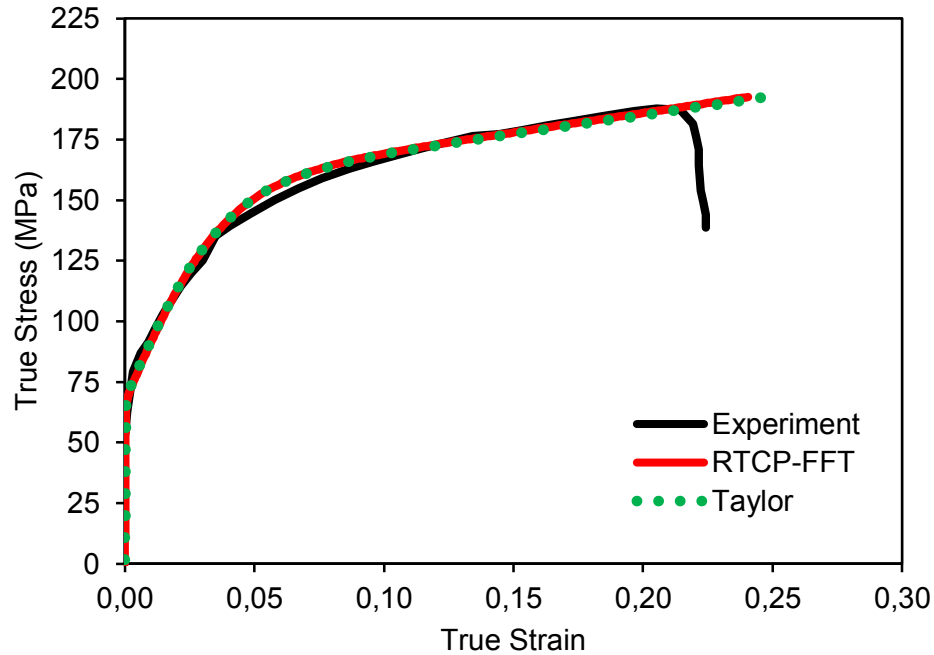


Figure 4.10: Comparison of overall stress-strain curves of measured data (Bagheriasl et al., 2011) and simulated response by calibrated-RTCP-FFT and Taylor models for AA3003-O under uniaxial tension along RD at 25 °C.

4.3.2.3 FLD Results and Discussion

For AA3003-O, the predicted FLDs using the MK-RTCP-FFT and the MK-Taylor models are shown in Figure 4.11(a). The critical values of imperfection band angles versus strain path are plotted in Figure 4.11(b). Simulations show that both the MK-Taylor and MK-RTCP-FFT models follow similar trend of evolution of critical band angle. However, overall, the MK-Taylor model under predicts the forming limit strains. It can be inferred that the MK-Taylor model accumulates higher shear rate on the slip systems to accommodate the imposed deformation that results in the prediction of premature failure prediction for each strain path. However, once again, with the proper grain morphologies being employed in the analyses, the MK-RTCP-FFT model predicts limit strains that show excellent agreement with experimental results.

Similar observations were presented by Tadano et al. (2013). In their work, a method using the plastic flow localization combined with a homogenization-based finite element model (FEM) to capture the response of a heterogeneous microstructure (provided that the RVE can still be found and can be reproduced using a FE method) was presented. They then used this approach to compare

the predicted forming limit strains for an aluminum polycrystal with predictions obtained from a Taylor-type crystal plasticity-based M-K model. Their findings showed that the results were similar in both cases. However, it should be mentioned that the major difference between this research and the approach presented by Tadano et al. (2013) is that the proposed modelling approach can account for the full richness of the 3D microstructures that include the heterogeneity in grain morphologies, grain interactions as well as textural gradients.

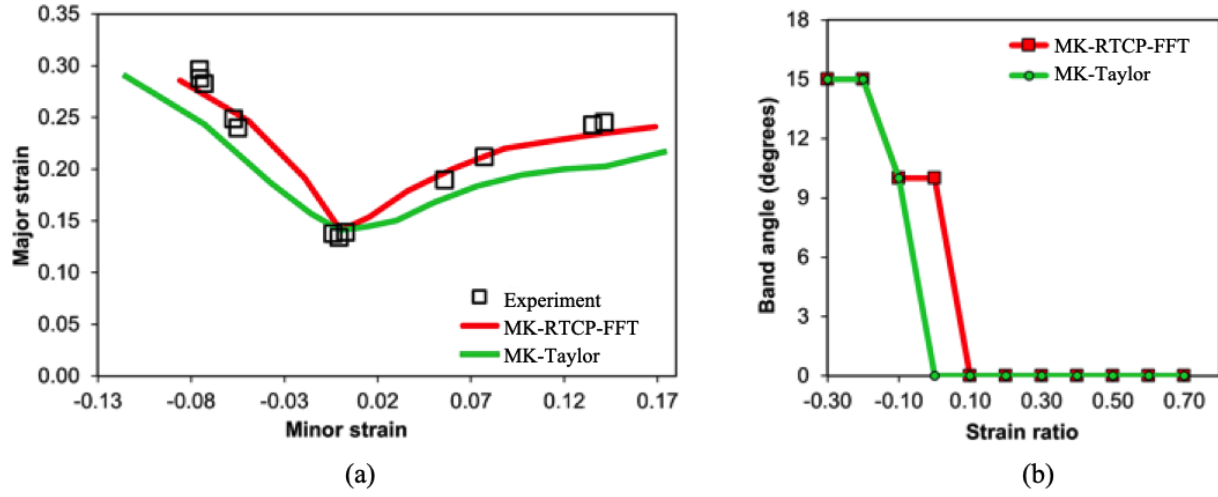


Figure 4.11: (a) Comparison of predicted FLDs for AA3003-O using MK-RTCP-FFT model and MK-Taylor model with experimental observations at 25 °C. (b) Comparison of evolution of imperfection band angle with strain ratio predicted using MK-RTCP-FFT model and MK-Taylor model.

4.4 Discussions

In the previous sections, the FLD predictions with the MK-RTCP-FFT model are presented for AA5754-O and AA3003-O sheet alloys. Since, the MK-RTCP-FFT model can account for the effects of 3D grain morphologies and interactions (neighborhood effect) on the predicted limit strains, it provides the unique capability to investigate the microstructural features that strongly influence the predicted forming limit strains. For this purpose, the AA3003-O sheet alloy is further studied. First, the effects of different grain morphologies (texture-based grain shapes) on the predicted FLDs are investigated in detail using three types of grain shapes; a) columnar, b) equiaxed, and c) elongated. Then the effects of grain interactions (neighborhood effect) and evolution of texture are further studied for each type of grain morphology.

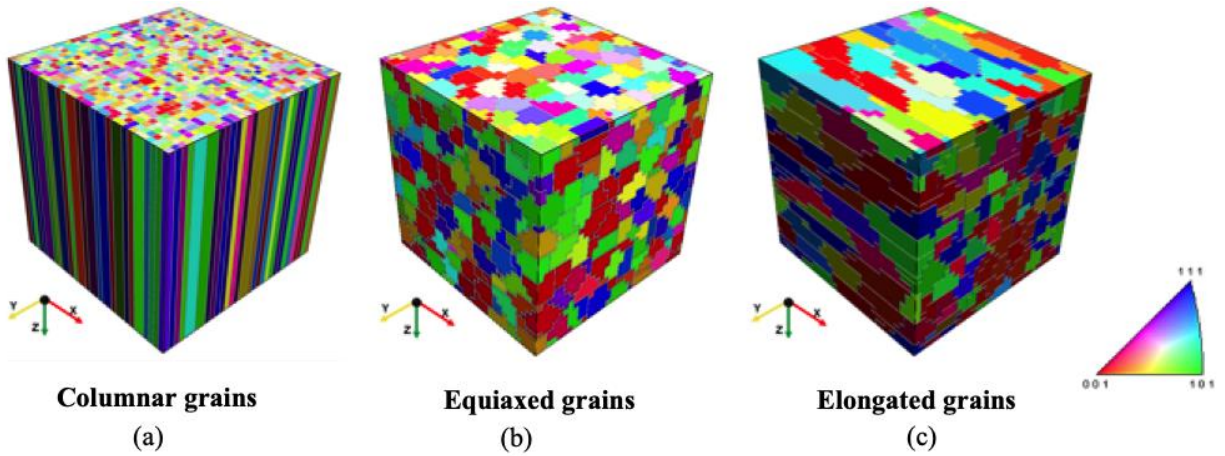


Figure 4.12: RVEs for model A, inverse pole figure maps showing initial texture distribution and grain morphology.

4.4.1 Effects of Grain Morphology on Localized Deformation

In this section, the effects of grain morphologies (in three dimensions) on the FLDs are investigated in detail. The inverse pole figure maps of three different RVEs with equiaxed grains, columnar grains and elongated grains are shown in Figure 4.12(a-c), respectively. The same RVE with equiaxed grains used in previous section is considered here for comparison with columnar and elongated grain structures. All three RVEs have 916 grains and a regular 64 x 64 x 64 Fourier grid along with the initial texture of AA3003-O.

For cases of equiaxed and elongated grains, the microstructures were generated by following a procedure as explained in Brahme et al. (2006) that minimizes the error of grain misorientations while assigning a triplet of Euler angles to a grain. To generate the columnar microstructure, first 916 voxels with randomly assigned orientations are created on a x-y plane using voronoi tessellation method and then this layer is extruded in z-direction. Collectively, these six RVEs (one inside band and one outside band for each type of grain morphology) are referred to as model ‘A’ here.

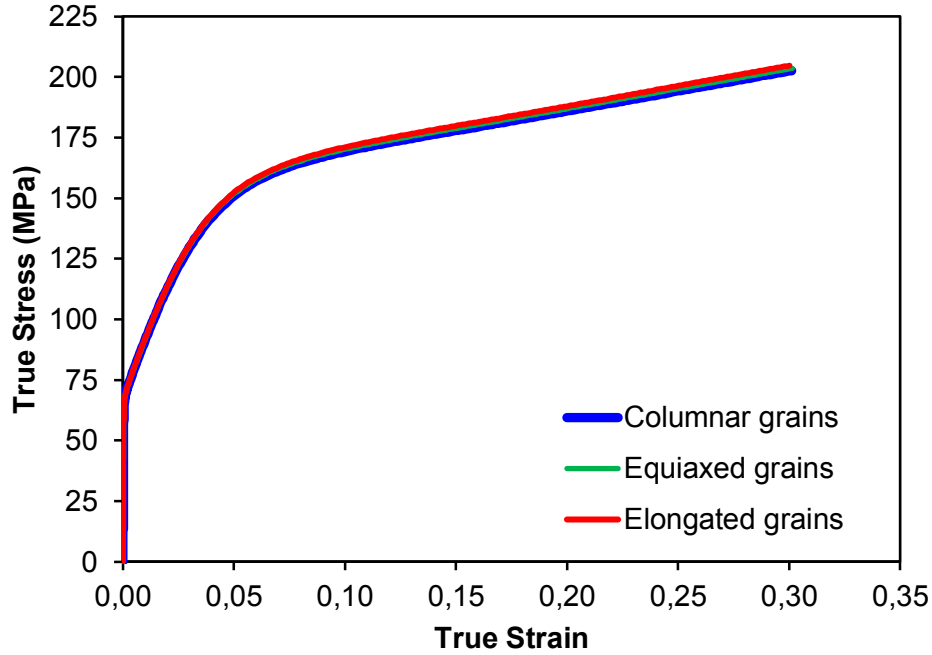


Figure 4.13: Comparison of overall stress-strain response of the RVEs for model A with columnar, equiaxed and elongated grain structure respectively under uniaxial tension along RD.

Then the MK-RTCP-FFT model is calibrated using uniaxial true stress-true strain experimental data. It should be noted that the average true stress-true strain response of each RVE of model A (Figure 4.13) is similar to response of the RVE with equiaxed grains as shown in Figure 4.10 for same material hardening parameters (Table 4.2). However, the local micromechanical fields vary significantly. To generate the FLDs using these three RVEs, first the in-plane plane strain point is fitted with the experimental data at 14.10% major strain (ϵ_{11}). Due to different grain shapes, different values of imperfection parameter, f , are required to fit the same in-plane plane strain point on FLD ($f = 0.9975$ for columnar grains; $f = 0.996$ for equiaxed grains and $f = 0.9958$ for elongated grains).

4.4.1.1 FLD Simulations with Different Grain Morphologies

The FLDs predicted from the model A microstructures are compared with experimental observations for AA3003-O (Figure 4.14). The results show significant differences in the predicted forming limit strains using different grain structures. The columnar grain structure shows a notable improvement in the predicted formability and significantly over predicts the FLD as compared to equiaxed grain structure (on both sides of the FLD). Finally, the elongated grain structure under

predicts the forming limit strains exhibiting a behavior close to predictions from the MK-Taylor model as shown in previous section. These significant differences in the predictions of FLDs are a direct result of the local partitioning of strains in the RVE. The different grain shapes lead to uneven subdivision of micromechanical fields inside the RVE. The causes are further investigated for the in-plane plane strain point ($\rho = 0$) where all the three RVEs (outside band) undergo the same average strain, i.e., $\varepsilon_{11} = 14.1\%$ (also same imperfection band angle) and thus, at this strain level their local strain partitioning can be compared. Signorelli et al. (2009) presented a study where they concluded that non-equiaxed grain morphology would lead to higher formability. The research presented in this chapter not only confirms this correlation between the grain morphology and forming limits but also investigates the underlying reasons for these correlations.

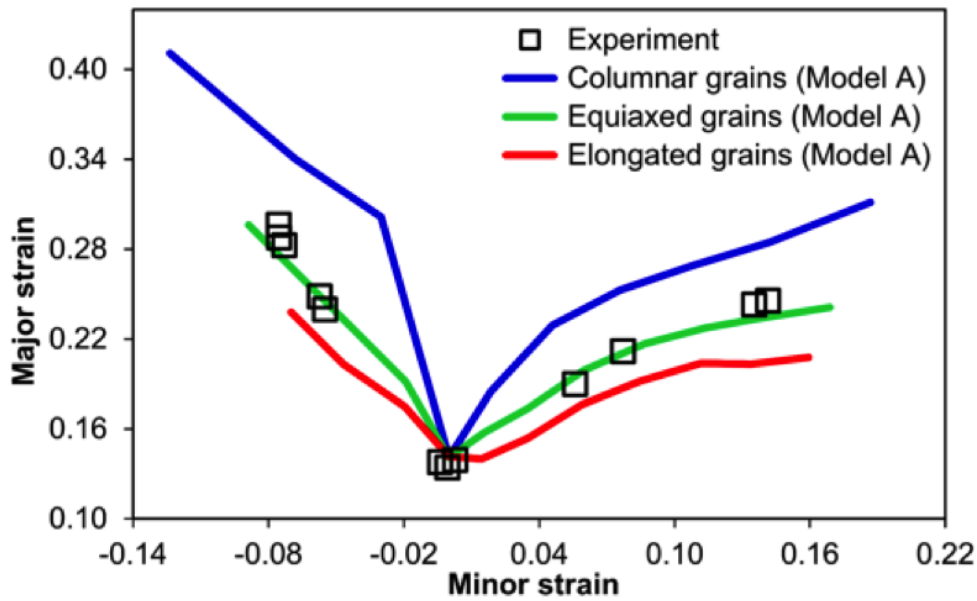


Figure 4.14: Comparison of predicted FLDs for using different grain morphologies (model A) with experimental observations.

4.4.1.2 Local Strain Partitioning

The equivalent local strains in the six RVEs for $\rho = 0$ obtained at the last time before reaching the limit strains are presented in Figure 4.15.

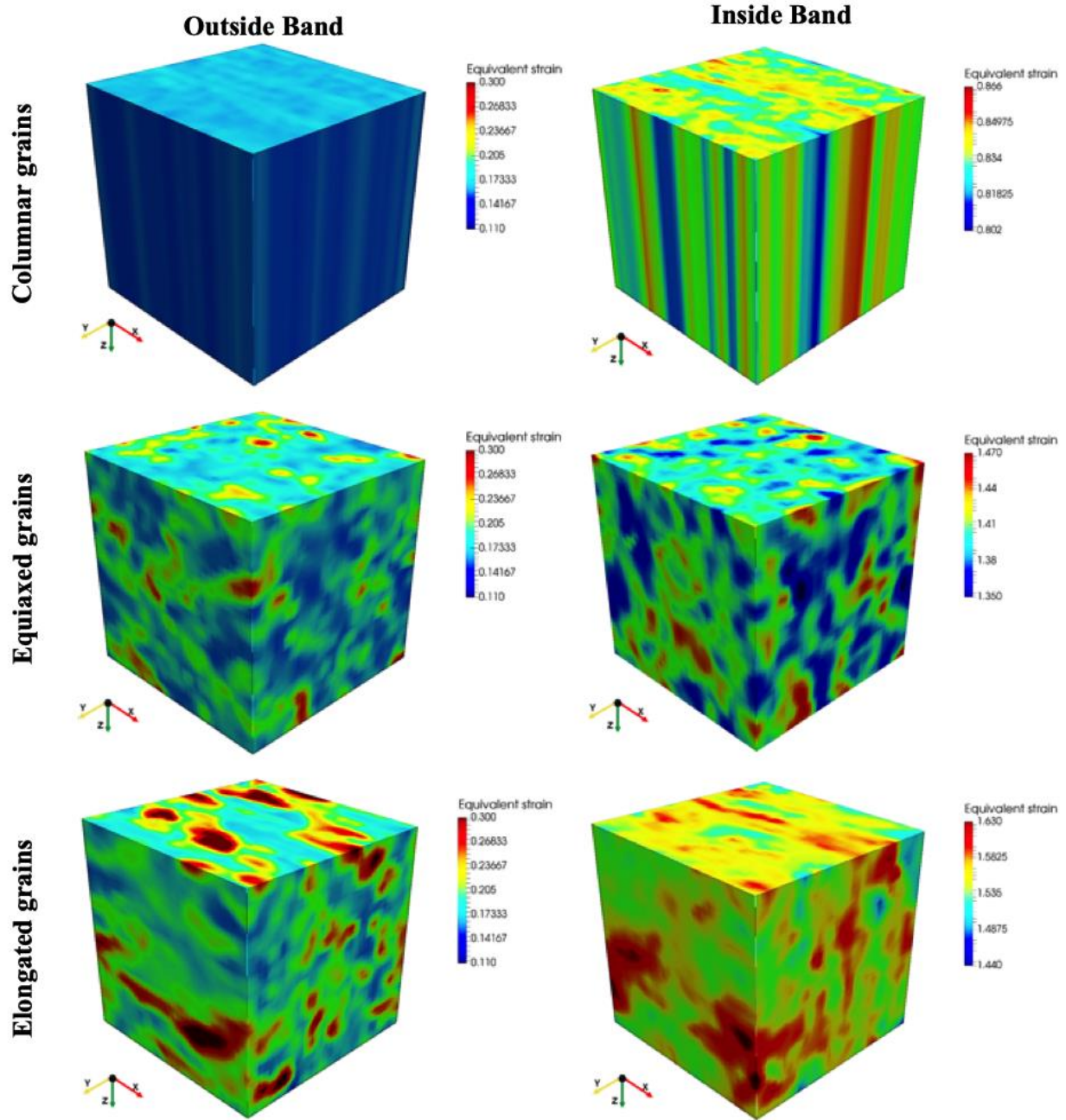


Figure 4.15: Results of in-plane plane strain tension: Distribution of equivalent strain on surface of RVEs inside and outside the imperfection band (columns) with different grain morphologies (rows).

In Figure 4.15, the distribution of local strains is shown for the RVEs inside the imperfection band as well as for RVEs outside the imperfection band for equiaxed, columnar and elongated grain structures, respectively. For outside the band region, the equivalent strain distribution in equiaxed, columnar and elongated grain structures were plotted on same scale and it is seen that at same

average strain (14.1%). Simulations show that variations in the local strains in the columnar grain structure is far less compared to the variations in the equiaxed and elongated grain structures, while the elongated grain structure shows highest local variations in strain as well as a greater number of hotspots of strains. Similar trends are seen in the RVEs inside the band.

However, since significant amount of strain is accumulated inside the imperfection band region, much more pronounced variations in local strain fields are seen among the different grain structures. To show location of hotspots properly, the equivalent strain inside the band are plotted at different scales for each RVE inside the band region. The maximum equivalent strain that occurs in the columnar grain structure is around 87%. On the contrary, very high amount (over 150%) of equivalent strain is accumulated in the cases of equiaxed and elongated grains. This can be directly correlated with the predicted FLDs; for each strain path, strain localization occurs faster in the elongated grains leading to lower limit strain predictions, while the columnar grain structure demonstrates delayed strain localization and thus, higher limit strain predictions.

4.4.1.3 Texture Evolution

Seven grains in each RVE (inside the band) are selected to analyze the effect of grain morphology on texture evolution. Figure 4.16 present the 001-inverse pole figure (IPF) for initial (blue) and final (orange) texture for selected grains. Initial texture of the selected grains is spread in the IPF space using the minimum misorientation between initial texture and IPF corners [001], [011] and [111]. The rotation of each voxel is tracked throughout the deformation and the final orientation of all voxels inside each grain is then averaged to obtain the final texture for the grain (Ali et al., 2016). For ease of comparison, the initial grains selected in each RVE (elongated, equiaxed and columnar grains) have similar orientations. This was done by finding the grains with the minimum misorientation between different RVEs (elongated, equiaxed and columnar grains).

As observed in the previous section for the case of local strain distribution, the trend for local texture evolution is also similar; the elongated grains experience highest rotation followed by equiaxed grains and columnar grains. For example, grains near [001] and [111] (Figure 4.16) show the highest rotation in elongated grains followed by equiaxed and columnar grains. This also demonstrates that elongated grains undergo more local deformation inside the band. While the analyses presented in Figure 4.16 might be informative it is not necessarily representative of the

complete microstructure since only seven discrete orientations (grains) are considered. Therefore, the average misorientation and maximum misorientation are presented in Figure 4.17. This is accomplished by tracking the texture evolution of each voxel in the microstructure and obtaining the misorientation between the initial and the deformed state. The same trends, as shown in Figure 4.16, are observed where the elongated grains undergo the highest average and maximum misorientation (Figure 4.17).

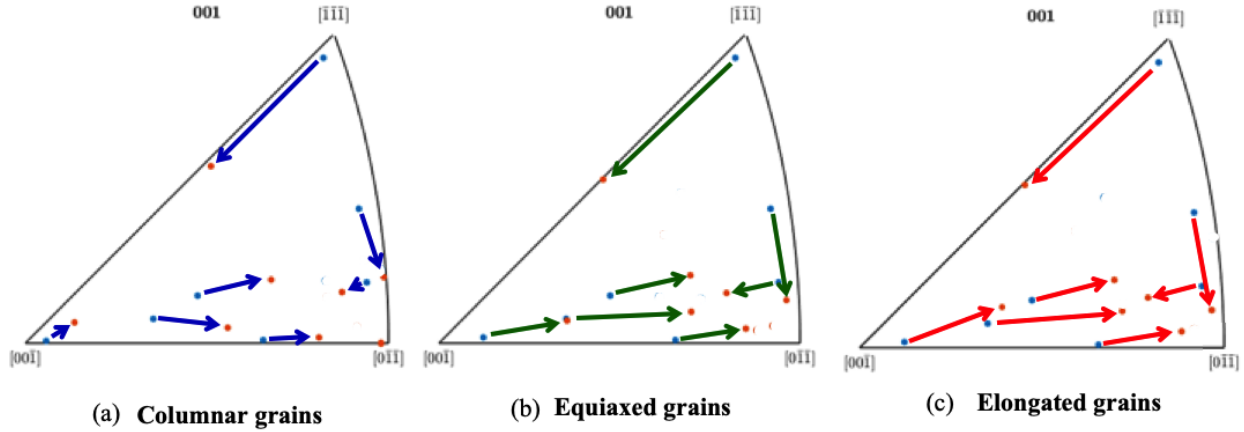


Figure 4.16: Inverse pole figures (IPFs) of selected 7 grains in (a) Columnar grains, (b) Equiaxed grains, (c) Elongated grains. Blue dot - initial texture, orange dot - deformed texture of grain in IPF after in-plane plane strain tension up to 14.1% true strain.

Figure 4.15. shows that for the three different RVEs studied (that all have the similar average initial texture as shown in Figure 4.9), for the same amount of applied strain, the localization patterns (location and intensity) are different. These differences in the localization patterns can be traced back to the amount of texture rotation in similarly oriented grains in the three RVEs (Figure 4.16). These observations combined with the results presented in Figure 4.16 indicate that for the same average strain, elongated grains experience the most local strains as they have the most average rotation.

Finally, the initial and deformed volume fractions of different texture components for columnar, equiaxed and elongated RVE are also calculated (Table 4.3). Simulations show that Cube, Goss and S decrease while Brass and Copper increase after deformation in each case. These trends agree with the observations presented in Wen and Lee (2000) for AA3003 sheets under plane strain tension. However, the percentage change of volume fractions of different texture components, for

each of the grain morphology studied, is different. This is closely linked to the local deformation of each Fourier point, which can be very different based on the grain morphology.

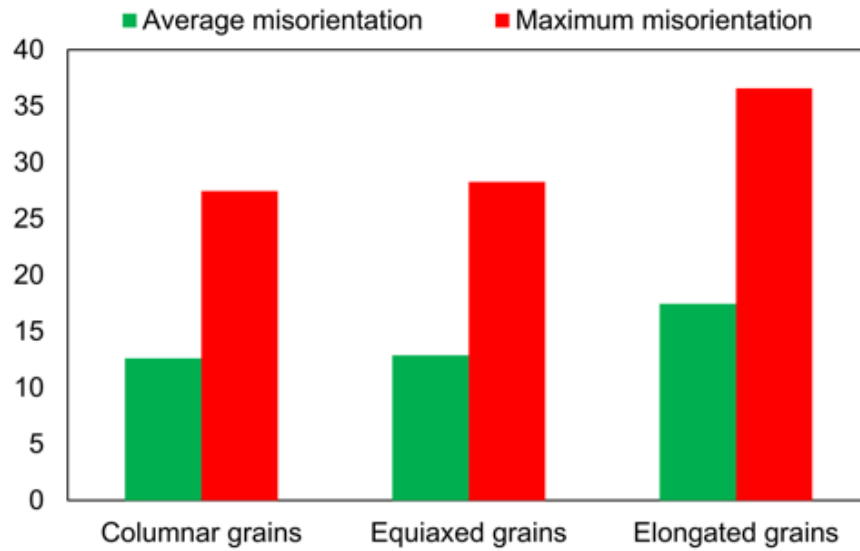


Figure 4.17: Comparison of predicted average and maximum misorientations for columnar grains, equiaxed grains, and Elongated grains after in-plane plane strain tension up to 14.1% true strain.

Table 4.3: Volume fraction of different texture components (within 15° from the exact component location); initial and after in-plane plane strain tension up to 14.1% true strain.

Texture component	Columnar grains			Equiaxed grains			Elongated grains		
	Initial	After	% change	Initial	After	% change	Initial	After	% change
Cube	4.5	3.0	-32.3	3.6	1.8	-48.3	3.9	1.4	-63.8
Goss	3.6	2.6	-26.5	4.0	2.3	-42.3	3.9	3.0	-23.6
Brass	4.0	6.6	65.4	4.2	6.6	55.8	4.4	6.7	54.0
Copper	2.5	3.1	23.3	2.7	4.3	57.2	2.8	4.8	74.0
S	1.8	1.2	-32.3	2.4	1.5	-39.4	1.7	1.5	-11.2

4.4.2 Effects of Local Grain Neighborhoods and Texture Evolution on FLDs

In the previous sections, it is demonstrated that the grain morphology strongly affects the FLD predictions. As a final study, a second set of microstructures for equiaxed, columnar and elongated grains are generated (model B). In this case, the grain structure inside the RVE is kept the same as of model A but the overall texture is shuffled; i.e., the same 916 independent grain orientations are now randomly assigned inside the RVE. This changes the local interactions of the grains as the grains now have different neighbors as compared to those in model A. Figure 4.18 shows the IPF maps of the RVEs of model B for equiaxed, columnar and elongated grain structures respectively. Furthermore, the effects of texture evolution on FLD predictions are also analyzed for each case.

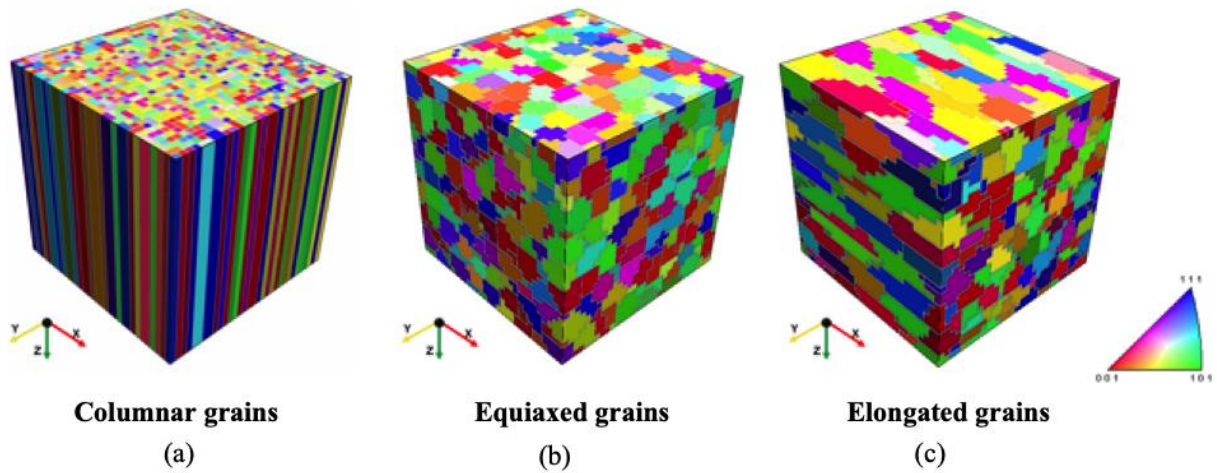


Figure 4.18: RVEs for model B, inverse pole figure maps showing initial texture distribution and grain morphology.

Using the same microstructures of model A, the texture evolution was turned off in the code and this set is referred to as model C. The MK-RTCP-FFT model is first calibrated for uniaxial tension and then the in-plane plane strain point on FLD is fitted for each case of model B and model C as well. Figure 4.19 shows the comparison of FLD predictions of models A, B and C for the RVEs with equiaxed grains, columnar grains and elongated grains respectively. These results show that the by changing the grain interactions (by shuffling texture or neglecting texture evolution), similar trends in predictions of forming limit strains are observed as compared to model A and a relatively narrow band of FLDs are obtained for each type of grain morphology.

The origin of the predicted different forming limits with the 3 RVEs studied in this work can be traced back to the fluctuations in micromechanical fields due to grain interactions & grain morphology. These fluctuations have significant effect on the anisotropy of plastic deformation (local strain partitioning) and texture evolution which, in turn plays an important role on the onset of necking and thus leading to different forming limit strains.

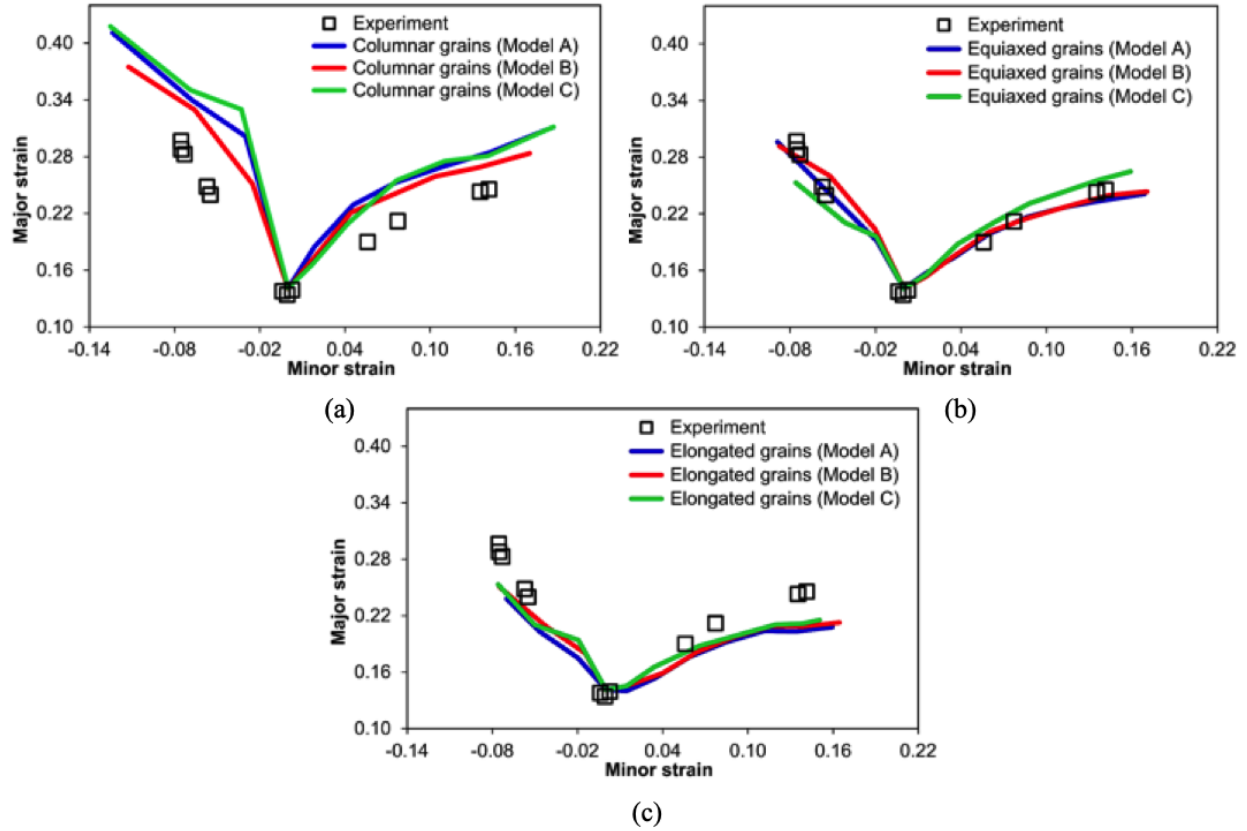


Figure 4.19: Comparison of predicted FLDs for models A, B and C; (a) columnar grains, (b) equiaxed grains, (c) elongated grains.

4.5 Summary

A rate tangent-fast Fourier transform-based elasto-viscoplastic crystal plasticity constitutive framework model was successfully implemented in a Marciniak-Kuczynski type analysis to predict the forming limit diagrams of FCC polycrystals. The proposed MK-RTCP-FFT model can account for the effects of three-dimensional grain morphologies, texture as well as the grain interactions on FLD predictions. The MK-RTCP-FFT was also employed to successfully predict

the FLD for AA3003-O and AA5754-O. The simulations presented in this research clearly demonstrated that among all microstructural features considered, the grain shapes (three-dimensional) had the most significant effect on the FLD predictions while the effects local grain neighborhoods and texture evolution both had relatively negligible effects. Furthermore, the effects of local grain neighborhoods and texture evolution on the predicted FLDs are all dependent on the initial grain morphologies.

Chapter 5. – Part 3: A New Micromechanics-Based Full-Field Numerical Framework to Simulate the Effects of Dynamic Recrystallization on the Formability of HCP Metals, submitted to International Journal of Plasticity

Jaspreet S. Nagra¹, Abhijit Brahme¹, Julie Lévesque², Raja Mishra³, Ricardo A. Lebensohn⁴,
Kaan Inal¹

¹ University of Waterloo, 200 University Ave. West, Waterloo, ON N2L 3G1, Canada

²Department of Mechanical Engineering, Laval University, Québec, Québec, G1V 0A6, Canada

³General Motors Research and Development Center, Warren, MI 48090, USA

⁴Los Alamos National Laboratory, MS G755, Los Alamos, NM 87845, USA

Abstract

This chapter presents a new full-field, efficient and mesh-free numerical framework to model microstructure evolution, dynamic recrystallization (DRX) and formability in hexagonal closed-packed (HCP) metals such as magnesium alloys at warm temperatures. A rate tangent-fast Fourier transform-based elasto-viscoplastic crystal plasticity constitutive model for HCP metals (RTCP-FFT-HCP) is coupled with a probabilistic cellular automata (CA) approach to model DRX (CA-DRX). Furthermore, this new model is coupled with the Marciniak-Kuczynski (M-K) approach to model formability of magnesium alloys at elevated temperatures. The RTCP-FFT-HCP model computes macro stress-strain, twinning volume fraction, micromechanical fields, texture evolution and local dislocation density. Nucleation of new grains and their subsequent growth is modeled using the cellular automata approach with probabilistic state switching rule. First, the proposed RTCP-FFT-HCP model is validated by comparing the simulated macro stress-strain responses

under uniaxial tension and compression with experimental measurements for AZ31 sheet alloy at room temperature. Furthermore, the texture evolution predicted with the new model is compared with experiments. Next, the forming limit diagrams (FLDs) are simulated at 100 °C, 200 °C and 300 °C respectively for AZ31 sheet alloy considering the effects of DRX. The predicted FLDs show very good agreement with the experimental measurements. The study reveals that the DRX strongly affects the deformed grain structure, grain size and texture evolution and also highlights the importance accounting for DRX during FLD simulations at high temperatures.

Keywords: Crystal plasticity-FFT, Dynamic recrystallization, Forming limit diagram, 3D microstructure, M-K model, Warm forming

5.1 Introduction

Magnesium alloys are getting significant attention by the transportation industry due to their light weight and high specific strength. However, the low formability at room temperature raises challenges to manufacture magnesium alloy components to desirable shapes for widespread usage (Bohlen et al., 2007). At room temperature, the low number of active slip systems (that accommodate plastic deformation), is believed to be one of the reasons for the poor formability of magnesium alloy sheets, e.g., AZ31 (Zhang et al., 2006; Chino et al., 2007; Wang et al., 2013). In addition to the crystallographic slip, the deformation twinning also plays an important role in the deformation behavior of magnesium alloys (Yang et al., 2008; Abdolvand and Daymond, 2012; Abdolvand et al., 2015; Lentz et al., 2016). Magnesium alloys have a total of twenty-four slip systems with eighteen primary slip systems and six twinning systems. Only four slip systems are active due to low critical resolved shear stress (CRSS) for basal and prismatic systems compared to those of other slip systems (i.e., pyramidal I and pyramidal II) at room temperature. Since the rolled magnesium alloy sheets possess a strong basal texture, therefore, it is difficult to reduce their thickness by the activation of the basal and prismatic slip systems alone (Yoshida, 2015).

Warm forming (i.e., up to 300 °C) of magnesium alloys leads to the activation of different deformation mechanisms, additional slip systems as well as grain boundary sliding, thus improving the formability (Nieh et al., 1998; Galiyev et al., 2001; Martin and Jonas, 2010). The elevated temperature processing is inevitably associated with the dynamic recrystallization (DRX) driven

by the stored energy of the material in the form of dislocations. Like any recrystallization process, the DRX proceeds by (a) nucleation of a new grain and (b) growth of a new grain at the expense of the deformed matrix (Rollett et al., 2004). The dislocation content evolves with strain in both the matrix and recrystallized region during the DRX. Experimental data shows that the nucleation is the slowest process and, therefore, the rate controlling one in magnesium alloys (Sivakesavam et al., 1993). The dislocation content in a material varies with the type of deformation mechanisms and processing temperature. At elevated temperatures, numerous plastic deformation mechanisms are operative in magnesium alloys. The active deformation mechanisms include basal, prismatic and pyramidal slip (1st and 2nd order), cross-slip, dislocation climb and twinning. Each deformation mechanism makes its own contribution to nucleation and grain growth process resulting in different recrystallization mechanisms operating under different conditions (Nieh et al., 1998; Galiyev et al., 2001; Martin and Jonas, 2010).

The DRX mechanisms are classified broadly into three types in magnesium alloys. (a) Continuous DRX (CDRX), which includes a gradual transformation of low angle grain boundaries (LAGBs) into high-angle grain boundaries (HAGBs) upon straining. New grains are formed progressively within the deformed grains by the continuous increase in misorientation across deformation-induced boundaries (Sivakesavam et al., 1993; Rollett et al., 2004; Xia et al., 2005; Beer and Barnett, 2007) (b) Discontinuous DRX (DDRX) involves the development of HAGBs via nucleation and growth of new grains. Nuclei form on original HAGBs due to the operation of a bulging mechanism which then grow and consume the deformed matrix resulting in decreased dislocation density, thus softening the material and increasing ductility. The above mechanism involves the development of high-angle grain boundaries via the nucleation and growth of new grains. It is closely related to the strain induced migration of initial boundaries (Beer and Barnett, 2007; Kaibyshev, 2012). DDRX generally occurs in materials with relatively low stacking fault energies (Rollett et al., 2004; Beer and Barnett, 2007; Kaibyshev, 2012). (c) DRX associated with twinning (TDRX), in which twinning leads to the formation of coarse lamellae surrounded by special grain boundaries (Muránsky et al., 2008). There are at least three processes by which TDRX can occur: mutual intersection of primary twins, the occurrence of secondary twinning within the primary twinning, and coarse twin lamellae can be subdivided by deformation induced LAGBs that transform into HAGBs upon further straining and provide chains of DRX grains

(Kaibyshev, 2012). Out of the three DRX mechanisms explained above, DDRX is characterized by absorption of significant amount of lattice dislocations by migrating HAGBs (Beer and Barnett, 2007).

Numerical models, especially based on crystal plasticity theory, serve as powerful and efficient tools since they can dramatically improve strategies for part optimization and can reduce the time-to-market by enabling ‘virtual laboratory’ of manufacturing processes. However, accurate modelling requires physics-based microstructural models that account for temperature dependent material properties, physical deformation mechanisms, the gradual evolution of microstructure and texture. In past decade, the crystal plasticity modelling of magnesium alloys with crystallographic slip being the primary deformation mechanism has been successfully used to model large deformation during finite plastic straining (Balasubramanian and Anand, 2002). However, it is well known that the deformation of magnesium alloys at low temperatures typically occurs by crystallographic slip accompanied by deformation twinning simultaneously (Kelley and Hosford, 1968). Van Houtte (1978) proposed the first model for modelling twinning in HCP polycrystals that considered the evolution of the volume fractions of the twinned regions in the grains. Later, Kalidindi, (1998) proposed a new model where the twinning was modeled as a pseudo-slip deformation mechanism and the parent-to-twin relationship was preserved in the entire deformation.

Various numerical modelling approaches, i.e., Taylor type, viscoplastic self-consistent (VPSC), finite elements-based crystal plasticity frameworks (CP-FEM) and the crystal plasticity fast-Fourier transform (CP-FFT), have been used to study deformation in magnesium and its alloys (Proust et al. 2009; Biswas et al., 2011; Wang et al., 2011; Jain et al., 2012; Oppedal et al., 2012; Steglich et al., 2012; Izadbakhsh et al., 2012; Chen et al., 2015; Popova et al., 2015; Qiao et al., 2016, Levesque et al. 2010, 2016). All these models have provided good predictions of texture evolution and macroscopic stress-strain curves. Abdolvand and Daymond (2012) evaluated several twin-parent interaction models to study the internal strains and the texture evolution during twinning for magnesium and zirconium alloys. They compared the model results with neutron diffraction measurements and concluded that the PTR (predominant twin reorientation) scheme provided better results for texture prediction and internal strains.

The concept of forming limit diagram (FLD) was first introduced by Keeler (1961). Since obtaining the FLDs experimentally is expensive and complex, several analytical and numerical methods have been developed to calculate FLDs. The so-called M-K approach, presented by Marciniak and Kuczyński (1967), is based on the presence of a thickness imperfection in an infinite sheet. By increasing the applied load, strain level in the imperfection zone increases and the sheet fails accordingly due to rapid thinning. The M-K approach has been employed successfully in many applications where FLDs were accurately predicted for various metals. Inal et al. (2005) used a rate-sensitive polycrystal plasticity model with the full constraint Taylor type homogenization scheme (FC-Taylor) to explain the differences in the formability of body-centered cubic (BCC) polycrystal and FCC polycrystals. Inal et al. (2005) reported that the number of slip systems strongly affects the occurrence of localized necking in a polycrystalline material, while Izadbakhsh et al. (2011) presented a numerical study to investigate the contribution of the various deformation mechanisms to the formability in magnesium single crystals. Recently, Nagra et al. (2018) extended the rate-tangent-crystal plasticity-fast Fourier (RTCP-FFT) framework developed by Nagra et al. (2017) to model formability of aluminum alloys using the M-K approach. They reported that among various microstructural features, the grain morphology strongly influences the forming limit strain predictions in aluminum alloys. To calculate FLDs for HCP polycrystals, Lévesque et al. (2010, 2016) have employed the M-K approach in a Taylor type polycrystal model. They presented a parametric study to explain the effects of crystallographic slip and twinning on the formability of magnesium alloys.

It is well-known that, along with crystallographic slip and mechanical twinning, the dynamic recrystallization (DRX) during processing at elevated temperatures also plays an important role on the formability of magnesium alloys (Samuha et al., 2018). However, modelling of DRX phenomenon is still a challenging problem. This is due to multi-scale nature of DRX phenomenon, which involves the effects of impurities, precipitation, dislocation motion, movement of the high angle grain boundaries etc. (Pond and Casey, 1992). Accordingly, there are several approaches in literature to model dynamic recrystallization in magnesium alloys. These approaches can be classified mainly into Monte-Carlo (MC), Cellular Automata (CA) and Phase Field (PF) methods. Monte-Carlo-based models simulate the microstructure evolution during DRX and can produce many features of the DRX process (Rollett et al., 1992; Peczak, 1995). However, these models are

unable to describe grain growth kinetics because of the lack of physical length and time scale. The phase field-based methods are powerful tools but they are computationally expensive models with focus on a continuous description of grain boundary. The CA method is based on the distinct cells with state variables that define the cell. An initial state is assigned to represent the microstructure. Switching the state of the cell defines the kinetics of CA and the switching of the state of the cell depends on its previous state as well as the state of the neighboring cell (Miodownik, 2002). The CA method is able to capture the local effects and is computationally efficient (Hallberg, 2011). However, the CA methods alone lack the ability to predict microstructure evolution during deformation. Therefore, coupling the CA approach with crystal plasticity-based finite element modelling (CP-FEM) has been shown to be an effective tool for modelling recrystallization. For instance, Popova et al. (2015) investigated the DRX in magnesium alloys using the coupled CA-CP-FEM framework for 2D microstructures. Popova et al. (2016) extended this model to study the effects of twinning on texture evolution at elevated temperature deformation accompanied by the DRX.

While the crystal plasticity-based modelling techniques discussed above are able model to various deformation phenomena in magnesium alloys, there is a lack of a single framework that can model the effects of DRX on the formability of magnesium alloys at elevated temperatures. The difficulty lies in proper modelling procedure of DRX phenomenon and the computational cost to generate forming limit strains for 3D microstructure. In this research, a new full-field numerical framework that can account for; (i) the full richness of the 3D microstructure (e.g., texture, grain morphologies, grain interactions, etc.) and (ii) the effects of DRX on micro/macro behavior is presented. Furthermore, this new full field numerical framework is incorporated in to an M-K type analysis to predict the formability of magnesium alloys at elevated temperatures.

In Section 5.2, the details of the proposed framework are presented while the proposed RTCP-FFT-HCP model is validated by comparing the predicted macroscopic (stress-strain) and microscopic (texture evolution) responses under uniaxial tension and compression with experimental measurements for AZ31 sheet alloy at room temperature in Section 5.5.2. Finally, the forming limit diagrams (FLDs) are predicted at 100 °C, 200 °C and 300 °C, respectively, considering the effects of DRX and without DRX. The predicted FLDs are then compared with experimental observations in Section 5.5.4.

5.2 Model Description

The well-known framework of Asaro and Needleman (Asaro and Needleman, 1985), that was modified by Kalidindi, (1998) and Lévesque et al. (2010, 2016) to incorporate deformation twinning is employed in the proposed framework. Lévesque et al. (2010, 2016) employed a crystal plasticity constitutive model for HCP metals based on the so-called Taylor-type homogenization scheme. This model was then implemented in to an M-K framework to predict the formability of various magnesium alloys. However, in order to model the dynamic recrystallization (DRX), there is a need of full-field model that accounts for the neighbourhood effects of the grains as well as the local strain partitioning. While finite element models can accurately provide the local strain partitioning, they would be extremely demanding in terms of CPU to compute the FLDs. Accordingly, the crystal plasticity constitute model for HCP materials is implemented into the rate tangent crystal plasticity-fast Fourier transform (RTCP-FFT) framework developed by (Nagra et al., 2017, 2018). The new numerical framework is then coupled with a cellular automata (CA) model and the M-K approach to investigate the formability of magnesium alloys at elevated temperatures.

In this section, first, the details of proposed rate tangent-crystal plasticity fast Fourier transform model for HCP alloys (RTCP-FFT-HCP) are presented. Then, the DRX model is explained followed by a brief overview of M-K method. An overall flowchart of the coupled framework is also presented.

5.2.1 Rate Tangent-Crystal Plasticity Fast Fourier Transform Model for HCP alloys (RTCP-FFT-HCP)

5.2.1.1 Constitutive Equations

The crystal plasticity formulation employed in this research is based on elastic-viscoplastic crystal plasticity. The constitutive model can account for both crystallographic slip and deformation twinning where a pseudo-slip approach is adopted for deformation twinning. More details of this constitutive formulation can be found in Levesque et al. (2010, 2016). Accordingly, the total deformation gradient \mathbf{F} is written as following

$$\mathbf{F} = \mathbf{F}^* \mathbf{F}^P \quad (5.1)$$

where \mathbf{F}^P consists of both part of deformation from crystallographic slip and twinning. \mathbf{F}^* embodies elastic deformation and rigid body rotations of crystal lattice. Note that, for simplicity, index notation and tensor notation are used interchangeably in this chapter.

Table 5.1: Slip and twinning systems used in proposed framework.

Slip systems	$\{0001\} \langle 1\bar{2}10 \rangle$	Basal
	$\{10\bar{1}0\} \langle 1\bar{2}10 \rangle$	Prismatic
	$\{1\bar{1}01\} \langle 11\bar{2}0 \rangle$	Pyramidal $\langle a \rangle$ - I
	$\{1\bar{2}12\} \langle 1\bar{2}1\bar{3} \rangle$	Pyramidal $\langle c+a \rangle$ - II
Twinning systems	$\{10\bar{1}2\} \langle \bar{1}011 \rangle$	Extension
	$\{1\bar{1}01\} \langle \bar{1}102 \rangle$	Contraction

The spatial velocity gradient \mathbf{L} in the current configuration is written as sum of its elastic and plastic parts as

$$\mathbf{L} = \mathbf{L}^* + \mathbf{L}^P = \dot{\mathbf{F}} \mathbf{F}^{-1} \quad (5.2)$$

where $\mathbf{L}^P = \mathbf{F}^* (\dot{\mathbf{F}}^P \mathbf{F}^{P^{-1}}) \mathbf{F}^{*-1}$ is the plastic velocity gradient in the intermediate or relaxed configuration.

The list of the active slip and twinning systems for magnesium alloys are summarized in Table 5.1. It is assumed that a crystal behaves as an elasto-viscoplastic solid in which the slip and twinning rates follow a power-law according to Hutchinson (1976). Thus, the slip rate on slip system α in the parent matrix region and the slip rate in twinned region, respectively, are given by

$$\dot{\gamma}_{sl}^{(\alpha)} = \dot{\gamma}_{sl}^0 \text{sgn } \tau_{sl}^{(\alpha)} \left| \frac{\tau_{sl}^{(\alpha)}}{g_{sl}^{(\alpha)}} \right|^{1/m} \quad (5.3)$$

$$\dot{\gamma}_{tw-sl}^{(\alpha)tw(\beta)} = \dot{\gamma}_{sl}^0 \text{sgn } \tau_{tw-sl}^{(\alpha)tw(\beta)} \left| \frac{\tau_{tw-sl}^{(\alpha)tw(\beta)}}{g_{tw-sl}^{(\alpha)tw(\beta)}} \right|^{1/m} \quad (5.4)$$

Accordingly, the rate of twinning on the twinning system β is defined as

$$\dot{f}_{tw}^{(\beta)} = \frac{\dot{f}_{tw}^0}{\gamma^{tw}} \left| \frac{\tau_{tw}^{(\beta)}}{g_{tw}^{(\beta)}} \right|^{1/m} \quad (5.5)$$

where $\dot{\gamma}_{sl}^0$ and \dot{f}_{tw}^0 are the reference shear and twinning rates. They are considered the same for all the slip and twinning systems. In addition, m is the strain-rate sensitivity index, $\tau_{sl}^{(\alpha)}$ is the resolved shear stress on the slip system α in parent matrix and $g_{sl}^{(\alpha)}$ is its hardness, $\tau_{tw-sl}^{(\alpha)tw(\beta)}$ is the resolved shear stress on the reoriented slip systems in twinned region and $g_{tw-sl}^{(\alpha)tw(\beta)}$ is its hardness and $\tau_{tw}^{(\beta)}$ is the resolved shear stress on the twin system β and $g_{tw}^{(\beta)}$ is its hardness.

5.2.1.2 Hardening Law

Hardening laws for the slip systems in matrix, slip systems in twinned region and the twinning systems, respectively, are defined as the rate of increase of the functions $g_{sl}^{(\alpha)}$, $g_{tw-sl}^{(\alpha)tw(\beta)}$ and $g_{tw}^{(\beta)}$, so that;

$$\dot{g}_{sl}^{(\alpha)} = \sum_{\beta} \mathbf{h}_{sl}^{(\alpha\beta)} |\dot{\gamma}_{sl}^{(\alpha)}| \quad (5.6)$$

$$\dot{g}_{tw-sl}^{(\alpha)tw\beta} = \sum_{\beta} \mathbf{h}_{tw-sl}^{(\alpha\beta)} |\dot{\gamma}_{tw-sl}^{(\alpha)tw(\beta)}| \quad (5.7)$$

$$\dot{g}_{tw}^{(\alpha)} = \sum_{\beta} \mathbf{h}_{(\alpha\beta)tw} |\dot{f}_{tw}^{(\beta)}| \quad (5.8)$$

where $\mathbf{h}_{sl}^{(\alpha\beta)}$, $\mathbf{h}_{tw-sl}^{(\alpha\beta)}$ and $\mathbf{h}_{tw}^{(\alpha\beta)}$ are the hardening moduli of the slip systems in matrix, slip systems in twinned region and the twinning systems, respectively. The hardening moduli employed in this study is similar to the work previously presented by Peirce et al. (1983) and Asaro and Needleman (1984),

$$\mathbf{h}_{sl}^{(\alpha\beta)} = \mathbf{q}^{(\alpha\beta)} \mathbf{h}_{sl}^{(\alpha)} \text{ (no sum on } \beta \text{)} \quad (5.9)$$

$$\mathbf{h}_{tw-sl}^{(\alpha\beta)} = \mathbf{q}^{(\alpha\beta)} \mathbf{h}_{tw-sl}^{(\alpha)tw(\beta)} \text{ (no sum on } \beta \text{)} \quad (5.10)$$

$$\mathbf{h}_{tw}^{(\alpha\beta)} = \mathbf{q}^{(\alpha\beta)} \mathbf{h}_{tw}^{(\beta)} \text{ (no sum on } \beta \text{)} \quad (5.11)$$

where $\mathbf{q}^{(\alpha\beta)}$ matrix describes the latent hardening of the crystallite. $\mathbf{h}_{sl}^{(\alpha)}$, $\mathbf{h}_{tw-sl}^{(\alpha)tw(\beta)}$ and $\mathbf{h}_{tw}^{(\beta)}$ are the single slip hardening. In this study, all latent hardening parameters $\mathbf{q}^{(\alpha\beta)}$ are set to one. The hardness of the slip and the twinning systems is represented by a power-law equation;

$$\mathbf{h}_{sl}^{(\alpha)} = \mathbf{h}_{sl}^0 \left[\frac{\mathbf{h}_{sl}^0 \gamma_{sl}^{(\alpha)}}{\tau_{0sl} n} + 1 \right]^{n-1} \quad (5.12)$$

$$\mathbf{h}_{tw-sl}^{(\alpha)tw(\beta)} = \mathbf{h}_{tw-sl}^0 \left[\frac{\mathbf{h}_{tw-sl}^0 \gamma_{tw-sl}^{(\alpha)tw(\beta)}}{\tau_{0tw-sl} n} + 1 \right]^{n-1} + \mathbf{h}_1 \quad (5.13)$$

$$\mathbf{h}_{tw}^{(\beta)} = \mathbf{h}_{tw}^0 \left[\frac{\mathbf{h}_{tw}^0 f_{tw}^{(\beta)}}{\tau_{0tw} n} + 1 \right]^{n-1} \quad (5.14)$$

where \mathbf{h}_{sl}^0 , \mathbf{h}_{tw-sl}^0 and \mathbf{h}_{tw}^0 are the initial hardness of the slip systems in matrix, slip systems in twinned region and the twinning systems, respectively. Accordingly, $\gamma_{sl}^{(\alpha)}$, $\gamma_{tw-sl}^{(\alpha)tw(\beta)}$ and $f_{tw}^{(\beta)}$ represent the sum of the accumulated slip and twin on all the slip systems in matrix, slip systems in twinned region and the twinning systems, respectively and n is the hardening exponent. In addition, a term that accounts for the hardening caused by the twin boundaries is also incorporated

in the formulation (h_1). This term enables to constitutive model to restrict dislocation motion. The increase of the volumetric fraction of the twins leads to the density of twin boundaries to increase. However, as twinning continues, the twins merge; thus, the twin boundaries disappear and the density of twin boundaries decreases. In other words, the parameter h_1 grows until the density of the twin boundaries within a grain reaches its highest value and then decreases. Thus;

If $\sum_{\beta} f^{\beta} \leq \zeta$ then

$$h_1 = h_{TB} \left(1 - \left| \frac{\zeta - \sum_{\beta} f^{\beta}}{\zeta} \right| \right)^e \quad (5.15)$$

If $\sum_{\beta} f^{\beta} > \zeta$ then

$$h_1 = h_{TB} \left(1 - \left| \frac{\zeta - \sum_{\beta} f^{\beta}}{1 - \zeta} \right| \right)^e \quad (5.16)$$

where ζ is the volume fraction of twins associated with the maximum twin boundary density and h_{TB} is a parameter corresponding to the effect of twin boundaries on the hardening of the slip systems. It has been experimentally observed that the volume fraction of twinned regions in many magnesium alloys reaches a maximum of 0.8 (Rémy, 1981; Kalidindi, 1998; Fernández et al., 2011). Thus, the value of ζ is taken as 0.8 in the present work.

5.2.1.3 Update of Shear Strain and Stress

At time t , the shear strain in the parent matrix, is updated as

$$\gamma_{sl}^{(\alpha)} = \dot{\gamma}_{sl,t-1}^{(\alpha)} + \sum_{\alpha} |\dot{\gamma}_{sl}^{(\alpha)}| \Delta t \quad (5.17)$$

whereas in the twinned region, it takes the form

$$\gamma_{\text{tw-sl}}^{(\alpha)\text{tw}(\beta)} = \sum_{\alpha} \left| \dot{\gamma}_{\text{tw-sl}}^{(\alpha)\text{tw}(\beta)} \right| \Delta t + \frac{f_{t-1}^{\beta}}{f^{\beta}} \gamma_{\text{tw-sl}}^{(\alpha)\text{tw}(\beta)} + c \frac{(f^{\beta} - f_{t-1}^{\beta})}{f^{\beta}} \gamma_{\text{tw-sl}}^{(\alpha)\text{tw}(\beta)} \quad (5.18)$$

where the coefficient c is the fraction of slip that is kept in the parent matrix when they twin. Since the slip systems are reoriented during twinning, this is a simplified way to account for the fact that they are not restored.

The increment in stresses in the matrix and the β -twinned region of the material point are calculated using the co-rotational Jaumann rate of the Cauchy stress as

$$\Delta \boldsymbol{\sigma}^{\text{mt}} = \mathbf{C}^{\text{tan}^{\text{mt}}} : \mathbf{D} - \dot{\boldsymbol{\sigma}}_0^{\text{mt}} + \boldsymbol{\Omega} \boldsymbol{\sigma} - \boldsymbol{\sigma} \boldsymbol{\Omega} - \boldsymbol{\sigma} \text{tr} \mathbf{D} \quad (5.19)$$

$$\Delta \boldsymbol{\sigma}^{\text{tw}\beta} = \mathbf{C}^{\text{tan}^{\text{tw}\beta}} : \mathbf{D} - \dot{\boldsymbol{\sigma}}_0^{\text{tw}\beta} + \boldsymbol{\Omega} \boldsymbol{\sigma} - \boldsymbol{\sigma} \boldsymbol{\Omega} - \boldsymbol{\sigma} \text{tr} \mathbf{D} \quad (5.20)$$

where $\mathbf{C}^{\text{tan}^{\text{mt}}}$ and $\mathbf{C}^{\text{tan}^{\text{tw}\beta}}$ are the elasto-viscoplastic tangent moduli for the matrix and twinned regions, respectively. These are calculated using the rate tangent integration scheme. More details of the rate tangent integration scheme can be found in Pierce et al. (1983) and Nagra et al. (2017). Using Equations (7.19) and (7.20), the stresses at time t are updated by the following equations

$$\boldsymbol{\sigma}^{\text{mt}} = \boldsymbol{\sigma}_{t-1}^{\text{mt}} + \Delta \boldsymbol{\sigma}^{\text{mt}} \quad (5.21)$$

$$\boldsymbol{\sigma}^{\text{tw}\beta} = \frac{f_{t-1}^{\beta} \boldsymbol{\sigma}_{t-1}^{\text{tw}\beta} + f_t^{\beta} \Delta \boldsymbol{\sigma}^{\text{tw}\beta} + \Delta f^{\beta} \boldsymbol{\sigma}_{t-1}^{\text{mt}}}{f_t^{\beta}} \quad (5.22)$$

By averaging the stresses in the twinned and un-twinned parts of the grain, the total Cauchy stress $\boldsymbol{\sigma}$ for the material point at time t is written as follows

$$\boldsymbol{\sigma} = \left(1 - \sum_{\beta=1}^{N^{tw}} f^{\beta}\right) \Delta \boldsymbol{\sigma}^{mt} + \sum_{\beta=1}^{N^{tw}} (f^{\beta} \Delta \boldsymbol{\sigma}^{tw\beta}) \quad (5.23)$$

Note that, in the proposed framework, all twin variants are considered active at all time, even in cases where their twinning rate is equal to zero. Using the matrix stress as the stress of the additional twinned fraction ensures that the twins do not possess abnormal value of stress, in cases where they become active later in the simulation, due to rotation of the parent grain or change in the stress state.

5.2.1.4 Stress Equilibrium and Microstructural Heterogeneity

The model presented in this study obtains the solutions for a 3D heterogeneous volume element chosen to be statistically representative of the microstructure of a given HCP material. The proposed model is based on the assumption that the heterogeneity of a crystalline material can be modeled using the convolution integrals between Green functions associated with the local response of an equivalent linear reference medium with polarization field and Eigen strains. In the conventional FFT-based methods, the polarization field is unknown apriori and the non-linear constitutive equations result in high mechanical contrast that results in diverging solutions of micromechanical fields at large strain. However, in the proposed RTCP-FFT model, the numerical analysis employs the rate tangent method with a semi-explicit integration scheme to obtain the heterogenous micromechanical fields using the rate form of the elasto-viscoplastic constitutive equations. Furthermore, the FFT method is used satisfy the quasi-static linear momentum balance condition, i.e., $\nabla \cdot \boldsymbol{\sigma} = 0$, for each discrete material point. Details of an analogous formulation for face-centered cubic (FCC) polycrystals are presented in Nagra et al. (2017).

In the simulations, periodic boundary conditions are applied to enforce mechanical equilibrium within the RVE in order to link the micromechanical fields to the effective material behavior at the macroscale. To predict the evolution of micromechanical fields and intragranular texture during deformation, the space resolved configuration of the grid points and the grain interactions must be considered in the whole RVE. The proposed numerical approach requires a regular Fourier grid $\{\mathbf{x}_k\}$, i.e., defined as

$$\{\mathbf{x}_k\} = \left\{ \left((i_1 - 1) \frac{L_1}{N_1}, (i_2 - 1) \frac{L_2}{N_2}, (i_3 - 1) \frac{L_3}{N_3} \right); i_k = 1, \dots, N_k, k = 1, 2, 3 \right\} \quad (5.24)$$

where, L_k is the length of the grid and N_k is the number of Fourier points in each direction, k . In proposed numerical approach, each grid point represents a voxel inside a grain and to consider the interaction of each grid point with all the other points in the RVE, the following problem for heterogeneous RVE needs to be solved at each grid point to obtain micromechanical fields, written as follows

$$\begin{cases} \boldsymbol{\sigma} = \mathbf{C}^{\text{tan}} : \boldsymbol{\varepsilon} \\ \nabla \cdot \boldsymbol{\sigma} = 0 \\ \text{Periodic boundary conditions across RVE} \end{cases} \quad (5.25)$$

where, $\boldsymbol{\varepsilon}$ and $\boldsymbol{\sigma}$ are the total local strain and the total local stress fields. The total elasto-viscoplastic stiffness \mathbf{C}^{tan} has the contributions from the stiffness of matrix region and stiffness of twinned region and is obtained as follows

$$\mathbf{C}^{\text{tan}} = \left(1 - \sum_{\beta=1}^{N^{\text{tw}}} f^{\beta} \right) \mathbf{C}^{\text{tan}^{\text{mt}}} + \sum_{\beta=1}^{N^{\text{tw}}} \left(f^{\beta} \mathbf{C}^{\text{tan}^{\text{tw}\beta}} \right) \quad (5.26)$$

Because of heterogeneity in microstructure, fluctuations in the local strain arises. Thus, the total local strain is given by

$$\boldsymbol{\varepsilon} = \tilde{\boldsymbol{\varepsilon}} + \mathbf{E} \quad (5.27)$$

where, $\tilde{\boldsymbol{\varepsilon}}$ is the strain fluctuation in the crystal due to heterogeneity and \mathbf{E} is the average strain imposed on the RVE. The local strain fluctuation can be found using Green function method if local stress polarization field is known. Finding local stress polarization involves \mathbf{C}^0 , an average elastic moduli of a linear reference medium. Accordingly, the stress tensor can be written as

$$\boldsymbol{\sigma} = \boldsymbol{\sigma} + \mathbf{C}^0 : \boldsymbol{\varepsilon} - \mathbf{C}^0 : \boldsymbol{\varepsilon} \quad (5.28)$$

or,

$$\boldsymbol{\sigma} = \mathbf{C}^0 : \boldsymbol{\varepsilon} + \tilde{\boldsymbol{\sigma}} \quad (5.29)$$

where, $\tilde{\boldsymbol{\sigma}}$ is the local stress polarization.

The compatible strain tensor $\boldsymbol{\varepsilon}$ is related to displacement gradient \mathbf{u} as

$$\boldsymbol{\varepsilon} = (\mathbf{u} + \mathbf{u}^T)/2 \quad (5.30)$$

Thus, the local problem for heterogeneous RVE becomes:

$$\left\{ \begin{array}{l} \boldsymbol{\sigma} = \mathbf{C}^0 : \boldsymbol{\varepsilon} + \tilde{\boldsymbol{\sigma}} \\ \nabla \cdot \boldsymbol{\sigma} = 0 \\ \text{Periodic boundary conditions across RVE} \end{array} \right. \quad (5.31)$$

To satisfy stress equilibrium locally, the divergence of local Cauchy stress tensor at each Fourier point must be equal to zero, i.e.,

$$\nabla \cdot (\mathbf{C}^0 : \boldsymbol{\varepsilon} + \tilde{\boldsymbol{\sigma}}) = 0 \quad (5.32)$$

The Green's function method is used to solve the equilibrium Equation (5.32) for an applied strain \mathbf{E} that requires the solution of following problem (Lebensohn et al., 2012):

$$C_{ijkl}^0 G_{km,lj}(\mathbf{x} - \mathbf{x}') + \delta_{im} \delta(\mathbf{x} - \mathbf{x}') = 0 \quad (5.33)$$

where $G_{km,lj}(x - x')$ is the Green's function associated with the displacement field. Note that, for simplicity, index notation is employed to derive an expression for strain fluctuations. Accordingly, the local strain fluctuations can be expressed as convolutions in the real space so that

$$\tilde{\varepsilon}_{kl}(x) = \int_{R^3} G_{ki,jl}(x - x') \tilde{\sigma}_{ij}(x') dx' \quad (5.34)$$

For the periodic microstructure, the FFT algorithm can be used to reduce these convolution integrals in the real space to a simple product in the Fourier space. Accordingly, Equation (5.34) is solved in the Fourier space that makes the FFT-based implementations computationally efficient for computing the local response. Thus, the Fourier transforms are used to: (a) transform the polarization field into Fourier space, (b) obtain the product of polarization field and the appropriate kernel function in the Fourier space, and (c) anti-transform the product in Fourier space back to the real space to obtain strain fluctuations. Using the convolution theorem, the local strain fluctuations in Fourier space are given by

$$\hat{\tilde{\varepsilon}}_{kl}(\xi) = \hat{\Gamma}_{ijkl}^0(\xi) \hat{\tilde{\sigma}}_{kl}(\xi) \quad (5.35)$$

where “ $\hat{\cdot}$ ” indicates forward Fourier transform, and ξ is the frequency point in the Fourier space. Furthermore, the Green operator in Fourier space $\hat{\Gamma}_{ijkl}^0$, which is the kernel function of the average stiffness tensor of the reference medium \mathbf{C}_{ijkl}^0 and the frequency, is given by

$$\hat{\Gamma}_{ijkl}^0(\xi) = -\xi_j \xi_l \hat{G}_{ik}(\xi), \quad \hat{G}_{ik}(\xi) = [\mathbf{C}_{ijkl}^0 \xi_l \xi_j]^{-1} \quad (5.36)$$

In the present work, an average kernel function of linear reference medium which is two times stiffer than reference medium is employed. This ensures a converged solution of micromechanical fields in a single step of stress and plastic strain integration provided the time step is kept sufficiently small.

The local strain fluctuations in real space can be obtained by taking the inverse Fourier transform of Equation (5.35) such as

$$\tilde{\varepsilon}_{kl}(x) = \text{fft}^{-1}(\text{sym}(\hat{\Gamma}_{ijkl}^0(\xi))\hat{\sigma}_{kl}(\xi)) \quad (5.37)$$

Finally, the total local strain is given by

$$\boldsymbol{\varepsilon} = \text{fft}^{-1}(\text{sym}(\hat{\Gamma}^0(\xi)) \hat{\boldsymbol{\sigma}}(\xi)) + \mathbf{E} \quad (5.38)$$

It should be mentioned that the proposed framework gives stable results even at extremely large strains, such as those that will be obtained in FLD simulations.

5.2.1.5 Grain Morphology Update

Due to the heterogeneity of the material, the set of convected Fourier points no longer forms a regular grid as the deformation progresses. However, a regular Fourier grid is needed in order to compute the strain fluctuation (Eq. 5.37) using the convolution theorem. Therefore, in the present work, the following scheme is adopted for updating coordinates of the Fourier points, neglecting contribution from strain fluctuations and using volume averaged strain rate, so that the Fourier grid remains regular with deformation (Lebensohn et al., 2008)

$$\mathbf{x}_k = \mathbf{x}_k^{t-1} + \mathbf{D}_{\text{avg}} \mathbf{x}_k^{t-1} \times \Delta t \quad \forall k \in 1,3 \quad (5.39)$$

After each time step increment, the distances between adjacent Fourier points change, but the Fourier grid remains regular, thus determining an “average stretching” of the grains in the RVE.

Using the RTCP-FFT-HCP model as outlined above, the full field solutions of micromechanical fields are computed for a polycrystal RVE subjected to periodic boundary conditions. The DRX framework and its coupling with the RTCP-FFT-HCP model are described in the next section.

5.2.2 Dynamic Recrystallization (DRX) Model

The probabilistic cellular automata model that is coupled with the crystal plasticity-fast Fourier transform method (described in the previous section) to model dynamic recrystallization (DRX) in HCP metals. In the proposed framework, a Fourier point represents a voxel inside a grain in the 3D microstructure. Each Fourier point is modeled as a cell and the corresponding state variables are obtained using RTCP-FFT-HCP model. Note that, the terms cell, material point or Fourier point are used interchangeably in this chapter, since they overlap and represent the same spatially resolved 3D grid. The proposed DRX approach can be divided into four main parts: (a) Onset of DRX, (b) Kinematics of nucleation, (c) Kinematics of grain growth, and (d) Cellular automata model for state switching of cells.

5.2.2.1 Onset of DRX

During deformation, the onset of the dynamic recrystallization (DRX) depends on various factors. In general, there are two types of criteria used in literature for the onset of DRX: (a) based on the critical value of dislocation density (Bailey and Hirsch, 1962) and (b) the geometrical criterion, i.e., once the pre-existing grain boundary bulging reaches a critical value (Sandström and Lagneborg, 1975; Roberts and Ahlblom, 1978). The dislocation density-based criterion used in Takaki et al. (2009) is adopted in the present work. Thus, the DRX starts once dislocation density ρ reaches the critical value given by

$$\rho_{cr} = \left(\frac{20SD}{3bLM\lambda^2} \right)^{1/3} \quad (5.40)$$

where D is the local strain rate, S is the Read and Shockley (1950) grain boundary energy per unit area. M is the grain boundary mobility and $\lambda = c\mu b^2$, b is burgers vector, $L = K/c_2\sqrt{\rho}$ is the mean free path of dislocation. Accordingly, K and c are the fitting parameters and are determined by calibration with the experimental stress-strain curve. Similar to the hardening parameters, K and c also vary when temperature changes.

5.2.2.2 Kinematics of Nucleation (Popova et al. (2015, 2016))

Two main concepts of nucleation and growth have been generally employed in numerical models; (a) pre-existing nucleated sites that grow with deformation, and (b) nuclei are not pre-existing, but new nuclei form and evolve with deformation. Cahn (1950) introduced the concept of recrystallization nuclei as initiators of grain growth based on the dislocation density where identifying regions with high contrast in dislocation density with the surroundings was the main focus. Popova et al. (2015, 2016) employed this concept in a coupled CA-CPFEM model to simulate DRX in magnesium alloys. In addition, Popova et al. (2016) showed that twins can also serve as a nucleation site and the DRX can be observed along the twin boundaries where high contrast in dislocation density occurs.

In the present work, only GNDs are considered and modelling SSDs are left as improvements for future works. The density of GNDs can be obtained using screw dislocation and edge dislocation (Arsenlis and Parks, 1999).

Accordingly, the accumulated edge ($\rho_{\text{GN}(\text{edge})}$) and screw dislocations ($\rho_{\text{GN}(\text{screw})}$) are calculated using the reoriented lattice vectors ($\mathbf{m}_{\text{sl}}^{*(\alpha)}$, $\mathbf{s}_{\text{sl}}^{*(\alpha)}$) and shear strain $\gamma_{\text{sl}}^{(\alpha)}$ on each slip system α as follows

$$\rho_{\text{GN}(\text{edge})}b^2 = - \sum_{\alpha=1}^{N^{\text{sl}}} \nabla \left(\gamma_{\text{sl}}^{(\alpha)} \cdot \mathbf{m}_{\text{sl}}^{*(\alpha)} \right) \quad (5.41)$$

$$\rho_{\text{GN}(\text{screw})}b^2 = - \sum_{\alpha=1}^{N^{\text{sl}}} \nabla \gamma_{\text{sl}}^{(\alpha)} \cdot \left(\mathbf{s}_{\text{sl}}^{*(\alpha)} \times \mathbf{m}_{\text{sl}}^{*(\alpha)} \right) \quad (5.42)$$

The magnitude of total GND density can be obtained as

$$\rho_{\text{GN}} = \sqrt{(\rho_{\text{GN}(\text{edge})}^\alpha)^2 + (\rho_{\text{GN}(\text{screw})}^\alpha)^2} \quad (5.43)$$

Furthermore, the total dislocation density, ρ_{GN} , is used to calculate the mismatch in dislocation densities, $d\rho_{ij}$, between the material points such as

$$d\rho_{ij} = \left| \rho_{GN_i} - \rho_{GN_j} \right| \quad (5.44)$$

where ρ_{GN_i} , ρ_{GN_j} are the total dislocation densities of the material points i and j, respectively.

5.2.2.3 Kinematics of Grain Growth

Based on stored deformation energy (P) and mobility of the grain boundary (M), Gottstein and Shvindlerman (1999) have demonstrated that velocity of the grain boundary, v , can be calculated as

$$v = MP \quad (5.45)$$

While the stored deformation energy can be calculated as

$$P = \frac{1}{2} \rho \mu b^2 \quad (5.46)$$

where μ is the shear modulus and ρ is dislocation density.

Furthermore, the mobility (M) of the grain boundary depends on the temperature and misorientation angle and follows Arrhenius type of the equation:

$$M = \begin{cases} 0, & \text{if } \theta < \theta_{cr} \\ M_0 \exp\left(-\frac{H_m}{kT}\right), & \text{if } \theta \geq \theta_{cr} \end{cases} \quad (5.47)$$

where T is the temperature, H_m is the activation enthalpy, k is the Boltzmann constant, and M_0 is the pre-exponential factor that depends on grain boundary misorientation. To calculate

misorientation between two materials point, the crystal orientation for each material is stored as a 2nd order orientation matrix (φ). Using rotation matrices, the disorientation, θ , is calculated between current material point i and its neighboring material point j as follows

$$\theta = \min \left[\cos^{-1} \left(\frac{\text{tr}(\varphi_i \varphi_j^T) - 1}{2} \right) \right] \quad (5.48)$$

where φ_i and φ_j are the rotation matrices of the elements i and j respectively. This disorientation is then used to calculate the mobility of the boundary, (M_{ij}), between elements i and j (Eq. 5.47).

Doherty (1997) has demonstrated that during the DRX, the grain boundaries move leaving behind a strain free grain, and as a result, the dislocation density over the entire sample decreases. Therefore, DRX is known to soften the response of the grain. Accordingly, in this implementation, the flow stress is relaxed for the recrystallized material points.

The above formulation is used in the current work and calculated as a part of RTCP-FFT-HCP simulation. The probabilistic cellular automata approach is then used to determine nucleation sites as well as their growth.

5.2.2.4 Probabilistic Cellular Automata Model

In the present work, the probabilistic CA is used to (a) identify potential nucleation sites and (b) grow the nuclei in the matrix. In order to model DRX using CA, the microstructure is divided into cells with state variables (Janssens, 2010). A cell in the current framework corresponds to a material point or a Fourier point, therefore, no mapping procedure is needed. A probabilistic switching rule is defined that depends on the state of the neighboring cell. In the present work, a modified Moore neighborhood is used, since it provides more freedom for the grain to grow in the 3D space. The neighborhood used in the present work has spherical boundary and thus, all the first order, 26 neighbors are considered for the state switching rule (Figure 5.1).

In this research, an RVE with lengths of 64 μm in each of X, Y and Z directions, respectively, is employed in all the simulations. The spacing between two neighboring material points (nearest), Δx , is 1 μm . To define the neighborhood in 3D, a sphere with fixed radius r , where r is 1.74 x Δx ,

is used. Since the farther material points (i.e., at middle and corners of a plane with respect to material point at center) are harder to recrystallize, proportionality of 0.48 and 0.25, respectively, are used. It is already well documented that length and time scales are some of the main challenges in the CA models (Hallberg, 2011). The parameter Δt_{DRX} is implemented in order to define the correlation between simulation time and the DRX time step such as;

$$\Delta t_{\text{DRX}} = C_T \times \frac{\Delta x}{v_{\text{avg}}^{\text{gb}}} \quad (5.49)$$

where $v_{\text{avg}}^{\text{gb}}$ is an average grain boundary velocity, Δx is the cell size, i.e., the spacing between to material points, C_T is a constant, which is calibrated through a nucleation process. DRX step occurs once the velocity of the grain boundary is high enough to surpass the size of the cell. Since, the parameter Δt_{DRX} depends on the cell size, Δt_{DRX} should have a lower value for a finer Fourier grid compared to that for a coarse grid.

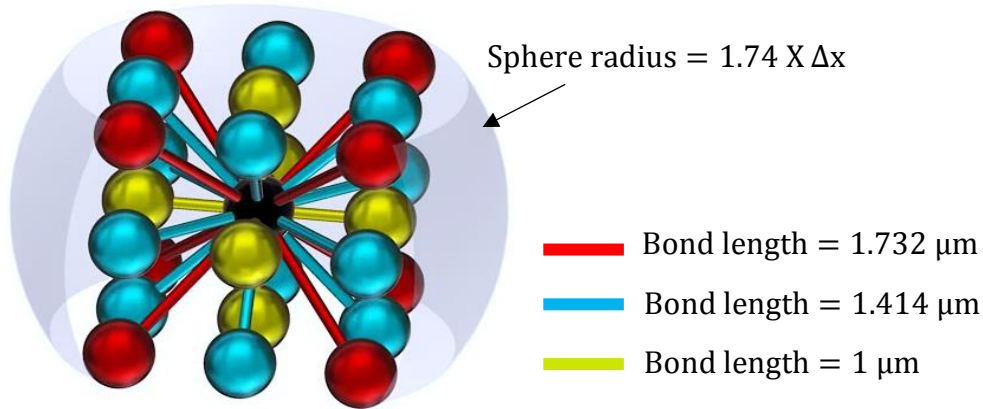


Figure 5.1: Modified Moore neighborhood is used in the present work; defining a material point and its neighbors in 3D space using a spherical boundary with 26-point scheme. A material point interacts with all other material points that lie at distance less than the radius of the sphere.

Three state variables are used in the cellular automata model; (a) 2nd order crystal orientation matrix, ϕ ; (b) dislocation density, ρ ; (c) the variable, N , that can take the values 0 or 1 depending on whether the material point is a new nucleus or apriori recrystallized material point. At the beginning of a simulation, all the CA cells (i.e., material points in the present work) are assigned

$N = 0$ indicating that there are no pre-existing nuclei and then DRX computations are performed based on the criteria discussed earlier in this section. During the DRX step, the following sequences are observed;

(1) the potential nucleation sites are determined, i.e., based on high contrast in dislocation density inside between two materials points at a time (Eq. 5.44). If the total dislocation density ρ_{GN} is more than the critical value ρ_{cr} , then nucleation can take place. If $\theta \geq \theta_{cr}$ and $d\rho \geq \rho_{cr}$ for the current material point, then the site is identified as a potential nucleus. In addition, the viable nuclei are chosen with a probability depending on the grain boundary mobility and stored energy difference. This step ensures that identified nucleation site has a high chance of growing. The switching parameter used to determine the probability is based on the velocity of the grain boundary is given by

$$\omega_{switch} = \begin{cases} \frac{v_{ij}}{v_{max}}, & \text{if } d_{ij} \leq \Delta x \\ 0.48 \frac{v_{ij}}{v_{max}}, & \text{if } \Delta x < d_{ij} \leq \sqrt{2}\Delta x \\ 0.25 \frac{v_{ij}}{v_{max}}, & \text{if } \sqrt{2}\Delta x < d_{ij} \leq r \end{cases} \quad (5.50)$$

where d_{ij} is the distance between material point i and its neighbor j , r is the radius of sphere that defines neighborhood of each material point ($r = 1.75 \times \Delta x$, constant, in the present work), v_{max} is the maximum velocity of the grain boundary in the computational domain (obtained from the RTCP-FFT-HCP) and v_{ij} is the velocity of the boundary between the current element i with respect to its neighbor j . During the probabilistic step, a random number $\xi \in [0,1]$ is generated and if $\xi \leq \omega_{switch}$ then the current material point is a feasible nucleus, and the switching variable for nucleation N takes a value of 1, otherwise $N = 0$.

(2) The nucleus grows by consuming the neighboring matrix cells. To determine if the current material point would be consumed by one of its neighbors, the following procedure is used. The current material, i , that hasn't been recrystallized in the previous steps, has to have at-least one recrystallized neighbor, i.e., $N_i = 0$ and $N_j = 1$. If this condition is satisfied then the difference in stored dislocation energy and the grain boundary mobility (based on the misorientation between

the two material points) are calculated using Equations (5.44) and (5.47). The state of the current element is then changed based on the velocity obtained from Equation (5.45). Similar to the nucleation criteria, the probability of getting consumed by material point j for material point i is based on the velocity. Furthermore, a random number $\xi \in [0,1]$ is generated when a growth step is taken. If $\xi \leq \omega_{\text{switch}}$ then the current material point i is recrystallized by material point j only if the material point j is already a nucleus or previously recrystallized element, i.e., $N_j = 1$. Finally, if the material point i is successfully recrystallized by material point j , i.e., $\varphi_i = \varphi_j$, $N = 0$ and its stress is relaxed.

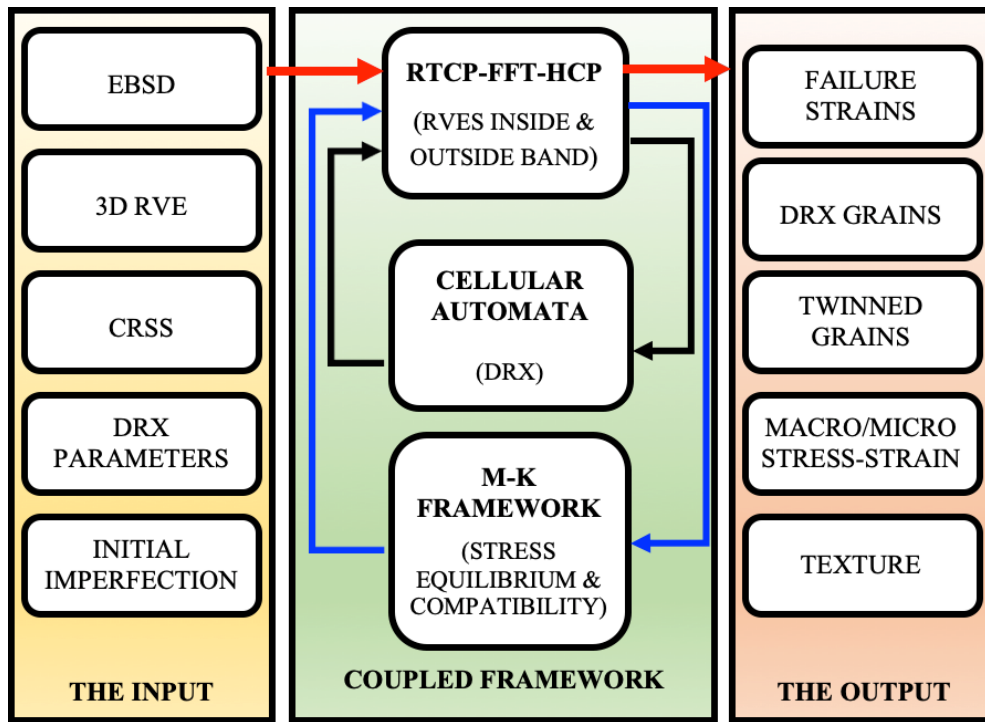


Figure 5.2: Flowchart for the proposed numerical framework.

A flowchart for the proposed numerical framework is presented in Figure 5.2. The DRX formulation explained above is incorporated in the RTCP-FFT-HCP model and then coupled with the well-known M-K framework to determine the failure strains for magnesium alloys.

5.2.3 Marciniak and Kuczyński (M-K) Framework

The well-known Marciniak and Kuczyński formulation (Marciniak and Kuczyński, 1967) is used to model and study the effects of the dynamic recrystallization on formability predictions of rolled

AZ31 magnesium alloy sheet at different temperatures. The M-K model employed in this research follows the implementations presented by Wu et al. (1997) and used by Inal et al. (2005, 2010), Lévesque et al. (2010, 2016), Mohammadi et al. (2014) and Nagra et al. (2018). In M-K framework, an infinitely long orthotropic sheet with axes transverse direction (TD) and rolling direction (RD, respectively, is considered to have an imperfection band that is inclined to the RD at an initial angle, ψ . Figure 5.3 presents a schematic of M-K framework showing an orthotropic sheet with an inclined imperfection band. The rolled sheet is assumed to contain a geometrical imperfection, such as a narrow band or groove across the sheet's width, which is slightly thinner than the rest of the sheet and this is defined as the imperfection factor (f^{imp}) given by

$$f^{imp} = \frac{h_0^b}{h_0} \quad (5.51)$$

where, h_0^b is the initial thickness of band region and h_0 is the initial thickness of the region outside band. To model the effect of this imperfection on sheet formability, two 3D RVEs with identical initial texture and grain morphology, one outside the imperfection band and other in the imperfection band, are employed in the present work.

Compatibility and equilibrium conditions are satisfied across the band interface assuming a plane stress condition, i.e., $\sigma_{33} = 0$.

The boundary conditions applied to the sheet can be written as

$$\begin{cases} \rho = \frac{D_{22}}{D_{11}} = \text{constant}, -0.5 \leq \rho \leq 1.0 \\ \Omega_{ij} = 0 \quad \forall i = j \\ D_{ij} = 0 \quad \forall i \neq j \end{cases} \quad (5.52)$$

where, Ω_{ij} is spin rate, ρ is the applied strain ratio, D_{11} and D_{22} are principal strain rates. The band angle at time t , $\psi(t)$, is related to the initial band angle through

$$\tan \psi_{t-1} = \exp[(1 - \nu)D_{33t-1}\Delta t] \tan \psi \quad (5.53)$$

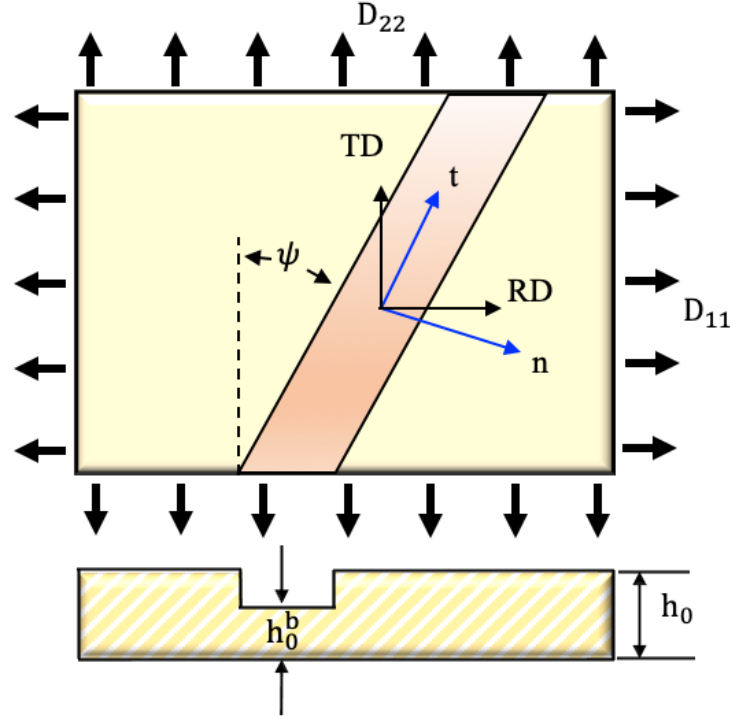


Figure 5.3: Schematic of M-K framework: initial configuration of an orthotropic sheet showing imperfection band direction vectors (n and t), band angle, initial thicknesses and boundary conditions.

As the deformation in the simulation progresses, the onset of localized necking is assumed to have occurred when the thinning rate inside band increases rapidly compared to thinning rate outside band, i.e., the failure strains are obtained when $D_{33}^b > 10^4 \times D_{33}$ and the accumulated plastic strain outside band is 16 times greater than accumulated plastic strain inside band.

5.3 Experimental Data

The LEO 1450 scanning electron microscope (SEM) fitted with a TSL EBSD camera was used to obtain all the EBSD scans for the magnesium sheet alloy AZ31. In the present work, the scan size selected was $2000 \times 2000 \mu\text{m}$. The average grain size over this sample is $\sim 14 \mu\text{m}$. The EBSD data was analyzed using the TSL OIM Analysis™ software and following the analysis presented by Brahme et al. (2012), an area of $800 \times 300 \mu\text{m}$ was assumed to be the representative scan size.

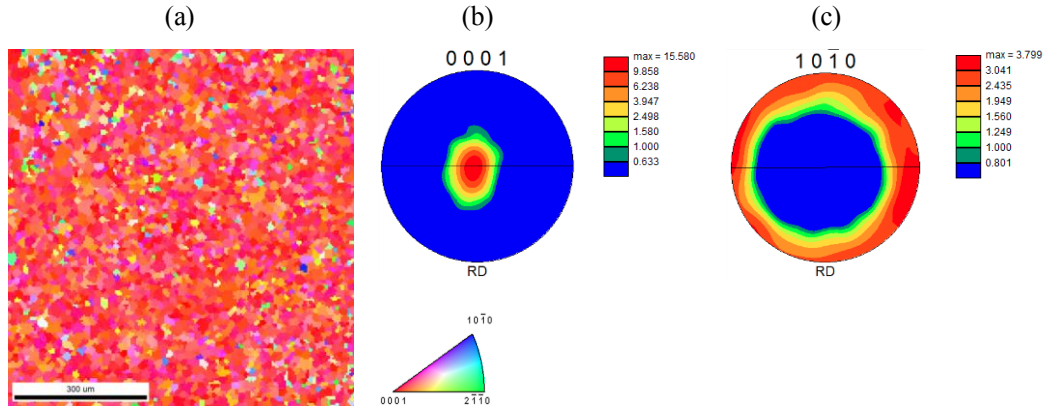


Figure 5.4: Experimentally measured microstructure; (a) EBSD scan, (b) 0001 polefigure, and (c) 10-10 polefigure.

Using the TSL Grain Dilation feature, the cropped EBSD data was cleaned to remove the bad data points by setting the grain tolerance angle to 5° and the minimum grain size to 10 data pixels. Only data points having a confidence index (CI) above 0.2 were retained for the analysis. Using the misorientation tolerance of 10° , the grains were identified with the TSL Single Orientation per Grain option set to 10° , i.e., A grain is identified by grouping all the pixels having a misorientation of less than 10° . Grains with less than 10 data points were excluded from the analysis. The pixels within the identified grains were then assigned average orientation of the grain. Consequently, the misorientation of any two pixels within a grain is zero.

5.4 Synthetic 3D Microstructure

For all the studies presented in this work, a representative volume element (RVE) that contains 276 grains (Figure 5.5a) is employed with $64 \times 64 \times 64$ Fourier points. The grains are constructed as equiaxed (similar to the measured microstructure) and have a grain size of $9.83 \mu\text{m}$. Each of the grains is assigned an orientation such that the overall texture of the RVE (Figure 5.5) is similar to the experimentally measured texture (Figure 5.4). The assigned texture also exhibits strong basal pole, as evident from the 0001 polefigure showing a strong pole at the center with a texture strength ~ 11 . It should be mentioned that the same RVE is used to (i) first calibrate the model, (ii) simulate dynamic recrystallization at elevated temperatures and (iii) predict forming limit diagrams at elevated temperatures.

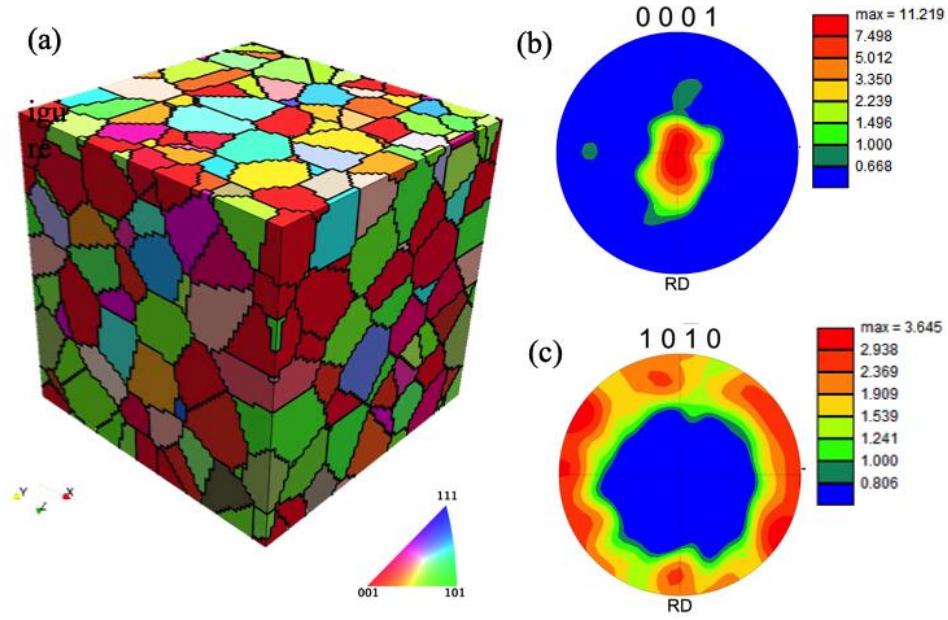


Figure 5.5: Regenerated synthetic microstructure with 276 grains, shown in (a), (b) and (c) show 0001 and 10-10 polefigures.

5.5 Results and Discussions

In the next sections, the results obtained from the numerical model as well as comparisons with experimental observations are presented.

5.5.1 Calibration of RTCP-FFT-HCP Model

The model parameters for the slip and twin systems are calibrated by curve fitting the uniaxial tension and compression (along RD) stress-strain responses from the model to the experimental measurements. To obtain the model parameters, first the slip system parameters are determined such that the resultant stress-strain response closely matches the experimentally measured uniaxial tension response (Figure 5.6a). Then, the twin parameters are determined so that, with the same slip system parameters used for uniaxial tension, the uniaxial compression curve matches the measured uniaxial compression response (Figure 5.6b). The calibrated values are reported in Table 5.2. Note that, the results from the compression use the absolute values of true stress and true strain.

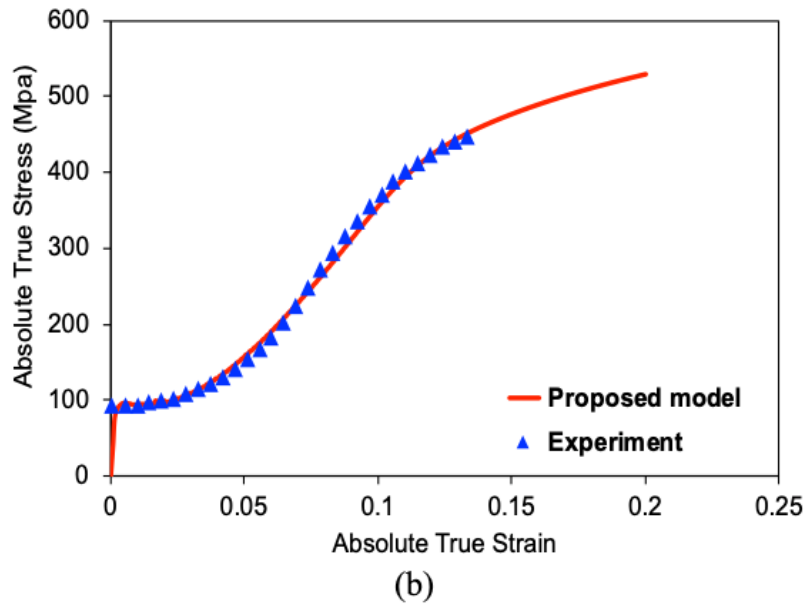
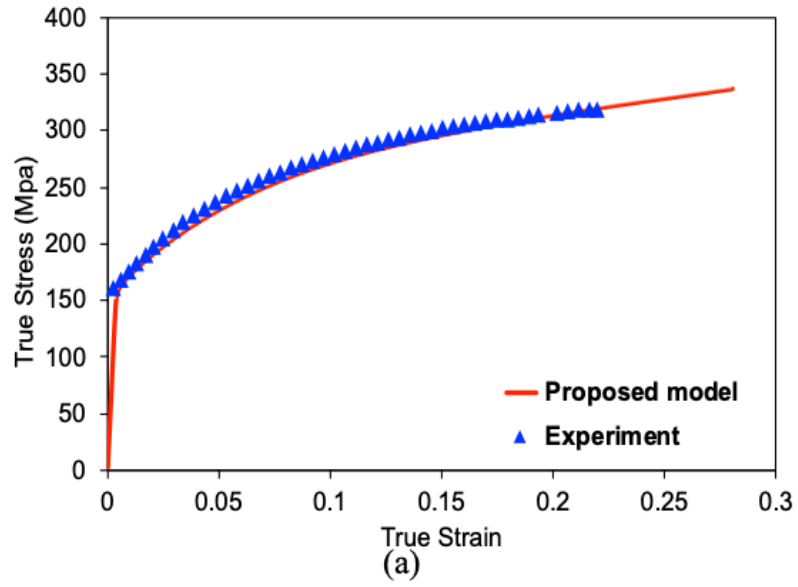


Figure 5.6: Comparison of the simulated flow curves (Red) and experimentally measured responses (Blue triangles) for uniaxial; (a) tension, and (b) compression.

Table 5.2: Constitutive parameters used to calibrate proposed model for RD uniaxial tension and compression at room temperature.

<i>Slip Parameters</i>				
<i>Parameter</i>	<i>Basal</i>	<i>Prismatic</i>	<i>Pyramidal</i>	<i>Pyramidal $c + a$</i>
τ_0 (Mpa)	1.8	72.0	76.5	76.5
h_1	2.0	45.0	150.0	150.0
c	6.0	6.0	6.0	6.0
h_{TB} (Mpa)	850.0			
<i>Twinning Parameters</i>				
$\tau_{0,twinning}$ (Mpa)	100.0			
$h_{0,twinning}$ (Mpa)	0.01			

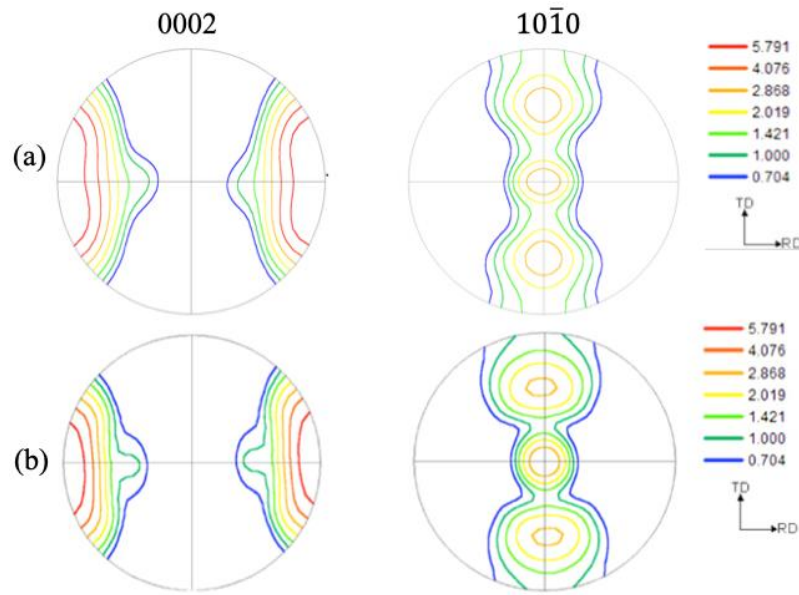


Figure 5.7: Predicted texture after 8% uniaxial compression, shown in (a) and compared to that reported by Khan et al. (2011) shown in (b).

5.5.2 Validation of RTCP-FFT-HCP Model

The predictive capability of the proposed model is validated by comparing the evolved texture predictions from the model with those published in literature. Khan et al. (2011) studied a similar AZ31 alloy under various loading conditions and reported, amongst other findings, the deformed texture after compressive loadings along RD. Comparing, the textures predicted by the proposed

model with the measurements presented in Khan et al. (2011) show that the proposed model can accurately capture the texture evolution (Figure 5.7).

Since twinning is clearly a dominant mechanism during compression along RD, to understand the role of slip as well as the twin systems play in accommodating the overall deformation, the activities of the slip and the twin systems are plotted as a function of the absolute true strain during compression (Figure 5.8). The activity plot shows that initial yielding is primarily due to the basal glide. The prismatic slip is also active initially. During uniaxial compression along RD, the ND has to undergo extension for the given sample of AZ31 alloy due to strong basal texture as seen in Figure 5.4. This implies that the deformation along ND has to be accommodated by c-axis extension.

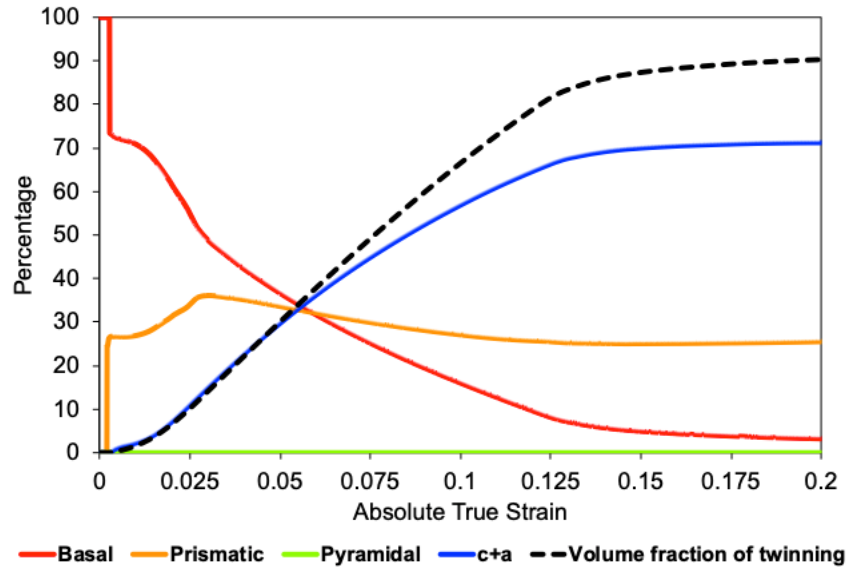


Figure 5.8: Slip and twin system activity during uniaxial compression along RD till 20% uniaxial compression.

The available mechanisms to accommodate the deformation of c-axis in HCP materials are the pyramidal $\langle c+a \rangle$ slip and the twinning. Of these two, twinning is a polar deformation with the different twin mechanisms active during extension and contraction of c axis. To accommodate extension of c axis the 10-12 family of twin systems needs to be activated.

At room temperature, CRSS for extension twins (10-12 family) is lower than the $\langle c+a \rangle$ slip system. When the average true stress reaches about 100 MPa, the twinning becomes active, as can

be seen from the twin activity picking up right after macro-yielding. Twinning also reorients the crystallographic texture of the lattice in the twinned region such that the c axis is aligned to the compression direction, in the present case, towards the RD. Hence, in the twinned orientation neither basal or pyramidal slip are favorable as the deformation is compressive along c axis. As a result, the twinned region accommodates this deformation via $\langle c+a \rangle$ slip. As the amount of twinning increases, the volume of the microstructure which is reoriented increases and the activity of pyramidal $\langle c+a \rangle$ also increases (Figure 5.8).

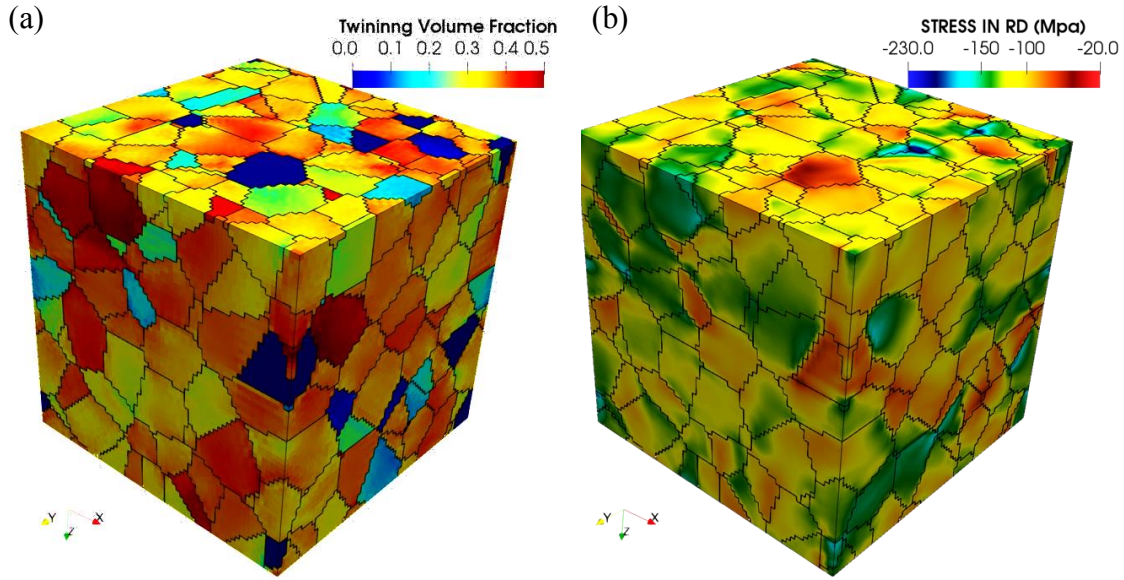


Figure 5.9: (a) Distribution of volume fraction of twins and (b) stress distribution in the microstructure at 8% uniaxial compression along RD (X).

Figure 5.9(a) shows the local distribution of regions which are twinned in the microstructure after 8%. Note that the loading is applied along the X axis in Figure 5.9. It is immediately clear that there is no “preferred” location for twin formation in the microstructure; twinning seems to be prevalent everywhere. Since the twinning in the current model is determined by the resolved shear stress on the twin system, the compressive stress distribution in the microstructure is also shown in Figure 5.9(b). Comparing these two, it is observed that the regions that show twinning have higher values of stress. This is expected as the stress in the material point increases the resolved stress on the twin system increases and when it satisfies the twinning criterion twin appears.

Table 5.3: Constitutive parameters used to calibrate coupled MK-CA-RTCPFFT-HCP model for RD uniaxial tension at 100 °C, 200 °C and 300 °C, respectively.

<i>Parameter</i>	<i>Basal</i>	<i>Prismatic</i>	<i>Pyramidal</i>	<i>Pyramidal $c + a$</i>
Temperature: 100 °C				
τ_0 (Mpa)	0.8	25.0	85.0	82.0
h_1	0.5	2.0	20.0	20.0
c	16.0	16.0	16.0	16.0
h_{TB} (Mpa)	200.0			
Temperature: 200 °C				
τ_0 (Mpa)	0.8	25.0	57.0	57.0
h_1	0.5	25.0	85.0	85.0
c	16.0	16.0	16.0	16.0
h_{TB} (Mpa)	200.0			
Temperature: 300 °C				
τ_0 (Mpa)	0.8	20.0	35.0	38.0
h_1	0.5	2.0	20.0	20.0
c	16.0	16.0	16.0	16.0
h_{TB} (Mpa)	200.0			

5.5.3 Coupled Model Calibration at Elevated Temperatures

The main goal of the present work is to predict the elevated temperature formability of magnesium alloys with the proposed numerical model that accounts for not only deformation twinning and crystallographic slip, but also the dynamic recrystallization. Accordingly, the parameters of the numerical model, including the parameters that account for dynamic recrystallization, are calibrated for various elevated temperatures.

For magnesium alloys, the twinning CRSS has been shown to be athermal, hence the twinning CRSS is not changed in the model. For the CRSS of the slip systems, the model parameters are adjusted so that they match the flow curves at the elevated temperatures until the onset of DRX. The onset of DRX leaves a clear signature on the flow curve by a marked softening in the stress with the increasing strain. This point and the subsequent softening are used to calibrate the criterion

for nucleation and growth kinematics of the nucleated grains governed by Equations (5.44) and (5.45) respectively. Accordingly, the parameters for the numerical model are calibrated for 100, 200 and 300 °C, the model parameters are calibrated for these temperatures. These constitutive parameters are highlighted in Table 5.3. The experimental macroscopic stress-strain responses at different elevated temperatures employed in this study are shown in Figure 5.10 (Chen et al., 2003).

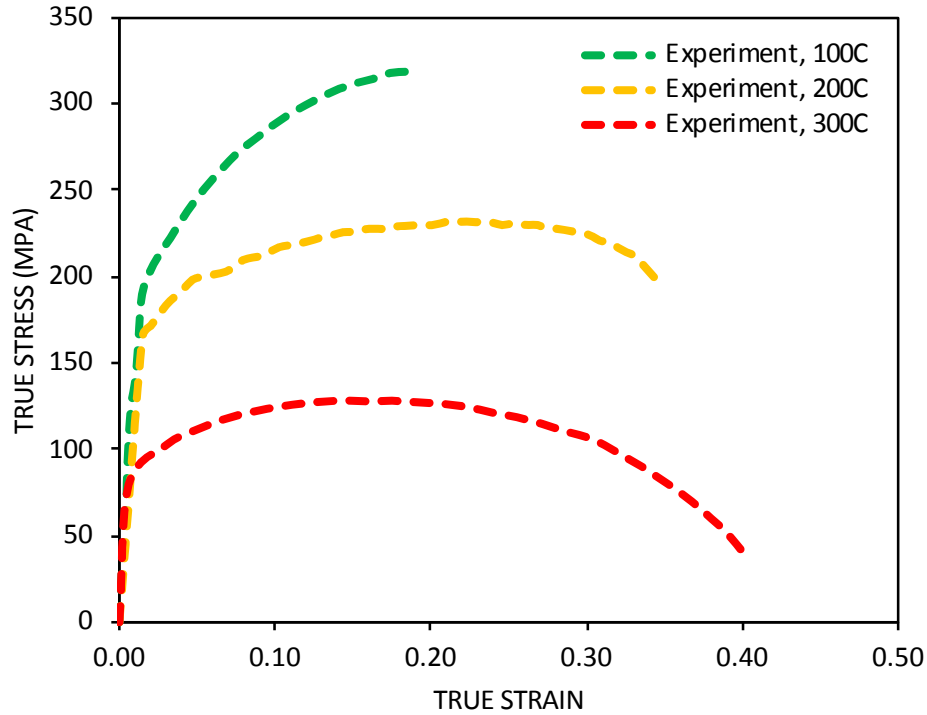


Figure 5.10: Experimental true stress-strain curves for AZ31 sheet alloy at 100 °C, 200 °C, and 300 °C, respectively, reproduced from Chen et al. (2003).

A comparison between the simulated stress-strain curves and the experimental measurements (Chen et al., 2003) are presented in Figure 5.11. In the Figure 5.11, the simulated stress-strain curves with and without DRX, as can be expected (due to limited DRX at this temperature), show similar behavior at 100 °C. However, as the temperature increases, DRX becomes more pronounced where the onset of DRX is defined by a saturation of the flow stress immediately followed by softening behavior (Figure 5.11).

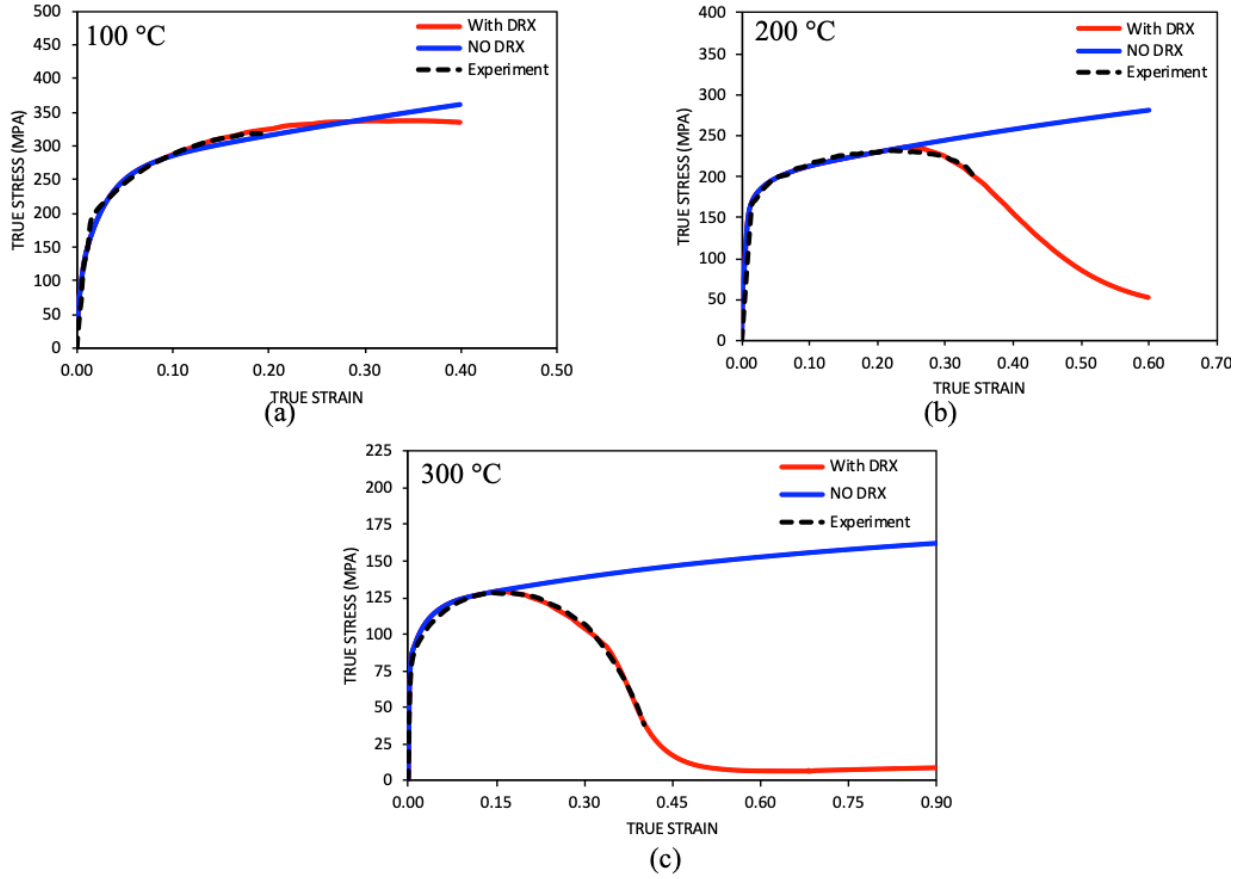


Figure 5.11: True stress-strain for AZ31 alloy at (a) 100 °C, (b) 200 °C, and (c) 300 °C. Black dashed line shows experimental data (Chen et al., 2003), the model prediction with and without DRX are shown with red and blue lines, respectively.

Finally, for each of the temperatures studied, the M-K analysis requires an imperfection parameter. The imperfection parameter is calibrated so that the forming limit strain for the plane-strain condition predicted by the model matches the experimentally measured limit strain (Cyr et al., 2018). For comparison purposes, 2 different numerical models are used to predict the FLDs; (i) model with DRX and (ii) model without DRX. Note that, for both of these models, the same imperfection parameter obtained for the model with DRX is used in the M-K analysis.

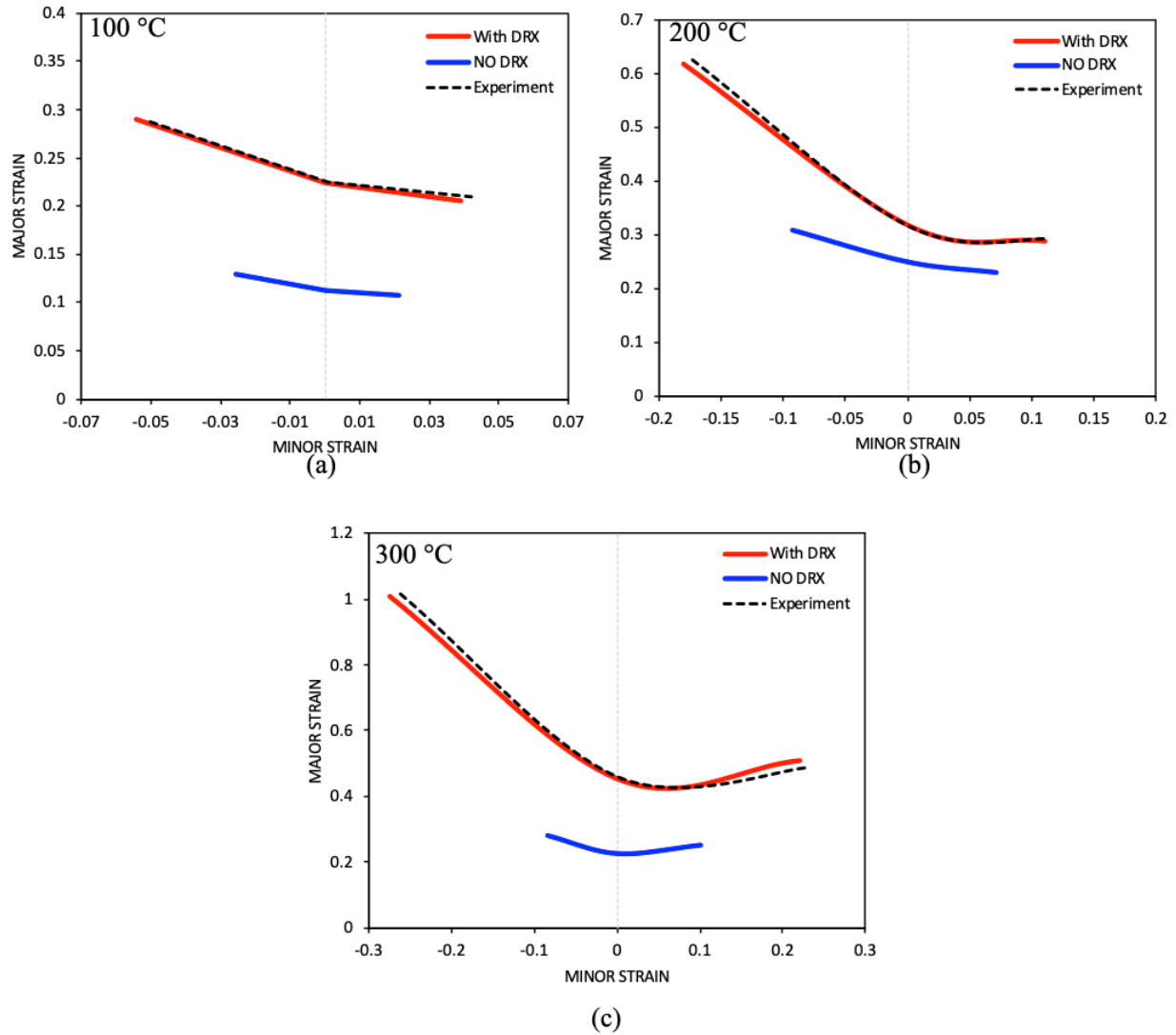


Figure 5.12: Comparison of predicted FLD (with and without DRX) with experimental FLD of AZ31 sheet alloy strain at (a) 100 °C, (b) 200 °C, and (c) 300 °C.

5.5.4 FLD Predictions with and without DRX at Elevated Temperatures

In this section, the numerical model is employed to predict the FLDs at 100, 200 and 300 °C. Furthermore, for each of the temperatures studied, the predictions are compared to the FLDs reported in literature by Chen et al. (2003). The predicted FLDs by the above models as well as experimental limit strains at 100, 200 and 300°C are presented in Figure 5.12. Simulations show

that the model with DRX provides accurate predictions of forming limit diagrams for all three temperatures.

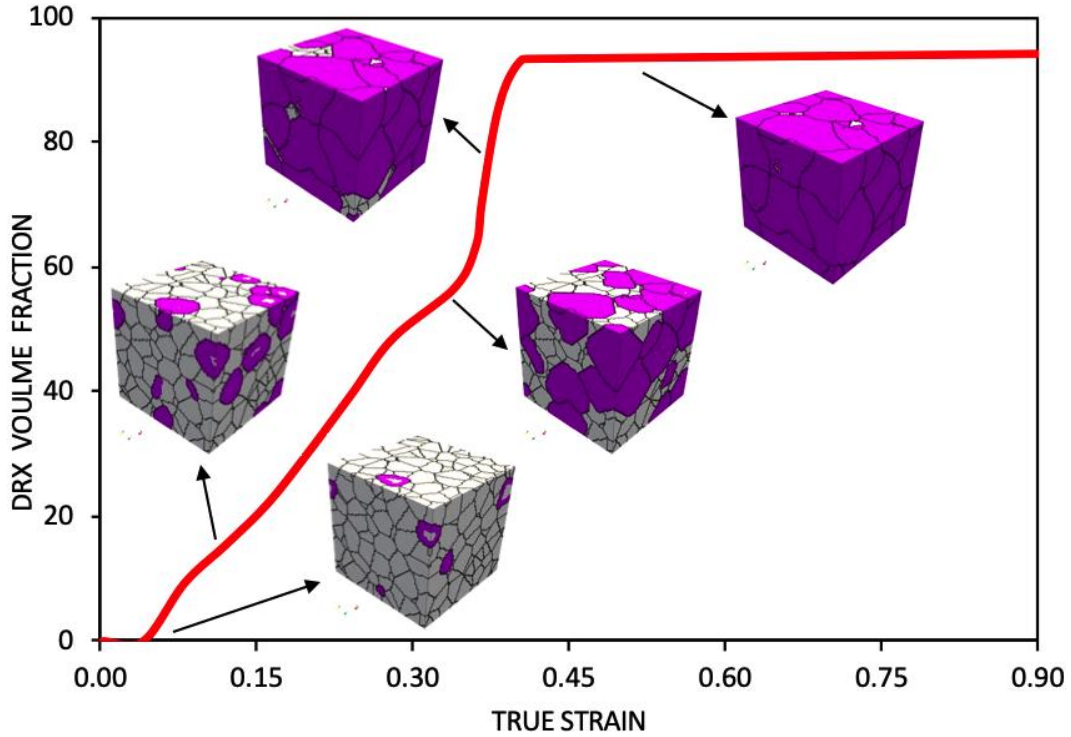


Figure 5.13: Evolution of recrystallized volume fraction (percentage) during deformation for uniaxial tension ($\rho = -0.5$) at 300 °C. The microstructure showing location of the recrystallized grain structure is overlaid on top.

As the temperature increases, experimentally measured FLDs shows a significant increase in the limit strains for both the uniaxial and biaxial sides of the. This increase can be directly attributed to the DRX taking place at these temperatures. Contrary to this, the model without DRX predicts significantly lower forming limits for all three temperatures. Furthermore, the model with DRX can successfully predict the initial decrease in the limit strains in the biaxial stretching region followed by increase in limit strains towards balanced biaxial tension (also observed experimentally at both 200 and 300°C).

To better understand the effects of DRX on the deformation, various other analyses are performed as explained in the next sections.

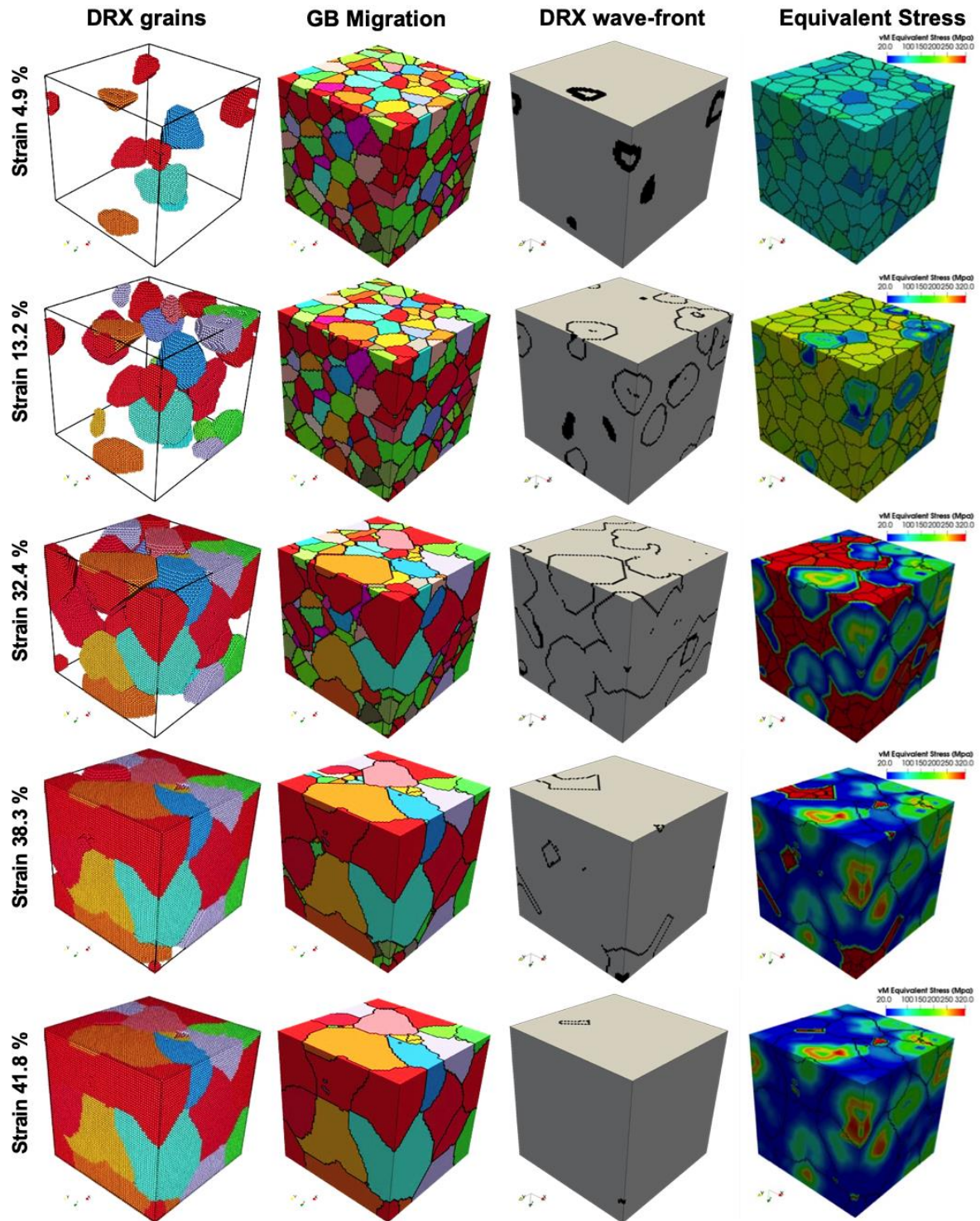


Figure 5.14: Showing evolution of (i) recrystallized grains, (ii) grain boundary migration, (iii) DRX wave-front and (iv) the equivalent stress distribution in the microstructure for uniaxial tension ($\rho = -0.5$) at 300 °C.

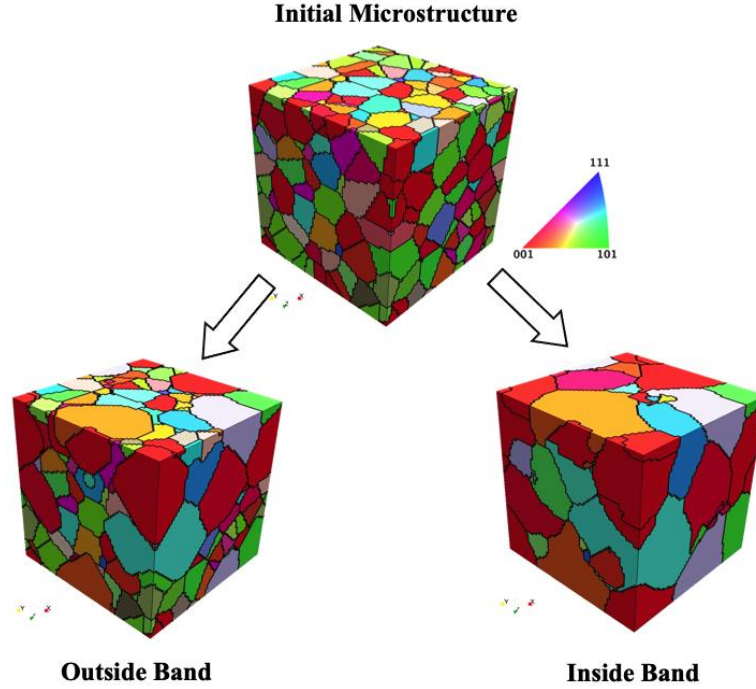


Figure 5.15: Showing at the top the initial RVE, which is identical both inside and outside the band. The resultant microstructure at failure strains outside and inside the band for biaxial tension ($\rho = 0.2$) at 300 °C are shown below. Both these show different evolution with regards to amount of DRX.

5.5.5 Evolving Microstructure during DRX at 300 °C Inside Band

Figure 5.13 shows the evolution of volume fraction for dynamically recrystallized grains during deformation under uniaxial tension. The numerical simulation shows that DRX sets in at 4.9% strain, and then rapidly increases throughout the RVE. Around 42% strain, most of the microstructure has seen DRX (more than 90%). After this point, no more DRX is observed for rest of the simulation. The deformed microstructures including DRX at various strain levels are also presented in Figure 5.13.

Figure 5.14 shows the entire microstructure with the recrystallized grains, recrystallization wave-front and the equivalent stress distributions in the RVE after onset of DRX till the entire microstructure is recrystallized, i.e., at the same time steps viz. 4.9% strain, 13.2% strain, 32.4% strain, 38.3% strain and 41.8% strain. Figure 5.13 and Figure 5.14 show that the first set of material points that undergo recrystallization/nucleation are all decorating the boundaries. The decoration of nuclei along grain boundaries forming a necklace structure has been observed in many

experimental works on elevated temperature deformation in magnesium alloys (Al-Samman and Gottstein, 2008). From Figure 5.14, it can also be seen that these points are not necessarily either high or low stress locations.

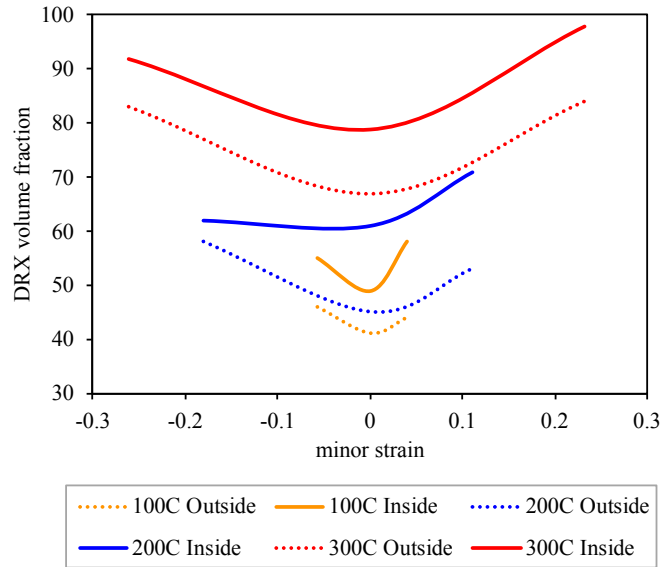


Figure 5.16: DRX volume fraction (percentage) inside and outside band with minor strain at failure strains at 100, 200 and 300°C.

As the deformation proceeds, more locations promote nucleation along with the growth of the existing recrystallized grains. The new nucleation events seen at 13.2% strain also show the same grain boundary decoration. After 32.4% strain, when the volume fraction of recrystallized grains is about 50% (Figure 5.13), both Figure 5.13 and Figure 5.14 suggest that there are almost no new nucleation events and from this point onwards, the increase in the volume fraction of DRX is primarily due to growth of the nuclei.

The stress contours at the corresponding strain levels show that even though the initial nucleation might not be correlated with stress gradients, the presence and growth of the nuclei affects the stress distribution. As the deformation proceeds and nuclei form the local stress in the DRX region drops significantly, as the model assigns new texture to the recrystallized region as well as relaxes the stress. This continues till the entire microstructure is recrystallized.

5.5.6 Recrystallization Outside and Inside Band

The FLD framework implemented in this study uses two RVEs one in the band and one outside the band. The strains in the band can go very high even though the macrostrain at forming limit is low. Hence, accurate representation of microstructure evolution at higher strains like the ones presented above are of extreme significance. To illustrate this, the initial and evolved microstructures for $\rho = 0.2$ at 300 °C are shown in Figure 5.15. Initially, the RVE is identical inside and outside the band as shown at the top in Figure 5.15.

During deformation, the regions inside and outside the band experience different amount of strain based on the orientation of the band groove angle and texture evolution. As a result, the two RVEs, inside and outside, evolve differently as shown at the bottom of Figure 5.15. For comparison purposes, the amount of DRX at failure strains corresponding to strain paths of the predicted FLDs at 100, 200 and 300°C are reported in Figure 5.16.

From Figure 5.15 and Figure 5.16, it can be concluded that not only they have undergone different amount of DRX with the region in the band having more DRX than the RVE outside the band implicating higher strain levels inside the band but also the nucleation and grain growth is quite different in both RVEs.

5.5.7 Effects of Initial Imperfection on FLD Predictions without DRX

To assess the importance of including DRX in the M-K analysis to predict FLDs, the same exercise presented in 5.5.4 is repeated for the model without DRX, but this time, the imperfection factor is calibrated so that the plane strain ($\rho = 0.0$) limit strain predicted by the model without DRX matches the experimental limit strain for plane strain (Figure 5.17). Figure 5.17 clearly shows that even though the plane strain point is calibrated, the rest of the FLD curve deviates from the measurements. Furthermore, for 200 and 300 °C, the model without DRX cannot predict the initial decrease in the limit strains in the biaxial stretching region, followed by the increase in limit strains towards balanced biaxial tension.

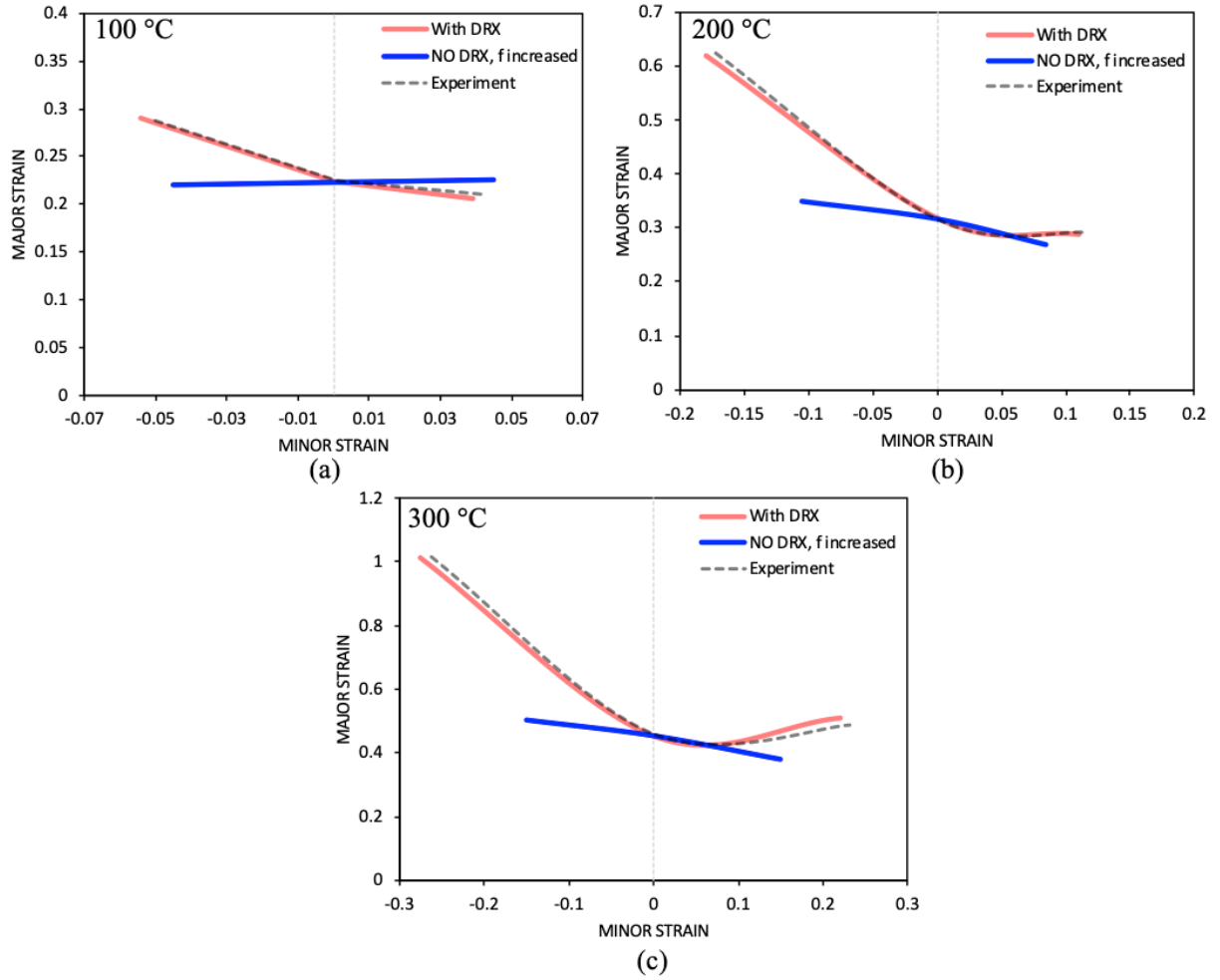


Figure 5.17: Comparison of predicted FLDs without DRX model (re-calibrated plane strain limit strain) with reduced imperfection (i.e., higher imperfection factor, f^{imp} in Equation (5.52)) with DRX model as well as with the experimental FLD of AZ31 sheet alloy strain at (a) 100 °C, (b) 200 °C, and (c) 300 °C.

5.6 Conclusions

A new full-field, efficient and mesh-free numerical framework, to model microstructure evolution, dynamic recrystallization (DRX) and formability in magnesium alloys at warm temperatures, is presented in this work. This coupled framework combines three approaches; (a) CP modelling of HCP alloys, (b) DRX model, and (c) Marciniak-Kuczynski (M-K) approach into the FFT-based method.

The developed framework is validated at each level of the coupling for the magnesium sheet alloy, AZ31. Simulations of FLDs with the new modelling framework demonstrated the importance of accounting for DRX in the model to accurately predict the limit strains for magnesium alloys at high temperatures; even if the plane strain point is calibrated to match the corresponding experimental measurement, the numerical model without DRX was not able to accurately capture the FLDs. Furthermore, the new framework with DRX was able to capture various phenomena observed experimentally such as a decrease in the limit strains followed by an increase towards balanced biaxial tension in the FLD simulations for 200 and 300°C.

Finally, the numerical analyses presented in this research revealed that the DRX strongly affects the deformed grain structure, grain size and texture evolution and thus, clearly demonstrated the need to properly account for the DRX mechanism for accurate predictions of FLDs for magnesium alloys at high temperatures.

In next chapter, the research conducted in this thesis is concluded and the scope for future work is provided.

Chapter 6. Conclusions and Future Work

Aluminum and magnesium alloys are polycrystalline materials. Automotive industry has significant interest in these materials as they are light weight and have high specific strength compared to the other engineering materials. For the improvement of vehicle fuel economy and reduced environmental impact of the automotive industry, the light-weighting of vehicles is crucial. Nowadays, in automotive industries, an important part of the design and testing of new light-weight components relies on the numerical simulation of aluminum and magnesium parts with crystal plasticity models. Better understanding of microstructure evolution of aluminum and magnesium alloys can significantly improve the accuracy of predictions of the material response using crystal plasticity theory. To achieve this, the crystal plasticity model must capture the important microstructural features such as texture, 3D grain morphology, grain interactions and recrystallization mechanisms. Therefore, in this thesis, five new and advanced micromechanics-based elasto-viscoplastic crystal plasticity models have been developed for modelling various deformation phenomena in polycrystalline materials.

The mechanical behavior of a polycrystalline material is also governed by the spatial distribution of the crystals and dynamics of crystalline defects. In order to establish the relationship between microstructure and properties of a polycrystalline materials undergoing plastic deformation, an accurate prediction of the micromechanical behavior based on directional material properties and gradual development of substructure of the constituent grains is required. Accordingly, in Chapter 3, a new, computationally efficient full-field crystal plasticity model based on fast Fourier transforms was developed to study the microstructure-property relations for FCC metals. The new numerical framework (**RTCP-FFT**) is developed by coupling a tangent modulus method-based crystal plasticity formulation with the fast Fourier transform (FFT) method to simulate large strain phenomena. The RTCP-FFT model is able to compute 3-D spatially resolved local micromechanical fields and effective response with high intragranular resolution. The RTCP-FFT show good agreement with EVP-FFT model at small strains (section 3.3) and excellent agreement with CP-FEM at large strains (Appendix - A). This framework is further used as a predictive tool for obtaining material response in new strain-paths with minimal calibration for aluminum alloys. The predicted macroscopic response (stress-strain curves) and microscopic response (texture

evolution) show excellent agreement with the experiments for various strain paths. Simulations also showed that the RTCP-FFT model has greatly improved efficiency when compared to the well-established EVP-FFT model, developed by Lebensohn et al. (2012), in terms of CPU time; an acceleration of about two orders of magnitude is achieved over the augmented Lagrangians procedure-based FFT methods.

The improved computational efficiency of the RTCP-FFT model makes it an excellent candidate to study the formability of polycrystalline metals since it can also account for the richness of three-dimensional microstructures. Therefore, in Chapter 4, the RTCP-FFT model was successfully implemented in a Marciniak-Kuczynski (M-K) type analysis (**MK-RTCP-FFT**) to predict the forming limit diagrams of FCC polycrystals. The MK-RTCP-FFT model can account for the effects of three-dimensional grain morphologies, texture as well as the grain interactions on FLD predictions. The MK-RTCP-FFT was employed to successfully predict the FLD for AA3003-O and AA5754-O. The simulations presented in Chapter 4 demonstrated that

1. employing the developed full-field model in M-K approach, for simulating formability of aluminum alloys, significantly improves the accuracy of predicted forming limit strains compared to MK-Taylor and MK-VPSC models.
2. amongst all microstructural features considered, the grain shapes (three-dimensional) had the most significant effect on the FLD predictions while the effects local grain neighborhoods and texture evolution both had relatively smaller effects.

To accurately predict the formability of HCP materials at elevated temperature, the developed approaches in Chapter 3 and Chapter 4 are extended to HCP materials and then further enhanced by including the effects of the dynamic recrystallization (DRX) and finally used for formability simulations. To achieve this goal, first the RTCP-FFT model developed in Chapter 3 is extended to model deformation slip, deformation twinning, texture evolution and micro/macro behavior in HCP alloys (**RTCP-FFT-HCP**) as outlined in Chapter 5. Then this model is coupled with cellular automata to simulate DRX and is named as **CA-RTCPFFT-HCP**. Finally, this is further coupled with M-K instability criteria to model effects of DRX on formability of magnesium alloys (**MK-CA-RTCP-FFT-HCP**). The developed framework is validated at each level of the coupling for

the magnesium sheet alloy, AZ31. Simulations of the FLDs for AZ31 sheet alloy at elevated temperatures with the new modelling framework have demonstrated

1. the importance of accounting for DRX in the model to accurately predict the limit strains for magnesium alloys at high temperatures;
2. the recalibration of plane strain point, alone, to the corresponding experimental measurement, is not sufficient to accurately capture the FLDs without considering the effects of DRX.

Furthermore, the new framework with DRX was able to capture various phenomena observed experimentally such as a decrease in the limit strains followed by an increase towards balanced biaxial tension in the FLD simulations for 200 and 300°C. The numerical analyses presented in Chapter 5 revealed that the DRX strongly affects the deformed grain structure, grain size and texture evolution and thus, clearly demonstrated the need to properly account for the DRX mechanism for accurate predictions of FLDs for magnesium alloys at high temperatures.

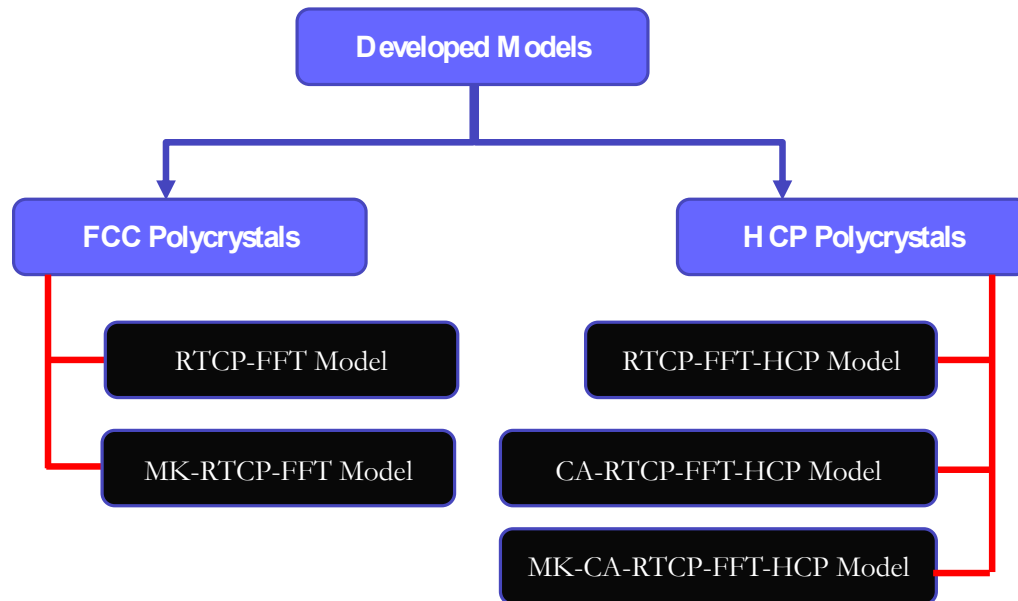


Figure 6.1: Summary of the developed models in present thesis.

A high-level flowchart that outlines the contributions of this thesis is presented in Figure 6.1.

Since the models developed in this thesis are based on the FFT approach for solving partial differential equations (PDEs), the developed models also inherit its advantages and disadvantages.

In next section, the overall advantages and limitations of the models developed in this thesis are presented.

6.1 Advantages of the Developed Models

- One of the main advantages of the fast Fourier transform-based crystal plasticity models developed in this thesis is the extremely small computational cost required to obtain response of an RVE with very high resolution of discretised FFT grid.
- The developed models don't require 3D meshes those especially conforming to microstructure that are notoriously time consuming and difficult to make, e.g., in case of CP-FEM.
- The FFT method requires a discrete grid of Fourier points for integration of constitutive equations. Therefore, complex input microstructures can be easily generated by sampling with a grid of Fourier points.
- Since the developed models are meshless, direct instantiation with 3D images from serial sectioning, 3D X-ray microscopy, or other sources is also possible.

6.2 Limitations of the Developed Models

- The developed models are intended for modelling material response using an RVE and are not suitable for solving dynamic boundary value problems.
- To solve the PDEs in Fourier space using the convolution theorem, periodic structure with regular grid of integration points is required which shortens their scope and limits their applicability to only RVE-based problems with periodic microstructure.

6.3 Scope for Future Work

In future work, the new FFT-based crystal plasticity models developed in this thesis will be further explored and developed. Due to their excellent computational efficiency and robustness, these models can be further coupled with phenomenological modelling approaches, e.g., FEM or Peridynamics, to model mechanical response of lab-scale components. This multi-scale model can be of hierarchal nature, i.e., the deformation gradient at each material point in the component can be obtained using either FEM or peridynamics which can then be used as an input to, e.g., RTCP-FFT model. After computing the microstructural information using RTCP-FFT model, it can be passed to FEM or peridynamics solver that will, in-turn, affect the macroscopic response of the component.

References

- Abdolvand, H., Daymond, M.R., 2012. Internal strain and texture development during twinning: Comparing neutron diffraction measurements with crystal plasticity finite-element approaches. *Acta Mater.* 60, 2240–2248. <https://doi.org/10.1016/j.actamat.2012.01.016>
- Abdolvand, H., Majkut, M., Oddershede, J., Schmidt, S., Lienert, U., Diak, B.J., Withers, P.J., Daymond, M.R., 2015. On the deformation twinning of Mg AZ31B: A three-dimensional synchrotron X-ray diffraction experiment and crystal plasticity finite element model. *Int. J. Plast.* 70, 77–97. <https://doi.org/10.1016/j.ijplas.2015.03.001>
- Al-Samman, T., Gottstein, G., 2008. Room temperature formability of a magnesium AZ31 alloy: Examining the role of texture on the deformation mechanisms. *Mater. Sci. Eng. A* 488, 406–414. <https://doi.org/10.1016/j.msea.2007.11.056>
- Alharbi, H.F., Kalidindi, S.R., 2015. Crystal plasticity finite element simulations using a database of discrete Fourier transforms. *Int. J. Plast.* 66, 71–84. <https://doi.org/10.1016/j.ijplas.2014.04.006>
- Ali, U., Brahme, A.P., Mishra, R.K., Inal, K., 2016. New Methodology to Determine Stable Texture Components Under Cold Rolling in FCC Metals, in: *Light Metals 2016*. John Wiley & Sons, Inc., pp. 157–161. <https://doi.org/10.1002/9781119274780.ch27>
- Anderson, M.P., Grest, G.S., Doherty, R.D., Li, K., Srolovitz, D.J., 1989. Inhibition of grain growth by second phase particles: Three dimensional Monte Carlo computer simulations. *Scr. Metall.* 23, 753–758. [https://doi.org/10.1016/0036-9748\(89\)90525-5](https://doi.org/10.1016/0036-9748(89)90525-5)
- Anglin, B.S., Lebensohn, R.A., Rollett, A.D., 2014. Validation of a numerical method based on Fast Fourier Transforms for heterogeneous thermoelastic materials by comparison with analytical solutions. *Comput. Mater. Sci.* 87, 209–217. <https://doi.org/10.1016/j.commatsci.2014.02.027>
- Ardeljan, M., Beyerlein, I.J., Knezevic, M., 2017. Effect of dislocation density-twin interactions on twin growth in AZ31 as revealed by explicit crystal plasticity finite element modelling. *Int. J. Plast.* 99, 81–101. <https://doi.org/10.1016/j.ijplas.2017.09.002>

- Armstrong, R.W., Walley, S.M., 2008. High strain rate properties of metals and alloys. *Int. Mater. Rev.* 53, 105–128. <https://doi.org/10.1179/174328008X277795>
- Arsenlis, A., Parks, D.M., 2002. Modeling the evolution of crystallographic dislocation density in crystal plasticity. *J. Mech. Phys. Solids* 50, 1979–2009. [https://doi.org/10.1016/S0022-5096\(01\)00134-X](https://doi.org/10.1016/S0022-5096(01)00134-X)
- Arsenlis, A., Parks, D.M., 1999. Crystallographic aspects of geometrically-necessary and statistically-stored dislocation density. *Acta Mater.* 47, 1597–1611. [https://doi.org/10.1016/S1359-6454\(99\)00020-8](https://doi.org/10.1016/S1359-6454(99)00020-8)
- Arsenlis, A., Parks, D.M., Becker, R., Bulatov, V. V., 2004. On the evolution of crystallographic dislocation density in non-homogeneously deforming crystals. *J. Mech. Phys. Solids* 52, 1213–1246. <https://doi.org/10.1016/j.jmps.2003.12.007>
- Arul Kumar, M., Mahesh, S., Parameswaran, V., 2011. A “stack” model of rate-independent polycrystals. *Int. J. Plast.* 27, 962–981. <https://doi.org/10.1016/j.ijplas.2010.10.010>
- Asaro, R.J., Needleman, A., 1985. Overview no. 42 Texture development and strain hardening in rate dependent polycrystals. *Acta Metall.* 33, 923–953. [https://doi.org/10.1016/0001-6160\(85\)90188-9](https://doi.org/10.1016/0001-6160(85)90188-9)
- Asaro, R.J., Rice, J.R., 1977. Strain localization in ductile single crystals, *Journal of the Mechanics and Physics of Solids*. Office of Scientific and Technical Information ({OSTI}). [https://doi.org/10.1016/0022-5096\(77\)90001-1](https://doi.org/10.1016/0022-5096(77)90001-1)
- Avrami, M., 1939. Kinetics of phase change. I: General theory. *J. Chem. Phys.* 7, 1103–1112. <https://doi.org/10.1063/1.1750380>
- Azrin, M., Backofen, W.A., 1970. The deformation and failure of a biaxially stretched sheet. *Metall. Trans.* 1, 2857–2865. <https://doi.org/10.1007/BF03037824>
- Bagheriasl, R., Ghavam, K., Worswick, M., 2011. Formability analysis of aluminum alloy sheets at elevated temperatures with numerical simulation based on the M-K method, in: *AIP Conference Proceedings*. pp. 1517–1522. <https://doi.org/10.1063/1.3589732>

Bailey, J.E., Hirsch, P.B., 1962. The Recrystallization Process in Some Polycrystalline Metals. *Proc. R. Soc. A Math. Phys. Eng. Sci.* 267, 11–30. <https://doi.org/10.1098/rspa.1962.0080>

Balasubramanian, S., Anand, L., 2002. Plasticity of initially textured hexagonal polycrystals at high homologous temperatures: Application to titanium. *Acta Mater.* 50, 133–148. [https://doi.org/10.1016/S1359-6454\(01\)00326-3](https://doi.org/10.1016/S1359-6454(01)00326-3)

Barlat, F., 1989. Forming Limit Diagrams-Predictions based on some microstructural aspects of materials. *Form. Limit Diagrams Concepts, methods Appl.* 275–301.

Barlat, F., 1987. Crystallographic texture, anisotropic yield surfaces and forming limits of sheet metals. *Mater. Sci. Eng.* 91, 55–72. [https://doi.org/10.1016/0025-5416\(87\)90283-7](https://doi.org/10.1016/0025-5416(87)90283-7)

Barlat, F., Brem, J.C., Yoon, J.W., Chung, K., Dick, R.E., Lege, D.J., Pourboghra, F., Choi, S.H., Chu, E., 2003. Plane stress yield function for aluminum alloy sheets - Part 1: Theory. *Int. J. Plast.* 19, 1297–1319. [https://doi.org/10.1016/S0749-6419\(02\)00019-0](https://doi.org/10.1016/S0749-6419(02)00019-0)

Bassani, J., Hutchinson, J., Neale, K., 1979. On the prediction of necking in anisotropic sheets. *Met. Form. Plast.* https://doi.org/10.1007/978-3-642-81355-9_1

Bauer, O., Baneth, G., Eshkol, T., Shaw, S.E., Harrus, S., 2006. Polygenic detection of *Rickettsia felis* in cat fleas (*Ctenocephalides felis*) from Israel. *Am. J. Trop. Med. Hyg.* 74, 444–448. [https://doi.org/10.1016/S0022-5096\(02\)00032-7](https://doi.org/10.1016/S0022-5096(02)00032-7)

Beer, A.G., Barnett, M.R., 2007. Microstructural development during hot working of Mg-3Al-1Zn. *Metall. Mater. Trans. A Phys. Metall. Mater. Sci.* 38, 1856–1867. <https://doi.org/10.1007/s11661-007-9207-5>

Biswas, S., Suwas, S., Sikand, R., Gupta, A.K., 2011. Analysis of texture evolution in pure magnesium and the magnesium alloy AM30 during rod and tube extrusion. *Mater. Sci. Eng. A* 528, 3722–3729. <https://doi.org/10.1016/j.msea.2011.01.021>

Bohlen, J., Letzig, D., Kainer, K.U., 2007. New Perspectives for Wrought Magnesium Alloys. *Mater. Sci. Forum* 546–549, 1–10. <https://doi.org/10.4028/www.scientific.net/MSF.546-549.1>

- Boudeau, N., Gelin, J.C., 2000. Necking in sheet metal forming. Influence of macroscopic and microscopic properties of materials. *Int. J. Mech. Sci.* 42, 2209–2232. [https://doi.org/10.1016/S0020-7403\(00\)00003-5](https://doi.org/10.1016/S0020-7403(00)00003-5)
- Boudeau, N., Gelin, J.C., Salhi, S., 1998. Computational prediction of the localized necking in sheet forming based on microstructural material aspects. *Comput. Mater. Sci.* 11, 45–64. [https://doi.org/10.1016/S0927-0256\(97\)00153-5](https://doi.org/10.1016/S0927-0256(97)00153-5)
- Brahme, A., Alvi, M.H., Saylor, D., Fridy, J., Rollett, A.D., 2006. 3D reconstruction of microstructure in a commercial purity aluminum. *Scr. Mater.* 55, 75–80. <https://doi.org/10.1016/j.scriptamat.2006.02.017>
- Brahme, A., Staraselski, Y., Inal, K., Mishra, R.K., 2012. Determination of the minimum scan size to obtain representative textures by electron backscatter diffraction. *Metall. Mater. Trans. A Phys. Metall. Mater. Sci.* 43, 5298–5307. <https://doi.org/10.1007/s11661-012-1364-5>
- Brahme, A.P., Inal, K., Mishra, R.K., Saimoto, S., 2011. A new strain hardening model for rate-dependent crystal plasticity. *Comput. Mater. Sci.* 50, 2898–2908. <https://doi.org/10.1016/j.commatsci.2011.05.006>
- Brenner, R., Lebensohn, R.A., Castelnau, O., 2009. Elastic anisotropy and yield surface estimates of polycrystals. *Int. J. Solids Struct.* 46, 3018–3026. <https://doi.org/10.1016/j.ijsolstr.2009.04.001>
- Brisard, S., Dormieux, L., 2010. FFT-based methods for the mechanics of composites: A general variational framework. *Comput. Mater. Sci.* 49, 663–671. <https://doi.org/10.1016/j.commatsci.2010.06.009>
- Bronkhorst, C.A., Kalidindi, S.R., Anand, L., 1992. Polycrystalline Plasticity and the Evolution of Crystallographic Texture in FCC Metals. *Philos. Trans. R. Soc. A Math. Phys. Eng. Sci.* 341, 443–477. <https://doi.org/10.1098/rsta.1992.0111>
- Bunge, H.J., Esling, C., 1984. Texture development by plastic deformation. *Scr. Metall.* 18, 191–195. [https://doi.org/10.1016/0036-9748\(84\)90506-4](https://doi.org/10.1016/0036-9748(84)90506-4)

- Cahn, R.W., 1950. A new theory of recrystallization nuclei. *Proc. Phys. Soc. Sect. A* 63, 323–336. <https://doi.org/10.1088/0370-1298/63/4/302>
- Callister Jr, W.D., 2000. *Materials Science and Engineering - An Introduction* (5th ed.). Anti-Corrosion Methods Mater. 47, acmm.2000.12847aae.001. <https://doi.org/10.1108/acmm.2000.12847aae.001>
- Chang, Y.W., Asaro, R.J., 1981. An experimental study of shear localization in aluminum-copper single crystals. *Acta Metall.* 29, 241–257. [https://doi.org/10.1016/0001-6160\(81\)90103-6](https://doi.org/10.1016/0001-6160(81)90103-6)
- Chen, F.K., Huang, T. Bin, Chang, C.K., 2003. Deep drawing of square cups with magnesium alloy AZ31 sheets. *Int. J. Mach. Tools Manuf.* 43, 1553–1559. [https://doi.org/10.1016/S0890-6955\(03\)00198-6](https://doi.org/10.1016/S0890-6955(03)00198-6)
- Chen, L., Chen, J., Lebensohn, R.A., Ji, Y.Z., Heo, T.W., Bhattacharyya, S., Chang, K., Mathaudhu, S., Liu, Z.K., Chen, L.Q., 2015. An integrated fast Fourier transform-based phase-field and crystal plasticity approach to model recrystallization of three dimensional polycrystals. *Comput. Methods Appl. Mech. Eng.* 285, 829–848. <https://doi.org/10.1016/j.cma.2014.12.007>
- Chiba, R., Takeuchi, H., Kuroda, M., Hakoyama, T., Kuwabara, T., 2013. Theoretical and experimental study of forming-limit strain of half-hard AA1100 aluminium alloy sheet. *Comput. Mater. Sci.* 77, 61–71. <https://doi.org/10.1016/j.commatsci.2013.04.025>
- Chino, Y., Iwasaki, H., Mabuchi, M., 2007. Stretch formability of AZ31 Mg alloy sheets at different testing temperatures. *Mater. Sci. Eng. A* 466, 90–95. <https://doi.org/10.1016/j.msea.2007.02.027>
- Choi, S.H., Brem, J.C., Barlat, F., Oh, K.H., 2000. Macroscopic anisotropy in AA5019A sheets. *Acta Mater.* 48, 1853–1863. [https://doi.org/10.1016/S1359-6454\(99\)00470-X](https://doi.org/10.1016/S1359-6454(99)00470-X)
- Conway, J.H., Sloane, N.J.A., 1993. *Sphere Packings and Kissing Numbers*. pp. 1–30. https://doi.org/10.1007/978-1-4757-2249-9_1

- Crumbach, M., Goerdeler, M., Gottstein, G., 2002. Nucleation spectra for recrystallization simulated with the grain interaction model for deformation textures. *Textures Mater. Pts 1 2* 408–4, 425–432. <https://doi.org/10.4028/www.scientific.net/msf.408-412.425>
- Curtin, W.A., Miller, R.E., 2003. Atomistic/continuum coupling in computational materials science. *Model. Simul. Mater. Sci. Eng.* 11, R33–R68. <https://doi.org/10.1088/0965-0393/11/3/201>
- Cyr, E., Mohammadi, M., Brahme, A., Mishra, R.K., Inal, K., 2017. Modeling the formability of aluminum alloys at elevated temperatures using a new thermo-elasto-viscoplastic crystal plasticity framework. *Int. J. Mech. Sci.* 128–129, 312–325. <https://doi.org/10.1016/j.ijmecsci.2017.05.005>
- Cyr, E.D., Brahme, A., Mohammadi, M., Mishra, R.K., Inal, K., 2018. A new crystal plasticity framework to simulate the large strain behaviour of aluminum alloys at warm temperatures. *Mater. Sci. Eng. A* 727, 11–28. <https://doi.org/10.1016/j.msea.2018.04.020>
- Cyr, E.D., Mohammadi, M., Mishra, R.K., Inal, K., 2015. A three dimensional (3D) thermo-elasto-viscoplastic constitutive model for FCC polycrystals. *Int. J. Plast.* 70, 166–190. <https://doi.org/10.1016/j.ijplas.2015.04.001>
- de Geus, T.W.J., Vondřejc, J., Zeman, J., Peerlings, R.H.J., Geers, M.G.D., 2017. Finite strain FFT-based non-linear solvers made simple. *Comput. Methods Appl. Mech. Eng.* 318, 412–430. <https://doi.org/10.1016/j.cma.2016.12.032>
- Delannay, L., Kalidindi, S.R., Van Houtte, P., 2002. Quantitative prediction of textures in aluminium cold rolled to moderate strains. *Mater. Sci. Eng. A* 336, 233–244. [https://doi.org/10.1016/S0921-5093\(01\)01966-9](https://doi.org/10.1016/S0921-5093(01)01966-9)
- Delannay, L., Melchior, M.A., Signorelli, J.W., Remacle, J.F., Kuwabara, T., 2009. Influence of grain shape on the planar anisotropy of rolled steel sheets - evaluation of three models. *Comput. Mater. Sci.* 45, 739–743. <https://doi.org/10.1016/j.commatsci.2008.06.013>
- Doherty, R.D., 1997. Recrystallization and texture. *Prog. Mater. Sci.* 42, 39–58. [https://doi.org/10.1016/S0079-6425\(97\)00007-8](https://doi.org/10.1016/S0079-6425(97)00007-8)

- Eisenlohr, P., Diehl, M., Lebensohn, R.A., Roters, F., 2013. A spectral method solution to crystal elasto-viscoplasticity at finite strains. *Int. J. Plast.* 46, 37–53. <https://doi.org/10.1016/j.ijplas.2012.09.012>
- Eisenlohr, P., Tjahjanto, D.D., Hochrainer, T., Roters, F., Raabe, D., 2009. Texture prediction from a novel grain cluster-based homogenization scheme. *Int. J. Mater. Form.* 2, 523–526. <https://doi.org/10.1007/s12289-009-0561-2>
- Eisenlohr, P., Tjahjanto, D.D., Hochrainer, T., Roters, F., Raabe, D., 2009. Comparison of texture evolution in fcc metals predicted by various grain cluster homogenization schemes. *Int. J. Mater. Res.* 100, 500–509. <https://doi.org/10.3139/146.110071>
- Engler, O., Crumbach, M., Li, S., 2005. Alloy-dependent rolling texture simulation of aluminium alloys with a grain-interaction model. *Acta Mater.* 53, 2241–2257. <https://doi.org/10.1016/j.actamat.2005.01.032>
- Erinosho, T.O., Collins, D.M., Wilkinson, A.J., Todd, R.I., Dunne, F.P.E., 2016. Assessment of X-ray diffraction and crystal plasticity lattice strain evolutions under biaxial loading. *Int. J. Plast.* 83, 1–18. <https://doi.org/10.1016/j.ijplas.2016.03.011>
- Eshelby, J.D., 1957. The Determination of the Elastic Field of an Ellipsoidal Inclusion, and Related Problems. *Proc. R. Soc. A Math. Phys. Eng. Sci.* 241, 376–396. <https://doi.org/10.1098/rspa.1957.0133>
- Eyre, D.J., Milton, G.W., 1999. A fast numerical scheme for computing the response of composites using grid reenement. *Eur. Phys. Journal-Applied Phys.* 6, 41–47. <https://doi.org/10.1051/epjap:1999150>
- Fernández, A., Pérez Prado, M.T., Wei, Y., Jérusalem, A., 2011. Continuum modelling of the response of a Mg alloy AZ31 rolled sheet during uniaxial deformation. *Int. J. Plast.* 27, 1739–1757. <https://doi.org/10.1016/j.ijplas.2011.05.002>

- Furu, T., Ørsund, R., Nes, E., 1995. Subgrain growth in heavily deformed aluminium-experimental investigation and modelling treatment. *Acta Metall. Mater.* 43, 2209–2232. [https://doi.org/10.1016/0956-7151\(94\)00410-2](https://doi.org/10.1016/0956-7151(94)00410-2)
- Galiyev, A., Kaibyshev, R., Gottstein, G., 2001. Correlation of plastic deformation and dynamic recrystallization in magnesium alloy ZK60. *Acta Mater.* 49, 1199–1207. [https://doi.org/10.1016/S1359-6454\(01\)00020-9](https://doi.org/10.1016/S1359-6454(01)00020-9)
- Gardner, C.J., Adams, B.L., Basinger, J., Fullwood, D.T., 2010. EBSD-based continuum dislocation microscopy. *Int. J. Plast.* 26, 1234–1247. <https://doi.org/10.1016/j.ijplas.2010.05.008>
- Ghaffari Tari, D., Worswick, M.J., Ali, U., Gharghouri, M.A., 2014. Mechanical response of AZ31B magnesium alloy: Experimental characterization and material modelling considering proportional loading at room temperature. *Int. J. Plast.* 55, 247–267. <https://doi.org/10.1016/j.ijplas.2013.10.006>
- Goetz, R.L., Seetharaman, V., 1998. Modeling dynamic recrystallization using cellular automata. *Scr. Mater.* 38, 405–413. [https://doi.org/10.1016/S1359-6462\(97\)00500-9](https://doi.org/10.1016/S1359-6462(97)00500-9)
- Goodwin, G.M., 1968. Application of Strain Analysis to Sheet Metal Forming Problems in the Press Shop, in: SAE Technical Paper. SAE International. <https://doi.org/10.4271/680093>
- Gottstein, G., 2004. Physical foundations of materials science, Materials Today. Springer Berlin Heidelberg, Berlin, Heidelberg. [https://doi.org/10.1016/S1369-7021\(04\)00348-7](https://doi.org/10.1016/S1369-7021(04)00348-7)
- Gottstein, G., Molodov, D.A., Shvindlerman, L.S., 1998. Grain Boundary Migration in Metals : Recent Developments, Interface Science. Taylor & Francis. <https://doi.org/10.1023/A:1008641617937>
- Grennerat, F., Montagnat, M., Castelnau, O., Vacher, P., Moulinec, H., Suquet, P., Duval, P., 2012. Experimental characterization of the intragranular strain field in columnar ice during transient creep. *Acta Mater.* 60, 3655–3666. <https://doi.org/10.1016/j.actamat.2012.03.025>

- Grilli, N., Janssens, K.G.F., Nellesen, J., Sandlöbes, S., Raabe, D., 2018. Multiple slip dislocation patterning in a dislocation-based crystal plasticity finite element method. *Int. J. Plast.* 100, 104–121. <https://doi.org/10.1016/j.ijplas.2017.09.015>
- Gurtin, M.E., Lusk, M.T., 1999. Sharp-interface and phase-field theories of recrystallization in the plane. *Phys. D Nonlinear Phenom.* 130, 133–154. [https://doi.org/10.1016/S0167-2789\(98\)00323-6](https://doi.org/10.1016/S0167-2789(98)00323-6)
- Hallberg, H., 2011. Approaches to Modeling of Recrystallization. *Metals (Basel)*. 1, 16–48. <https://doi.org/10.3390/met1010016>
- Hantson, P., Jaeger, A., 2006. Décontamination et élimination des toxiques médicamenteux, Reanimation. <https://doi.org/10.1016/j.reaurg.2006.06.017>
- Hausöl, T., Höppel, H.W., Göken, M., 2010. Tailoring materials properties of UFG aluminium alloys by accumulative roll bonded sandwich-like sheets. *J. Mater. Sci.* 45, 4733–4738. <https://doi.org/10.1007/s10853-010-4678-y>
- Hill, R., 1952. On discontinuous plastic states, with special reference to localized necking in thin sheets. *J. Mech. Phys. Solids* 1, 19–30. [https://doi.org/10.1016/0022-5096\(52\)90003-3](https://doi.org/10.1016/0022-5096(52)90003-3)
- Houtte, P. Van, 1978. Simulation of the rolling and shear texture of brass by the Taylor theory adapted for mechanical twinning. *Acta Metall.* 26, 591–604. [https://doi.org/10.1016/0001-6160\(78\)90111-6](https://doi.org/10.1016/0001-6160(78)90111-6)
- Hu, L., Rollett, A.D., Iadicola, M., Foecke, T., Banovic, S., 2012. Constitutive relations for AA 5754 based on crystal plasticity. *Metall. Mater. Trans. A Phys. Metall. Mater. Sci.* 43, 854–869. <https://doi.org/10.1007/s11661-011-0927-1>
- Hutchinson, J.W., 1976. Bounds and Self-Consistent Estimates for Creep of Polycrystalline Materials. *Proc. R. Soc. A Math. Phys. Eng. Sci.* 348, 101–127. <https://doi.org/10.1098/rspa.1976.0027>

Hutchinson, J.W., Neale, K.W., 1978a. Sheet Necking-II. Time-Independent Behavior, in: *Mechanics of Sheet Metal Forming*. Springer Nature, pp. 127–153. https://doi.org/10.1007/978-1-4613-2880-3_6

Hutchinson, J.W., Neale, K.W., 1978b. Sheet Necking-III. Strain-Rate Effects, in: *Mechanics of Sheet Metal Forming*. Springer Nature, pp. 269–285. https://doi.org/10.1007/978-1-4613-2880-3_11

Iadicola, M.A., Foecke, T., Banovic, S.W., 2008. Experimental observations of evolving yield loci in biaxially strained AA5754-O. *Int. J. Plast.* 24, 2084–2101. <https://doi.org/10.1016/j.ijplas.2008.03.003>

Inal, K., Mishra, R.K., 2012. Crystal plasticity based numerical modelling of large strain deformation in hexagonal closed packed metals, in: *Procedia IUTAM*. pp. 239–273. <https://doi.org/10.1016/j.piutam.2012.03.016>

Inal, K., Mishra, R.K., Cazacu, O., 2010. Forming simulation of aluminum sheets using an anisotropic yield function coupled with crystal plasticity theory. *Int. J. Solids Struct.* 47, 2223–2233. <https://doi.org/10.1016/j.ijsolstr.2010.04.017>

Inal, K., Neale, K.W., Aboutajeddine, A., 2005. Forming limit comparisons for FCC and BCC sheets. *Int. J. Plast.* 21, 1255–1266. <https://doi.org/10.1016/j.ijplas.2004.08.001>

Inal, K., Neale, K.W., Wu, P.D., 2002. Parallel finite element algorithms for the analysis of multiscale plasticity problems, *Advances in High Performance Computing*.

Inal, K., Wu, P.D., Neale, K.W., 2002a. Finite element analysis of localization in FCC polycrystalline sheets under plane stress tension. *Int. J. Solids Struct.* 39, 3469–3486. [https://doi.org/10.1016/S0020-7683\(02\)00162-2](https://doi.org/10.1016/S0020-7683(02)00162-2)

Inal, K., Wu, P.D., Neale, K.W., 2002b. Instability and localized deformation in polycrystalline solids under plane-strain tension. *Int. J. Solids Struct.* 39, 983–1002. [https://doi.org/10.1016/S0020-7683\(01\)00246-3](https://doi.org/10.1016/S0020-7683(01)00246-3)

- Izadbakhsh, A., Inal, K., Mishra, R.K., Niewczas, M., 2011. New crystal plasticity constitutive model for large strain deformation in single crystals of magnesium. *Comput. Mater. Sci.* 50, 2185–2202. <https://doi.org/10.1016/j.commatsci.2011.02.030>
- Jain, J., Poole, W.J., Sinclair, C.W., 2012. The deformation behaviour of the magnesium alloy AZ80 at 77 and 293K. *Mater. Sci. Eng. A* 547, 128–137. <https://doi.org/10.1016/j.msea.2012.04.003>
- Janssens, K.G.F., 2010. An introductory review of cellular automata modelling of moving grain boundaries in polycrystalline materials. *Math. Comput. Simul.* 80, 1361–1381. <https://doi.org/10.1016/j.matcom.2009.02.011>
- Janssens, K.G.F., 2003. Random grid, three-dimensional, space-time coupled cellular automata for the simulation of recrystallization and grain growth. *Model. Simul. Mater. Sci. Eng.* 11, 157–171. <https://doi.org/10.1088/0965-0393/11/2/304>
- Jeong, Y., Gnäupel-Herold, T., Barlat, F.G., Iadicola, M., Creuziger, A., Lee, M.G., 2015. Evaluation of biaxial flow stress based on elasto-viscoplastic self-consistent analysis of X-ray diffraction measurements. *Int. J. Plast.* 66, 103–118. <https://doi.org/10.1016/j.ijplas.2014.06.009>
- Jeong, Y., Pham, M.S., Iadicola, M., Creuziger, A., Foecke, T., 2016. Forming limit prediction using a self-consistent crystal plasticity framework: A case study for body-centered cubic materials. *Model. Simul. Mater. Sci. Eng.* 24, 055005. <https://doi.org/10.1088/0965-0393/24/5/055005>
- Kabel, M., Fliegner, S., Schneider, M., 2016. Mixed boundary conditions for FFT-based homogenization at finite strains. *Comput. Mech.* 57, 193–210. <https://doi.org/10.1007/s00466-015-1227-1>
- Kaibyshev, R., 2012. Dynamic recrystallization in magnesium alloys. *Adv. Wrought Magnes. Alloy. Fundam. Process. Prop. Appl.* 42, 186–225. <https://doi.org/10.1016/B978-1-84569-968-0.50005-3>

- Kalidindi, S.R., 1998. Incorporation of deformation twinning in crystal plasticity models. *J. Mech. Phys. Solids* 46, 267–290. [https://doi.org/10.1016/S0022-5096\(97\)00051-3](https://doi.org/10.1016/S0022-5096(97)00051-3)
- Kalidindi, S.R., Bronkhorst, C.A., Anand, L., 1992. Crystallographic texture evolution in bulk deformation processing of {FCC} metals. *J. Mech. Phys. Sol.* 40, 536–569. [https://doi.org/10.1016/0022-5096\(92\)80003-9](https://doi.org/10.1016/0022-5096(92)80003-9)
- Kalidindi, S.R., Duvvuru, H.K., 2005. Spectral methods for capturing crystallographic texture evolution during large plastic strains in metals. *Acta Mater.* 53, 3613–3623. <https://doi.org/10.1016/j.actamat.2005.04.017>
- Kalidindi, S.R., Duvvuru, H.K., Knezevic, M., 2006. Spectral calibration of crystal plasticity models. *Acta Mater.* 54, 1795–1804. <https://doi.org/10.1016/j.actamat.2005.12.018>
- Kapoor, R., 2017. Severe Plastic Deformation of Materials. *Mater. Under Extrem. Cond.* 44, 717–754. <https://doi.org/10.1016/B978-0-12-801300-7.00020-6>
- Karel, J., Casoli, F., Lupo, P., Nasi, L., Fabbri, S., Righi, L., Albertini, F., Felser, C., 2016. Evidence for in-plane tetragonal c-axis in $\text{Mn}_x\text{Ga}_{1-x}$ thin films using transmission electron microscopy. *Scr. Mater.* 114, 165–169. <https://doi.org/10.1016/j.scriptamat.2015.11.019>
- Keeler, S., Backofen, W., 1964. Plastic instability and fracture in sheets stretched over rigid punches. *ASM Trans. Quart. Massachusetts Institute of Technology, Cambridge, MA.* <https://doi.org/10.1007/s12143-011-9087-8>
- Kelley, E.W., Hosford, W.F., 1968. The Deformation Characteristics of Textured Magnesium. | National Technical Reports Library - NTIS. *Trans. TMS-AIME*, 242 242, 654–661.
- Khan, A.S., Pandey, A., Gnäupel-Herold, T., Mishra, R.K., 2011. Mechanical response and texture evolution of AZ31 alloy at large strains for different strain rates and temperatures. *Int. J. Plast.* 27, 688–706. <https://doi.org/10.1016/j.ijplas.2010.08.009>
- Kocks, U.F., Tomé, C.N., Wenk, H.R., 2005. *Texture and Anisotropy: Preferred Orientations in Polycrystals and their Effect on Materials Properties*. Cambridge University Press.

Lebensohn, R.A., 2001. N-site modelling of a 3D viscoplastic polycrystal using Fast Fourier Transform. *Acta Mater.* 49, 2723–2737. [https://doi.org/10.1016/S1359-6454\(01\)00172-0](https://doi.org/10.1016/S1359-6454(01)00172-0)

Lebensohn, R.A., Brenner, R., Castelnau, O., Rollett, A.D., 2008. Orientation image-based micromechanical modelling of subgrain texture evolution in polycrystalline copper. *Acta Mater.* 56, 3914–3926. <https://doi.org/10.1016/j.actamat.2008.04.016>

Lebensohn, R.A., Kanjarla, A.K., Eisenlohr, P., 2012. An elasto-viscoplastic formulation based on fast Fourier transforms for the prediction of micromechanical fields in polycrystalline materials. *Int. J. Plast.* 32–33, 59–69. <https://doi.org/10.1016/j.ijplas.2011.12.005>

Lebensohn, R.A., Liu, Y., Castañeda, P.P., 2004. On the accuracy of the self-consistent approximation for polycrystals: Comparison with full-field numerical simulations. *Acta Mater.* 52, 5347–5361. <https://doi.org/10.1016/j.actamat.2004.07.040>

Lebensohn, R.A., Rollett, A.D., Suquet, P., 2011. Keeping up with emerging characterization methods of crystalline materials: Fast Fourier Transform-based modelling for the determination of micromechanical fields in polycrystals Ricardo A. Lebensohn, Anthony D. Rollett and Pierre Suquet 3, 13–18.

Lebensohn, R.A., Rollett, A.D., Suquet, P., 2011. Fast fourier transform-based modelling for the determination of micromechanical fields in polycrystals. *Jom* 63, 13–18. <https://doi.org/10.1007/s11837-011-0037-y>

Lebensohn, R.A., Tomé, C.N., 1993. A self-consistent anisotropic approach for the simulation of plastic deformation and texture development of polycrystals: Application to zirconium alloys. *Acta Metall. Mater.* 41, 2611–2624. [https://doi.org/10.1016/0956-7151\(93\)90130-K](https://doi.org/10.1016/0956-7151(93)90130-K)

Lebensohn, R.A., Tomé, C.N., Castañeda, P.P., 2007. Self-consistent modelling of the mechanical behaviour of viscoplastic polycrystals incorporating intragranular field fluctuations. *Philos. Mag.* 87, 4287–4322. <https://doi.org/10.1080/14786430701432619>

Lee, E.H., 1969. Elastic-Plastic Deformation at Finite Strains. *J. Appl. Mech.* 36, 1. <https://doi.org/10.1115/1.3564580>

- Lee, M.G., Kim, S.J., Han, H.N., 2010. Crystal plasticity finite element modelling of mechanically induced martensitic transformation (MIMT) in metastable austenite. *Int. J. Plast.* 26, 688–710. <https://doi.org/10.1016/j.ijplas.2009.10.001>
- Lee, W.S., Lam, H.F., 1996. The deformation behaviour and microstructure evolution of high-strength alloy steel at high rate of strain. *J. Mater. Process. Technol.* 57, 233–240. [https://doi.org/10.1016/0924-0136\(95\)02068-3](https://doi.org/10.1016/0924-0136(95)02068-3)
- Lentz, M., Risse, M., Schaefer, N., Reimers, W., Beyerlein, I.J., 2016. Strength and ductility with {10 11}-{1012} double twinning in a magnesium alloy. *Nat. Commun.* 7, 11068. <https://doi.org/10.1038/ncomms11068>
- Lévesque, J., Inal, K., Neale, K.W., Mishra, R.K., 2010. Numerical modelling of formability of extruded magnesium alloy tubes. *Int. J. Plast.* 26, 65–83. <https://doi.org/10.1016/j.ijplas.2009.05.001>
- Lévesque, J., Mohammadi, M., Mishra, R.K., Inal, K., 2016. An extended Taylor model to simulate localized deformation phenomena in magnesium alloys. *Int. J. Plast.* 78, 203–222. <https://doi.org/10.1016/j.ijplas.2015.10.012>
- Li, H., Sun, X., Yang, H., 2016. A three-dimensional cellular automata-crystal plasticity finite element model for predicting the multiscale interaction among heterogeneous deformation, DRX microstructural evolution and mechanical responses in titanium alloys. *Int. J. Plast.* 87, 154–180. <https://doi.org/10.1016/j.ijplas.2016.09.008>
- Lippmann, B.A., Schwinger, J., 1950. Variational principles for scattering processes. I. *Phys. Rev.* 79, 469–480. <https://doi.org/10.1103/PhysRev.79.469>
- Liu, B., Raabe, D., Roters, F., Eisenlohr, P., Lebensohn, R.A., 2010. Comparison of finite element and fast Fourier transform crystal plasticity solvers for texture prediction. *Model. Simul. Mater. Sci. Eng.* 18, 085005. <https://doi.org/10.1088/0965-0393/18/8/085005>

- Liu, Y.S., Delannay, L., Van Houtte, P., 2002. Application of the Lamel model for simulating cold rolling texture in molybdenum sheet. *Acta Mater.* 50, 1849–1856. [https://doi.org/10.1016/S1359-6454\(02\)00037-X](https://doi.org/10.1016/S1359-6454(02)00037-X)
- Lusk, M.T., 1999. A phase-field paradigm for grain growth and recrystallization. *Proc. R. Soc. A Math. Phys. Eng. Sci.* 455, 677–700. <https://doi.org/10.1098/rspa.1999.0329>
- Madej, L., Sitko, M., Perzynski, K., Sieradzki, L., Radwanski, K., Kuziak, R., 2016. Multi scale cellular automata and finite element based model for cold deformation and annealing of a ferritic-pearlitic microstructure. *Multiscale Mater. Model. Approaches to Full Multiscaling* 77, 235–254. https://doi.org/10.1515/9783110412451_014
- Mahesh, S., 2010. A binary-tree based model for rate-independent polycrystals. *Int. J. Plast.* 26, 42–64. <https://doi.org/10.1016/j.ijplas.2009.05.002>
- Marciniak, Z., Kuczyński, K., 1967. Limit strains in the processes of stretch-forming sheet metal. *Int. J. Mech. Sci.* 9, 609–620. [https://doi.org/10.1016/0020-7403\(67\)90066-5](https://doi.org/10.1016/0020-7403(67)90066-5)
- Marciniak, Z., Kuczyński, K., Pokora, T., 1973. Influence of the plastic properties of a material on the forming limit diagram for sheet metal in tension. *Int. J. Mech. Sci.* 15, 789–800. [https://doi.org/10.1016/0020-7403\(73\)90068-4](https://doi.org/10.1016/0020-7403(73)90068-4)
- Marks, R.J., 2009. *Handbook of Fourier Analysis & Its Applications*. Oxford University Press. <https://doi.org/>:
- Martin, É., Jonas, J.J., 2010. Evolution of microstructure and microtexture during the hot deformation of Mg-3% Al. *Acta Mater.* 58, 4253–4266. <https://doi.org/10.1016/j.actamat.2010.04.017>
- Merklein, M., Böhm, W., Lechner, M., 2012. Tailoring Material Properties of Aluminum by Local Laser Heat Treatment. *Phys. Procedia* 39, 232–239. <https://doi.org/10.1016/j.phpro.2012.10.034>
- Michel, J.C., Moulinec, H., Suquet, P., 2001. A computational scheme for linear and non-linear composites with arbitrary phase contrast. *Int. J. Numer. Methods Eng.* 52, 139–160. <https://doi.org/10.1002/nme.275>

- Miodownik, M.A., 2002. A review of microstructural computer models used to simulate grain growth and recrystallisation in aluminium alloys. *J. Light Met.* 2, 125–135. [https://doi.org/10.1016/S1471-5317\(02\)00039-1](https://doi.org/10.1016/S1471-5317(02)00039-1)
- Mohammadi, M., Brahme, A.P., Mishra, R.K., Inal, K., 2014. Effects of post-necking hardening behavior and equivalent stress-strain curves on the accuracy of M-K based forming limit diagrams. *Comput. Mater. Sci.* 85, 316–323. <https://doi.org/10.1016/j.commatsci.2014.01.017>
- Molinari, A., Ahzi, S., Kouddane, R., 1997. On the self-consistent modelling of elastic-plastic behavior of polycrystals. *Mech. Mater.* 26, 43–62. [https://doi.org/10.1016/S0167-6636\(97\)00017-3](https://doi.org/10.1016/S0167-6636(97)00017-3)
- Molinari, A., Canova, G.R., Ahzi, S., 1987. A self consistent approach of the large deformation polycrystal viscoplasticity. *Acta Metall.* 35, 2983–2994. [https://doi.org/10.1016/0001-6160\(87\)90297-5](https://doi.org/10.1016/0001-6160(87)90297-5)
- Moulinec, H., Suquet, P., 1998. A numerical method for computing the overall response of nonlinear composites with complex microstructure. *Comput. Methods Appl. Mech. Eng.* 157, 69–94. [https://doi.org/10.1016/S0045-7825\(97\)00218-1](https://doi.org/10.1016/S0045-7825(97)00218-1)
- Moulinec, H., Suquet, P., 1994. A fast numerical method for computing the linear and nonlinear mechanical properties of composites. *Comptes rendus l'Académie des Sci. Série II, Mécanique, Phys. Chim. Astron.* 318, 1417–1423.
- Muhammad, W., Mohammadi, M., Kang, J., Mishra, R.K., Inal, K., 2015. An elasto-plastic constitutive model for evolving asymmetric/anisotropic hardening behavior of AZ31B and ZEK100 magnesium alloy sheets considering monotonic and reverse loading paths. *Int. J. Plast.* 70, 30–59. <https://doi.org/10.1016/j.ijplas.2015.03.004>
- Muramatsu, M., Tadano, Y., Shizawa, K., 2008. A Phase-Field Simulation of Nucleation from Subgrain and Grain Growth in Static Recrystallization. *Mater. Sci. Forum* 584–586, 1045–1050. <https://doi.org/10.4028/www.scientific.net/MSF.584-586.1045>

- Muránsky, O., Carr, D.G., Barnett, M.R., Oliver, E.C., Šittner, P., 2008. Investigation of deformation mechanisms involved in the plasticity of AZ31 Mg alloy: In situ neutron diffraction and EPSC modelling. *Mater. Sci. Eng. A* 496, 14–24. <https://doi.org/10.1016/j.msea.2008.07.031>
- Nagra, J.S., Brahme, A., Lebensohn, R.A., Inal, K., 2017. Efficient fast Fourier transform-based numerical implementation to simulate large strain behavior of polycrystalline materials. *Int. J. Plast.* 98, 65–82. <https://doi.org/10.1016/j.ijplas.2017.07.001>
- Nagra, J.S., Brahme, A., Mishra, R., Lebensohn, R.A., Inal, K., 2018. An efficient full-field crystal plasticity-based M-K framework to study the effect of 3D microstructural features on the formability of polycrystalline materials. *Model. Simul. Mater. Sci. Eng.* 26, 075002. <https://doi.org/10.1088/1361-651X/aadc20>
- Nakashima, K., Nagai, T., Kawasaki, K., 1989. Scaling behavior of two-dimensional domain growth: Computer simulation of vertex models. *J. Stat. Phys.* 57, 759–787. <https://doi.org/10.1007/BF01022831>
- Needleman, A., Tvergaard, V., 1984. Limits of Formability in Rate-Sensitive Metal Sheets., in: *Mechanical Behaviour of Materials*. Elsevier, pp. 51–65. <https://doi.org/10.1016/B978-1-4832-8372-2.50008-7>
- Nemat-Nasser, S., Ni, L., Okinaka, T., 1998. A constitutive model for fee crystals with application to polycrystalline OFHC copper. *Mech. Mater.* 30, 325–341. [https://doi.org/10.1016/S0167-6636\(98\)00055-6](https://doi.org/10.1016/S0167-6636(98)00055-6)
- Nieh, T.G., Hsiung, L.M., Wadsworth, J., Kaibyshev, R., 1998. High strain rate superplasticity in a continuously recrystallized Al-6%Mg-0.3%Sc alloy. *Acta Mater.* 46, 2789–2800. [https://doi.org/10.1016/S1359-6454\(97\)00452-7](https://doi.org/10.1016/S1359-6454(97)00452-7)
- Niewczas, M., 2010. Lattice correspondence during twinning in hexagonal close-packed crystals. *Acta Mater.* 58, 5848–5857. <https://doi.org/10.1016/j.actamat.2010.06.059>

- Ohashi, T., Barabash, R.I., Pang, J.W.L., Ice, G.E., Barabash, O.M., 2009. X-ray microdiffraction and strain gradient crystal plasticity studies of geometrically necessary dislocations near a Ni bicrystal grain boundary. *Int. J. Plast.* 25, 920–941. <https://doi.org/10.1016/j.ijplas.2008.04.009>
- Oppedal, A.L., El Kadiri, H., Tomé, C.N., Kaschner, G.C., Vogel, S.C., Baird, J.C., Horstemeyer, M.F., 2012. Effect of dislocation transmutation on modelling hardening mechanisms by twinning in magnesium. *Int. J. Plast.* 30–31, 41–61. <https://doi.org/10.1016/j.ijplas.2011.09.002>
- Partridge, P.G., 1967. The crystallography and deformation modes of hexagonal close-packed metals. *Metall. Rev.* 12, 169–194. <https://doi.org/10.1179/mtlr.1967.12.1.169>
- Paufler, P., 1994. W. F. Hosford. The mechanics of crystals and textured polycrystals. Oxford University Press, New York–Oxford 1993. 248 Seiten, Preis £ 30,–. ISBN 0-19-507744-X. *Cryst. Res. Technol.* 29, 532–532. <https://doi.org/10.1002/crat.2170290414>
- Peczak, P., 1995. A Monte Carlo study of influence of deformation temperature on dynamic recrystallization. *Acta Metall. Mater.* 43, 1279–1291. [https://doi.org/10.1016/0956-7151\(94\)00280-U](https://doi.org/10.1016/0956-7151(94)00280-U)
- Peirce, D., Asaro, R.J., Needleman, A., 1983. Material rate dependence and localized deformation in crystalline solids. *Acta Metall.* 31, 1951–1976. [https://doi.org/10.1016/0001-6160\(83\)90014-7](https://doi.org/10.1016/0001-6160(83)90014-7)
- Peirce, D., Asaro, R.J., Needleman, A., 1983. Material rate dependence and localized deformation in ductile single crystals. *Acta Met.* 31, 1951–1976.
- Peirce, D., Asaro, R.J., Needleman, A., 1982. An analysis of nonuniform and localized deformation in ductile single crystals. *Acta Metall.* 30, 1087–1119. [https://doi.org/10.1016/0001-6160\(82\)90005-0](https://doi.org/10.1016/0001-6160(82)90005-0)
- Peirce, D., Shih, C.F., Needleman, A., 1984. A tangent modulus method for rate dependent solids. *Comput. Struct.* 18, 875–887. [https://doi.org/10.1016/0045-7949\(84\)90033-6](https://doi.org/10.1016/0045-7949(84)90033-6)
- Piekoś, K., Tarasiuk, J., Wierzbowski, K., Bacroix, B., 2008. Generalized vertex model of recrystallization - Application to polycrystalline copper. *Comput. Mater. Sci.* 42, 584–594. <https://doi.org/10.1016/j.commatsci.2007.09.014>

- Pinna, C., Lan, Y., Kiu, M.F., Efthymiadis, P., Lopez-Pedrosa, M., Farrugia, D., 2015. Assessment of crystal plasticity finite element simulations of the hot deformation of metals from local strain and orientation measurements. *Int. J. Plast.* 73, 24–38. <https://doi.org/10.1016/j.ijplas.2015.05.015>
- Pond, R.C., Casey, S.M., 1992. Topological Theory of Line-Defects on Crystal Surfaces, and their Interactions with Bulk and Interfacial Defects, in: *Equilibrium Structure and Properties of Surfaces and Interfaces*. Springer US, Boston, MA, pp. 139–174. https://doi.org/10.1007/978-1-4615-3394-8_6
- Popova, E., Brahme, A.P., Staraselski, Y., Agnew, S.R., Mishra, R.K., Inal, K., 2016. Effect of extension {1012} twins on texture evolution at elevated temperature deformation accompanied by dynamic recrystallization. *Mater. Des.* 96, 446–457. <https://doi.org/10.1016/j.matdes.2016.02.042>
- Popova, E., Staraselski, Y., Brahme, A., Mishra, R.K., Inal, K., 2015. Coupled crystal plasticity - Probabilistic cellular automata approach to model dynamic recrystallization in magnesium alloys. *Int. J. Plast.* 66, 85–102. <https://doi.org/10.1016/j.ijplas.2014.04.008>
- Pouriaeyevali, H., Xu, B.X., 2017. Decomposition of dislocation densities at grain boundary in a finite-deformation gradient crystal-plasticity framework. *Int. J. Plast.* 96, 36–55. <https://doi.org/10.1016/j.ijplas.2017.04.010>
- Prakash, A., Lebensohn, R.A., 2009. Simulation of micromechanical behavior of polycrystals: Finite elements versus fast Fourier transforms. *Model. Simul. Mater. Sci. Eng.* 17, 064010. <https://doi.org/10.1088/0965-0393/17/6/064010>
- Proust, G., Tomé, C.N., Jain, A., Agnew, S.R., 2009. Modeling the effect of twinning and detwinning during strain-path changes of magnesium alloy AZ31. *Int. J. Plast.* 25, 861–880. <https://doi.org/10.1016/j.ijplas.2008.05.005>
- Qiao, H., Barnett, M.R., Wu, P.D., 2016. Modeling of twin formation, propagation and growth in a Mg single crystal based on crystal plasticity finite element method. *Int. J. Plast.* 86, 70–92. <https://doi.org/10.1016/j.ijplas.2016.08.002>

Quey, R., Dawson, P.R., Barbe, F., 2011. Large-scale 3D random polycrystals for the finite element method: Generation, meshing and remeshing. *Comput. Methods Appl. Mech. Eng.* 200, 1729–1745. <https://doi.org/10.1016/j.cma.2011.01.002>

Raabe, D., 2002. Cellular Automata in Materials Science with Particular Reference to Recrystallization Simulation. *Annu. Rev. Mater. Res.* 32, 53–76. <https://doi.org/10.1146/annurev.matsci.32.090601.152855>

Raabe, D., Roters, F., 2004. Using texture components in crystal plasticity finite element simulations. *Int. J. Plast.* 20, 339–361. [https://doi.org/10.1016/S0749-6419\(03\)00092-5](https://doi.org/10.1016/S0749-6419(03)00092-5)

Rai, R., Peng, G., Li, K., Lin, S.Y., 2007. DNA damage response: The players, the network and the role in tumor suppression. *Cancer Genomics and Proteomics* 4, 99–106. [https://doi.org/10.1016/0001-6160\(84\)90151-2](https://doi.org/10.1016/0001-6160(84)90151-2)

Rao, K.R., Kim, D.N., Hwang, J.-J., 2010. Fast Fourier Transform - Algorithms and Applications, Signals and Communication Technology. Springer Netherlands, Dordrecht. <https://doi.org/10.1007/978-1-4020-6629-0>

Raphanel, J.L., Van Houtte, P., 1985. Simulation of the rolling textures of b.c.c. metals by means of the relaxed taylor theory. *Acta Metall.* 33, 1481–1488. [https://doi.org/10.1016/0001-6160\(85\)90049-5](https://doi.org/10.1016/0001-6160(85)90049-5)

Rashid, M.M., Nemat-Nasser, S., 1992. A constitutive algorithm for rate-dependent crystal plasticity. *Comput. Methods Appl. Mech. Eng.* 94, 201–228. [https://doi.org/10.1016/0045-7825\(92\)90147-C](https://doi.org/10.1016/0045-7825(92)90147-C)

Read, W.T., Shockley, W., 1950. Dislocation models of crystal grain boundaries. *Phys. Rev.* 78, 275–289. <https://doi.org/10.1103/PhysRev.78.275>

Reinhart, G., Mangelinck-Noël, N., Nguyen-Thi, H., Schenk, T., Gastaldi, J., Billia, B., Pino, P., Härtwig, J., Baruchel, J., 2005. Investigation of columnar-equiaxed transition and equiaxed growth of aluminium based alloys by X-ray radiography. *Mater. Sci. Eng. A* 413–414, 384–388. <https://doi.org/10.1016/j.msea.2005.08.197>

- Rémy, L., 1981. The interaction between slip and twinning systems and the influence of twinning on the mechanical behavior of fcc metals and alloys. *Metall. Trans. A* 12, 387–408. <https://doi.org/10.1007/BF02648536>
- Resk, H., Delannay, L., Bernacki, M., Coupez, T., Logé, R., 2009. Adaptive mesh refinement and automatic remeshing in crystal plasticity finite element simulations. *Model. Simul. Mater. Sci. Eng.* 17, 75012. <https://doi.org/10.1088/0965-0393/17/7/075012>
- Rice, J.R., 1971. Inelastic constitutive relations for solids: An internal-variable theory and its application to metal plasticity. *J. Mech. Phys. Solids* 19, 433–455. [https://doi.org/10.1016/0022-5096\(71\)90010-X](https://doi.org/10.1016/0022-5096(71)90010-X)
- Richards, J.W., 1900. A treatise on crystallography, *Journal of the American Chemical Society*. Cambridge: Printed at the Pitt Press, for J. & J.J. Deighton. <https://doi.org/10.1021/ja02042a023>
- Roberts, W., Ahlblom, B., 1978. A nucleation criterion for dynamic recrystallization during hot working. *Acta Metall.* 26, 801–813. [https://doi.org/10.1016/0001-6160\(78\)90030-5](https://doi.org/10.1016/0001-6160(78)90030-5)
- Rollett, A., Humphreys, F., Rohrer, G.S., Hatherly, M., 2004. Recrystallization and Related Annealing Phenomena: Second Edition, *Recrystallization and Related Annealing Phenomena: Second Edition*. Elsevier. <https://doi.org/10.1016/B978-0-08-044164-1.X5000-2>
- Rollett, A.D., 1997. Overview of modelling and simulation of recrystallization. *Prog. Mater. Sci.* 42, 79–99. [https://doi.org/10.1016/S0079-6425\(97\)00008-X](https://doi.org/10.1016/S0079-6425(97)00008-X)
- Rollett, A.D., Luton, M.J., Srolovitz, D.J., 1992. Microstructural simulation of dynamic recrystallization. *Acta Metall. Mater.* 40, 43–55. [https://doi.org/10.1016/0956-7151\(92\)90198-N](https://doi.org/10.1016/0956-7151(92)90198-N)
- Rossiter, J., Brahme, A., Simha, M.H., Inal, K., Mishra, R., 2010. A new crystal plasticity scheme for explicit time integration codes to simulate deformation in 3D microstructures: Effects of strain path, strain rate and thermal softening on localized deformation in the aluminum alloy 5754 during simple shear. *Int. J. Plast.* 26, 1702–1725. <https://doi.org/10.1016/j.ijplas.2010.02.007>

Roters, F., Eisenlohr, P., Bieler, T.R., Raabe, D., 2010. Crystal Plasticity Finite Element Methods: In Materials Science and Engineering, Crystal Plasticity Finite Element Methods: In Materials Science and Engineering. Wiley-Blackwell. <https://doi.org/10.1002/9783527631483>

Roters, F., Eisenlohr, P., Hantcherli, L., Tjahjanto, D.D., Bieler, T.R., Raabe, D., 2010. Overview of constitutive laws, kinematics, homogenization and multiscale methods in crystal plasticity finite-element modelling: Theory, experiments, applications. *Acta Mater.* 58, 1152–1211. <https://doi.org/10.1016/j.actamat.2009.10.058>

Roters, F., Eisenlohr, P., Kords, C., Tjahjanto, D.D., Diehl, M., Raabe, D., 2012. DAMASK: The düsseldorf advanced material simulation kit for studying crystal plasticity using an fe based or a spectral numerical solver. *Procedia IUTAM* 3, 3–10. <https://doi.org/10.1016/j.piutam.2012.03.001>

Sachs, G., 1928. Zur ableitung einer gleissbedingung 72, 734.

Salem, A.A., Kalidindi, S.R., Doherty, R.D., 2003. Strain hardening of titanium: Role of deformation twinning. *Acta Mater.* 51, 4225–4237. [https://doi.org/10.1016/S1359-6454\(03\)00239-8](https://doi.org/10.1016/S1359-6454(03)00239-8)

Samuha, S., Kahana, E., Sadot, O., Shneck, R.Z., 2018. Improved formability of Mg-AZ80 alloy under a high strain rate in expanding-ring experiments. *Materials (Basel)*. 11, 329. <https://doi.org/10.3390/ma11020329>

Sandström, R., Lagneborg, R., 1975. A controlling factor for dynamic recrystallisation. *Scr. Metall.* 9, 59–65. [https://doi.org/10.1016/0036-9748\(75\)90146-5](https://doi.org/10.1016/0036-9748(75)90146-5)

Sandström, R., 1977. Subgrain growth occurring by boundary migration. *Acta Metall.* 25, 905–911. [https://doi.org/10.1016/0001-6160\(77\)90177-8](https://doi.org/10.1016/0001-6160(77)90177-8)

Schwartz, J.T., von Neumann, J., Burks, A.W., 1967. Theory of Self-Reproducing Automata. *Math. Comput.* <https://doi.org/10.2307/2005041>

Schwindt, C., Schlosser, F., Bertinetti, M.A., Stout, M., Signorelli, J.W., 2015. Experimental and Visco-Plastic Self-Consistent evaluation of forming limit diagrams for anisotropic sheet metals:

An efficient and robust implementation of the M-K model. *Int. J. Plast.* 73, 62–99. <https://doi.org/10.1016/j.ijplas.2015.01.005>

Serenelli, M.J., Bertinetti, M.A., Signorelli, J.W., 2011. Study of limit strains for FCC and BCC sheet metal using polycrystal plasticity. *Int. J. Solids Struct.* 48, 1109–1119. <https://doi.org/10.1016/j.ijsolstr.2010.12.013>

Seyed Salehi, M., Serajzadeh, S., 2012. Simulation of static recrystallization in non-isothermal annealing using a coupled cellular automata and finite element model. *Comput. Mater. Sci.* 53, 145–152. <https://doi.org/10.1016/j.commatsci.2011.09.026>

Shanthraj, P., Eisenlohr, P., Diehl, M., Roters, F., 2015. Numerically robust spectral methods for crystal plasticity simulations of heterogeneous materials. *Int. J. Plast.* 66, 31–45. <https://doi.org/10.1016/j.ijplas.2014.02.006>

Shiryayev, A.N., 1992. On The Statistical Theory of Metal Crystallization, in: *Selected Works of A. N. Kolmogorov*. Springer Netherlands, Dordrecht, pp. 188–192. https://doi.org/10.1007/978-94-011-2260-3_22

Signorelli, J.W., Bertinetti, M. de los A., 2012. Self-Consistent Homogenization Methods for Predicting Forming Limits of Sheet Metal. *Met. Form. - Process. Tools, Des.* 175–210. <https://doi.org/http://dx.doi.org/10.5772/50662>

Signorelli, J.W., Bertinetti, M.A., 2009. On the role of constitutive model in the forming limit of FCC sheet metal with cube orientations. *Int. J. Mech. Sci.* 51, 473–480. <https://doi.org/10.1016/j.ijmecsci.2009.04.002>

Signorelli, J.W., Bertinetti, M.A., Turner, P.A., 2009. Predictions of forming limit diagrams using a rate-dependent polycrystal self-consistent plasticity model. *Int. J. Plast.* 25, 1–25. <https://doi.org/10.1016/j.ijplas.2008.01.005>

Signorelli, J.W., Serenelli, M.J., Bertinetti, M.A., 2012. Experimental and numerical study of the role of crystallographic texture on the formability of an electro-galvanized steel sheet. *J. Mater. Process. Technol.* 212, 1367–1376. <https://doi.org/10.1016/j.jmatprotec.2012.01.020>

Sivakesavam, O., Rao, I.S., Prasad, Y.V.R.K., 1993. Processing map for hot working of as cast magnesium. *Mater. Sci. Technol.* 9, 805–810.

Spowart, J.E., Mullens, H.M., Puchala, B.T., 2003. Collecting and Analyzing Microstructures in Three Dimensions: A Fully Automated Approach. *Jom* 55, 35–37. <https://doi.org/10.1007/s11837-003-0173-0>

Srolovitz, D.J., Grest, G.S., Anderson, M.P., Rollett, A.D., 1988. Computer simulation of recrystallization-II. Heterogeneous nucleation and growth. *Acta Metall.* 36, 2115–2128. [https://doi.org/10.1016/0001-6160\(88\)90313-6](https://doi.org/10.1016/0001-6160(88)90313-6)

Steglich, D., Jeong, Y., Andar, M.O., Kuwabara, T., 2012. Biaxial deformation behaviour of AZ31 magnesium alloy: Crystal-plasticity- based prediction and experimental validation. *Int. J. Solids Struct.* 49, 3551–3561. <https://doi.org/10.1016/j.ijsolstr.2012.06.017>

Stören, S., Rice, J.R., 1975. Localized necking in thin sheets. *J. Mech. Phys. Solids* 23, 421–441. [https://doi.org/10.1016/0022-5096\(75\)90004-6](https://doi.org/10.1016/0022-5096(75)90004-6)

Takaki, T., Hisakuni, Y., Hirouchi, T., Yamanaka, A., Tomita, Y., 2009. Multi-phase-field simulations for dynamic recrystallization. *Comput. Mater. Sci.* 45, 881–888. <https://doi.org/10.1016/j.commatsci.2008.12.009>

Takuda, H., Mori, K., Takakura, N., Yamaguchi, K., 2000. Finite element analysis of limit strains in biaxial stretching of sheet metals allowing for ductile fracture. *Int. J. Mech. Sci.* 42, 785–798. [https://doi.org/10.1016/S0020-7403\(99\)00018-1](https://doi.org/10.1016/S0020-7403(99)00018-1)

Tang, C.Y., Tai, W.H., 2000. Material damage and forming limits of textured sheet metals. *J. Mater. Process. Technol.* 99, 135–140. [https://doi.org/10.1016/S0924-0136\(99\)00404-5](https://doi.org/10.1016/S0924-0136(99)00404-5)

Taylor, G.I., 1938. Plastic strain in metals. *J. Inst. Met.* 62, 307–324.

Tikare, V., Holm, E.A., Fan, D., Chen, L.Q., 1998. Comparison of phase-field and potts models for coarsening processes. *Acta Mater.* 47, 363–371. [https://doi.org/10.1016/S1359-6454\(98\)00313-9](https://doi.org/10.1016/S1359-6454(98)00313-9)

Tjahjanto, D.D., Eisenlohr, P., Roters, F., 2015. Multiscale deep drawing analysis of dual-phase steels using grain cluster-based RGC scheme. *Model. Simul. Mater. Sci. Eng.* 23, 45005. <https://doi.org/10.1088/0965-0393/23/4/045005>

Tóth, L.S., Dudzinski, D., Molinari, A., 1996. Forming limit predictions with the perturbation method using stress potential functions of polycrystal viscoplasticity. *Int. J. Mech. Sci.* 38, 805–824. [https://doi.org/10.1016/0020-7403\(95\)00109-3](https://doi.org/10.1016/0020-7403(95)00109-3)

Van Houtte, P., 1982. On the equivalence of the relaxed Taylor theory and the Bishop-Hill theory for partially constrained plastic deformation of crystals. *Mater. Sci. Eng.* 55, 69–77. [https://doi.org/10.1016/0025-5416\(82\)90085-4](https://doi.org/10.1016/0025-5416(82)90085-4)

Van Houtte, P., Delannay, L., Kalidindi, S.R., 2002. Comparison of two grain interaction models for polycrystal plasticity and deformation texture prediction. *Int. J. Plast.* 18, 359–377. [https://doi.org/10.1016/S0749-6419\(00\)00102-9](https://doi.org/10.1016/S0749-6419(00)00102-9)

Van Houtte, P., Delannay, L., Samajdar, I., 1999. Quantitative prediction of cold rolling textures in low-carbon steel by means of the LAMEL model. *Textures Microstruct.* 31, 109–149. <https://doi.org/10.1155/TSM.31.109>

Van Houtte, P., Li, S., Seefeldt, M., Delannay, L., 2005. Deformation texture prediction: From the Taylor model to the advanced Lamel model. *Int. J. Plast.* 21, 589–624. <https://doi.org/10.1016/j.ijplas.2004.04.011>

Vitek, V., Mrovec, M., Bassani, J.L., 2004. Influence of non-glide stresses on plastic flow: From atomistic to continuum modelling. *Mater. Sci. Eng. A* 365, 31–37. <https://doi.org/10.1016/j.msea.2003.09.004>

Vondřejc, J., Zeman, J., Marek, I., 2014. An FFT-based Galerkin method for homogenization of periodic media. *Comput. Math. with Appl.* 68, 156–173. <https://doi.org/10.1016/j.camwa.2014.05.014>

- Wang, H., Wu, P.D., Boyle, K.P., Neale, K.W., 2011. On crystal plasticity formability analysis for magnesium alloy sheets. *Int. J. Solids Struct.* 48, 1000–1010. <https://doi.org/10.1016/j.ijsolstr.2010.12.004>
- Wang, H., Wu, P.D., Tomé, C.N., Huang, Y., 2010. A finite strain elastic-viscoplastic self-consistent model for polycrystalline materials. *J. Mech. Phys. Solids* 58, 594–612. <https://doi.org/10.1016/j.jmps.2010.01.004>
- Wang, K., Lu, S., Mi, G., Li, C., Fu, H., 2010. Simulation of microstructural evolution in directional solidification of Ti-45.%Al alloy using cellular automation method. *China Foundry* 7, 47–51.
- Wang, L., Qiao, Q., Liu, Y., Song, X., 2013. Formability of AZ31 Mg alloy sheets within medium temperatures. *J. Magnes. Alloy.* 1, 312–317. <https://doi.org/10.1016/j.jma.2014.01.001>
- Wen, X.Y., Lee, W.B., 2000. Textures of Sheet in AA3003 Aluminum Alloy Under Biaxial Stretching. *Textures Microstruct.* 34, 217–225. <https://doi.org/10.1155/TSM.34.217>
- Wickramarachchi, S.J., Ikeda, T., Dassanayake, B.S., Keerthisinghe, D., Tanis, J.A., 2016. Incident energy and charge deposition dependences of electron transmission through a micro-sized tapered glass capillary. *Nucl. Instruments Methods Phys. Res. Sect. B Beam Interact. with Mater. Atoms* 382, 60–66. <https://doi.org/10.1016/j.nimb.2016.06.006>
- Wu, P.D., MacEwen, S.R., Lloyd, D.J., Neale, K.W., 2004. A mesoscopic approach for predicting sheet metal formability. *Model. Simul. Mater. Sci. Eng.* 12, 511–527. <https://doi.org/10.1088/0965-0393/12/3/011>
- Wu, P.D., Neale, K.W., Van Der Giessen, E., 1997. On crystal plasticity FLD analysis. *Proc. R. Soc. A Math. Phys. Eng. Sci.* 453, 1831–1848. <https://doi.org/10.1098/rspa.1997.0099>
- Wu, P.D., Neale, K.W., Van Der Giessen, E., 1996. Simulation of the behaviour of FCC polycrystals during reversed torsion. *Int. J. Plast.* 12, 1199–1219. [https://doi.org/10.1016/S0749-6419\(96\)00048-4](https://doi.org/10.1016/S0749-6419(96)00048-4)

Xia, K., Wang, J.T., Wu, X., Chen, G., Gurvan, M., 2005. Equal channel angular pressing of magnesium alloy AZ31. *Mater. Sci. Eng. A* 410–411, 324–327. <https://doi.org/10.1016/j.msea.2005.08.123>

Yamanaka, A., 2016. Multiscale Modelling of Sheet Metal Forming, *Journal of the Japan Society for Technology of Plasticity*, ESAFORM Bookseries on Material Forming. Springer International Publishing, Cham. <https://doi.org/10.9773/sosei.57.209>

Yang, H., Yin, S., Huang, C., Zhang, Z., Wu, S., Li, S., Liu, Y., 2008. EBSD study on deformation twinning in AZ31 magnesium alloy during quasi-in-situ compression. *Adv. Eng. Mater.* 10, 955–960. <https://doi.org/10.1002/adem.200800111>

Yoshida, K., 2015. Prediction of ductile fracture induced by contraction twinning in AZ31 sheet subjected to uniaxial and biaxial stretching modes. *Int. J. Plast.* 84, 102–137. <https://doi.org/10.1016/j.ijplas.2016.05.004>

Yoshida, K., 2014. Effects of grain-scale heterogeneity on surface roughness and sheet metal necking. *Int. J. Mech. Sci.* 83, 48–56. <https://doi.org/10.1016/j.ijmecsci.2014.03.018>

Yoshida, K., Ishizaka, T., Kuroda, M., Ikawa, S., 2007. The effects of texture on formability of aluminum alloy sheets. *Acta Mater.* 55, 4499–4506. <https://doi.org/10.1016/j.actamat.2007.04.014>

Zeman, J., Vondřejc, J., Novák, J., Marek, I., 2010. Accelerating a FFT-based solver for numerical homogenization of periodic media by conjugate gradients, *Journal of Computational Physics*. <https://doi.org/10.1016/j.jcp.2010.07.010>

Zeng, W., Larsen, J.M., Liu, G.R., 2014. Smoothing technique based crystal plasticity finite element modelling of crystalline materials. *Int. J. Plast.* 65, 250–268. <https://doi.org/10.1016/j.ijplas.2014.09.007>

Zhang, C., Li, H., Eisenlohr, P., Liu, W., Boehlert, C.J., Crimp, M.A., Bieler, T.R., 2015. Effect of realistic 3D microstructure in crystal plasticity finite element analysis of polycrystalline Ti-5Al-2.5Sn. *Int. J. Plast.* 69, 21–35. <https://doi.org/10.1016/j.ijplas.2015.01.003>

Zhang, K.F., Yin, D.L., Wu, D.Z., 2006. Formability of AZ31 magnesium alloy sheets at warm working conditions. *Int. J. Mach. Tools Manuf.* 46, 1276–1280. <https://doi.org/10.1016/j.ijmachtools.2006.01.014>

Zhou, Y., Neale, K.W., 1995. Predictions of forming limit diagrams using a rate-sensitive crystal plasticity model. *Int. J. Mech. Sci.* 37, 1–20. [https://doi.org/10.1016/0020-7403\(94\)00052-L](https://doi.org/10.1016/0020-7403(94)00052-L)

Zienkiewicz, O., Taylor, R., Zhu, J.Z., 1977. *The Finite Element method*, CRC Press.

Appendix - A. Comparison of RTCP-FFT Model with CP-FEM Model

In section 3.3, the verification case is presented in which the predictions using developed model (RTCP-FFT) are compared with those obtained from EVP-FFT (Lebensohn et al., 2012) model at very low strain values (elasto-viscoplastic transition region) by matching stress-strain curves for a copper polycrystal and then comparing predictions for an artificial polycrystal. In order to ascertain the capability of the new RTCP-FFT model to simulate large strain behavior, a numerical experiment comparing the RTCP-FFT and CP-FEM was performed.

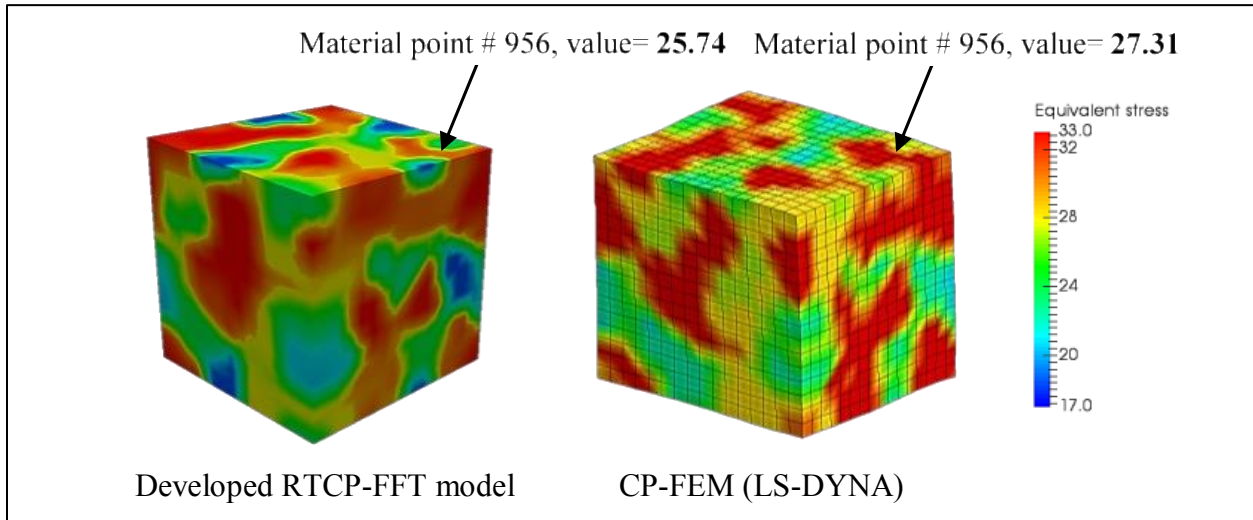


Figure AA - 1: Comparison of local distribution of equivalent stress at 9% true strain in uniaxial tension, results show that the developed model (RTCP-FFT) is in good agreement with CP-FEM model.

To compare the predictions of micromechanical fields at large strains, the case of copper polycrystal, from the verification case mentioned above, is extended up to 9% tensile strain. In this case, results from CP-FEM code are chosen as a benchmark. The comparison of predicted local stress distribution in the RVE is shown in Figure AA - 1. Note that the same microstructure is simulated using CP-FEM code (UMAT) in LS-DYNA. The predicted local stress distribution using the developed model (RTCP-FFT) are in good agreement with CP-FEM. This study verifies that the developed model can capture both elasto-viscoplastic transition (at very low strain) as well as large strain behavior accurately.